SEISMIC IMAGING OF THE VELOCITY STRUCTURE AND THE LOCATION OF A HYDROFRAC IN A GEOTHERMAL RESERVOIR

by

Lisa V. Block and C.H. Cheng

Earth Resources Laboratory
Department of Earth, Atmospheric, and Planetary Sciences
Massachusetts Institute of Technology
Cambridge, MA 02139

Michael C. Fehler and W. Scott Phillips

Los Alamos National Laboratory
Los Alamos, NM 87545

ABSTRACT

The Los Alamos Hot Dry Rock Reservoir is an experimental geothermal project in north–central New Mexico. A fractured zone was created within otherwise impermeable igneous and metamorphic rock by injecting water into a borehole under high pressure, at about 3.5 km depth. During the injection process, the seismic waves created by the fracturing events were recorded by seismometers located in four nearby boreholes. A subset of the arrival times from these microearthquakes is iteratively inverted for the three-dimensional P-wave and S-wave velocity structures and the hypocenter parameters, using the separation of parameters technique. The inversion results indicate that the P-wave and S-wave velocities decrease by at least 20% within the fractured zone. Also, the hypocenters are rotated into a more compact distribution relative to the initial locations found using a homogeneous velocity model, suggesting that the hypocenter locations are significantly improved.

INTRODUCTION

The "hot dry rock", or "HDR", concept consists of extracting heat energy from the earth's crust by circulating water through man-made fractures between two deep wellbores, within otherwise "impermeable" rock (Harlow and Pracht, 1972). While the fractured "reservoir" is being created (by hydrofracturing), geophones may be used to monitor the induced microseismic events. The purpose of this study is to invert the

arrival times from these microearthquakes to determine the three-dimensional P-wave and S-wave velocity structures of the fractured region and the hypocenter coordinates. There are two objectives. First, this type of joint velocity-hypocenter inversion should yield more accurate hypocenter locations than can be obtained by simply locating the earthquakes using a homogeneous velocity model. These locations can be used in a scheme, such as the procedure developed by Fehler et al. (1987), to estimate the orientations of the major seismically-active fracture planes. Secondly, the velocities obtained from the inversion may give some direct insights into reservoir characteristics which can constrain models used to predict reservoir performance.

Background

The Los Alamos Hot Dry Rock Project was initiated in 1973 to develop the technology and procedures for making the HDR concept feasible. The project is funded by the U.S. Department of Energy and is administered by the Los Alamos National Laboratory. The Los Alamos HDR site is located at Fenton Hill, about 30 miles west of Los Alamos, New Mexico. This region is located on the boundary between the Colorado Plateau and the Rio Grande Rift, as shown in Figure 1. The area has undergone recent volcanic activity, with major caldera collapses occurring 1.4 Ma, forming the Toledo Caldera, and 1.1 Ma, forming the approximately coincident Valles Caldera. A simplified geologic cross section of the HDR site, adapted from Laughlin et al. (1983), is shown in Figure 3. The uppermost formation, the Bandelier Tuff, was deposited when the Toledo and Valles Calderas collapsed. Underlying the Bandalier Tuff are the volcanic Paliza Canyon and Abiquiu Formations and the sedimentary Abo and Magdalena Formations. The Precambrian basement, composed of silicic igneous and metamorphic rocks, lies at a depth of about 730 m at the Fenton Hill site. These impermeable crystalline rocks, in a region of high thermal gradient, provide an ideal setting for a hot dry rock reservoir.

The Los Alamos HDR Project has developed in two major stages. A preliminary "research system", known as the Phase I system, was developed during the 1970's. It was a fairly small reservoir, lying between about 2.6 and 3.0 km in depth (See Figure 3.) Beginning in 1980, two wells were drilled to approximately 4 km depth for development of the larger Phase II system. In 1982 hydrofracturing of the Phase II system began. Several fracturing experiments were carried out to create a large reservoir and to connect the injection well, known as EE-2, to the recovery well, EE-3. During these fracturing experiments, many microearthquakes were recorded at geophones located in nearby boreholes. Data from one of these experiments, called Experiment 2032, were chosen for this study. During Experiment 2032, in December of 1983, hydrofracturing was done continuously for 61 hours. Approximately 21,300 m^3 of water were injected with a pumping pressure of about 48 MPa. The injection zone was at a depth of about 3460 m in well EE-2 (Franke and Nunz, 1985). The data collected during this experiment are described below.

METHOD

In this section the joint hypocenter-velocity inversion is described. Tests on synthetic data demonstrate that the joint inversion converges much more quickly than iterating between independent velocity inversion and hypocenter relocation steps. Thurber (1981) also claims that the final solution is less sensitive to the starting model when the joint inversion is performed. The joint hypocenter-velocity inversion is most efficiently implemented using the separation of parameters technique described by Pavlis and Booker (1980). This technique allows the joint inversion to be implemented by two separate, but coupled, inversion steps: a "modified" velocity inversion that indirectly takes into account the effects of changes in the hypocenter parameters, followed by hypocenter relocation based on the updated velocity model. This algorithm enables a large number of events to be included in the inversion without requiring a correspondingly large amount of computer memory.

Since there are many combinations of earthquake locations, origin times, and velocities which may yield approximately the same arrival time root-mean-square residuals (due to incomplete ray coverage and/or noise in the data), it is very helpful to apply additional constraints to the inversion. Three types of constraints are applied to the velocity models. To prevent wild fluctuations in the velocity structures at poorly resolved nodes, a smoothness constraint is added. This is accomplished by minimizing the spatial velocity derivatives in addition to the arrival time residuals. This method is referred to as regularization and has been utilized by a number of authors (Shaw and Orcutt, 1985; Lees, 1989; Scales et al., 1990; Phillips and Fehler, 1991). Another constraint is applied to keep the velocities within specified bounds. It is implemented by applying a penalty for velocities which fall outside the desired range, and then minimizing the penalties during the subsequent iteration.

The velocity inversion is solved via the constrained least squares method, and then the hypocenters are relocated using simple, undamped least squares. Resolution and covariance matrices are derived separately for the two inversion steps. The chapter concludes with a discussion on estimating the variance of the noise in the data.

The Joint Hypocenter-Velocity Formulation

The nonlinear joint hypocenter-velocity inversion is solved by iterating the linearized problem. The linearized inversion is constructed as follows. Let t_{obs} = an observed arrival time (either P or S); t_{calc} = the calculated arrival time, based on initial estimates of the velocity structure, earthquake location and origin time, and station correction; and r = the residual = $t_{obs} - t_{calc}$. The goal is to change the model parameters so that

the new calculated arrival time, $t_{calc} + \Delta t_{calc}$, is equal to the observed arrival time:

$$t_{calc} + \Delta t_{calc} = t_{obs},$$

or equivalently:

$$\Delta t_{calc} = t_{obs} - t_{calc} = r. \tag{1}$$

Expanding Δt_{calc} in terms of changes in the model parameters and keeping only the first order terms gives:

$$\Delta t_o + \frac{\partial t}{\partial x}\Delta x + \frac{\partial t}{\partial y}\Delta y + \frac{\partial t}{\partial z}\Delta z + \sum_{j=1}^{nnode} \frac{\partial t}{\partial v_j}\Delta v_j + \Delta sc = r, \tag{2}$$

where t_o is the earthquake origin time, x, y, and z are the hypocenter coordinates, v_j is the velocity of the jth node, *nnode* is the number of velocity nodes in the inversion grid, and *sc* is the station correction. All of the observations for one earthquake, say for the i^{th} earthquake, yield a set of equations which can be put into matrix form:

$$\begin{bmatrix} 1 & \partial t_1/\partial x_i & \partial t_1/\partial y_i & \partial t_1/\partial z_i \\ . & . & . & . \\ . & . & . & . \\ . & . & . & . \\ 1 & \partial t_{narr}/\partial x_i & \partial t_{narr}/\partial y_i & \partial t_{narr}/\partial z_i \end{bmatrix} \begin{bmatrix} \Delta t_{oi} \\ \Delta x_i \\ \Delta y_i \\ \Delta z_i \end{bmatrix} +$$

$$\begin{bmatrix} \partial t_1/\partial v_1^P & - & \partial t_1/\partial v_{nnode}^P & \partial t_1/\partial v_1^S & - & \partial t_1/\partial v_{nnode}^S \\ . & - & . & . & - & . \\ . & - & . & . & - & . \\ . & - & . & . & - & . \\ \partial t_{narr}/\partial v_1^P & - & \partial t_{narr}/\partial v_{nnode}^P & \partial t_{narr}/\partial v_1^S & - & \partial t_{narr}/\partial v_{nnode}^S \\ \partial t_1/\partial sc_1^P & - & \partial t_1/\partial sc_{nsta}^P & \partial t_1/\partial sc_1^S & - & \partial t_1/\partial sc_{nsta}^S \\ . & - & . & . & - & . \\ . & - & . & . & - & . \\ . & - & . & . & - & . \\ \partial t_{narr}/\partial sc_1^P & - & \partial t_{narr}/\partial sc_{nsta}^P & \partial t_{narr}/\partial sc_1^S & - & \partial t_{narr}/\partial sc_{nsta}^S \end{bmatrix} \begin{bmatrix} \Delta v_1^P \\ | \\ \Delta v_{nnode}^P \\ \Delta v_1^S \\ | \\ \Delta v_{nnode}^S \\ \Delta sc_1^P \\ | \\ \Delta sc_{nsta}^P \\ \Delta sc_1^S \\ | \\ \Delta sc_{nsta}^S \end{bmatrix}$$

$$= \begin{bmatrix} r_1 \\ . \\ . \\ . \\ r_{narr} \end{bmatrix},$$

expressed concisely by:

$$\mathbf{H_i}\underline{\triangle h_i} + \mathbf{M_i}\underline{\triangle m} = \underline{r_i}. \tag{3}$$

narr is the number of arrival times recorded for the event, and *nsta* is the number of stations. $\mathbf{M_i}$ is a sparse matrix. For a particular row, the only nonzero partial derivatives with respect to velocity are those which correspond to nodes along the ray path for the appropriate phase. Only the station correction partial derivative corresponding to the appropriate station and phase is nonzero and has a value of +1. The velocity and hypocenter partial derivatives are computed analytically as described in the next section.

For an inversion which finds the V_S/V_P ratios, rather than the S-wave velocities, the partial derivatives of the S-wave travel times with respect to the S-wave velocities are replaced by the partial derivatives of the S-wave travel times with respect to the V_S/V_P ratios. Also, in this case, the partial derivatives of the S-wave travel times with respect to the P-wave velocities are nonzero. These issues are discussed in more detail in the next section.

In general, observed P arrival times are more precise than S arrival times and are therefore often given greater weighting in arrival-time inversions. Data weighting may be incorporated at this step by multiplying each row of Eq. (3) by an appropriate constant. Ideally, this constant should be equal to the inverse of the standard deviation of the corresponding observed arrival time (Hatton et al., 1986). However, since the standard deviation of an individual arrival time is usually not known, one can implement a more general weighting scheme by weighting all of the P observations by the same constant.

Separation of Parameters

Let t_{obs} = an observed arrival time, t_{calc} = the calculated arrival time based on an initial model, and r = the residual = $t_{obs} - t_{calc}$. The goal is to perturb the model parameters so that the change in the calculated arrival time, $\triangle t_{calc}$, is equal to the residual r. Expanding $\triangle t_{calc}$ in terms of changes in the model parameters and keeping only the first order terms gives:

$$r = \triangle t_{calc} = \triangle t_o + \frac{\partial t}{\partial x}\triangle x + \frac{\partial t}{\partial y}\triangle y + \frac{\partial t}{\partial z}\triangle z + \sum_{j=1}^{nvel}\frac{\partial t}{\partial v_j}\triangle v_j + \triangle sc, \tag{4}$$

where t_o, x, y, and z are the hypocenter parameters, v_j is the velocity at the jth node, and *sc* is the station correction. All of the observations for one earthquake, say for the i^{th} earthquake, yield a set of equations which can be put into matrix form:

$$\underline{r_i} = \mathbf{H_i}\,\underline{\triangle h_i} + \mathbf{M_i}\,\underline{\triangle m}. \tag{5}$$

$\underline{r_i}$ contains the residuals, $\mathbf{H_i}$ contains the hypocenter partial derivatives, and $\mathbf{M_i}$ contains the velocity and station correction partial derivatives. The vectors $\underline{\triangle h_i}$ and $\underline{\triangle m}$ contain the hypocenter perturbations and the velocity and station correction perturbations, respectively.

If there are more than 4 observed arrival times, then there exists a matrix $\mathbf{T_i}$ such that $\mathbf{T_i^T H_i} = 0$. (Pavlis and Booker, 1980; Thurber, 1983). Multiplying both sides of Eq. (5) by $\mathbf{T_i^T}$ gives:

$$\mathbf{T_i^T}\,\underline{r_i} = \mathbf{T_i^T}\,\mathbf{M_i}\,\underline{\triangle m},$$

or

$$\underline{r_i'} = \mathbf{M_i'}\,\underline{\triangle m}. \tag{6}$$

This procedure is done for each earthquake and then the results are combined into one matrix equation:

$$\underline{r'} = \begin{bmatrix} \underline{r_1'} \\ \underline{r_2} \\ | \\ \underline{r'_{nquake}} \end{bmatrix} = \begin{bmatrix} \mathbf{M_1'} \\ \mathbf{M_2'} \\ | \\ \mathbf{M'_{nquake}} \end{bmatrix} \underline{\triangle m} = \mathbf{M'}\,\underline{\triangle m}. \tag{7}$$

Velocity and station correction perturbations are computed by constrained least squares, and then the hypocenters are relocated using the revised model. The entire process is repeated until the root mean square arrival time residuals are no longer improving significantly, typically 10 to 15 iterations.

Constraints

Since the joint hypocenter-velocity inversion is very non-unique, it is necessary to constrain the model. An easy and effective constraint to apply is to require the P-wave and S-wave velocity models to be "smooth" using the method of regularization. In addition to minimizing the arrival time residuals, the second derivatives of the P-wave and S-wave velocities in the x, y, and z directions are also minimized. The second velocity derivatives after one inversion step may be expressed as a matrix equation involving the solution vector of velocity perturbations, $\underline{\triangle m}$:

$$\textit{Second Derivatives} = \underline{c} + \mathbf{K}\,\underline{\triangle m}, \tag{8}$$

where $\underline{c}$ contains the second velocity derivatives before the iteration, and $\mathbf{K}$ contains numerical second derivative operators.

A constraint is also applied to keep the P-wave and S-wave velocity values within specified ranges. Specifically, the velocity values are not allowed to be larger than the velocities of the unfractured basement rock. These upper velocity bounds are applied

by computing a penalty for each velocity which is larger than the maximum allowable velocities and then minimizing these penalties. A simple linear penalty function works well:

$$P(v) = \begin{cases} A(v - v_{max}) & v > v_{max} \\ 0 & v \leq v_{max} \end{cases} . \tag{9}$$

The penalties after an inversion step may be expressed in terms of the solution vector $\underline{\triangle m}$:

$$Penalties = \underline{p} + \partial \mathbf{P}\, \underline{\triangle m}, \tag{10}$$

where $\underline{p}$ contains the penalties before the iteration, and $\partial \mathbf{P}$ is a diagonal matrix containing the partial derivatives of the penalty function with respect to perturbations in the velocities.

The Constrained Least Squares Solution

The constrained least squares solution is found by minimizing:

$$\begin{gathered} \sum (arrival\ time\ residuals)^2 \\ +\lambda \sum (velocity\ second\ derivatives)^2 \\ +\gamma \sum (penalties)^2 . \end{gathered} \tag{11}$$

The solution is given by:

$$\begin{aligned} \underline{\triangle m} \;=\; & \left(\mathbf{M'^T M'} + \lambda \mathbf{K^T K} + \gamma \partial \mathbf{P^T} \partial \mathbf{P}\right)^{-1} \\ & \left(\mathbf{M'^T} \underline{r'} - \lambda \mathbf{K^T} \underline{c} - \gamma \partial \mathbf{P^T} \underline{p}\right). \end{aligned} \tag{12}$$

λ and γ are Lagrangian multipliers. γ is fixed at a value of 100 to heavily weight the penalty functions, and the value of λ is varied.

DATA

Seismic data were recorded at four borehole geophones during Experiment 2032. The station geometry is shown in Figure 2. A Cartesian coordinate system was constructed with East and North coordinates referenced to the northeast corner of section 13 on the 1:24,000 USGS topography map titled "Seven Springs, New Mexico". The depths are referenced to 8700 ft (about 2652 m) above sea level. The station coordinates in this system are listed in Table 1. Stations EE-1, EE-3, and GT-1 were located within the Precambrian basement rocks. Station PC-1 was situated within a cavernous limestone of the Magdalena Group, approximately 150 to 200 meters above the basement. Extremely

Station Name	N-S Coord. (m)	E-W Coord. (m)	Depth (m)
EE-1	-480.8	-562.3	2854.6
EE-3	-182.4	-234.4	3301.7
GT-1	1976.6	-229.8	816.9
PC-1	-954.4	613.5	570.6

Table 1: Station coordinates in the Cartesian system.

few S wave arrival times could be picked on the data recorded at Station PC-1, probably due to interference from a converted wave from the metamorphic/sedimentary boundary.

During Experiment 2032, approximately 10,000 recorded events were large enough to have clear P-wave and S-wave arrival times at enough stations to be reliably located. A small fraction of these, roughly 700 events, are plotted in Figure 2 to illustrate the general extent of the source region. Events with less than six arrival times are not used in the joint hypocenter-velocity inversion. Spectral analysis of typical events yield corner frequencies of about 400 Hz (Fehler and Phillips, 1991), corresponding to wavelengths of about 16 m for P waves and 9 m for S waves.

Travel time data from several shots were recorded during the year following Experiment 2032. Some of the shot data are incorporated into the inversion to help constrain the results. The shot data recorded at stations EE-1 and EE-3 are presented in Table 2. Most of these data are included in the joint inversion. However, the following arrival times are inconsistent with the rest of the shot data and are therefore not used: 2038-1b, EE-1 P and S arrivals; 2048-1, EE-1 P and S arrivals; 2048-2b, EE-1 S arrival. Although some of these arrival time picks may be poor, it will be shown later that the velocities may actually have changed between the times when the different groups of shots were fired. Shot data were also recorded at Stations GT-1 and PC-1 but are not used in the inversion because either the station location had moved between the time of the hydrofracturing and the times when the shots were fired (PC-1) or the arrival time picks appear to be poor due to low signal to noise ratio (GT-1).

PROCEDURE

Data from a fracturing experiment carried out in December of 1983, referred to as Experiment 2032, were chosen for this study. During Experiment 2032, hydrofracturing was done continuously for 61 hours, and thousands of microseismic events were recorded at four borehole geophones (Figure 1). When implementing the joint hypocenter–velocity inversion, the data is divided into subsets containing approximately 700 events.

Shot No.	Shot Coordinates (m)			Travel Times (ms)			
	North	East	Depth	EE-1		EE-1	
				P	S	P	S
2038 1a	-272.8	-448.4	3267.2	80.6	139.0	39.2	66.5
2038 1b	-273.1	-449.0	3265.7	81.8	140.6	39.0	65.9
2038 2a	-270.1	-442.2	3282.6	84.1	143.3	37.4	63.0
2038 2b	-270.4	-442.8	3281.1	83.8	142.6	37.6	63.7
2038 3a	-290.9	-501.9	3109.9	55.9	93.3	58.6	97.3
2038 3b	-291.1	-502.4	3108.1	54.8	93.3	58.8	97.1
2048 1	-270.3	-442.6	3281.7	82.9	141.3		
2048 2a	-291.0	-502.2	3108.6	54.0			
2048 2b	-291.2	-502.9	3106.5	53.8	91.4		

Table 2: Shot data recorded after Experiment 2032 which were incorporated into the inversion.

The inversion results for one of these subsets, recorded during the 11^{th} to 19^{th} hours of Experiment 2032, are described below.

The P-wave and S-wave velocity models are represented by rectangular grids of velocity nodes. The velocity at any point within the grid is computed by linear interpolation of the velocities at the eight surrounding nodes. The node spacing for these inversions is 50 m in the East-West direction and 100 m in the North-South direction and in depth. Only the velocities in the vicinity of the source region vary during the inversion. The velocities outside of this region are fixed at values computed from shot data (5.92 km/s for the P-wave and 3.50 km/s for the S-wave). Station corrections are included in the inversion to help correct for velocity variations outside of the source region. Travel time data from eight shots recorded during the nine month period following Experiment 2032 are incorporated into the inversion to help constrain the results.

The joint inversion is performed using P-wave and S-wave arrival time data simultaneously. The inversion finds the P-wave and S-wave velocities independently, except for the indirect coupling through the hypocenters. The data set used here consists of arrivals from only four stations (Figure 2). Recall from above that the hypocenter location problem must be overdetermined to apply the separation of parameters technique. This technique greatly reduces the amount of computer memory required and therefore allows a larger number of earthquakes to be included in the inversion. Since this data

set has only four stations, both P-wave and S-wave data must be used to be able to implement separation of parameters. Also, the hypocenters are much better constrained by both phases than by either phase alone.

Much of this paper is devoted to studying the inversion procedure and discussing various factors which may affect the results. Some of these factors are strictly numerical – such as data weighting and velocity regularization weighting schemes. Other factors are physical – such as possible error in a station location. Ambiguities between P-wave velocities, S-wave velocities, and hypocenters are investigated using the resolution matrix. A few alternative modeling schemes are also examined to explore the non-uniqueness of the problem. All of these topics are addressed in an effort to understand how well the velocities and hypocenters are actually constrained by the data.

Model Parameters

The average P-wave and S-wave velocities of the mostly unfractured crystalline rock outside the earthquake region are known from shot data and are therefore held constant during the inversion. This is accomplished by keeping the velocities of the outer two "layers" of velocity nodes fixed, as shown in Figure 4. The P-wave and S-wave velocities of these nodes will hereafter be referred to as the "background velocities". The velocities of the other, inner nodes vary during the inversion. This set of nodes is referred to as the "inversion grid". Second derivative velocity regularization is applied to the velocities of the inversion grid. This regularization is also applied between the inversion grid and the background nodes to avoid abrupt velocity discontinuities at the edges of the inversion grid.

For most of the inversions, the values of the backgound velocities correspond to the homogeneous velocity models used by House (1987): 5.92 km/s P-wave velocity and 3.50 km/s S-wave velocity. (Later the effects of using different background velocities are investigated.) These values are the averages of the velocities computed from the shot data of Experiment 2038, shown in Table 3. Since the shots are located shallower than most of the seismic activity, these velocities should be reasonable estimates of the average velocities of the unfractured basement rock. Note, however, that the velocities estimated from the shot data recorded at station EE-1 are consistently slightly lower than those estimated from the shot data recorded at station EE-3. There are several possible explanations for this:

1. Station EE-3 is located within a deviated wellbore, and error in its location may contribute to this velocity discrepancy.

2. It is possible that the rock velocities near station EE-1 were affected by fracturing of the Phase I reservoir a few years earlier.

Shot Number	Velocities Computed from Observed Travel Times			
	EE-1; P	EE-3; P	EE-1; S	EE-3; S
1a	5.90	5.99	3.42	3.53
1b	5.80	6.04	3.37	3.58
2a	5.85	6.05	3.43	3.59
2b	5.85	6.04	3.44	3.57
3a	5.84	5.91	3.47	3.56
3b	5.88	5.92	3.45	3.58

Table 3: Velocities computed from Experiment 2038 shot data.

3. Velocity anisotropy may be affecting the results.

4. The two stations are probably located in different formations (see the simplified geologic cross section in Figure 3) which may have slightly different velocities.

Velocity variations outside the inversion grid may be at least partially compensated by applying station corrections. This method works especially well for velocity variations which are close to the stations, such as the relatively low-velocity sedimentary rocks at station PC-1. The station corrections are added to the computed arrival times, so that positive corrections indicate velocities which are slower than the background velocities, and negative corrections indicate velocities which are faster than the background velocities. The station corrections are included directly in the inversion as described Block (1991).

The P-wave data are given a weighting factor of 2 relative to the S-wave data, to reflect the relatively greater confidence in the P-wave arrival time picks. In general, a homogeneous initial velocity model (corresponding to the background velocities) is used. Initial earthquake locations and station corrections are determined by iteratively inverting the earthquake data and shot data for the station corrections and then relocating the events, using the separation of parameters technique described earlier. (The homogeneous velocities are fixed.)

Fracture Planes

After implementing the joint hypocenter-velocity inversion, the final microearthquake locations may be analyzed with the three-point method developed by Fehler et al. (1987). Application of this method to the hypocenters determined from the inversion is a convenient way to look for changes in the patterns of the earthquake locations. The three-

point method estimates the orientations of the fracture planes represented by clustering of earthquake hypocenters. All of the possible combinations of three earthquake locations are used to compute all of the possible plane orientations. This grouping is limited by a specified maximum distance between hypocenters for which the earthquakes may be considered to be on the same fracture plane. Since certain plane orientations will be more prevalent than others due strictly to the shape of the source region, a shape correction must be applied. After this correction, a statistical test is performed to determine if significant earthquake clustering occurs for any plane orientation. If so, the most common orientation which passes the test is taken to be the most active fracture plane. The earthquakes falling along this fracture plane may than be "eliminated", and the procedure may be repeated to find the second most active plane, and so on.

IMPLEMENTATION ISSUES

A number of issues must be addressed when implementing the joint hypocenter-velocity inversion. These issues include: what, if any, velocity penalty function should be applied; whether any of the station corrections should be fixed during the inversion; how uncertainties in fixed model parameters, such as the background velocities, will affect the results; and what value should be used for the regularization parameter λ. Another consideration is how variables which are not taken into account during the inversion may affect the results – such as error in the location of a station in a deviated wellbore. These issues are investigated in this section. Some of these topics are studied using synthetic data and others using field data.

To make the procedure more efficient, some of these issues are examined using straight ray paths for the travel time computations, when the effects being examined are stronger than, or relatively independent of, the effects of ray bending. Straight ray paths are generally used for the early tests, and bent rays are used in the later sections when finer details of the inversion results are studied.

Since it would be extremely complicated to look at all of the final P-wave and S-wave velocities for each inversion, four cross sections were selected for comparing different inversion results: the P-wave and S-wave vertical East-West cross sections at -300 m North, and the P-wave and S-wave horizontal cross sections at 3500 m depth. In some of the later sections, vertical North-South cross sections at -350 m East are also shown. These sections traverse the center of the source region. The velocities are interpolated at 10 meter increments and plotted using a gray scale. In order to be able to see the details of each section clearly, the most appropriate gray scale is chosen independently for each plot. Hence, shades do not necessarily correlate from one cross section to another. Projections of the final event locations are overlaid on the velocity plots. When studying these figures, one must keep in mind that some of the events are actually located far from the cross sections. For many of the inversions, the orientations

of the two most active fracture planes are also compared. (More fracture planes are probably present, but the comparisons in this section are limited to two planes due to the computational burden of computing numerous fracture planes.)

The Velocity Penalty Function

Synthetic data are first examined to investigate the need for a velocity penalty function. (A velocity penalty function may help constrain the inversion by forcing the velocities to remain within specified bounds.) Cross sections through the velocity models used to generate the synthetic data are shown in Figure 5. The 686 earthquake locations used to generate the data are projected onto these plots. These velocity models and event locations were taken from a preliminary inversion of actual field data. The velocities outside the anomalous region are homogeneous: 5.92 km/s P-wave velocity and 3.50 km/s S-wave velocity. The maximum percent velocity perturbations, compared to the background velocities, are about 11% for the P-wave velocities and 18% for the S-wave velocities. P-wave and S-wave arrival times were not generated for every source-receiver pair. Only those arrival times which could be picked on the actual field data were generated for the synthetic data. "Shot data" were also generated for the synthetic data, at the locations of the actual shot data. The arrival times were computed using straight ray paths. No station "errors" were added to this data and the following inversions are performed without any station corrections. Also, no random noise was added to the data. These simplifications allow the penalty function issue to be examined without concern about complications from other sources of error or ambiguity.

Initial earthquake locations were computed for each data set using a homogeneous velocity model consisting of the correct background velocities. Even for this noise-free synthetic data, it was found that occasionally an earthquake may become very poorly located, resulting in abnormally large arrival time residuals. A few very large residuals can seriously degrade the least squares inversion results. To avoid this problem, any event having a P-wave arrival time residual with absolute value larger than 4 ms or an S-wave arrival time residual with absolute value larger than 6 ms is excluded from the velocity inversion at each iteration. The following inversions are implemented with a regularization, or smoothing, parameter of 0.5. (The effects of varying this parameter are investigated later using field data.) The three-dimensional velocity grid has nodes at the following coordinates:

	Coordinates of Nodes (m)		
	Background Velocities	Inversion Grid	Background Velocities
N-S	-2000 -700	-600 -500 -400 -300 -200 -100 0 100	200 2500
E-W	-2000 -600	-550 -500 -450 -400 -350 -300 -250	-200 2000
Depth	-1000 3100	3200 3300 3400 3500 3600 3700 3800	3900 5000

As explained previously, the background velocities are fixed, and the velocities at the nodes of the inversion grid vary during the joint hypocenter-velocity inversion.

The inversion results illustrate the need for a velocity penalty function (Figure 6). Although only low-velocity anomalies exist in the original velocity model, the computed velocity structure contains some high-velocity anomalies, especially in the southeastern region. Studies of other synthetic data sets indicate that this tendency toward anomalously high velocities in certain regions becomes more severe when the inversion is less constrained (such as when station corrections are included in the inversion) or when the data are less consistent (such as when random noise is introduced). In order to better constrain the inversion, a penalty may be applied for velocities which are higher than the background velocities. A simple linear penalty function works well, as described in Block (1991). Figure 7 shows the results obtained when the penalty function

$$P(v) = \begin{cases} 50\,(v - v_{bg}) & v > v_{bg} \\ 0 & otherwise \end{cases} \quad , \; v_{bg} = background\ velocity \tag{13}$$

$$Lagrangian\ multiplier, \gamma, = 100$$

is applied. The erroneous high velocities are suppressed. Also, the final earthquake locations improve slightly. The average error of the final hypocenters is 12.0 m, compared to 15.8 m for the inversion without the penalty function. For comparison, the average error of the initial earthquake locations is 31.3 m.

The reason that the velocities have a tendency to increase in certain regions is because the regularization term, λ x (the sum of the squared velocity second derivatives), becomes smaller in this case. Consider the two inversions just presented. For the first inversion, with no penalty function, the sum of the squared velocity second derivatives is 81.4 $m^{-2}ms^{-2}$. Hence, the value of the regularization term is: λ x 81.4 = 0.5 x 81.4 = 40.7. For the second inversion, with the penalty function applied, the sum of the squared velocity second derivatives is 140.0 $m^{-2}ms^{-2}$, and the value of the regularization term is therefore 70.0. In conclusion, inversions incorporating regularization but not a penalty function are biased toward having high-velocity anomalies near the edges of the inversion grid (assuming that there is a low velocity anomaly in the center).

Inversion results of field data without a penalty function show velocities higher than the background values in the same regions as in the synthetic data. (These high velocity anomalies were removed from the field data inversion results used to generate the synthetic data above.) Hence, these high velocities are most likely an artifact of the inversion and do not depict the actual velocity structure. Also, the high velocities occur in regions with very low resolution, casting further doubt on their validity. For these reasons, it is prudent to constrain the velocities with a penalty function. The penalty function defined by Eq. 13 above is applied in the following inversions of field data.

Station Corrections

Many of the remaining issues are addressed using field data from 686 earthquakes recorded during the 11^{th} to 19^{th} hours of Experiment 2032. The velocity structure was probably changing relatively quickly at the beginning of the hydrofracturing, and therefore the earliest data may not be very consistent. For this reason, the data from the first few hours of the experiment were skipped. Histograms of the arrival time residuals for the initial homogeneous velocity model are shown in Figure 8. In order to eliminate poor data, events having any P residual with absolute value greater than 6 ms or any S residual with absolute value greater than 8 ms are excluded from the inversion at each iteration. The following velocity grid is used for all of the inversions unless stated otherwise:

		Coordinates of Nodes (m)	
	Background Velocities	Inversion Grid	Background Velocities
N-S	-2000 -700	-600 -500 -400 -300 -200 -100 0 100 200	300 2500
E-W	-2000 -600	-550 -500 -450 -400 -350 -300 -250 -200 -150	-100 2000
Depth	-1000 3100	3200 3300 3400 3500 3600 3700 3800	3900 5000

The inversion was first performed allowing all of the station corrections to vary (using straight rays). Results for one value of the regularization parameter, $\lambda = 10$, are shown in Figure 9. The velocities seem reasonable. The P-wave root mean square residual decreases from 1.14 ms to 0.98 ms (14.0%), and the S-wave rms residual decreases from 2.27 ms to 1.97 ms (13.2%). However, the final station corrections suggest a problem with the inversion results:

	P (ms)	S (ms)
EE-1	-1.3	-2.3
EE-3	-3.1	-6.8
GT-1	0.1	0.7
PC-1	16.9	28.3

Since station EE-3 is located within the inversion grid, its station corrections should be zero. If the velocities near Station EE-3 are actually slightly higher than the values used for the background velocities (5.92 km/s P-wave velocity and 3.50 km/s S-wave velocity), small negative station corrections at EE-3 are reasonable since velocities greater than the background velocities are penalized. For example, if the average P-wave velocity within 150 m of station EE-3 (which is approximately the shortest distance to the cluster of earthquakes) is actually 6.05 km/s rather than 5.92 km/s, then the corresponding station correction would be:

$$\frac{150\,m}{6.05\,m/ms} - \frac{150\,m}{5.92\,m/ms} = -0.54\,ms.$$

The station corrections observed at EE-3 are large, and, furthermore, the low S-wave velocity zone determined by the inversion extends completely to the station. These facts suggest that the shallow velocities have decreased over too large an area and have been compensated by negative station corrections. The negative station corrections at EE-1 also support this hypothesis. (Station corrections at EE-3 may also be non-zero due to error in its computed location within the deviated wellbore. However, it will shortly be shown that a modest error in the location of station EE-3 does not significantly affect the inversion results.)

To overcome the problem described above, the station corrections at stations EE-1 and EE-3 are fixed. Appropriate station corrections for EE-1 are found from the travel times for the four shots that were fired at about 3100 m depth, near the edge of the inversion grid (shots 2038-3a, 2038-3b, 2048-2a, and 2048-2b). The station corrections are determined simply by the average differences between the observed travel times and the travel times computed using the homogeneous velocity models (5.92 km/s P-wave velocity, 3.50 km/s S wave velocity). The resulting station corrections are:

	P (ms)	S (ms)
EE-1	0.2	1.0

The station corrections at station EE-3 are fixed at their "ideal" value of zero.

The inversion results obtained with the station corrections at EE-1 and EE-3 fixed are displayed in Figure 10. The P-wave velocities are about the same as before, but there are two noticable changes in the S-wave velocity structure. First, the shallow part of the S-wave velocity anomaly is weaker than before and is divided into two lobes. (Compare Figures 9b and 10b.) Second, a more prominent low S-wave velocity anomaly is associated with the southern cluster of microearthquakes than before. (Compare Figures 9d and 10d.) The final rms residuals are similar to those for the last inversion: 0.99 ms for the P-wave, and 1.93 ms for the S-wave. Compared to the previous results, the average difference in the hypocenters is 20 m and the average change in origin time is -4.1 ms. The final station corrections for this inversion are:

	P (ms)	S (ms)	
EE-1	0.2	1.0	(fixed)
EE-3	0.	0.	(fixed)
GT-1	3.7	6.9	
PC-1	19.6	33.1	

The station corrections at GT-1 and PC-1 have increased by 3 – 6 ms. The large station corrections for PC-1 are due to the relatively low-velocity sedimentary rocks at the station site. Some of the following inversion results will be compared to these results. For this reason, this inversion will often be referred to as the "reference inversion".

Background Velocities

The entire region outside the inversion grid is modeled as homogeneous rock having the "background" P-wave and S-wave velocities. Deviation of the actual velocities from this model is compensated (to first order) by station corrections. Until now, the *average* velocities computed from the shots in Table 3 have been used as the background velocities (5.92 km/s P-wave velocity and 3.50 km/s S-wave velocity). To investigate the sensitivity of the inversion to the values of the background velocities, the *maximum* velocities computed from the shot data are now used as the background velocities: 6.05 km/s (P) and 3.59 km/s (S). As before, the station corrections at station EE-3 are fixed at a value of zero, and the station corrections at station EE-1 are fixed at the values determined from the four shallow shots near the edge of the inversion grid:

	P (ms)	S (ms)
EE-1	1.3	3.3

Straight ray paths are used as before.

Results of the joint inversion are displayed in Figure 11 ($\lambda = 10$). Comparing these results to those from the previous inversion, the important observations are:

1. The overall, absolute velocity values are higher than before.

2. The velocity *patterns* show the same trends as before.

3. The *magnitudes* of the anomalies, in terms of percent difference from the background velocities, are similar. In the previous inversion (Figure 10), the maximum change in P-wave velocity is 28.2% and the maximum change in S-wave velocity is 18.6%. In the present results, the maximum change in P-wave velocity is 25.0% and the maximum change in S-wave velocity is 19.2%.

4. The event locations are very similar for the two inversions. Table 4 shows that the differences between the initial locations and final locations for each inversion are much more significant than the differences between the two sets of final locations. (Note that the initial earthquake locations for the two inversions are different since the initial homogeneous velocity models are not the same.) Table 5 lists the two most significant fracture planes computed by the three point method for each inversion. The orientations are nearly identical.

5. The rms of the final earthquake arrival time residuals are nearly identical for the two inversions. The P-wave rms residual is 0.99 ms for both inversions. The S-wave rms residual is 1.91 ms for the present inversion and 1.93 ms for the reference inversion.

Hypocenter Parameter	Average *Change* in Parameter *During* Inversion		Average *Difference* in Parameter *Between* Two Inv. Results*
	Ref Inv.	Inv. W. Higher Background Vels.	
North Coord. (m)	-5.4	-4.8	2.7
East Coord. (m)	-17.1	-17.2	7.7
Depth Coord. (m)	62.0	48.8	-13.2
Average Distance Event Moved During Inv. or Distance Between Two Final Event Locations (m)	69.6	56.6	19.5
Origin Time (ms)	-18.8	-13.5	5.9

* For the comparison between the two inversion results, the averages are given in terms of: (hypocenter parameter for inversion with higher background velocities) - (hypocenter parameter for reference inversion).

Table 4: 1. Average changes in the hypocenter parameters during the reference inversion and during the inversion with the higher background velocities; and comparision of the final hypocenter parameters for the two inversions.

	Strike	Dip	No. of Events on Plane
Reference	N 1° W	87° E	261
Inversion	N 25° W	86° W	144
Inv. With Higher	N 1° W	86° E	260
Background Vels.	N 24° W	86° W	177

Table 5: The two most significant fracture planes determined by the three point method for the reference inversion and the inversion with higher background velocities.

In conclusion, the inversion is not extremely sensitive to the values of the background velocities. The reason for this is that a shift in the background velocities is largely compensated by changes in the station corrections. The final station corrections for this inversion are:

	P (ms)	S (ms)	
EE-1	1.3	3.3	(fixed)
EE-3	0.	0.	(fixed)
GT-1	15.3	30.7	
PC-1	30.0	54.6	

Since the station corrections at station GT-1 are now very large, the smaller values of the background velocities used previously (5.92 km/s P-wave velocity and 3.50 km/s S-wave velocity) are preferred.

The Location of Station EE-3

Station EE-3 is located within a deviated wellbore. Its location was computed from a combination of a gyro survey, down to 3078 m depth along the borehole, and single shot surveys below this depth. Gyro surveys are said to be accurate to about 15 m, and single shot surveys are less accurate. Thus, the final location may be in error by as much as 25 m. In order to see how error in the location of station EE-3 may be affecting the inversion results, an inversion is performed in which the location of EE-3 is allowed to vary. Rather than beginning with a homogeneous velocity model, the inversion begins with the final velocities, event locations, and station corrections of the "reference" inversion (Figure 10). The coordinates of EE-3 and the station corrections are given small damping factors to make the inversion more stable. Also, the shot residuals are given a weighting factor of 2. (Straight rays are used.)

The final location of station EE-3 is:

-190.2 m North
-251.3 m East
3306.5 m Depth

The station has moved approximately 8 m south, 17 m west, and 5 m in depth. Thus, the absolute change in its location is about 19 m. The location of station EE-3 given above is not necessarily more accurate than the location computed from the well surveys. In fact, the rms residuals do not improve significantly during this inversion. (For reasons discussed previously, I believe the movement of EE-3 is controlled by the shot data.) The purpose of this inversion is simply to see how a reasonable error in station EE-3's location may affect the inversion results. Table 6 shows that the earthquakes have

Hypocenter Parameter	Average Change in Parameter During Inversion
North Coord. (m)	-7.1
East Coord. (m)	-10.4
Depth Coord. (m)	2.6
Average distance event moved (m)	15.8
Origin time (ms)	0.9

Table 6: Average changes in the event parameters during the inversion in which the location of station EE-3 varies.

	Strike	Dip	No. of Events on Plane
Reference	N 1° W	87° E	261
Inversion	N 25° W	86° W	144
Inv. in Which Loc.	N 3° W	86° E	332
of EE-3 Varies	N 25° W	86° W	145

Table 7: The two most significant fracture planes determined by the three point method for the reference inversion and the inversion in which the location of station EE-3 varies.

moved about 16 m on average, mostly to the southwest. This change has only a very slight effect on the orientations of the two most significant fracture planes found by the three point method, listed in Table 7.

Figure 12 contains cross sections through the final velocity models. As can be seen by comparing these results to those of the reference inversion (Figure 10), only very minor differences in the patterns and magnitudes of the velocity anomalies occur. The maximum absolute difference in the P-wave velocities is 0.24 km/s, and the maximum absolute difference in the S wave velocities is 0.20 km/s. Also, since the V_P/V_S ratios computed from the results of the joint inversion are examined in following sections, it should be noted that the maximum absolute difference in the V_P/V_S ratios for these two inversions is 0.08. The final rms residuals for the above inversion are about the same as those for the reference inversion: 0.99 ms for the P-wave and 1.92 ms for the S-wave

(compared to 0.99 ms (P) and 1.93 ms (S) for the reference inversion). In conclusion, a modest error in the location of station EE-3 has only minor effects on the results of the joint inversion.

The Regularization Parameter

Effects on Velocities

The regularization parameter λ determines the degree of "smoothness" of the final P-wave and S-wave velocity structures. The measure of smoothness for this case is the sum of the squares of the second velocity derivatives in the x, y, and z directions. Figure 13 illustrates how the magnitude of λ affects the final velocity structures. This figure shows the S-wave velocity horizontal cross sections for four inversions with different regularization parameters: $\lambda = 1$, 10 (the reference inversion), 20, and 40. (These results were computed using straight ray paths.) As can be seen, when the regularization parameter is very small ($\lambda = 1$), the velocities decrease by a large amount, about 40% maximum, over a larger region than that spanned by the microearthquakes. The velocity pattern is very "rough", having several local minima and maxima. When a large regularization parameter is used ($\lambda = 40$), the velocities decrease only a small amount, about 8% maximum, over a smaller region than that spanned by the microearthquakes. Thus, both the spatial extent and the magnitudes of the velocity anomalies are strongly affected by the value of the regularization parameter.

In Figure 13, the velocity structures for $\lambda = 20$ and $\lambda = 40$ simply look like smoothed versions of the result for $\lambda = 10$. Hence, these values of λ are most likely too large. The result for $\lambda = 1$, on the other hand, is considerably different from the others. However, these results were computed using straight ray paths, and ray bending is expected to have a relatively large effect on the results for $\lambda = 1$, since the magnitudes of the velocity anomalies are very large for this case. Inversion results for values of λ between 1 and 10, which were computed using bent rays, are now examined in some detail. Rather than beginning with the straight-ray results and performing several more iterations with bent rays, the inversions were completely re-computed using only bent rays and beginning with the same homogeneous velocity models as before. The reason for using this procedure is that some areas of the inversion grid have much greater ray coverage when straight rays are used than when bent rays are used. Tests suggest that if straight rays are used first, the velocities in these regions may be highly perturbed, and then when ray bending is added, these velocities may remain perturbed even though very few rays now pass through those regions. Using bent rays and beginning with homogeneous velocity models is less likely to bias the results in this way.

The final results for inversions using λ equal to 1, 4, 7, and 10 are presented in Figures 14 to 19. For convenience in comparing the results from the four different

λ	Maximum Decrease in Velocity		RMS Residual (ms)			Decrease in Total
	P-wave	S-wave	P-wave	S-wave	Total	Residual (%)
Initial Model	0%	0%	1.14	2.28	2.28	
10	22%	13%	1.00	2.01	2.01	11.8
7	29%	15%	0.96	1.98	1.95	14.5
4	36%	27%	0.93	1.93	1.905	16.4
1	43%	41%	0.89	1.91	1.83	19.7

Table 8: Summary of inversion results using different values of λ.

inversions, each figure contains one cross section from each inversion result. As already seen from the straight-ray inversions, the larger the value of λ, the "smoother" the final velocity structures are. Also, as λ is increased, the *magnitudes* of the velocity anomalies decrease. Table 8 lists the maximum P-wave and S-wave velocity perturbations, in terms of percent change from the background velocities of 5.92 and 3.50 km/s, for each inversion. The maximum velocity perturbations vary from about $10 - 20\%$ when $\lambda = 10$ to approximately 40% when $\lambda = 1$. Since the velocity structures corresponding to $\lambda = 10$ are very smooth, the velocity regularization is probably weighted a little too heavily for this case. Since the magnitudes of the velocity anomalies decrease as λ increases, the results for the case when $\lambda = 10$ provide minimum bounds on the magnitudes of the velocity perturbations. Thus, it is reasonable to conclude that the velocities decrease by *at least* $13 - 22\%$ in the most strongly perturbed regions of the reservoir. Table 8 also gives the final P-wave root-mean-square (rms) residual, S-wave rms residual, and total rms residual for each inversion. The total rms value is the root-mean-square of the *weighted* P-wave residuals (multiplied by 2.0, as explained previously) and the S-wave residuals. This is the actual value that the algorithm is trying to minimize, neglecting the constraint terms. The improvement in the total residual varies from 11.8% when $\lambda = 10$ to 19.7% when $\lambda = 1$.

Effects on the V_P/V_S Ratios

The *relative* changes in the P-wave and S-wave velocities are also influenced by the value of λ. Table 9 illustrates this point. This table lists the minimum and maximum V_P/V_S ratios for each inversion, as well as the coordinates of the nodes at which these extrema occur. From these results it is clear that the lower the value of λ, the more variable the V_P/V_S ratio becomes. It is interesting, however, that the minimum V_P/V_S

λ	Minimum V_P/V_S	Location of Minimum (m)	Maximum V_P/V_S	Location of Maximum (m)
initial model	1.69		1.69	
10	1.38	-300E,-200N,3500D	1.88	-400E,-400N,3200D
7	1.27	-300E,-200N,3500D	1.94	-400E,-400N,3200D
4	1.18	-300E,-200N,3500D	2.01	-400E,-400N,3200D
1	1.06	-300E,-200N,3500D	2.37	-350E,-200N,3700D

Table 9: Summary of V_P/V_S values for inversions using different values of λ.

value occurs at the same node for all of the inversions, and that it is located near the center of the inversion grid, where the resolution should be relatively good. Figure 20 shows the three cross sections through the V_P/V_S minimum, parallel to the coordinate axes, for the inversion with $\lambda = 4$. The maximum V_P/V_S value occurs at the same node, in the shallowest layer of the inversion grid, for the inversions with $\lambda = 4$, 7, and 10. The velocity results for this shallow layer may be affected by velocity variations outside the inversion grid. For the inversion with λ =1, the V_P/V_S maximum occurs deep in the inversion grid, where the resolution is poor.

For a rock with randomly-oriented, fluid-filled fractures, the V_P/V_S ratios increase compared to those of the unfractured state (O'Connell and Budiansky, 1974; Toksöz et al., 1976; Cheng, 1978). Low apparent V_P/V_S ratios may be observed in some situations due to anisotropy of parallel fractures. The plots in Figure 21 illustrate this point. Figure 21a shows the velocity of the P-wave and the faster S-wave (polarized parallel to the fractures) for a rock having parallel fractures, for angles from 0^o (parallel to fractures) to 90^o (perpendicular to fractures). These values were taken from Cheng (1978). (The angles are the phase angles, which are not, in general, the same as the ray angles in an anisotropic medium (Thomsen, 1986). However, for this general discussion, the distinction is not important.) Curves are shown for water-saturated fractures (solid lines) and dry fractures (dotted lines). The curves in Figure 21b are the corresponding apparent V_P/V_S ratios. The V_P/V_S ratio of the equivalent unfractured rock is 1.73. Hence, for any given angle, the apparent V_P/V_S ratio for the fractured rock is lower than that for the unfractured rock. The apparent V_P/V_S ratio is the lowest for wave propagation at large angles from the fracture orientation. The apparent V_P/V_S ratio is lower for dry fractures than for saturated ones, especially at high angles. For this particular model, the ratios are as low as 1.3 for dry cracks.

Although the major fracture planes of the Los Alamos reservoir may be subparallel (controlled by *regional* stresses), fractures are likely to occur on a smaller scale in

many directions (controlled by *local* stresses). The fractures within the reservoir are expected to be completely saturated, due to the high pumping pressures used during the hydrofracturing. Hence, based on the theory and laboratory measurements of rocks with randomly-oriented, fluid-filled fractures, the V_P/V_S ratios are expected to increase within the reservoir. Furthermore, even if most of the fractures within the reservoir were subparallel, the ray paths would be at fairly low angles to the fracture orientation (subvertical). Thus, even for this case, the observed V_P/V_S ratios should not be significantly lower than those of the unfractured rock. In short, the observed V_P/V_S values are not consistent with the results expected from theory. In a later section, relative P-wave and S-wave weighting parameters are investigated to see if the relative weighting schemes strongly bias the computed V_P/V_S ratios.

Effects on Hypocenters

The earthquake locations for all of the inversions rotate into a more vertical and more North–South orientation compared to the initial locations. This can be seen by examining the hypocenter projections shown in Figure 22. This figure contains vertical East–West projections of the initial earthquake locations (represented by the dots) and the final earthquake locations (represented by the plus signs) for the inversions with $\lambda = 10$ (Figure 22a) and $\lambda = 1$ (Figure 22b). (The results for the inversions with $\lambda = 4$ and $\lambda = 7$ are intermediate between the results shown in this figure.) The hypocenters define a two-lobed pattern – one lobe shallower than about 3450 – 3500 m depth, and the second lobe below that depth. The inversions produce no systematic change in the earthquake locations within the shallower lobe. The hypocenters within the deeper lobe, however, are systematically rotated into a more vertical orientation. The amount of this rotation increases as λ decreases. Also, the deeper lobe looks more "compact" after the inversions (most noticeable for the case when $\lambda = 1$, Figure 22b), suggesting that the hypocenters are also rotating into a more North–South orientation, perpendicular to the cross section. Figures 23 and 24 contain the horizontal and vertical North–South hypocenter projections, respectively. These projections show that the deepest earthquakes, which are moved deeper and to the west by the inversions, are located in the southern part of the source region. Also, the rotation into a more North–South orientation can be seen in Figure 23b, the horizontal projection for the inversion with $\lambda = 1$. The earthquakes in the northeastern corner of the source region are aligned more North–South after the inversion. The observation that the hypocenter rotation increases as λ decreases is reflected in Table 10. This table gives the average change in each hypocenter parameter, for each inversion, as well as the average absolute distance the hypocenters move.

Table 11 gives the orientations of the two most active fracture planes for each inversion result, as determined by the three point method. Also given are the orientations of the fracture planes computed from the initial earthquake locations. The results are

Hypocenter Parameter	Average Change in Parameter During Inversion			
	$\lambda = 10$	$\lambda = 7$	$\lambda = 4$	$\lambda = 1$
North Coord. (m)	-0.2	2.9	3.0	2.5
East Coord. (m)	-5.4	-6.2	-4.7	-8.4
Depth Coord. (m)	22.5	29.2	27.1	35.5
Average Distance event moved during inv.	31.8	40.2	41.3	53.5
Origin time (ms)	-9.5	-12.8	-14.6	-20.8

Table 10: 1. Average changes in the hypocenter parameters during the inversions with different values of λ.

	Strike	Dip	No. of Events on Plane
Initial Locations	N 9° W	77° E	399
	N 31° W	87° E	170
$\lambda = 10$	N 3° W	80° E	300
	N 20° W	87° W	156
$\lambda = 7$	N 2° W	81° E	242
	N 20° W	87° W	196
$\lambda = 4$	N 2° W	82° E	225
	N 20° W	87° W	203
$\lambda = 1$	N 1° W	82° E	238
	N 20° W	86° W	186

Table 11: The two most significant fracture planes determined by the three point method for the inversions with different values of λ.

consistent with the hypocenter rotation patterns described above. For all of the inversions, both fracture planes strike more North–South than the planes computed from the initial locations. The first fracture plane also has a steeper dip for all of the inversion results, compared to the dip of the initial plane. The orientation of this first fracture plane also illustrates the progressively stronger rotation as λ decreases. The strike of the plane varies from N 3° W when $\lambda = 10$ to N 1° W when $\lambda = 1$, and its dip varies from 80° E ($\lambda = 10$) to 82° E ($\lambda = 1$). (Both fracture planes involve earthquakes from approximately 3300 m depth to 3800 m depth.)

Since the cluster of earthquakes is rotating into an orientation which is more parallel to the axes of the velocity grid, it is important to investigate whether this rotation is an artifact of the inversion method. It is possible that the earthquake locations could be biased by the orientation of the velocity grid. To check this, the inversion was repeated using a different coordinate system. The velocity grid was rotated 45 degrees around a horizontal North-South axis, as illustrated by the diagram in Figure 25. The inversion using $\lambda = 4$ was repeated using this new grid orientation. The orientation of the final earthquake locations is the same as before – the earthquake cluster is still rotated into a more vertical and more North-South orientation. Hence, this earthquake rotation is not biased by the orientation of the velocity grid. As an additional note, the velocity minima for the inversion with the rotated grid generally occur in the same locations as before, especially for the S-wave velocity structure. Major differences in the velocity structures only occur in those areas with poor or no ray coverage. Also, the V_P/V_S minimum remains at the same location.

Weighting Schemes

The inversion results presented in the previous section consistently show P-wave velocity structures which have less detail than the corresponding S-wave velocity structures. Also, the V_P/V_S ratios consistently decrease to extremely low values in one region. Now we will determine if these results are biased by the relative P-wave and S-wave weighting schemes employed in the inversions. These weighting schemes are of two types:

1. Relative P-wave and S-wave data weighting.

2. Relative P-wave and S-wave velocity regularization weighting.

First, recall that the P-wave data has been given a weighting factor of 2.0 relative to the S-wave data (as explained previously). This weighting reflects the stronger confidence in the P-wave arrival times relative to the S-wave times. Now we wish to determine if this data weighting is biasing the velocity results, specifically the V_P/V_S

ratios. Here we examine results of an inversion performed with equal P-wave and S-wave data weighting.

Secondly, until now, the P-wave and S-wave second velocity derivatives have been given equal weighting in the regularization matrix. It may be argued that the P-wave velocity regularization should be given less weighting than the S-wave velocity regularization for the following reason. Consider the P-wave and S-wave velocity derivatives across three consecutive velocity nodes:

$$\begin{aligned} \textit{P wave velocity derivative} &= a_1 v_{i-1}^P - a_2 v_i^P + a_3 v_{i+1}^P \\ \textit{S wave velocity derivative} &= a_1 v_{i-1}^S - a_2 v_i^S + a_3 v_{i+1}^S. \end{aligned}$$

The $a's$ are constants which depend on the distances between the nodes. The P-wave velocity derivatives tend to be larger than the S-wave velocity derivatives simply because the P-wave velocities are larger than the S-wave velocities. To see this, assume that the V_P/V_S ratio is the same for the three consecutive nodes. Then the P-wave velocity derivative may be expressed in terms of the S-wave velocity derivative as follows:

$$\begin{aligned} \textit{P wave velocity derivative} &= a_1 v_{i-1}^P - a_2 v_i^P + a_3 v_{i+1}^P \\ &= a_1 v_{i-1}^S \left(\frac{v_{i-1}^P}{v_{i-1}^S}\right) - a_2 v_i^S \left(\frac{v_i^P}{v_i^S}\right) + a_3 v_{i+1}^S \left(\frac{v_{i+1}^P}{v_{i+1}^S}\right) \\ &= \left(\frac{V_P}{V_S}\right)\left(a_1 v_{i-1}^S - a_2 v_i^S + a_3 v_{i+1}^S\right) \\ &= \left(\frac{V_P}{V_S}\right)(\textit{S wave velocity derivative}). \end{aligned} \tag{14}$$

(This expression is a simplified representation of the relationship between the P-wave and S-wave velocity derivatives, since the V_P/V_S ratio was assumed to be constant.) Since the P-wave velocity derivatives tend to be larger than the S-wave velocity derivatives for numerical reasons, one may argue that the P-wave derivatives should be given less weighting than the S-wave derivatives in order for these two sets to have "equivalent effects" on the inversion results. Following this logic, the P-wave velocity regularization weighting should be on the order of V_S/V_P (from Eq. 14). Here we examine the results of inversions performed using P-wave velocity regularization weighting of 0.59, which is the V_S/V_P ratio of the background velocities. The specific objective of this investigation is to see if this regularization weighting scheme allows the final P-wave velocity structure to show more detail than the results from the earlier inversions.

The results of three inversions with different weighting schemes are examined:

1. P-wave data weighting = 2; P-wave velocity regularization weighting = 1 (same as all previous inversions);
2. P-wave data weighting = 2; P-wave velocity regularization weighting = 0.59;

P data wt.	P reg. wt.	Minimum V_P/V_S	Location of Minimum (m)	Maximum V_P/V_S	Location of Maximum (m)
initial model		1.69		1.69	
2	1	1.18	-300E,-200N,3500D	2.01	-400E,-400N,3200D
2	0.59	1.125	-300E,-200N,3500D	1.96	-400E,-400N,3200D
1	0.59	1.30	-300E,-200N,3600D	1.94	-400E,-400N,3200D

Table 12: Summary of V_P/V_S values for inversions using different weighting schemes. $\lambda = 4$ for all inversions.

3. P-wave data weighting = 1; P-wave velocity regularization weighting = 0.59.

In all cases, the regularization Lagrangian multiplier λ equals 4. Ray bending is used, beginning with a homogeneous initial model. Table 12 lists the minimum and maximum V_P/V_S ratios for each of the three inversions. The strong V_P/V_S minimum is present in all of the results. The minimum V_P/V_S value differs by a modest amount between the inversions, similar to the differences seen in the last section for the inversions using different values of λ. These differences are at least partially due to the fact that changing the relative P-wave and S-wave weighting schemes also changes the relative importance of the arrival time residuals and velocity derivatives, similar to changing the value of λ. Also, note that the location of the V_P/V_S minimum for the third weighting scheme is 100 m deeper than for the others. The important conclusion from this study is that the relative P-wave and S-wave weighting schemes do not dramatically affect the location and value of the prominent V_P/V_S minimum.

Horizontal P-wave velocity cross sections (at 3500 m depth) for each of the three inversions are presented in Figure 26. The amount of detail in the P-wave velocity structure does not vary significantly between the results. Thus, decreasing the weighting of the P-wave velocity regularization, or smoothing, does not produce a more detailed V_P model.

EVALUATING THE RESULTS

In the previous sections, we examined the effects of various weighting parameters, approximations, and possible sources of error on the inversion results. Those types of studies provide some insight into the stability of the inversion. In the following sections, the resolution and uniqueness of the inversion results are investigated. Conventional analysis of the resolution matrix allows the trade-offs, or ambiguities, between

the various model parameters to be examined. These ambiguities include "smearing" among adjacent velocity nodes, $V_P - V_S$ trade-offs, and ambiguities between velocities and hypocenters. The conventional "standard errors" from the model covariance matrix provide *lower bounds* on the velocity and hypocenter errors. They are not, however, good estimates of the *absolute* errors, since they do not account for the basic non-uniqueness of this joint inverse problem. The non-uniqueness of this problem is examined in another way, by performing inversions with different types of constraints than those applied up to this point. The goal of these studies is to understand how well the velocities and hypocenters are constrained by the data, and to what extent they are determined by the constraints. Inversions of synthetic data also yield insights into this issue. Since the ray coverage is limited, and since the inversion results cannot be confirmed by independent information, these types of analyses are very important.

Resolution and Standard Errors

In this section, the resolution and standard errors of the velocity models from the joint inversion are quantified, as well as the standard errors of the hypocenters. We examine in some detail the resolutions and errors for the inversion performed with $\lambda = 4$, P data weighting = 2, and equal P-wave and S-wave regularization weighting (Figures 14c – 19c). The effects of varying some of these parameters are discussed. It is computationally intensive to compute resolutions and errors for all of the velocity nodes. For this reason, the following analysis is confined to the velocity nodes of the vertical East-West cross sections at -300 m North.

Spatial Velocity Resolution

The diagonal elements of the resolution matrix have been interpolated and contoured for the vertical East-West cross sections, shown in Figure 27. The resolution contours are superimposed onto the velocity gray scale plots. The velocities in the lower, western region are not resolved at all simply because there are no rays passing through that region. The resolution is best in the upper, eastern region of the reservoir, but even these numbers are low: 0.2 – 0.6. These results indicate that the computed velocity at a particular node is significantly influenced not only by the actual velocity at that node, but also by the values of other parameters in the model. In order to see which of these other parameters are influencing the velocity at any particular node, the off-diagonal elements of the row of the resolution matrix corresponding to that node must be examined. For example, consider the P-wave velocity node at (-300 m East, -300 m North, 3500 m depth). Some of the off-diagonal elements of the corresponding row of the resolution matrix are interpolated and contoured in Figure 28. Figure 28a shows the row elements corresponding to the vertical East-West P-wave velocity cross

section through the node under consideration, and Figure 28b shows the row elements corresponding to the horizontal P-wave velocity cross section through the node. The dots represent the velocity nodes over which the velocity second derivative regularization is done. From this figure one sees that the nodes over which the regularization is done are having some influence on the P-wave velocity solution at (-300 m East, -300 m North, 3500 m depth). Similar results are obtained for the S-wave velocity node.

One way to quantify the influence of the adjacent nodes over which regularization is done is to sum the corresponding off-diagonal elements of the resolution matrix and the diagonal element, and compare this total sum with the magnitude of the diagonal element alone. The total sum described above was computed for all of the nodes of these vertical East-West cross sections, and the results are shown in Figure 29. These total sums are almost twice as large as the magnitudes of the diagonal elements alone (compare to Figure 27). Hence, the combined influence of the velocities at the adjacent nodes is almost as significant as the influence of the central node alone. In conclusion, the spatial velocity "resolution" is not on the order of the node spacing (50 – 100 m), but is on the order of the distance over which the regularization is done (100 – 200 m). Thus, applying the regularization constraints with $\lambda = 4$ is similar to using a larger node spacing. The important difference is that using a small node spacing with the regularization gives the model more flexibility than using a larger node spacing.

Note that the P-wave velocity resolutions are less than the S-wave resolutions (Figure 27a and b). Recall that the P-wave and S-wave velocity regularizations are given equal weighting in this inversion. However, since the P-wave velocity derivatives are, in general, larger than the S-wave velocity derivatives, the overall P-wave regularization is actually stronger than the S wave regularization. For an inversion performed with less P-wave regularization weighting (weight = 0.59), the P-wave velocity resolutions improve and become slightly larger than the S-wave resolutions. (However, as shown previously, this inversion still produces a P-wave velocity structure which shows little detail.)

$V_P - V_S$ Trade-Offs

In addition to the smearing or "trade-off" between adjacent velocity nodes described above, trade-off also exists between corresponding P-wave and S-wave velocity nodes. This type of trade-off exists because of the uncertainty in the hypocenter locations, and because of the inherent ambiguities between changes in hypocenter location (especially depth), origin time, and velocities. The interdependence of the P-wave and S-wave velocities can be demonstrated by considering once again the row of the resolution matrix corresponding to the P-wave velocity node at (-300 m East, -300 m North, 3500 m depth). The off-diagonal elements corresponding to the vertical East-West and horizontal P-wave velocity cross sections through the node were previously examined

(recall Figure 28). Now the off-diagonal elements of this row of the resolution matrix which correspond to the vertical East-West and horizontal S wave velocity cross sections through the node are presented in Figure 30. The values near the point (-300 m East, -300 m North, 3500 m depth) are non-zero, indicating trade-off between the P-wave and S-wave velocities at this point. Notice that these off-diagonal elements are negative. This means that a P-wave velocity decrease at this node may trade off with an S-wave velocity increase at the same node, and vice versa. The magnitude of the largest off-diagonal element is 0.155, compared to a value of 0.47 for the diagonal element. Thus, in terms of percentages, the influence of the corresponding S wave velocity node is 33% of the influence of the P-wave node.

To examine qualitatively the nature of the trade-off between P-wave and S-wave velocities, synthetic data were created having only a P-wave velocity anomaly, and these data were inverted allowing both P-wave and S-wave velocities to vary. Vertical and horizontal cross sections of the simple rectangular P-wave velocity model used to generate the data are shown in Figure 31. The P-wave velocity decreases to 4.9 km/s in the center of the anomaly, which is a decrease of 17% compared to the background velocity of 5.92 km/s. The S-wave velocity is homogeneous and has a value of 3.5 km/s. The data were created using the final earthquake locations of the old straight-ray "reference inversion" (See Figure 10), and no noise was added to the data. Ray bending was used when creating and inverting the data. The inversion grid is the same as for the inversions of the field data. The regularization parameter $\lambda = 10$, the P data weighting = 2, and the P-wave and S-wave regularization weightings are equal. No velocity penalty function is applied so that the velocity trade-offs can be clearly seen. Cross sections through the final velocity structures are shown in Figures 32 and 33. In Figure 32, the P-wave velocities are plotted at the same scale as in Figure 31, so that the final velocity values may be easily compared to the correct values. In Figure 33, the P-wave and S-wave velocities are plotted in terms of the percent difference from the background values of 5.92 and 3.50 km/s, respectively. This type of scale makes it easy to compare the relative magnitudes of the V_P and V_S anomalies. The P-wave velocities decrease to about 5.35 km/s, a change of 9.6%. As expected, the S-wave velocities increase in the region of the P-wave low velocity anomaly, to about 3.65 km/s. This is a 4% increase over the correct value. As a side-note, the computed V_P/V_S ratio of the anomaly is approximately 1.47, close to the correct value of 1.40.

Ambiguities Between Velocities and Hypocenters

The velocities also trade off with the earthquake locations and origin times. The velocity resolutions computed above indirectly take into account the ambiguities between the velocities and hypocenters because the resolution matrix is computed using the joint inversion formulation. The resolutions could also be computed for the equivalent problem, but with the hypocenters assumed to be fixed. This calculation is done

by simply skipping the separation of parameters step. When this procedure is done, the resolutions improve significantly. The average increase in the resolution values, compared to those computed previously with the joint inversion formulation (Figure 27), is about 0.2. To put this in perspective, the mean resolution value increases by 79%.

The substantial improvement in the resolutions when the hypocenters are assumed to be fixed indicates that significant ambiguities exist between the velocities and the earthquake locations and origin times. Another way to study the effects of these ambiguities is to see what kind of improvement in the velocity results would be achieved if the hypocenters were known. This comparison can be made using synthetic data. The synthetic data for the simple block model described earlier were inverted with the earthquake locations and origin times fixed at the correct values. Cross sections through the resulting P-wave velocity model are presented in Figure 34. The images are much sharper than before, and the velocity values are much more accurate. The minimum P-wave velocity is now 4.88 km/s, compared to the value of 5.35 achieved before. (The corrrect solution is 4.90.) Also, since the hypocenters are fixed, the P-wave and S wave velocities are not coupled, so there are no $V_P - V_S$ trade-offs.

Velocity Standard Errors

Another measure often used to evaluate the result of an inverse problem is the model covariance matrix. This matrix provides an estimate of the variance of the model parameters due to "noise" in the data. This noise may be a combination of the arrival time picking errors and arrival time discrepancies caused by factors which are not compensated for in the inversion – such as velocity variations outside the inversion grid, small velocity variations which cannot be accurately modeled due to the discretization of the grid or the regularization applied, or variations due to anisotropy. The square root of the diagonal elements of the covariance matrix, usually referred to as the standard errors, were computed for the vertical East-West cross sections. An estimate of the noise, or data, variance is required for this analysis. The data variance is estimated from the final arrival time residuals, as described previously. The number of independent parameters in the model must be specified when estimating the data variance. Since velocity regularization, or smoothing, is applied to the problem, the number of independent velocities is less than the number of nodes in the inversion grid. For the particular inversion considered here, the resolution analysis indicates that the size of the spatial velocity resolution is on the order of twice the node spacing. In other words, the number of independent velocities in each direction is about half of the number of nodes in each direction. So the total number of independent velocities is approximately $(nx/2)$x$(ny/2)$x$(nz/2)$, where nx, ny, and nz are the number of nodes in the inversion grid in the x, y, and z directions. This number must then be multiplied by 2 since there are P and S nodes. Using this approach to determine the number of independent velocities, a value of 9.9 ms^2 is obtained for the data variance. (This value is the variance of

the *weighted* data, in which the P-wave residuals are multiplied by a factor of 2.) The corresponding standard errors range from about 0.08 to 0.13 km/s (in the areas where the velocities are resolved).

It is very important to remember that the standard errors are the expected errors in the model parameters **due to the data, or noise, variance**, for a particular inversion result. Other errors exist due to the basic non-uniqueness of the problem. This fact is demonstrated by the differences in the velocity values for different values of λ (Table 8). The differences in the velocity values for different values of λ are greater than the size of the standard errors. Hence, for this non-unique problem, the standard errors are not meaningful measures of the absolute velocity errors.

The velocity resolutions and standard errors change as λ is varied. As λ decreases, the resolutions increase, but the standard errors also increase, and vice versa. For example, the resolution and error analyses were computed for the same vertical East-West cross sections as above, for the inversion with $\lambda = 1$. The resolutions increased by about 40%, and the standard errors increased by about 77%.

Hypocenter Standard Errors

The standard errors for the hypocenter parameters have been computed for the inversion studied above (inversion with $\lambda = 4$). The data variance estimated as described in the last section, 9.9 ms^2, is used in these calculations. Histograms of the standard errors of the hypocenter parameters are shown in Figure 35. The mean standard errors are:

Parameter	Mean Standard Error
North-South Coordinates	12.8 m
East-West Coordinates	10.4 m
Depth Coordinates	22.6 m
Origin Times	4.4 ms

Again, one must remember that these errors are only those due to the data "noise", or variance. When computing these values, the velocity model is assumed to be correct. Therefore this analysis does not directly take into account any errors in the velocities, and the above errors in the hypocenter parameters should be thought of as the *minimum* expected hypocenter errors.

Alternative Models

The joint inversions yield a range of results for various values of λ and other weighting parameters. In all cases, the arrival time residuals are substantially reduced. These results are obtained by requiring the velocity models to be smooth and to have values within specified bounds. However, since this joint hypocenter-velocity inverse problem is non-unique, it is possible that different types of constraints may yield models which satisfy the data equally well. In this section we examine some other modeling schemes. The goal is to investigate the non-uniqueness of the problem, and to determine if the inversion results obtained by our method fit the data better than results from alternative procedures.

One-Block Model

Instead of having many velocity nodes and regularizing the problem by requiring smooth models, an inversion was performed with a very simple velocity parameterization. Only eight nodes were in the inversion grid, forming a rectangular box around the source region. These nodes were required to have the same velocity values, so that the velocity model was essentially a "block" structure. The grid was rotated so that it was alligned parallel to the trend of the final earthquake locations obtained from the earlier inversions, and it was chosen such that it fit rather "tightly" around the source region. The inversion was performed with all of the station corrections varying and with no velocity bounds applied. Bent rays were used. The final velocities within the source region are 5.65 km/s (P) and 3.26 km/s (S), which yield a V_P/V_S ratio of 1.73. The arrival time residuals decrease very little, however. The root-mean-square values are 1.13 ms for the P-wave and 2.20 ms for the S-wave, compared to initial values of 1.14 and 2.28 ms, respectively.

The improvement in the arrival time residuals is much better for all of the earlier inversions (such as those shown in Table 8) than for the inversion performed here with the simplified velocity model. To determine if the greater improvement in the arrival time residuals obtained when many nodes are used in the inversion grid is meaningful, a statistical test was done. The F test determines the probability that the difference in the data variances for models which have different numbers of parameters is simply due to the difference in the number of degrees of freedom (Mendenhall et al., 1986, p. 478). In other words, if the probability determined by the F test is very small, then the model with the larger number of parameters truely satisfies the data better than the alternative model. This test was used to compare the results from the simplified inversion above to those from the inversion with λ =4. The number of independent velocities for the latter inversion was estimated from the resolution analysis, as explained earlier. This F test yields a probability of less than 0.5% (which is the smallest category in the distribution

table). Hence, the greater improvement in the arrival time residuals when many nodes are used in the inversion grid is statistically significant, suggesting that those inversions yield reliable information about the shapes of the velocity anomalies.

Fitting the Hypocenters onto One Plane

Until now, constraints have been applied to the velocity models, such as regularization and velocity bounds, but no constraints have been applied to the hypocenters. Analysis of the two most active fracture planes by the three point method yields orientations which are within 20^o of each other (Table 11). One test of the non-uniqueness of the earthquake locations is to determine if the data can be satisfied equally well if all of the earthquakes are required to lie on one plane.

The inversion procedure was reformulated slightly, so that each hypocenter is required to satisfy an equation for a plane:

$$Ax_i + By_i + Cz_i = D, \tag{15}$$

where (x_i, y_i, z_i) are the location coordinates for the i^{th} earthquake. The location and orientation of the plane are allowed to vary, by allowing the four coefficients to vary. The requirement, therefore, is that the new coefficients and the new hypocenter coordinates satisfy the equation:

$$(A+\triangle A)(x_i+\triangle x_i)+(B+\triangle B)(y_i+\triangle y_i)+(C+\triangle C)(z_i+\triangle z_i)=(D+\triangle D) \tag{16}$$

Expanding Eq. (16), neglecting second order terms, and rearranging the remaining terms gives:

$$\begin{bmatrix} A & B & C \end{bmatrix} \begin{bmatrix} \triangle x_i \\ \triangle y_i \\ \triangle z_i \end{bmatrix} + \begin{bmatrix} x_i & y_i & z_i & -1 \end{bmatrix} \begin{bmatrix} \triangle A \\ \triangle B \\ \triangle C \\ \triangle D \end{bmatrix} = D - Ax_i - By_i - Cz_i. \tag{17}$$

By adding some zeros, the above equation can be written in terms of the hypocenter perturbation vector $\underline{\triangle h_i}$ and the velocity/station correction perturbation vector $\underline{\triangle m}$ (See Eq. 5):

$$\begin{bmatrix} 0 & A & B & C \end{bmatrix} \underline{\triangle h_i} + \begin{bmatrix} 2\,\mathrm{x}\,(nnode+nsta)\,0's & x_i & y_i & z_i & -1 \end{bmatrix} \begin{bmatrix} \underline{\triangle m} \\ \triangle A \\ \triangle B \\ \triangle C \\ \triangle D \end{bmatrix} = D - Ax_i - By_i - Cz_i. \tag{18}$$

Eq. (18) is added as an additional row to the joint hypocenter-velocity matrix equation (Eq. 5). This row is multiplied by a constant weighting factor, W_{pl}, which determines how strongly the hypocenters are constrained to lie on the plane. The separation of parameters step is then implemented as usual.

The coefficients (A, B, C) define the normal vector to the plane. These coefficients are not unique since they may be scaled by any constant factor and the same plane would be specified. To make the inversion more stable, we require the magnitude of this normal vector to be unity:

$$(A + \triangle A)^2 + (B + \triangle B)^2 + (C + \triangle C)^2 = 1. \tag{19}$$

Eq. (19) is expanded, and the second order terms $((\triangle A)^2, (\triangle B)^2, (\triangle C)^2)$ are dropped. The result is expressed in terms of the velocity/station correction perturbation vector $\triangle m$:

$$\left[\begin{array}{ccccc} 2\,x\,(nnode + nsta)\;0's & 2A & 2B & 2C & 0 \end{array}\right] \left[\begin{array}{c} \triangle m \\ \triangle A \\ \triangle B \\ \triangle C \\ \triangle D \end{array}\right] = 1 - A^2 - B^2 - C^2. \tag{20}$$

After the data from each earthquake are "processed", this additional row is added to the final separated matrix equation (Eq. 7). The coefficients A, B, C, and D are updated at the same time as the velocities and station corrections, and then the earthquakes are relocated on the new plane. The entire procedure is iterated as usual.

For the sake of saving time, straight rays were used for this test. (Ray bending would not change the conclusions of the test.) The final velocities and hypocenters of the old straight-ray "reference inversion" were used as the starting model. First, the best-fitting plane through those earthquake locations was determined. The orientation of that plane was N9°W, dip 84° East. The earthquakes were then relocated so that they were situated on that plane. Next, the hypocenters, velocities, station corrections, and the orientation of the plane were allowed to vary simultaneously. Weak velocity regularization ($\lambda = 1$) and loose velocity bounds ($V_{P\,min} = 3.5$ km/s, $V_{P\,max} = 6.5$ km/s, $V_{S\,min} = 2.0$ km/s, $V_{S\,max} = 4.2$ km/s) were applied. The velocity models were not constrained heavily because we want to determine how small the arrival time residuals can be with the earthquakes confined to one plane. The fewer restrictions that are placed on the velocities, the lower the residuals will be. The constraint that the earthquakes lie on one plane was weighted such that some deviation from the plane was allowed. The inversion was difficult to implement because either the hypocenters deviated too far from the plane, or the velocities varied too wildly. When the velocities vary too randomly, the hypocenter relocation scheme sometimes does not converge, and as a result many earthquakes are eliminated from the inversion. A satisfactory

convergence of the algorithm was not achieved. Results from an intermediate step in the iterative procedure were selected which satisfy two requirements: most of the hypocenters are properly relocated, and the deviation of the hypocenters from the plane is on the order of the expected error in the earthquake locations due to the data variance. The maximum deviation of the hypocenters from the chosen plane is about 25 m. The orientation of the plane is N7°W, dip 76° East.

The root-mean-square arrival time residuals for this model are 1.32 ms for the P-wave arrival times and 2.53 ms for the S-wave arrival times. These residuals are higher than those observed for any of the previous inversions. Of course, since an additional constraint is applied to each hypocenter, the number of independent hypocenter parameters has decreased. To determine if the increase in the arrival time residuals is simply due to the change in the number of degrees of freedom, a statistical F test was done. For this test, the number of independent model parameters must be known. If the earthquakes were required to lie exactly on one plane, then the number of independent hypocenter parameters for each earthquake would be 3 (2 location coordinates and the origin time). Since some deviation about the plane is allowed, the number of independent parameters for each earthquake is more than 3, but less than 4. As mentioned earlier, the number of independent parameters may be determined from the resolution matrix. The trace of the resolution matrix is equal to the number of independent model parameters. The resolution matrix for this constrained hypocenter relocation problem is:

$$R = \left(\mathbf{H^T H} + W_{pl}^2 \, \underline{a}\,\underline{a}^T\right)^{-1} \mathbf{H^T H}, \tag{21}$$

where $\mathbf{H}$ is the hypocenter partial derivative matrix for the unconstrained relocation problem, $\underline{a}^T$ is (0 A B C), and W_{pl} is the relative weighting for the plane constraint. The trace of the resolution matrix was computed for each earthquake, and these numbers were summed to determine the total number of independent hypocenter parameters. (The average trace is 3.52.) The F test yields a probability of less than 0.5% that the increase in the arrival time residuals when the hypocenters are confined to one plane is solely due to the corresponding change in the number of degrees of freedom. In conclusion, confining the hypocenters to one plane produces a model which does not satisfy the data, and therefore this test demonstrates that the earthquakes must occur along more than one fracture plane.

Synthetic Data Simulations

The V_P/V_S models computed from the velocity results of the joint inversion display a pronounced minimum, as shown in Figure 20. The minimum V_P/V_S value is in the range of 1.05 – 1.40 and depends on the particular weighting parameters used in the inversion. For comparison, the V_P/V_S ratio of the background velocities is 1.69. As explained in earlier, these very low V_P/V_S values are not consistent with the results anticipated,

based on theory and laboratory studies of fractured rock. These inconsistent ratios are especially troubling because they occur near the center of the inversion grid, where the velocity resolution is relatively good. In this section, synthetic data are inverted to evaluate the general reliability of the V_P/V_S ratios obtained from the joint inversion for the given ray geometry. This analysis also provides insight into two other observations: the fact that the P-wave velocity structures consistently exhibit less detail than the corresponding S-wave velocity structures, and the observation that the earthquakes systematically rotate during the joint inversion.

Synthetic arrival time data were generated using the S-wave velocity results from the inversion of the field data performed with the following parameters: $\lambda = 4$, P-wave data weighting = 2, P-wave velocity regularization weighting = 1 (from Figure 14c - 19c). The P-wave velocity model for the synthetic data was generated from the S-wave velocity structure and the V_P/V_S function shown in Figure 36. In this model, the V_P/V_S values increase as the S-wave velocities decrease. Thus, the S-wave velocities are perturbed more than the P-wave velocities, in terms of percentages, within the fractured "reservoir". This model is consistent with a zone of randomly-oriented, fluid-filled fractures (O'Connell and Budiansky, 1974; Toksöz et al., 1976; Cheng, 1978). The region outside the inversion grid has a homogeneous velocity structure with velocities of 5.92 km/s (P) and 3.50 km/s (S). Horizontal V_S, V_P, and V_P/V_S cross sections (at 3500 m depth) through the model are presented in Figure 37. These cross sections are used for evaluating the results from the inversions described below. Ray bending was used in generating the synthetic arrival times.

The joint inversion has been performed on three sets of the synthetic data:

1. Noise-free data.
2. Data with a low level of "noise", or variance, added.
3. Data with a high level of variance added.

The random noise added to the synthetic data has a normal distribution with zero mean and the standard deviations given in Table 13. More noise was added to the S-wave data than to the P-wave data because the measured P-wave arrival times are believed to be more accurate than the S-wave times. Also, more noise was added to the arrival times from the stations far from the source region than those close to it, since for the field data those arrival times may contain "errors" due to velocity variations outside the inversion grid. The initial velocity model for all of the inversions is the homogeneous structure with the correct background velocities. Ray bending is used in the inversions. The regularization parameter λ is 1 for the first two inversions. It is increased to 4 for the last inversion, since the data variance is high for that case. Equal P-wave and S-wave regularization weighting is used. As for the field data, the P-wave arrivals are

Station	Standard Deviation of Noise (ms)			
	Low Level		High Level	
	P Data	S Data	P Data	S Data
EE-1	0.5	0.75	1.5	2.5
EE-3	0.5	0.75	1.5	2.5
GT-1	1.0	1.5	2.2	4.0
PC-1	1.0	1.5	2.2	4.0

Table 13: Standard deviations of the random noise added to the synthetic data.

Inversion	RMS Error	Largest Error	Location of Largest Error(m)
No Noise	0.03	-0.13	-250E,-100N,3700D
Low Noise Level	0.05	-0.25	-300E,-200N,3600D
High Noise Level	0.09	-0.41	-300E,-200N,3600D

Table 14: Root-mean-square V_P/V_S errors and the largest V_P/V_S errors in the inversion results of the synthetic data.

weighted twice as heavily as the S-wave arrivals. The station corrections at stations PC-1 and GT-1 vary freely. Those at stations EE-1 and EE-3 are fixed at the correct values. Maximum P-wave and S-wave velocity bounds of 5.98 and 3.50 km/s, respectively, are applied. These values are the maximum velocities in the models used to generate the synthetic data.

Horizontal cross sections through the V_P/V_S structures computed from the final velocities for the three inversions are shown in Figure 38. As can be seen, as the data variance increases, the computed V_P/V_S structure becomes less accurate. When the data variance is high, the V_P/V_S ratios decrease in the central region of the inversion grid, similar to the results seen for the field data inversions. The rms V_P/V_S error (at the nodes) and the largest V_P/V_S error for each of the three inversions are listed in Table 14. For the inversion of the data with the high noise level, the rms V_P/V_S error is 0.09, and the largest error is -0.41. The minimum computed V_P/V_S value is 1.48. As observed in the inversions of the field data, if λ is decreased, the V_P/V_S minimum value decreases. For example, the data set with the high level of noise was also inverted with λ =1 (instead of 4), and in that case the minimum V_P/V_S value after 7 iterations is 1.1. (This inversion was terminated before it completely converged – the final V_P/V_S minimum value would be even lower.)

Inversion	P RMS (ms)	S RMS (ms)	Total RMS (ms)
No Noise	0.04	0.10	0.09
Low Noise Level	0.39	0.80	0.77
High Noise Level	0.98	2.21	2.09

Table 15: Final root-mean-square residuals for the three inversions of synthetic data.

The final P-wave, S-wave, and total rms arrival time residuals for the three inversions are given in Table 15. Comparing these values to the final rms residual values for the field data inversions (Table 8), we see that the third synthetic data set has a level of data variance which is comparable to that observed in the actual data. Hence, these results indicate that the V_P/V_S structure calculated from the final P-wave and S-wave velocity models of the joint inversion of the Los Alamos data is not reliable.

The reason why the V_P/V_S ratios are unreliable for high levels of data variance can best be seen by examining the final P-wave and S-wave velocity models. The horizontal V_S and V_P cross sections (at 3500 m depth) for the inversion of the data having the high noise level are presented in Figure 39. Note that the S-wave velocity structure is better defined than the P-wave velocity structure. Two "lobes" can be seen in the S-wave velocity cross section, but they are not resolved in the P-wave velocity model. These results are consistent with those of the field data inversions (Figures 16– 17). As noise is added to the synthetic data, the inversion loses its ability to properly resolve the V_P model faster than it loses its ability to resolve the V_S model. When this happens, the P-wave velocity model becomes dominated by the velocity regularization, and the final V_P model is very smooth. It is this relatively greater smoothing of the P-wave velocity model relative to the S-wave velocity model which causes the computed V_P/V_S structure to be incorrect.

Tests with the field data have shown that the phenomenon just described is not due to the relative P-wave and S-wave regularization weighting. Rather, it is due to the relative levels of "signal" and "noise" in the P-wave and S-wave data. For this example, "signal" is defined as the difference between the actual travel time through the correct velocity structure (with the correct earthquake location) and the travel time through the homogeneous velocity model corresponding to the background velocity (also with the correct earthquake location). Hence, the signals are the arrival time residuals due to the presence of the velocity anomaly. Since the velocities decrease within the anomaly, the signals are positive. The solid curves in Figure 40 represent the distributions of the P-wave signals (Figure 40a) and the S-wave signals (Figure 40b) for the synthetic data. The x axis is the arrival time residual, or "signal", in ms. For any signal value x_o, the corresponding y value is the fraction of the signals which are larger than x_o.

In other words, these curves are "inverse" cumulative distributions. (The distributions are plotted in this manner because the largest signals are of the most importance.) The dotted lines represent the high level noise distributions added to the synthetic data (defined in Table 13; only the positive values are included). As can be seen, the P-wave noise is large compared to the P-wave signal, whereas the S-wave noise is small compared to the S-wave signal. This poorer signal-to-noise level for the P-wave data relative to that for the S-wave data causes the relatively poorer P-wave velocity results shown in Figure 39. It should be noted that although the P-wave noise level is higher than the P-wave signal level (Figure 40a), the data still yield information about the P-wave velocities because the noise is random whereas the signals are not.

The poor signal-to-noise level for the P-wave data is not due to a large amount of noise, but to a small amount of signal. The P-wave signals are smaller than the S-wave signals for two reasons. The first reason is strictly numerical. Since the S-wave velocities are smaller than the P-wave velocities, the S-wave travel time changes are larger than the corresponding P-wave travel time changes for the same percent velocity perturbation. The relationship between the P-wave and S-wave travel time changes is easy to compute. Suppose the fractional decrease in velocities is f, and d is the length of the ray path within the anomaly. Then the P-wave and S wave travel time perturbations are given by:

$$\begin{aligned} \Delta t_p &= \frac{d}{v_p + \Delta v_p} - \frac{d}{v_p} \\ &= \frac{d/v_p}{1+f} - \frac{d}{v_p} \\ &= \frac{-df}{(v_p)(1+f)} \end{aligned} \tag{22}$$

$$\Delta t_s = \frac{-df}{(v_s)(1+f)} \tag{23}$$

The S wave signals are therefore related to the P-wave signals by:

$$\begin{aligned} \Delta t_s &= \frac{1}{v_s}\frac{-df}{1+f} \\ &= \frac{1}{v_s}\left(v_p \Delta t_p\right) \\ &= \frac{v_p}{v_s}\Delta t_p. \end{aligned} \tag{24}$$

For example, for a V_P/V_S ratio of 1.7, the S-wave signals would be 70% larger than the P-wave signals, for the same fractional decrease in velocity. The second reason for the difference in the P-wave and S-wave signals is due to the physical model. We have assumed a region of randomly-oriented, saturated fractures, for which case the V_P/V_S ratios increase relative to the background value. Hence, for this model the percent S-

wave velocity perturbation due to the anomaly is larger than the percent P-wave velocity perturbation. This fact increases the differences between the P-wave and S-wave signals.

The inversion results of the synthetic data with the high level of noise also demonstrate that the hypocenters may be systematically rotated relative to the correct locations. Figure 41 shows the vertical East-West projection of the final earthquake locations from the inversion of the data with the high noise level, as well as the correct locations. (The results shown here are for the inversion performed with $\lambda = 1$, since these results show the earthquake rotation more clearly than the results for $\lambda = 4$.) The rotation of the hypocenters seen here is not as pronounced as for the field data, and for that reason a heavy dashed line has been drawn in Figure 41 to define the approximate boundary of the deep cluster of the correct hypocenters. The deep cluster of final hypocenters is rotated to the west, relative to the correct locations, similar to the changes seen between the initial and final earthquake locations in the field data inversions. This observation is discouraging, since it implies that the final earthquake locations from the joint inversion of the Los Alamos data may actually be worse than the initial locations. This rotation is linked to the erroneous V_P/V_S ratios. The distance from a station to a hypocenter is controlled by the difference in the P-wave and S-wave arrival times, $t_p - t_s$. Let $t_p - t_s$ be represented by Δt_{ps}. For a given V_P/V_S ratio, Δt_{ps} is directly proportional to the distance from the station to the hypocenter. For this model, and most likely for the field data as well, some of the ray paths to the deep earthquakes pass through a zone in which V_P/V_S is too low. This causes the Δt_{ps} of the computed arrival times to be less than the Δt_{ps} of the observed arrival times. To counteract this problem, the hypocenters are moved farther from the stations which have ray paths passing through the low V_P/V_S anomaly – predominantly stations EE-3 and PC-1. This trade-off can occur because there is no ray coverage to the west of the source region. The ambiguity between the earthquake locations and the V_P/V_S ratios indicates that the V_P/V_S structure obtained from the joint inversion would be improved if more stations were available, since the hypocenters would then be better constrained.

INCONSISTENCY OF THE SHOT DATA

The final arrival time residuals of the shots display a negative skew. The final shot residuals for the inversion discussed earlier with $\lambda = 4$ are presented in Figure 42. The small filled circles represent P-wave residuals, and the large open circles represent S-wave residuals. The shot residuals are divided into three groups:

1. Residuals for the four shallow shots which were used to determine the station corrections at station EE-1 (Figure 42a).

2. Residuals for the remaining shots recorded at station EE-1 (Figure 42b).

3. The shot residuals at station EE-3 (Figure 42c).

The first group of shot residuals, those used to determine the station corrections at EE-1, are approximately centered around zero and lie between -1 ms and +1 ms. They are nearly identical for all of the inversions performed. This result is expected, since the shots are near the boundary of the inversion grid and therefore their computed travel times are almost unaffected by the velocity inversion. The deviation of these residuals about zero gives a measure of the error in the shot arrival times. One would expect the remaining shots to have approximately the same amount of scatter and, if the inversion model is correct, to also be centered about zero. Plots 42b and c show that this is not the case. The remaining shot residuals at station EE-1 show a small negative bias, about -1.35 ms. The residuals at station EE-3 show a substantially larger bias, approximately -2.1 ms for the P residuals and -3.7 ms for the S residuals. The shot residuals display similar trends for the inversions performed with different values of λ. Several factors could be contributing to this shift in the shot residuals:

1. The upper velocity bounds could be too low. Recall that the velocity penalty functions prevent the velocities from being larger than the background velocities. If there are actually velocities larger than the background velocities (5.92 km/s (P) and 3.50 km/s (S)), the event locations and origin times could be shifted to account for the differences in travel times, but the shots are fixed and thus would have negative residuals. In fact, most of the shot arrival times at station EE-3 yield average velocities which are larger than 5.92 and 3.50 km/s (Table 3). However, when the largest velocities determined from the shot data are used as the background velocities, and therefore also as the upper velocity bounds (Section), the shot residuals increase by only 0.5 to 1.0 ms. This test shows that although the choice of the upper velocity bounds may contribute to the bias in the final shot residuals, it is not the dominant cause.

2. Error in the location of station EE-3 could also contribute to the trend of the shot residuals, if the station is actually located closer to the shots than computed. In this scenario, too, the events are shifted to counteract the error in the station location. For the inversion in which the location of station EE-3 is allowed to vary, the final shot residuals for station EE-3 are approximately centered about zero. (The shot data were weighted, essentially forcing the station to move such that the shot residuals would be satisfied.) However, although the shot residuals for station EE-1 have also improved, they still display a small negative bias, about -0.4 ms.

3. The low residuals may be due to actual differences in the seismic velocities between the time the earthquakes were recorded and the time the shot data were gathered. The events were recorded while water was being pumped into the rock under a pressure of 48 MPa. The pumping pressure acts to increase the pore pressure,

thereby decreasing the effective pressure. When the pumping is terminated, the pore pressure gradually decreases to the hydrostatic pressure. Hence, the effective pressure increases. This process causes microcracks to close, thereby increasing the seismic velocities. The shot data were collected several months after the fracturing experiment ended, when the pore pressure was at or close to the hydrostatic pressure. The issue of velocity changes due to these changes in effective pressure is investigated in the remainder of this section.

In addition to the bias of the final shot residuals, indirect evidence that the seismic velocities were significantly different when the shot data were collected than when the hydrofracturing occurred is obtained from results of the joint inversion performed with and without the shot data included. First, consider the vertical East-West velocity cross sections in Figure 43. These results are from an inversion in which the shot data are included (as in all of the earlier inversions). The grid was extended vertically to 2800 m depth, so that it now incorporates station EE-1 (at 2855 m depth). (The velocities at 2800 m depth are actually fixed at the values of the background velocities – those at 2900 m depth are the shallowest velocities which vary during the inversion.) During this inversion, the P-wave and S-wave station corrections at stations EE-1 and EE-3 are fixed at a value of zero, since the stations are within the inversion grid. The regularization parameter λ is 4, and bent rays are used. The cross sections in Figure 43 are at -230 m North, which is about midway between the North-South coordinate of station EE-3 and the average North-South coordinate of the shots. Superimposed on the cross sections are projections of the straight ray paths from the shallowest and deepest shots to station EE-3. The other shots are at about the same East-West coordinate as these shots, at intermediate depths. As is clearly seen in the cross sections, the cone-shaped region of influence of the shot data has higher average P-wave and S-wave velocities than the regions immediately above and below. The presence of the low-velocity zones shallower than the shots is not consistent with the concept that low velocities, fracturing, and seismicity are correlated, since they are located in an aseismic zone. Although these velocities are not well resolved due to the limited ray coverage, they must be caused by some signal in the data. Otherwise, the regularization would force the velocities to be smooth – either homogeneous or smoothly tapering. It is possible that these low-velocity anomalies are due to the shallower Phase I reservoir, although this hypothesis seems unlikely since that reservoir was created mostly above 2700 m depth. The same type of inversion performed without the shot data yields the results shown in Figure 44. For purposes of comparison, the same shot ray paths are superimposed on these cross sections as on the previous ones. The velocities in that cone-shaped region have decreased significantly compared to the results of the previous inversion. The shallowest velocity anomalies are no longer isolated. The decreases in velocity above the seismic zone are probably due to poor ray coverage coupled with the velocity regularization. They may also be partly due to velocity variations outside the inversion grid. It should be noted that the final rms residuals for these two inversions

are about the same, indicating that both models satisfy the data equally well.

If we assume that the inversion performed without the shot data yields the correct velocities for the time of the fracturing, then we can compare those results to the velocities computed from the shot data to estimate the changes in the velocities due to the change in effective pressure. The average P-wave and S-wave velocities along the straight ray paths from the shot locations to stations EE-1 and EE-3 were computed using the final velocity models for the inversion described above (Figure 44). The average velocities were simply computed by dividing the straight ray path lengths by the travel times. Likewise, average P-wave and S-wave velocities were also computed from the shot data. The results are compared in Table 16. (Note that the shot data which were judged to be too inconsistent to use in the inversion are included in this table.) Several trends are present in the results. First, the differences between the velocities computed from the inversion results and those calculated from the shot data are consistently larger for station EE-3 than for station EE-1. This result is reasonable, since only a small fraction of the ray paths from the shots to station EE-1 lie within the seismic zone (which is assumed to be the most fractured region), whereas most of the ray paths from the shots to station EE-3 lie within, or very near, the seismic zone. The shallowest shots are shots 2038-3a,3b and 2048-2a,2b. (These shot numbers are preceded by an asterisk in Table 16 to make them easy to identify.) These shots were located at about 3108 m depth. The remaining shots were located between 3265 and 3283 m depth. The velocities for the shallow shots consistently show smaller changes than the velocities for the deeper shots. The reason for this trend is the same as described above – a smaller fraction of the ray paths from the shallow shots lie within or near the fractured zone than those from the deeper shots.

The third trend in the velocities listed in Table 16 is subtle. To see this trend, the information must be rearranged. Shots 2038-3a,3b and 2048-2a,2b were located at nearly identical locations but the data were collected at different times. Likewise, shots 2038-2a,2b and 2048-1 were located at almost the same location. The shot data in group 2038 were collected about 4 months after the fracturing experiment, and those in group 2048 were collected about 10 months after the hydrofracturing. Arrival times were not recorded at station EE-3 during Experiment 2048, so only the data for station EE-1 are considered in the following analysis. In Table 17, the velocities corresponding to the shots listed above are divided into two groups based on the shot locations:

1. Shots 2038-3a,3b and 2048-2a,2b (-502 m E, -291 m N, 3108 m D)
2. Shots 2038-2a,2b and 2048-1 (-442 m E, -270 m N, 3281 m D).

Within each location group, the velocities are divided into three time periods: during the fracturing (velocities computed from the inversion results), 4.25 months after the fracturing (shot group 2038), and 10.35 months after the fracturing (shot group

Ray Paths to Station EE-1						
	P-wave Velocities			S Wave Velocities		
Shot	From Inversion (km/s)	From Shots (km/s)	% Difference	From Inversion (km/s)	From Shots (km/s)	% Difference
2038-1a	5.35	5.90	10.3	3.21	3.42	6.5
2038-1b	5.35	5.80	8.4	3.21	3.37	5.0
2038-2a	5.32	5.85	10.0	3.20	3.43	7.2
2038-2b	5.33	5.85	9.8	3.20	3.44	7.5
* 2038-3a	5.64	5.79	2.7	3.35	3.47	3.6
* 2038-3b	5.65	5.88	4.1	3.35	3.45	3.0
2048-1	5.33	5.92	11.1	3.20	3.47	8.4
* 2048-2a	5.65	5.98	5.8			
* 2048-2b	5.65	5.96	5.5	3.35	3.51	4.8

Ray Paths to Station EE-3						
	P-wave Velocities			S Wave Velocities		
Shot	From Inversion (km/s)	From Shots (km/s)	% Difference	From Inversion (km/s)	From Shots (km/s)	% Difference
2038-1a	4.95	5.99	21.0	3.13	3.53	12.8
2038-1b	4.95	6.04	21.3	3.13	3.58	14.4
2038-2a	4.93	6.05	22.7	3.13	3.59	14.7
2038-2b	4.93	6.04	22.5	3.13	3.57	14.1
* 2038-3a	5.15	5.91	14.8	3.18	3.55	11.6
* 2038-3b	5.15	5.92	15.0	3.18	3.58	12.6

Table 16: Comparison of the average velocities computed (along the shot-to-receiver straight ray paths) from the results of the inversion performed without the shot data, and the average velocities computed from the shot data. * identifies shallower shots.

First Shot Location Group (2038-3a,3b; 2048-2a,2b)			
	Velocities (km/s)		
Station	During Fracturing (shots 2038-3a,3b; 2048-2a,2b)	4.25 Months After Fracturing (shots 2038-3a,3b)	10.35 Months After Fracturing (shots 2048-2a,2b)
EE-1, P	5.65	5.845	5.97
EE-1, S	3.35	3.46	3.51

Second Shot Location Group (2038-2a,2b; 2048-1)			
	Velocities (km/s)		
Station	During Fracturing (shots 2038-3a,3b; 2048-2a,2b)	4.25 Months After Fracturing (shots 2038-3a,3b)	10.35 Months After Fracturing (shots 2048-2a,2b)
EE-1, P	5.325	5.85	5.92
EE-1, S	3.20	3.435	3.47

Table 17: Subsets of the velocities from Table 16, corresponding to shots which had nearly identical locations. The averages of the velocities computed for each time interval are listed.

2048). The velocities computed for each time interval were averaged, and the mean values are listed in the table. From these results it is clear that the velocities were not only higher when the shot data were recorded than during the fracturing, but also the velocities were higher when the later set of shot data was collected than when the earlier set was gathered. The increases in velocity from the early shot data to the late shot data are small but consistent. It is not clear if the velocity changes between the fourth and tenth months are solely due to continuing pore pressure decreases within the fractured reservoir. During the time interval between collection of the first and second sets of shot data, another hydrofracturing experiment was performed (Experiment 2042; May, 1984). The injection zone was in well EE-3, at approximately 3500 m depth. No hydraulic connection was made to the reservoir of Experiment 2032, and most of the earthquakes occurred deeper than 3400 m and east of well EE-3. Hence, this hydrofracturing probably did not affect the pore pressure within the fractured zone near the shot locations. However, it may have altered the stress field such that the confining pressure on the shot region was increased. Crack healing may also have contributed to the continuing increase in the seismic velocities with time. Smith and Evans (1984) claim that fluid-filled microcracks in quartz have "geologically short lifetimes at temperatures above 200°C", on the order of several months to a few years. This conclusion is applicable to the Los Alamos situation since the rocks are silicic and the reservoir temperatures are between 200 and 300°C (Smith et al., 1987).

The ray paths which traverse the most seismically active region, and therefore the region which is believed to be the most fractured, are those from the deeper shots to station EE-3 (shots 2038-1a,1b,2a,2b). Table 16 shows that the velocity changes for these ray paths range from 13 to 23%. We can compare these values to those measured in the laboratory if we know the corresponding change in effective pressure. From studies of the pumping pressures and flow rates, Dash et al. (1984) have estimated the fracture extension pressure – the pressure required to create new fractures – to be 69 MPa. Hence, this value is the approximate pore pressure during the hydrofracturing. We have estimated the confining, or overburden, pressure to be about 91 MPa at 3.5 km depth, and therefore the effective pressure during the hydrofracturing was 22 MPa. After the pumping stopped, the pore pressure eventually returned to the hydrostatic value of 35 MPa (Dash et al., 1984). Hence, the effective pressure at that time was approximately 56 MPa. Coyner and Cheng (1985) measured velocity changes for Westerly granite on the order of 2% for saturated cracks and 3 – 5% for dry cracks, over an approximate range of 22 to 56 MPa of the effective pressure. Nur and Simmons (1969) measured velocity changes for Troy granite of 1 – 3% for saturated cracks and 3 % for dry cracks over the same pressure range. From these observations, it is apparent that the velocity changes computed from the inversion results and the shot data are significantly larger than those measured in the laboratory over the corresponding pressure range. Since fractures have been induced in the reservoir rock, the velocity changes in the reservoir are expected to be larger than those changes measured in laboratory samples of rocks which contain only "natural" fractures. Also, the effect of crack healing may be important in the field

but is not measured in laboratory studies carried out over short time periods. Note that the percent P wave velocity changes are almost always larger than the percent S-wave velocity changes (Table 16). This result is not consistent with randomly-oriented, completely saturated cracks (Cheng, 1978; O'Connell and Budiansky, 1974; Toksöz et al., 1976), and cannot be trusted since the V_P/V_S ratios obtained from the joint inversion have been shown to be unreliable.

To summarize, of the three proposed causes of the bias of the final shot residuals, only the third one satisfies all of the data. We conclude that the shot residuals are biased because the velocity structure was actually different when the shots were collected than when the earthquakes occurred. The inversion results performed with and without the shot data support this hypothesis (Figures 43 and 44). The magnitudes of the velocity changes observed in the Los Alamos reservoir, compared to those measured in laboratory samples, suggest that the rock has been significantly fractured.

A DIFFERENT MODEL: CONSTRAINING V_P/V_S

The V_P/V_S structure computed from the final V_P and V_S models of the joint inversion displays a pronounced minimum near the center of the inversion grid. These V_P/V_S values are not physically reasonable for the reasons given previously. Also, synthetic data simulations demonstrate that the V_P/V_S ratios computed from the inversion results are not reliable. Erroneous V_P/V_S anomalies cause systematic bias in the earthquake locations.

Since the results from the joint inversion are not adequately constrained by the data and the velocity regularization and bounds which have been applied, we seek an additional constraint. Specifically, we wish to avoid the bias in the earthquake locations due to the erroneous low V_P/V_S ratios. The most straight forward approach is to apply a lower bound to V_P/V_S by adding a penalty function for the V_P/V_S ratios. These penalties are easily incorporated into the inversion. Extra rows are simply added to the penalty function matrix equation (see Block, 1991):

$$\begin{bmatrix} P((V_P/V_S)_1 + \Delta(V_P/V_S)_1) \\ | \\ P((V_P/V_S)_{nnode} + \Delta(V_P/V_S)_{nnode}) \end{bmatrix} = \begin{bmatrix} P((V_P/V_S)_1) \\ | \\ P((V_P/V_S)_{nnode}) \end{bmatrix}$$

$$+\begin{bmatrix} \frac{\partial P((V_P/V_S)_1)}{\partial v_1^P} & 0 & \frac{\partial P((V_P/V_S)_1)}{\partial v_1^S} & 0 \\ 0 & \frac{\partial P((V_P/V_S)_{nnode})}{\partial v_{nnode}^P} & 0 & \frac{\partial P((V_P/V_S)_{nnode})}{\partial v_{nnode}^S} \end{bmatrix} \cdot \begin{bmatrix} \triangle v_1^P \\ | \\ \triangle v_{nnode}^P \\ \triangle v_1^S \\ | \\ \triangle v_{nnode}^S \end{bmatrix} \cdot \tag{25}$$

The partial derivatives are found by the chain rule:

$$\frac{\partial P((V_P/V_S)_i)}{\partial v_i^P} = \left(\frac{\partial P((V_P/V_S)_i)}{\partial (V_P/V_S)_i}\right)\left(\frac{\partial (V_P/V_S)_i}{\partial v_i^P}\right) = \left(\frac{\partial P((V_P/V_S)_i)}{\partial (V_P/V_S)_i}\right)\left(\frac{1}{v_i^S}\right) \tag{26}$$

$$\frac{\partial P((V_P/V_S)_i)}{\partial v_i^S} = \left(\frac{\partial P((V_P/V_S)_i)}{\partial (V_P/V_S)_i}\right)\left(\frac{\partial (V_P/V_S)_i}{\partial v_i^S}\right) = \left(\frac{\partial P((V_P/V_S)_i)}{\partial (V_P/V_S)_i}\right)\left(\frac{-v_i^P}{(v_i^S)^2}\right) \tag{27}$$

The inversion is performed exactly as before, except that when any V_P/V_S value falls below the minimum bound, the next iteration step forces the V_P/V_S ratio to increase.

The V_P/V_S ratios within the fractured reservoir should be higher than those of the background velocities (1.69) if the fractures are fluid-filled and randomly oriented. To allow for some flexibility in the model, such as effects due to anisotropy or effects due to the velocity structure outside the inversion grid, a lower V_P/V_S bound of 1.60 is applied. The V_P/V_S penalty function is:

$$P(V_P/V_S) = \begin{cases} 50\,(1.60 - V_P/V_S) & V_P/V_S < 1.60 \\ 0 & otherwise \end{cases} . \tag{28}$$

Two inversions were performed: one inversion with the regularization parameter λ equal to 4, and the other with λ equal to 1. (Bent rays were used.) V_P, V_S, and V_P/V_S cross sections through the final velocity models are presented in Figures 45 – 53. Comparing these results to those determined previously without a V_P/V_S lower bound (Figures 14 – 19), one sees that the P-wave velocity structure has changed more than the S-wave velocity structure. This observation is consistent with the hypothesis that the P-wave velocities are not constrained as well by the data as the S-wave velocities. Since the P-wave velocities are poorly determined by the data, they are sensitive to the constraints applied during the inversion. Although the V_P/V_S ratios do not decrease to very low values in these inversions, the ratios are still lower than the value for the unfractured rock, 1.69, in many regions. This result is likely due to the greater smoothing of the P wave velocities relative to the S-wave velocities, which is a consequence of the low signal-to-noise ratio in the P-wave data. In these new models, the V_P/V_S ratios increase in some of the seismically active regions. This structure is consistent with rock containing randomly-oriented fluid-filled fractures.

λ	Final RMS Residual (ms) P-wave	S-wave	Total	Decrease in Total Residual (%)
initial model	1.14	2.28	2.28	
4	1.03	1.99	2.03	11.0
1	0.96	1.91	1.93	15.4

Table 18: Final rms residuals for the inversions performed with a lower V_P/V_S bound of 1.60.

The final root-mean-square residuals for these two inversions are listed in Table 18. The values are *comparable* to those for the inversions performed without a V_P/V_S lower bound (Table 8). However, for a given value of λ, the residuals for the inversion performed with the V_P/V_S lower bound are higher than those for the corresponding inversion performed without the bound. Since many of the velocities are constrained by the V_P/V_S bound in these new inversions, the number of free parameters has decreased. The statistical F test determines if the change in the residuals is simply due to the change in the number of free parameters. It is not clear how to count the number of free parameters when the V_P/V_S bound is applied. The final number of V_P/V_S values which are lower than the bound of 1.60 is not a good measure of the number of velocities which are actually constrained by the bound because many other V_P/V_S values may just have been pushed above the bound on the previous iteration. A better measure of the number of velocities constrained by the V_P/V_S lower bound is found by counting the final number of ratios which are less than 1.60 in the results for the earlier inversions performed without the V_P/V_S bound. When the difference in the number of free parameters is counted in this way, the F test indicates that the increase in the residuals when the V_P/V_S ratios are constrained is due to the change in the number of free parameters. In short, the models from these new inversions performed with a lower bound applied to the V_P/V_S ratios statistically satisfy the data as well as those from the previous inversions. Since these constrained V_P/V_S structures are more geologically reasonable than those determined previously, we conclude that the velocity structures (and therefore the earthquake locations) from these new inversions are more reliable than those determined previously with no V_P/V_S bound.

Projections of the initial and final earthquake locations for the inversion performed with λ equal to 1 are given in Figure 54. The results for the inversion with λ equal to 4 look similar. The hypocenters are *not* systematically rotated as before. In fact, the overall trend of the hypocenters is not obviously altered by the joint inversion. Table 19 gives the average change in each hypocenter parameter, for each inversion, as well as

Hypocenter Parameter	Average Change in Parameter During Inversion	
	$\lambda = 4$	$\lambda = 1$
North Coord. (m)	1.2	4.3
East Coord. (m)	-0.9	6.5
Depth Coord. (m)	-8.7	-16.4
Average Distance Event Moved During Inv.	20.6	27.4
Origin Time (ms)	-1.9	-1.8

Table 19: 1. Average changes in the hypocenter parameters during the inversions performed with a lower V_P/V_S bound of 1.60.

the average absolute distance the hypocenters move. The average absolute change in the earthquake locations is 20.6 m for the inversion with $\lambda = 4$ and 27.4 m for the inversion with $\lambda = 1$. For both inversions the earthquakes move shallower on average. Given the non-uniqueness of the inversion results, especially the P-wave velocities and the V_P/V_S ratios, it is impossible to claim simply from the reduction in the residuals that the earthquake locations have been improved by the joint inversion. Future studies may indicate whether the new locations better define the major fracture planes of the reservoir.

CONCLUSIONS

In this paper a detailed study of the joint hypocenter-velocity inversion was carried out using microearthquake arrival time data from the Los Alamos Hot Dry Rock geothermal site. The goal was to determine if this type of inversion could improve the earthquake locations and if the three-dimensional P-wave and S-wave velocity structures of the fractured reservoir could be determined. The strengths and limitations of the method, as applied to this data set, were investigated. The results are summarized below.

The joint hypocenter-velocity inversions yield S wave velocity structures which generally correlate well with the earthquake locations. Studies of synthetic data show that the locations and general shapes of the V_S anomalies are reliable in regions where the ray coverage is adequate. The magnitudes of the velocities cannot be precisely determined. The percent velocity perturbations increase as the velocity regularization weighting de-

creases. Studies of inversions performed using different regularization weightings suggest that the S-wave velocities decrease by at least 13% in the most intensively fractured regions of the reservoir.

The joint inversions yield very smooth P-wave velocity structures. The minimum P-wave velocities occur in an aseismic region, decreasing as much as 22 – 43% compared to the velocity of the unfractured rock. Presence of these very low P-wave velocities in an aseismic region is not consistent with the hypothesis that the fractured reservoir is defined by the earthquake locations. Also, if no constraints are applied to the V_P/V_S ratios, then the V_P/V_S structures computed from the final V_P and V_S models display a broad, pronounced minimum at the location of the lowest V_P values. The minimum V_P/V_S values range from 1.06 to 1.38, depending on the amount of velocity regularization applied. These values are not reasonable either for the mostly unfractured rock outside the reservoir or for the rock containing fluid-filled fractures within the reservoir. Synthetic data simulations demonstrate that the P-wave velocity models and the V_P/V_S structures determined by the joint inversion are not reliable for the given station geometry. Since the travel time perturbations caused by the fluid-filled fractures are much smaller for P waves than for S waves, the P-wave velocities are less constrained by the data than the S-wave velocities. If the data variance from other sources – such as arrival time picking errors, velocity variations outside the inversion grid, and velocity anisotropy – is as large as the perturbations due to the fractured reservoir, the shape of the reservoir is not resolved in the final V_P model. Rather, the P-wave velocity structure is strongly influenced by the velocity regularization, which biases the V_P model toward a smoother shape. This bias results in erroneous V_P/V_S ratios.

If no constraints are applied to the V_P/V_S ratios, then the hypocenters are rotated into a more vertical and more North-South orientation during the joint inversion of the Los Alamos data. As synthetic data tests show, the poor V_P/V_S ratios cause systematic error in the earthquake locations. Hence, the earthquake rotation observed in the inversions of the field data is an artifact of the error in the P-wave velocity structure. The trade-offs between the V_P/V_S ratios and the earthquake locations are strong for this problem because the azimuthal ray coverage with the four seismometers is poor.

Inversions performed with a lower bound of 1.60 applied to the V_P/V_S ratios yield models which satisfy the data as well as the models from the inversions performed without the bound, and they yield more geologically reasonable V_P/V_S structures. The residuals decrease 11 – 15% during the inversions. The P-wave velocity structure is much more strongly affected by the addition of the V_P/V_S bound than the S-wave velocity structure. This observation is consistent with the hypothesis given above that the P wave velocities are not constrained by the data as well as the S-wave velocities. For these inversions, the final earthquake locations are *not* systematically rotated with respect to the initial locations. The average absolute change in the earthquake locations

during these inversions is 20 – 27 m. Unfortunately, given the non-uniqueness of the inversion results, it is impossible to claim simply from the reduction in the residuals that the earthquake locations have been improved by the joint inversion. Future studies may indicate whether the new locations better define the major fracture planes of the reservoir.

Increasing the number of seismometers used during the hydrofracturing would greatly improve the results obtained from the joint inversion for several reasons:

1. The increased ray coverage would directly improve the spatial resolution of the velocity models.

2. The increased number of arrival times would better constrain the hypocenters, especially if the azimuthal ray coverage were improved. Because of the trade-offs between velocities and hypocenters, the velocities would also be better constrained.

3. Since the uncertainties in the earthquake locations would be reduced, the trade-offs between P-wave and S-wave velocities would decrease.

4. If the hypocenters were better constrained, the V_P/V_S ratios would also be better constrained. The increased control of the V_P/V_S ratios would result in a more reliable P-wave velocity structure.

Another way to improve the results would be to fire shots deep within the source region, so that the ray paths propagate through the unknown velocity structure of the reservoir. One or more fixed sources deep in the region of investigation would greatly reduce the trade-offs between the V_P/V_S ratios and the hypocenters, even if the azimuthal ray coverage were limited. Since studies performed here have shown that the velocities are significantly affected by the change in the effective pressure when high pumping pressures are applied, the shot data would be most useful if they were collected at the time of the hydrofracturing, or at least under some pressurized condition.

ACKNOWLEDGEMENTS

The authors wish to thank Leigh House for his assistence with the data and for providing the hypocenter location program used in the initial phases of this work, and Cliff Thurber for providing his approximate ray bending code. This research was supported by Department of Energy Grant #DE-FG02-86ER13636 and the Full Waveform Acoustic Logging Consortium at M.I.T. Lisa Block was partially supported by a Phillips Petroleum Fellowship.

REFERENCES

Barr, K.G., and G.R. Robson, Seismic Delays in the Eastern Caribbean, *Geophys. J.*, *7*, 342–349, 1963.

Block, L.V., *Joint Hypocenter-Velocity Inversion of Local Earthquake Arrival Time Data in Geothermal Regions*, Sc.D. Thesis, Massachusetts Institute of Technology, Cambridge, Massachusetts, 1991.

Cheng, C.H., *Seismic Velocities in Porous Rocks: Direct and Inverse Problems*, Sc.D. thesis, Massachusetts Institute of Technology, Cambridge, Massachusetts, 1978.

Coyner, K.B., and C.H. Cheng, The Effects of Confining Pressure and Fluid Saturation on Ultrasonic Velocities in Rocks, *M.I.T. Full Waveform Acoustic Logging Consortium Annual Report.* 1985.

Dash, Z., I. Matsunaga, and H.D. Murphy, Injection Pressures and Flow Rates, *Experiment 2032 Report*; Internal report, ESS-4-70-84, Los Alamos National Laboratory, Los Alamos, New Mexico, 1984.

Fehler, M., L. House, and H. Kaieda, Determining Planes Along Which Earthquakes Occur: Method and Application to Earthquakes Accompanying Hydraulic Fracturing, *J. Geophys. Res., 92*, 9407–9414, 1987.

Fehler, M., and W.S. Phillips, Simultaneous Inversion for Q and Source Parameters of Microearthquakes Accompanying Hydraulic Fracturing in Granitic Rock, *Bull. Seis. Soc. Am.*, in press, 1991.

Franke, P.R., and G.J. Nunz, Recent Developments in the Hot Dry Rock Geothermal Energy Program, Preprints, *Geothermal Resources Council Annual Meeting, Kailua-Kona, Hawaii*, 1–4, 1985.

Harlow, F.H., and W.E. Pracht, A Theoretical Study of Geothermal Energy Extraction, *J. Geophys. Res., 77*, 7038–7048, 1972.

Hatton, L., M.H. Worthington, and J. Makin, *Seismic Data Processing, Theory and Practice*, Blackwell Scientific Publications, Inc., Palo Alto, California, 1986.

House, L., Locating Microearthquakes Induced by Hydraulic Fracturing in Crystalline Rock, *Geophys. Res. Letters*, **14**, 919–921, 1987.

Laughlin, A.W., A.C. Eddy, R. Laney, and M.J. Aldrich, Jr., Geology of the Fenton Hill, New Mexico, Hot Dry Rock Site, *J. of Volcanology and Geothermal Res., 15*, 21–41, 1983.

Lees, J.M., *Seismic Tomography in Western Washington* Ph.D. Thesis, Univ. of Washington, Seattle, Washington, 1989.

Mendenhall, W., R.L. Scheaffer, and D.D. Wackerly, Mathematical Statistics with Applications, Third Edition, PWS Publishers, Boston, Massachusetts, 1986.

Nur, A.M., and G. Simmons, The Effect of Saturation on Velocity in Low Porosity Rocks, *Earth Plan. Sci. Letters, 7*, 183–193, 1969.

O'Connell, R.J., and B. Budiansky, Seismic Velocities in Dry and Saturated Cracked Solids, *J. Geophys. Res., 79*, 5412–5426, 1974.

Pavlis, G.L., and J.R. Booker, The Mixed Discrete-Continuous Inverse Problem: Application to the Simultaneous Determination of Earthquake Hypocenters and Velocity Structure, *J. Geophys. Res., 85*, 4801–4810, 1980.

Phillips, W.S., and M.C. Fehler, Traveltime tomography: a comparison of popular methods, *Geophysics*, submitted, 1991.

Scales, J.A., P. Doherty, and A. Gersztenkorn, Regularization of nonlinear inverse problems: Imaging the near surface weathering layer, *Inverse Problems, 6*, 115–131, 1990.

Shaw, P.R., and J.A. Orcutt, Waveform inversion of seismic refraction data and applications to young Pacific crust, *J. R. Astr. Soc., 82*, 375–414, 1985.

Smith, D.L., and B. Evans, Diffusional Crack Healing in Quartz, *J. Geophys. Res., 89*, 4125–4135, 1984.

Smith, M.C., R.H. Hendron, H.D. Murphy, and M.G. Wilson, *Hot Dry Rock Geothermal Energy Development Program Annual Report, Fiscal Year 1987*, Los Alamos National Lboratory, Los Alamos, New Mexico, 1987.

Thomsen, L., Weak Elastic Anisotropy, *Geophysics, 51*, 1954–1966, 1986.

Thurber, C.H., *Earth Structure and Earthquake Locations in the Coyote Lake Area, Central California*, Ph.D. thesis, Massachusetts Institute of Technology, Cambridge, Massachusetts, 1981.

Thurber, C.H., Earthquake locations and three-dimensional crustal structure in the Coyote Lake area, Central California, *J. Geophys. Res., 94*, 8226–8236, 1983.

Toksöz, M.N., C.H. Cheng, and A. Timur, Velocities of Seismic Waves in Porous Rocks, *Geophysics, 41*, 621–645, 1976.

Um, J., and C.H. Thurber, A Fast Algorithm for Two-Point Seismic Ray Tracing, Bull. Seis. Soc. Am., 77, 972–986, 1987.

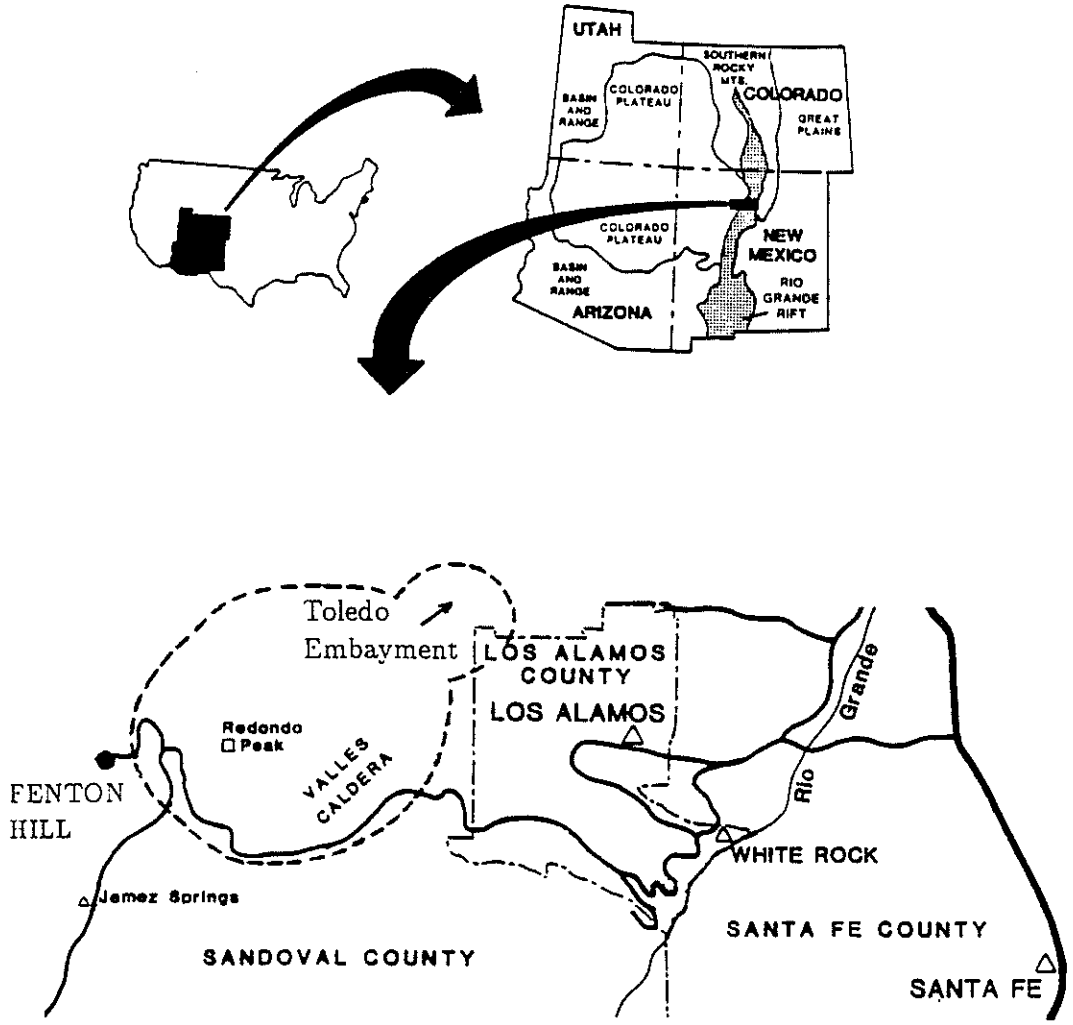

Figure 1: Location map for Fenton Hill, the Los Alamos Hot Dry Rock site.

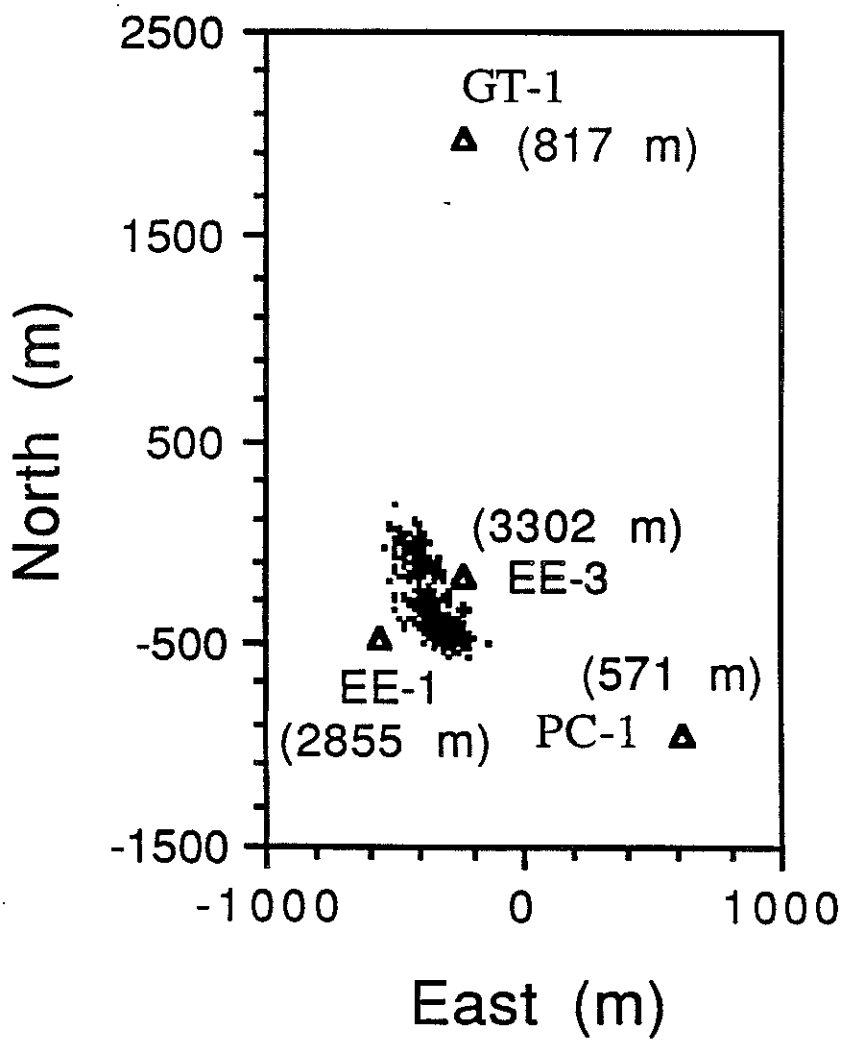

Figure 2: Plane view of the station geometry for Experiment 2032. The station depths are given in parentheses. The cluster of dots represents the earthquake epicenters.

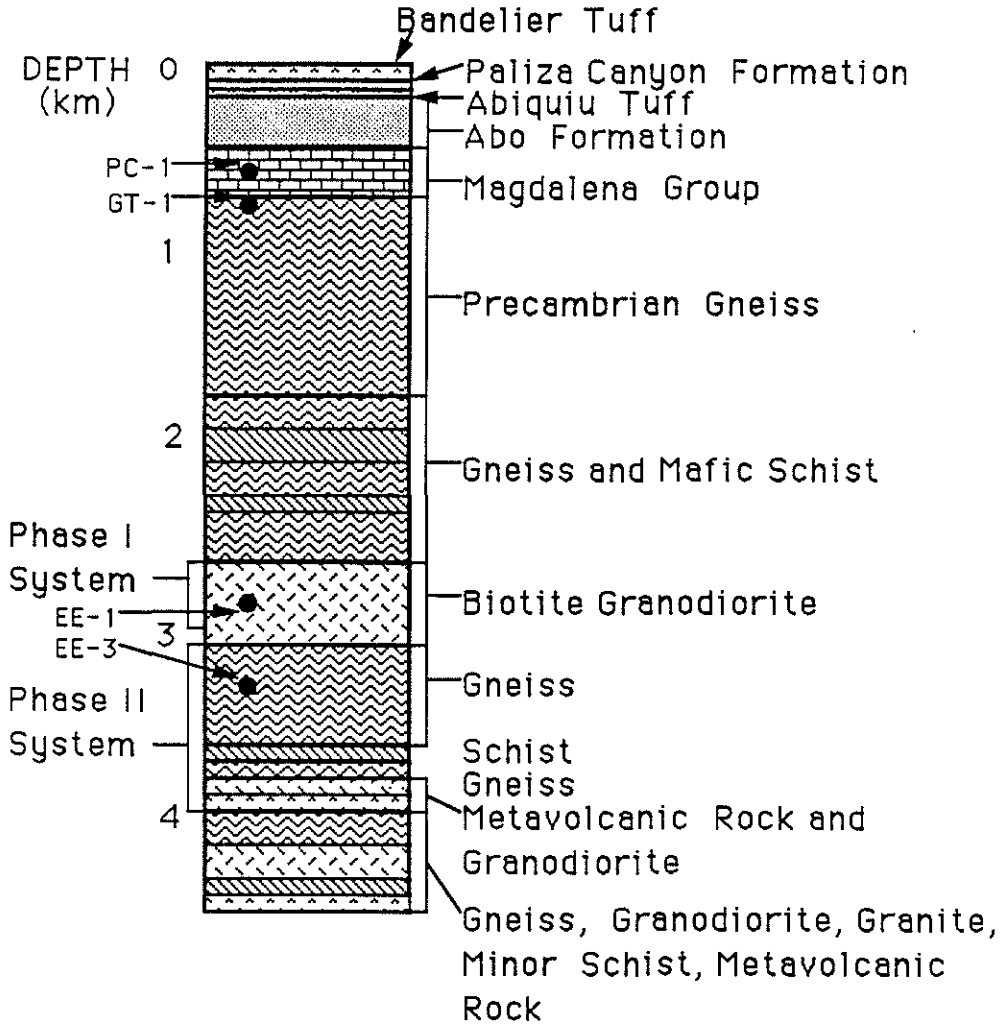

Figure 3: Simplified geologic cross section for the Los Alamos Hot Dry Rock site (adapted from Laughlin et al., 1983).

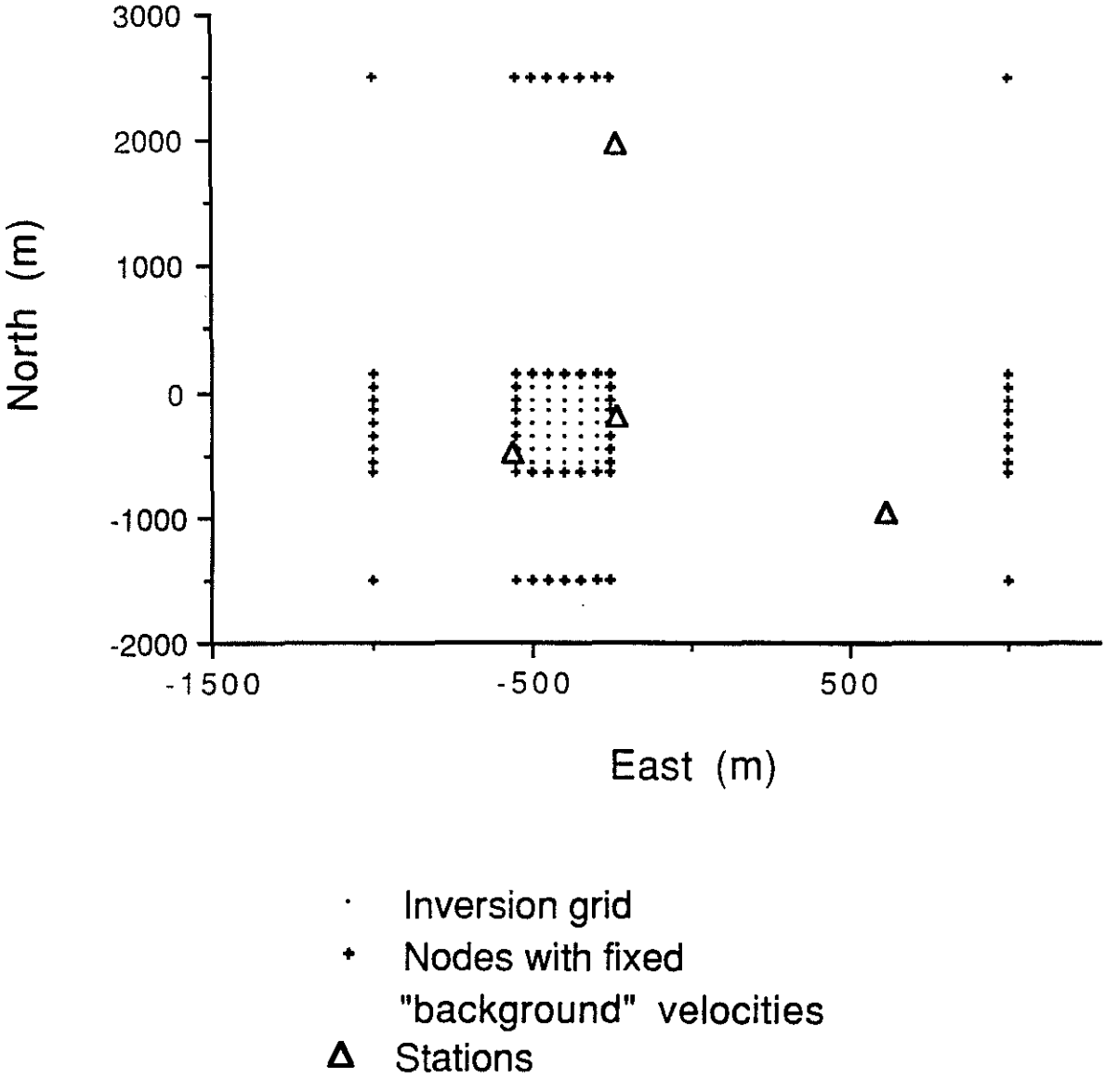

Figure 4: Skematic representation of the velocity nodes for the Los Alamos inversions.

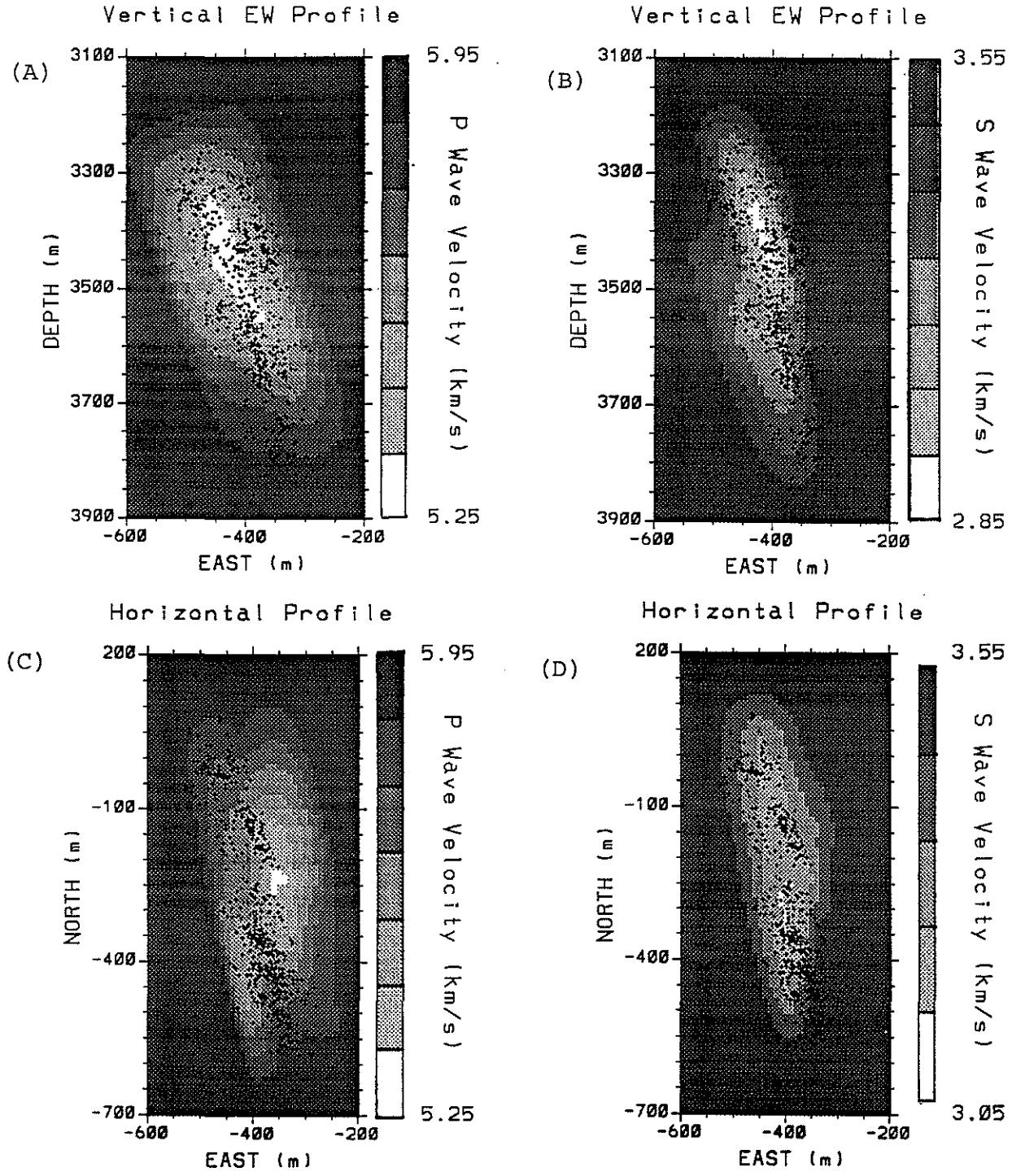

Figure 5: Velocity model used to generate synthetic arrival time data. (A) and (B) Vertical East-West V_P and V_S cross sections at -300 m North. (C) and (D) Horizontal V_P and V_S cross sections at 3500 m depth.

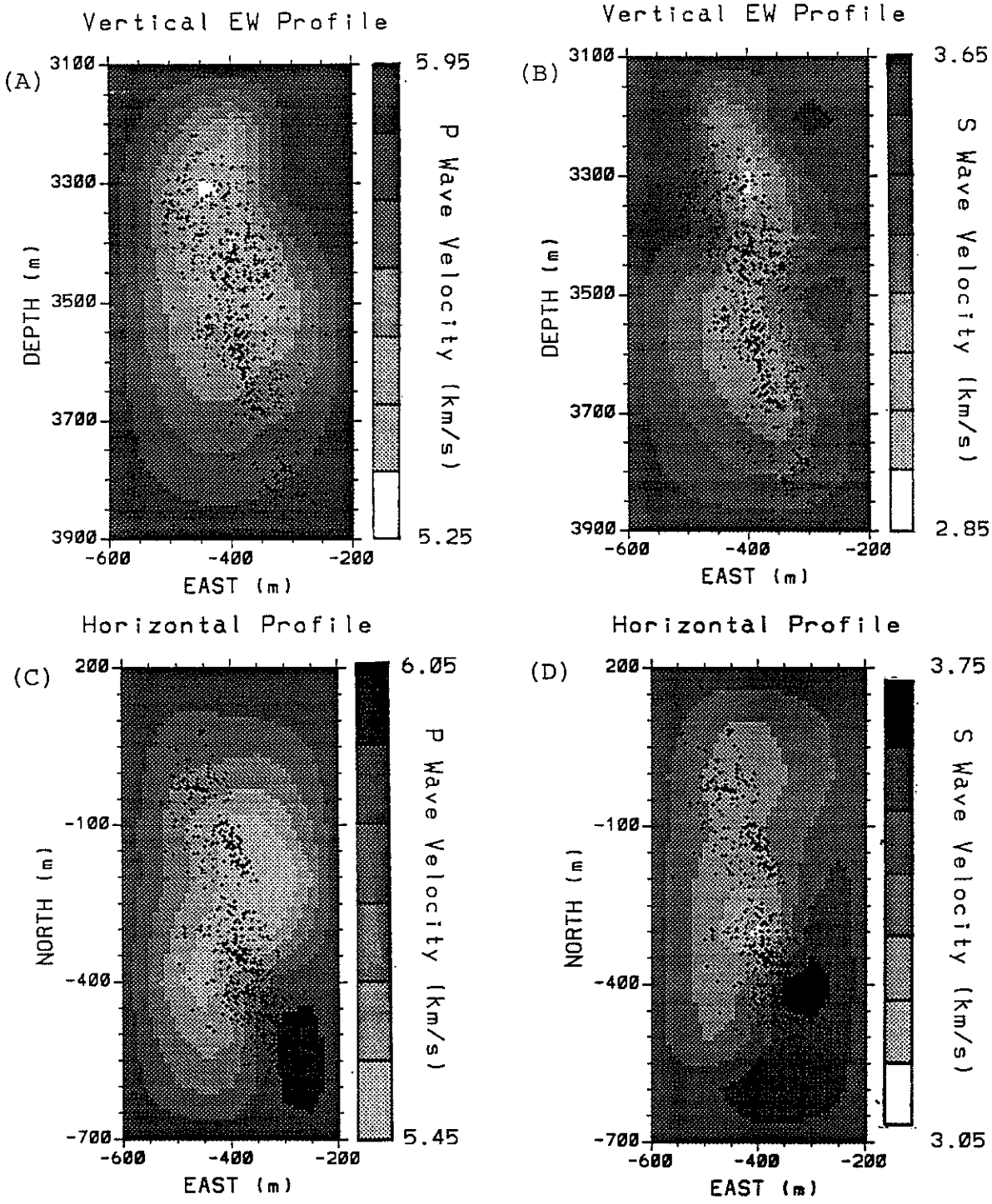

Figure 6: Results of the joint inversion of the synthetic data, performed without velocity bounds. (A) and (B) Vertical East-West V_P and V_S cross sections at -300 m North. (C) and (D) Horizontal V_P and V_S cross sections at 3500 m depth.

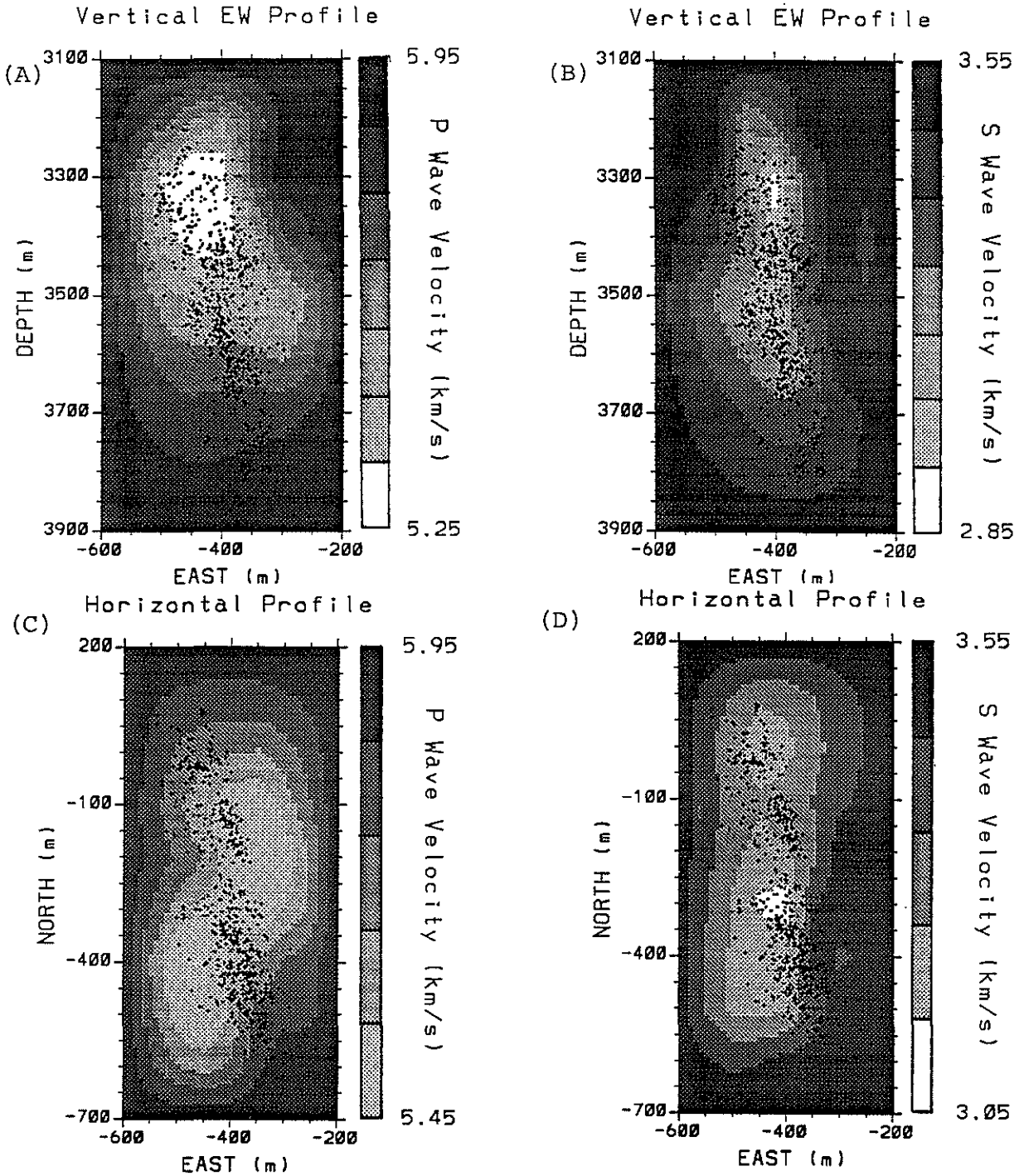

Figure 7: Results of the joint inversion of the synthetic data, performed with upper velocity bounds equal to the background velocities. (A) and (B) Vertical East-West V_P and V_S cross sections at -300 m North. (C) and (D) Horizontal V_P and V_S cross sections at 3500 m depth.

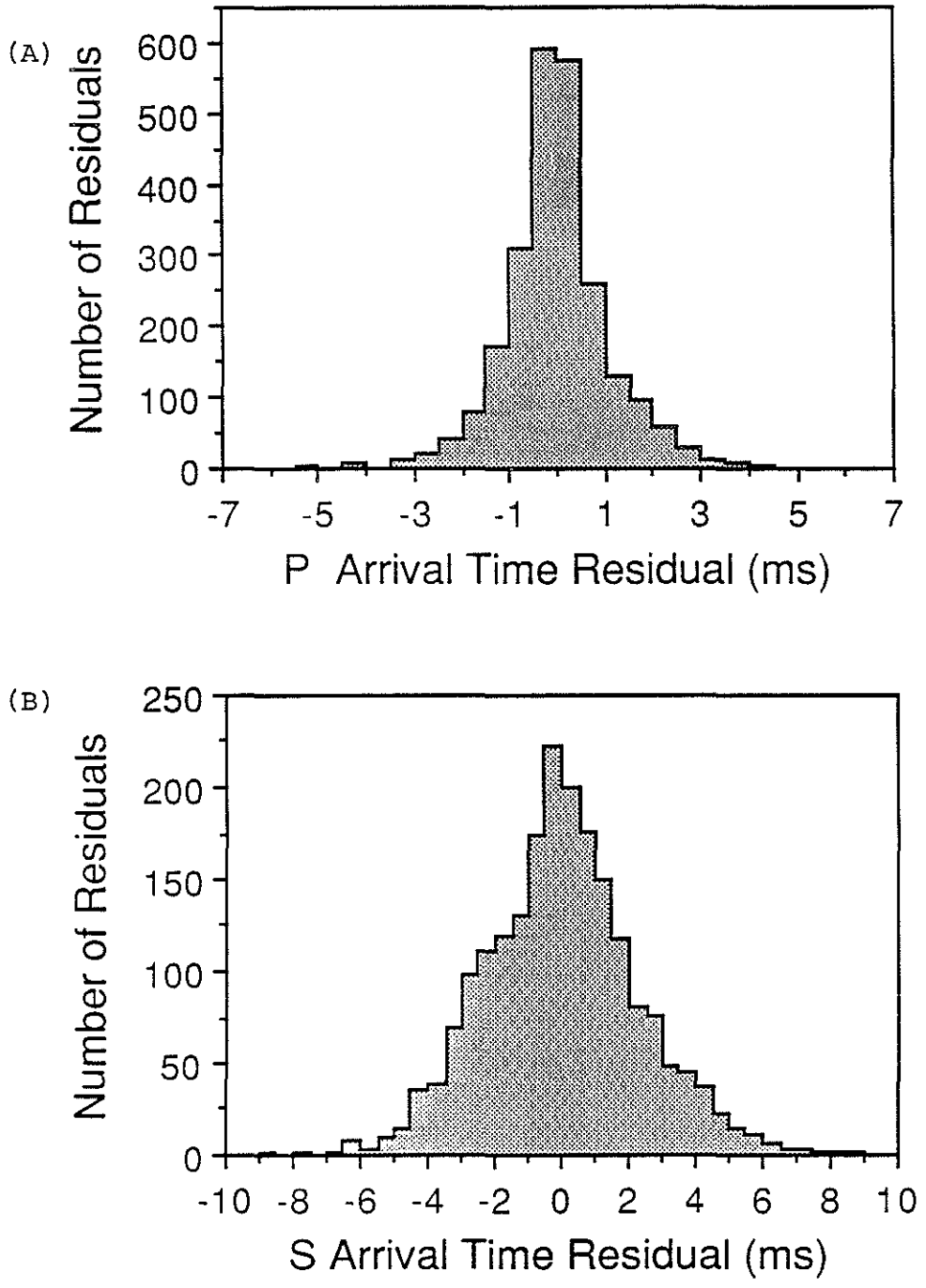

Figure 8: Histograms of the initial arrival time residuals for the inversions of the field data. (A) P residuals. (B) S residuals.

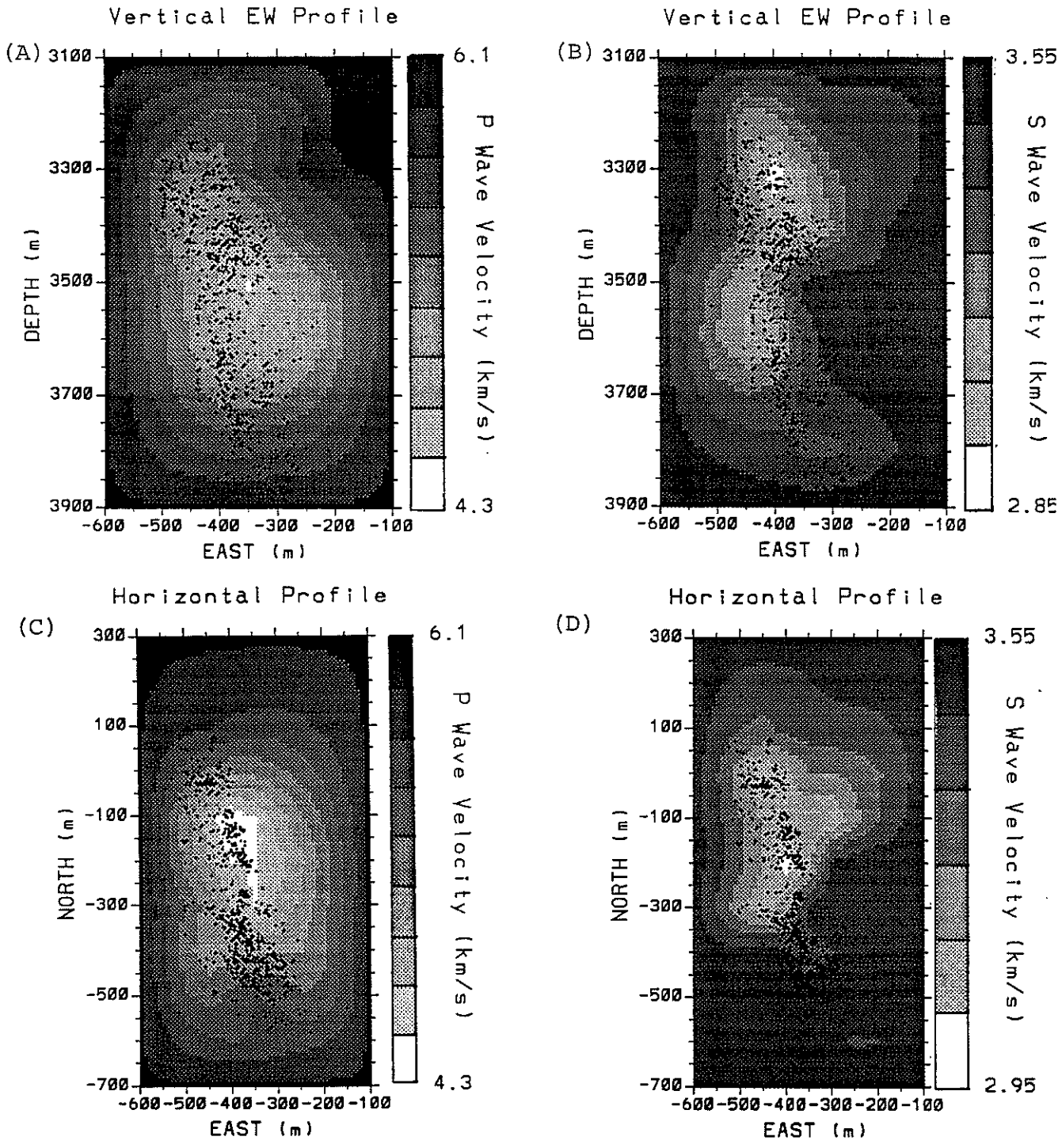

Figure 9: Results of the joint inversion of the field data, performed with all station corrections varying. (A) and (B) Vertical East-West V_P and V_S cross sections at -300 m North. (C) and (D) Horizontal V_P and V_S cross sections at 3500 m depth.

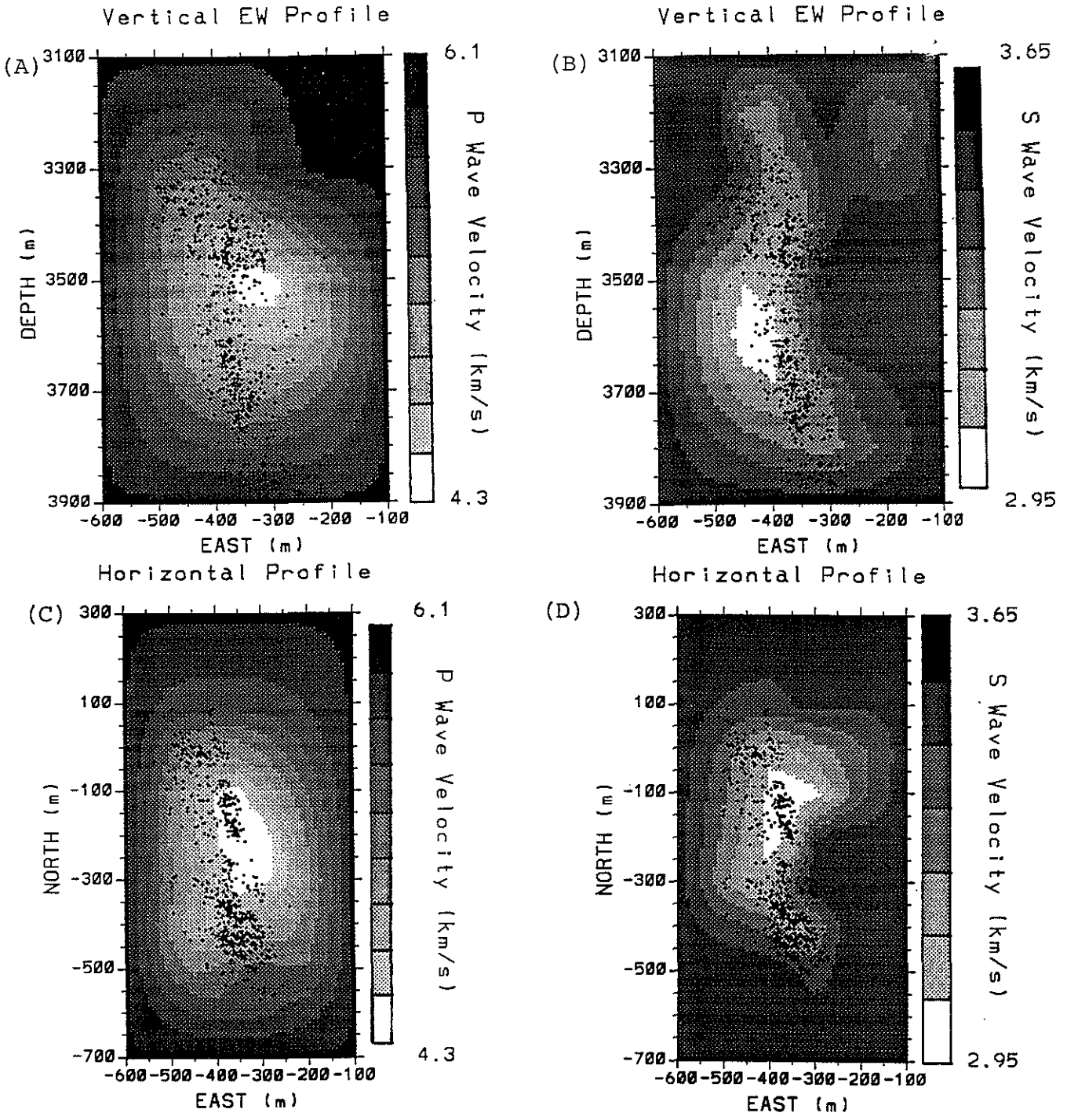

Figure 10: Results of the joint inversion of the field data, performed with the station corrections at stations EE-1 and EE-3 fixed. (A) and (B) Vertical East-West V_P and V_S cross sections at -300 m North. (C) and (D) Horizontal V_P and V_S cross sections at 3500 m depth.

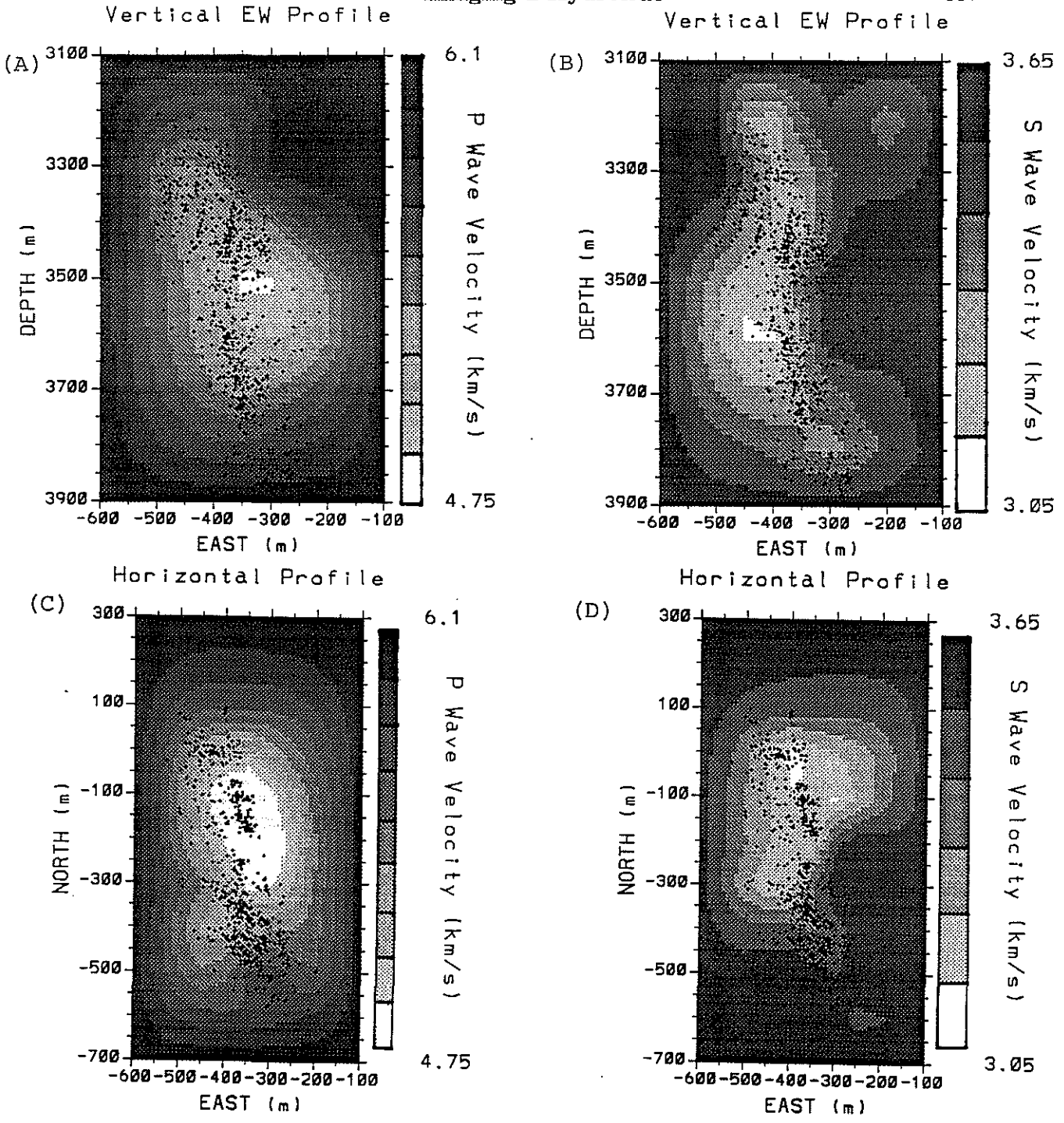

Figure 11: Results of the joint inversion of the field data, performed with high background velocities – 6.05 km/s (P) and 3.59 km/s (S). (A) and (B) Vertical East-West V_P and V_S cross sections at -300 m North. (C) and (D) Horizontal V_P and V_S cross sections at 3500 m depth.

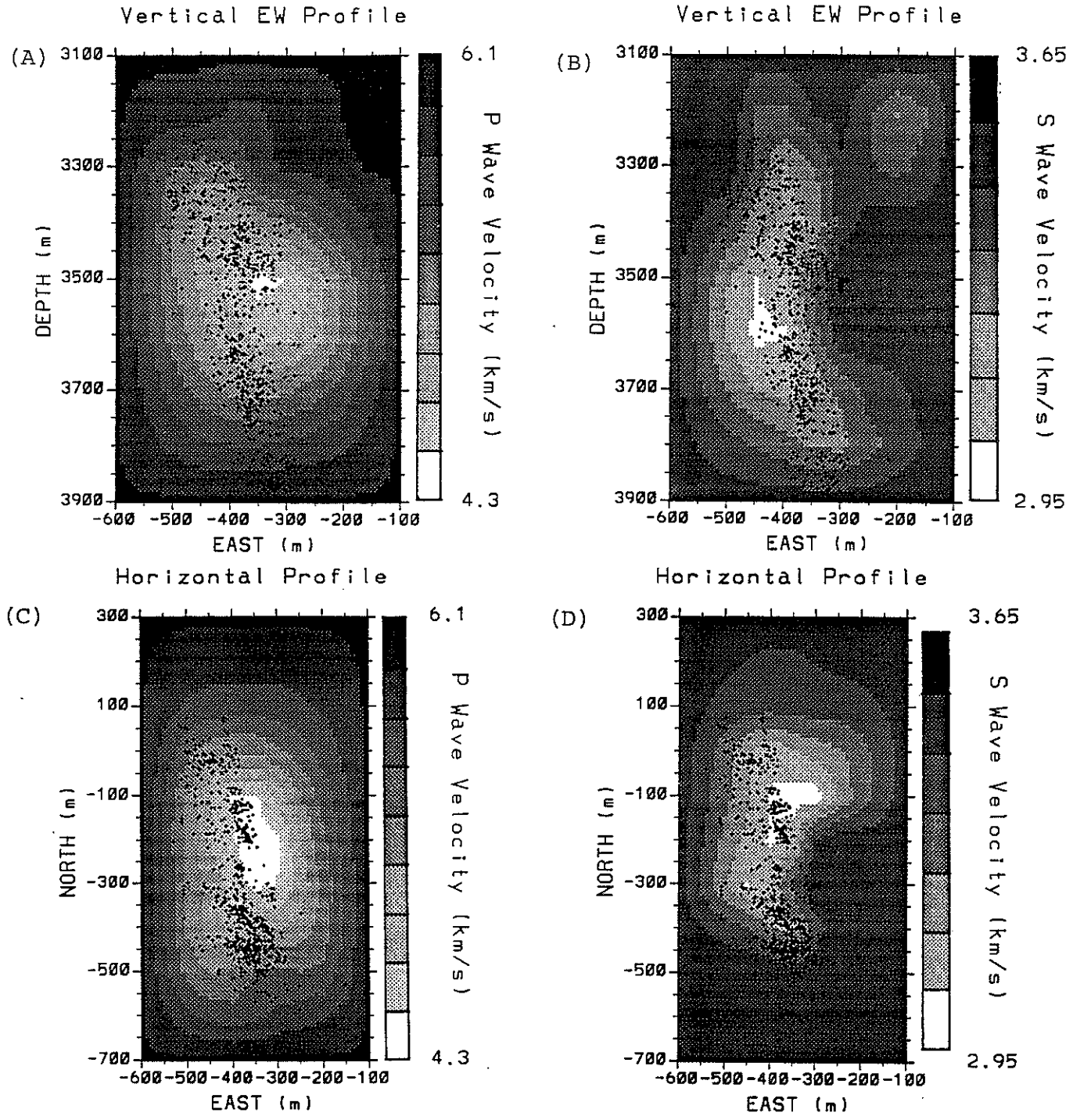

Figure 12: Results of the joint inversion of the field data, performed with the location of station EE-3 varying. (A) and (B) Vertical East-West V_P and V_S cross sections at -300 m North. (C) and (D) Horizontal V_P and V_S cross sections at 3500 m depth.

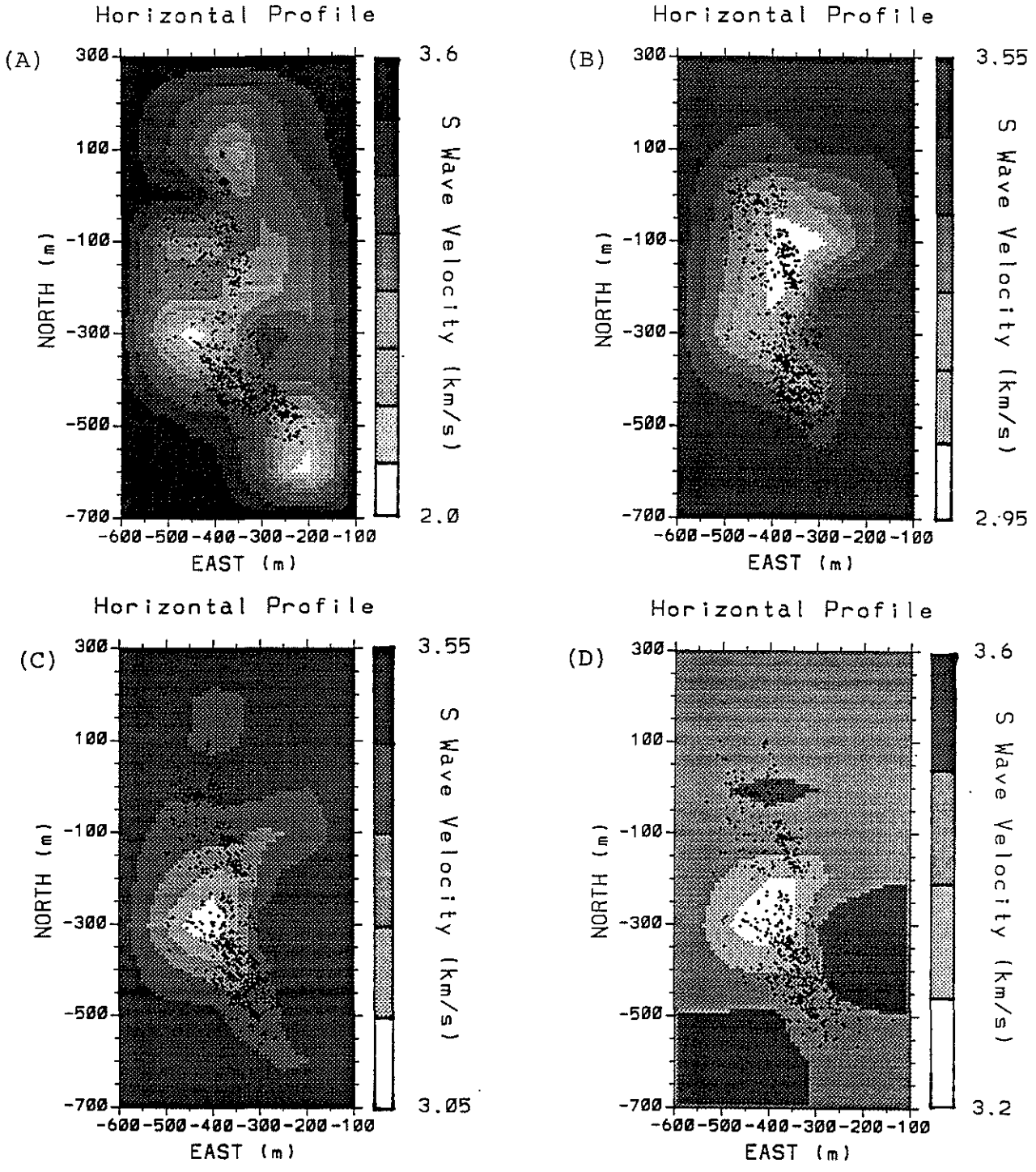

Figure 13: Results of the joint inversion performed with different values of λ. Straight rays used. Horizontal V_S cross sections at 3500 m depth. (A) $\lambda = 1$. (B) $\lambda = 10$. (C) $\lambda = 20$. (D) $\lambda = 40$.

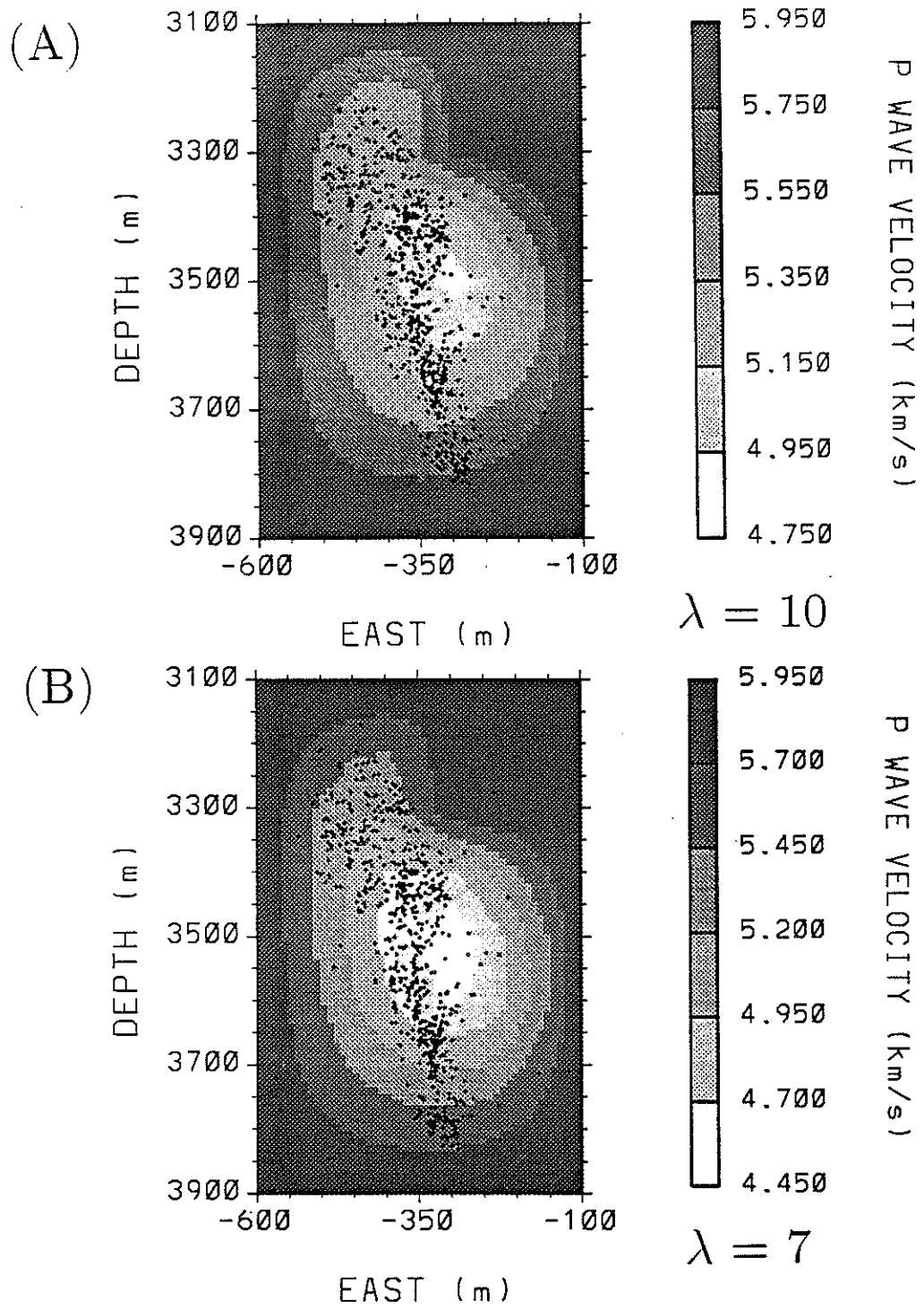

Figure 14: Results of the joint inversion performed with different values of λ. Bent rays used. Vertical East-West V_P cross sections at -300 m North. (A) $\lambda = 10$. (B) $\lambda = 7$. (C) $\lambda = 4$. (D) $\lambda = 1$.

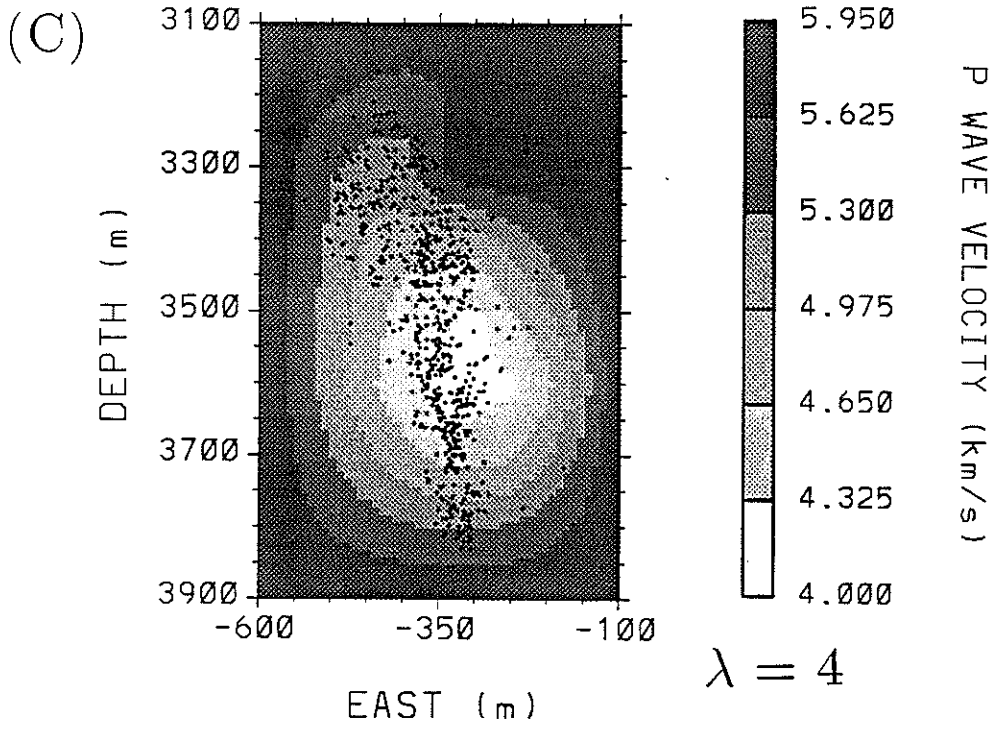
(C)
3100
3300
3500
3700
3900
DEPTH (m)
-600
-350
-100
EAST (m)
5.950
5.625
5.300
4.975
4.650
4.325
4.000
P WAVE VELOCITY (km/s)
λ = 4

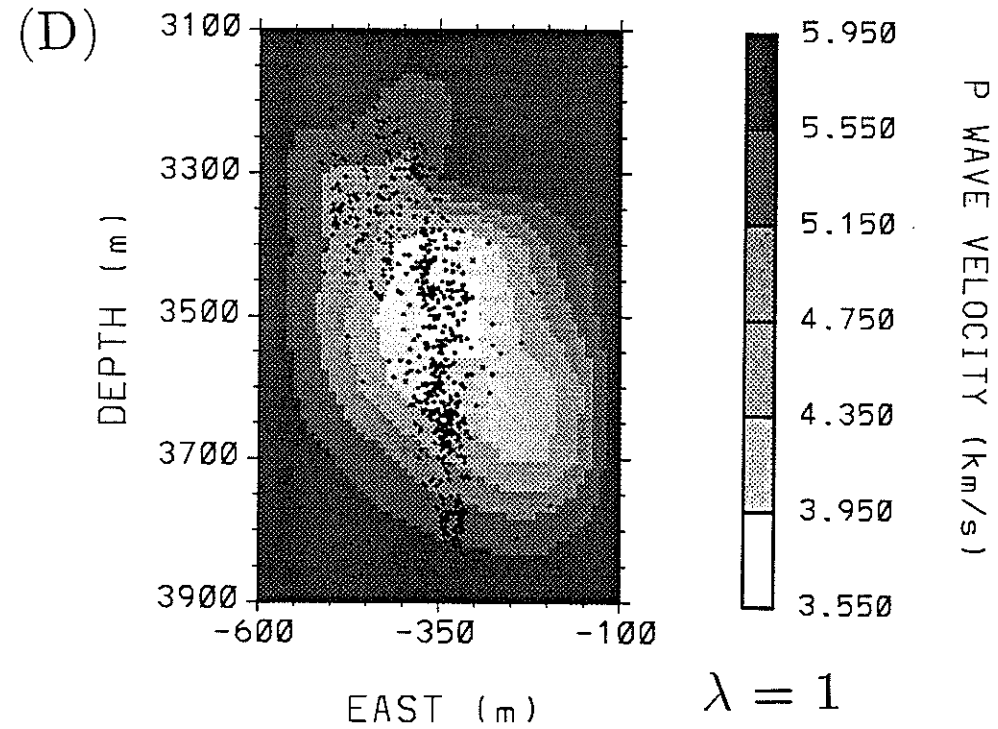
(D)
3100
3300
3500
3700
3900
DEPTH (m)
-600
-350
-100
EAST (m)
5.950
5.550
5.150
4.750
4.350
3.950
3.550
P WAVE VELOCITY (km/s)
λ = 1

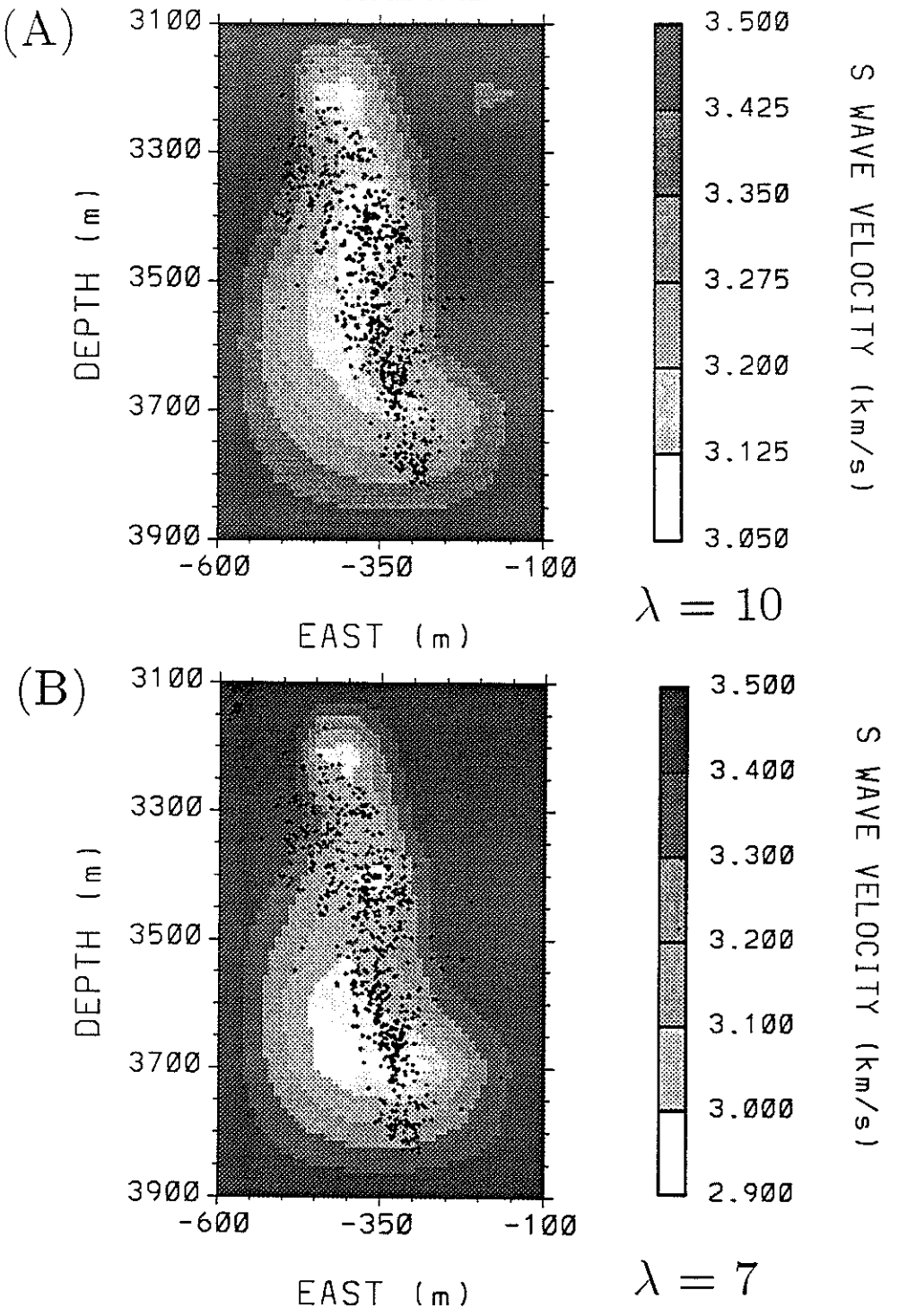

Figure 15: Results of the joint inversion performed with different values of λ. Bent rays used. Vertical East-West V_S cross sections at -300 m North. (A) $\lambda = 10$. (B) $\lambda = 7$. (C) $\lambda = 4$. (D) $\lambda = 1$.

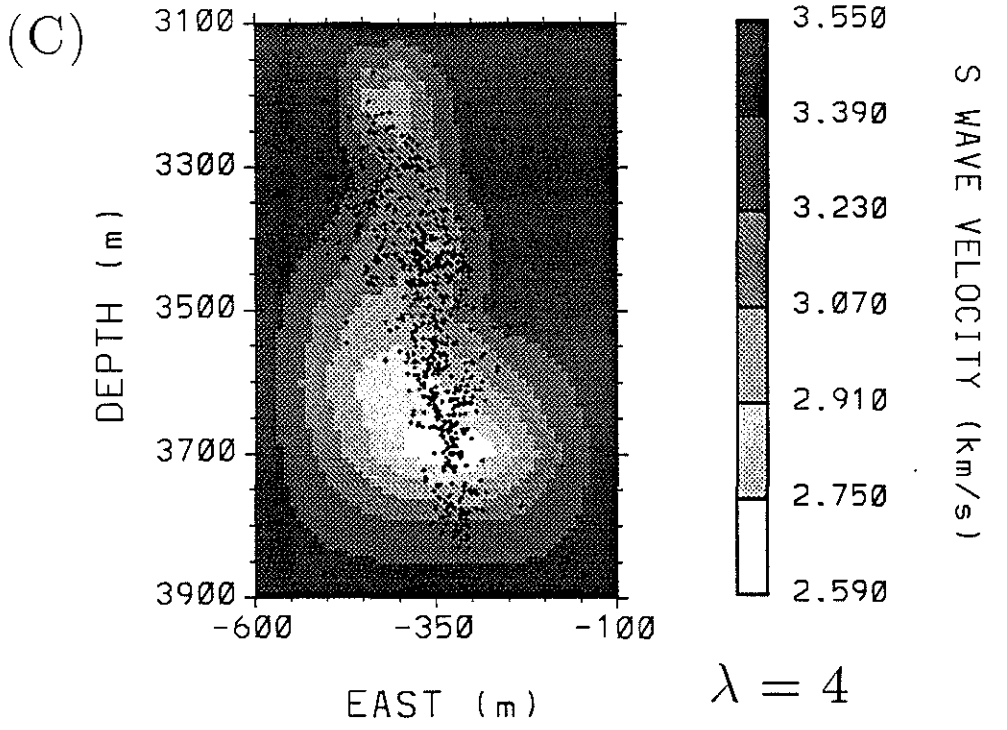
(C)
3100
3300
3500
3700
3900
DEPTH (m)
-600
-350
-100
EAST (m)
3.550
3.390
3.230
3.070
2.910
2.750
2.590
S WAVE VELOCITY (km/s)
λ = 4

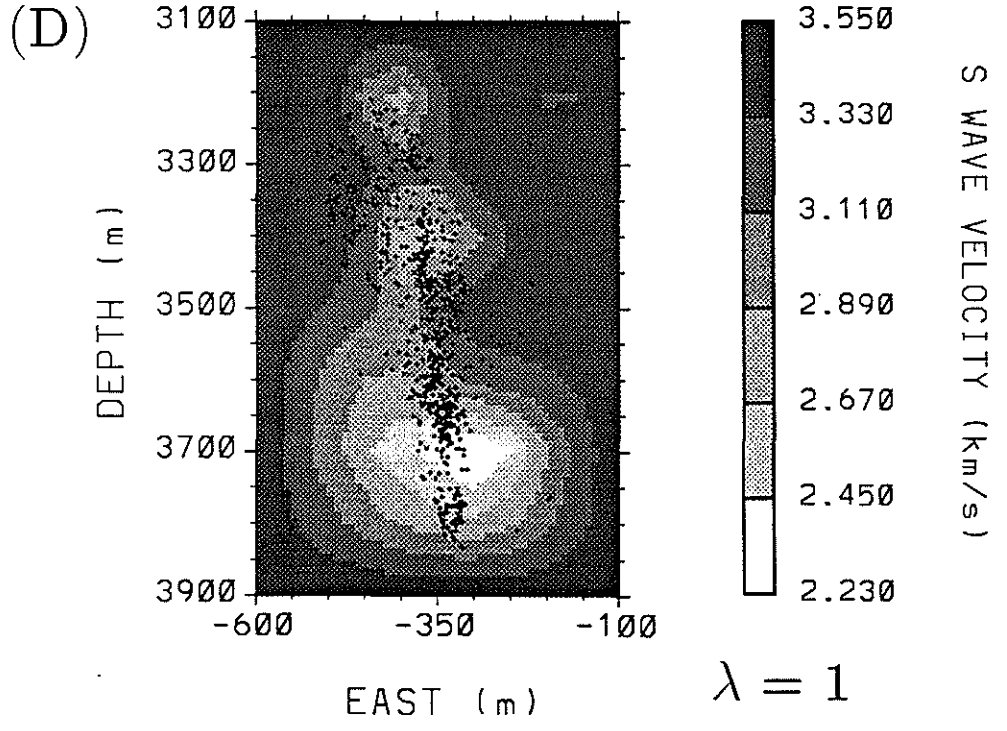
(D)
3100
3300
3500
3700
3900
DEPTH (m)
-600
-350
-100
EAST (m)
3.550
3.330
3.110
2.890
2.670
2.450
2.230
S WAVE VELOCITY (km/s)
λ = 1

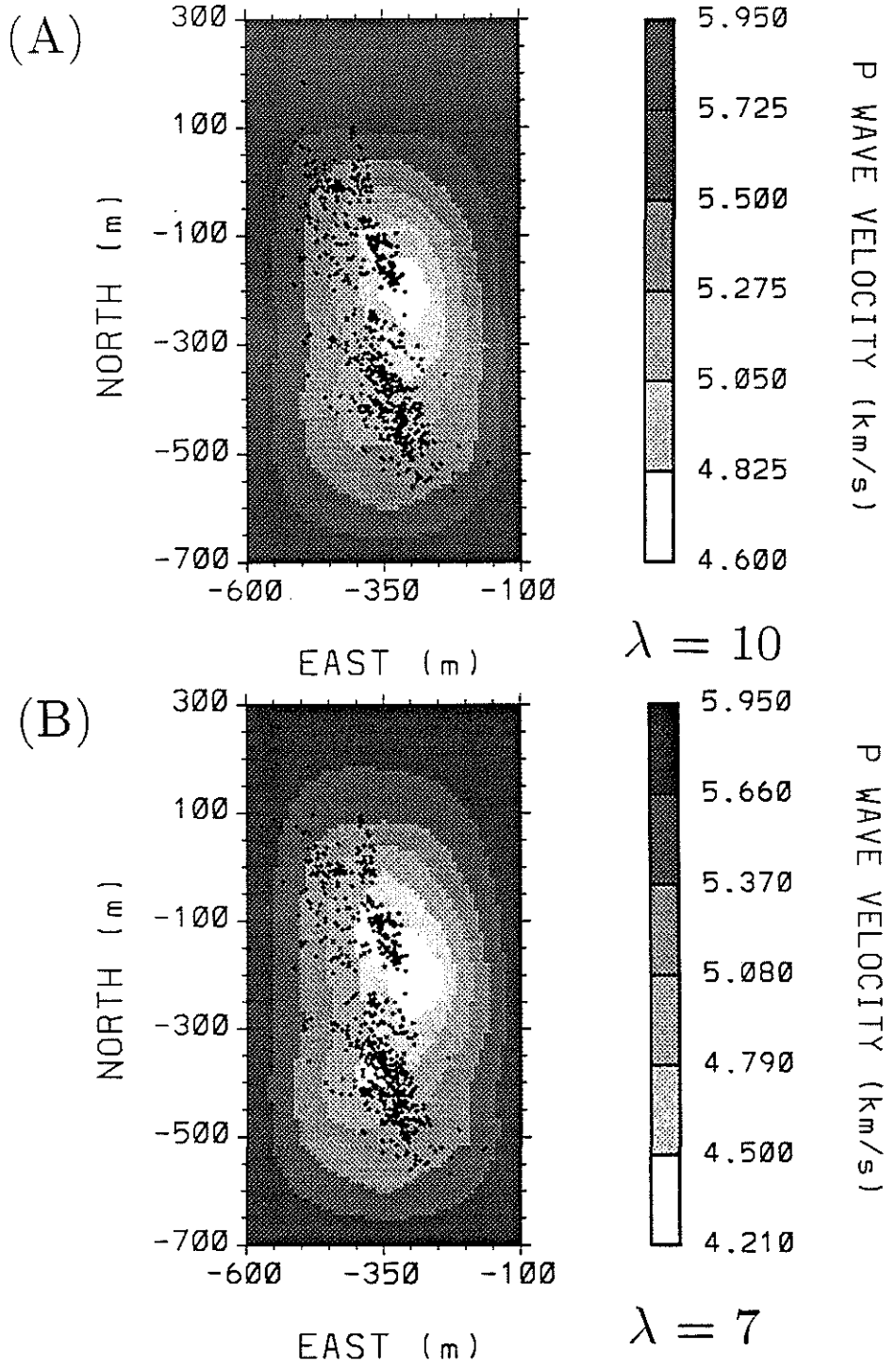

Figure 16: Results of the joint inversion performed with different values of λ. Bent rays used. Horizontal V_P cross sections at 3500 m depth. (A) $\lambda = 10$. (B) $\lambda = 7$. (C) $\lambda = 4$. (D) $\lambda = 1$.

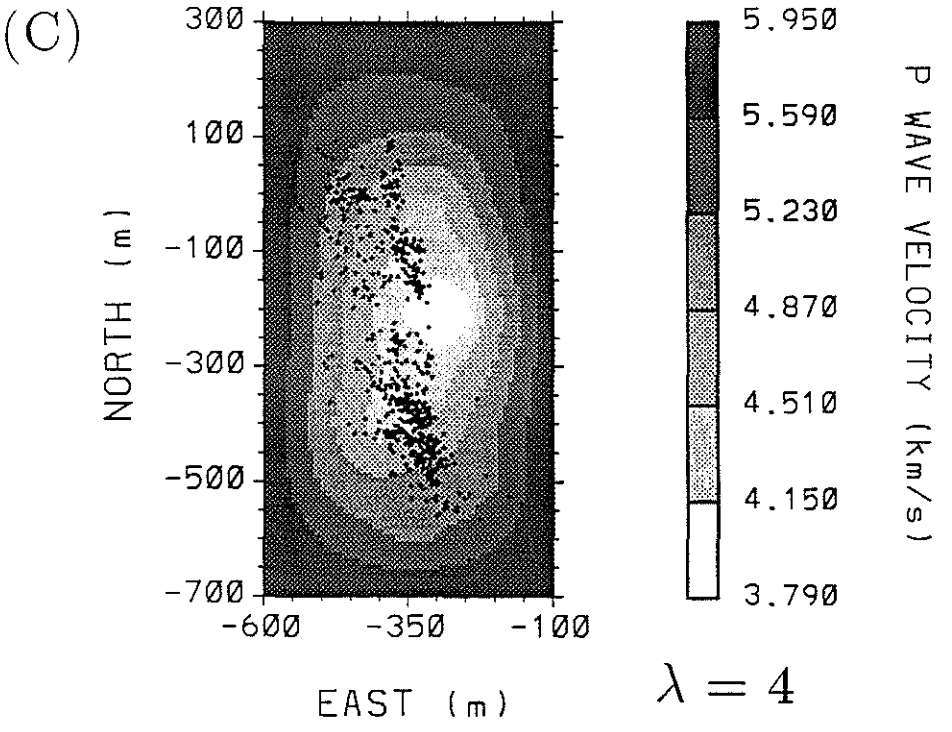
(C)
300
100
-100
-300
-500
-700
NORTH (m)
-600
-350
-100
EAST (m)
5.950
5.590
5.230
4.870
4.510
4.150
3.790
P WAVE VELOCITY (km/s)
λ = 4

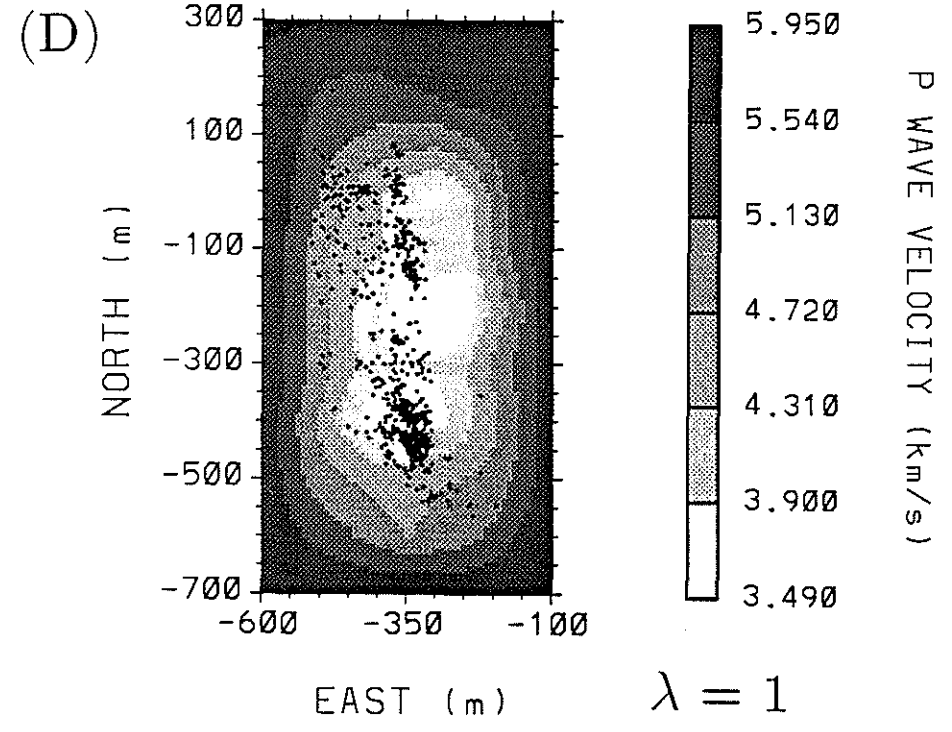
(D)
300
100
-100
-300
-500
-700
NORTH (m)
-600
-350
-100
EAST (m)
5.950
5.540
5.130
4.720
4.310
3.900
3.490
P WAVE VELOCITY (km/s)
λ = 1

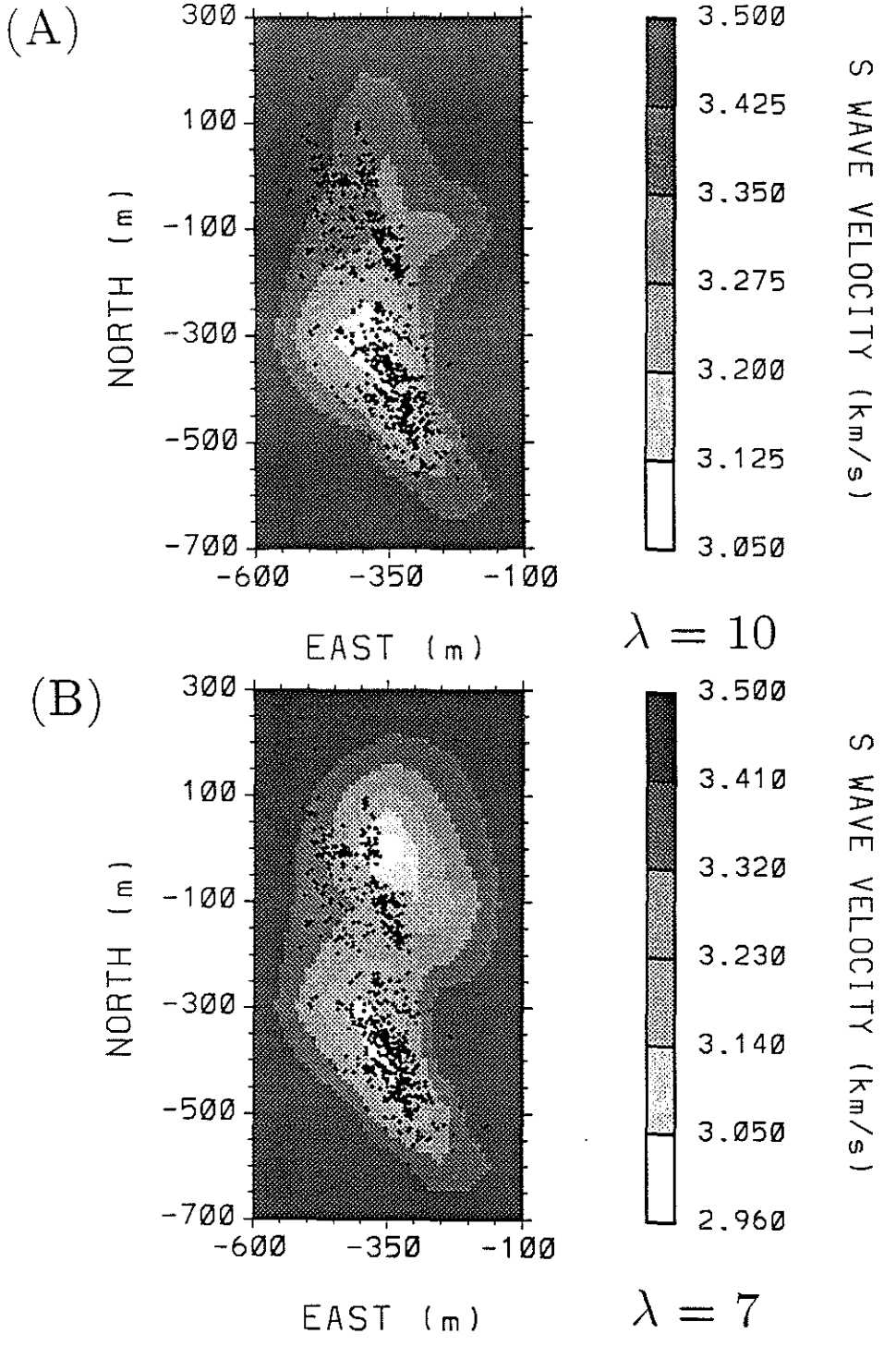

Figure 17: Results of the joint inversion performed with different values of λ. Bent rays used. Horizontal V_S cross sections at 3500 m depth. (A) $\lambda = 10$. (B) $\lambda = 7$. (C) $\lambda = 4$. (D) $\lambda = 1$.

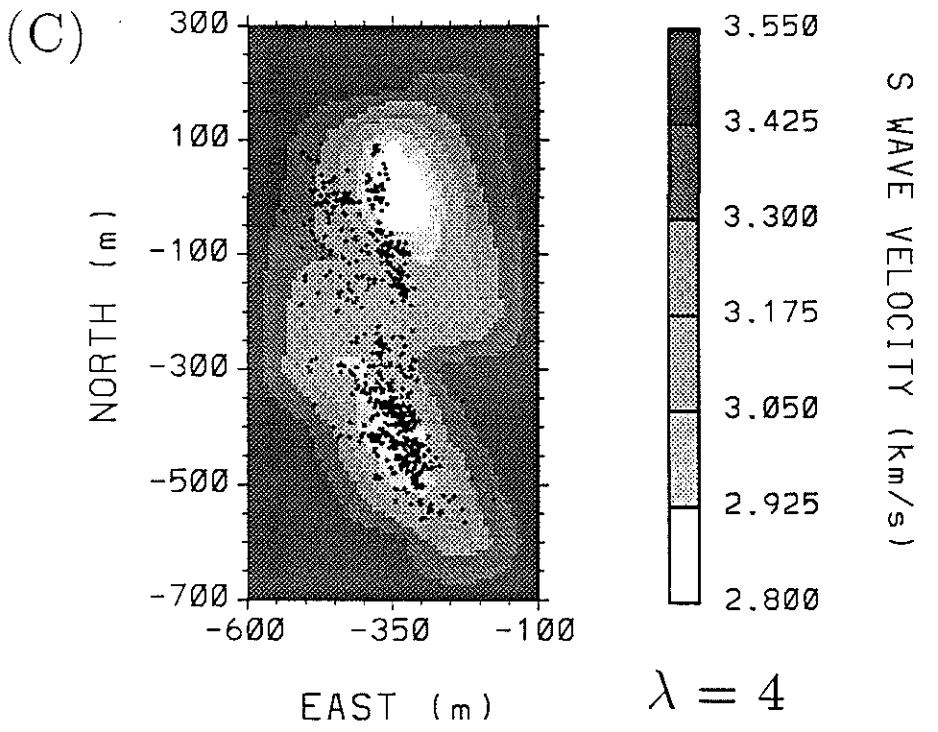
(C)
300
100
-100
-300
-500
-700
NORTH (m)
-600
-350
-100
EAST (m)
3.550
3.425
3.300
3.175
3.050
2.925
2.800
S WAVE VELOCITY (km/s)
λ = 4

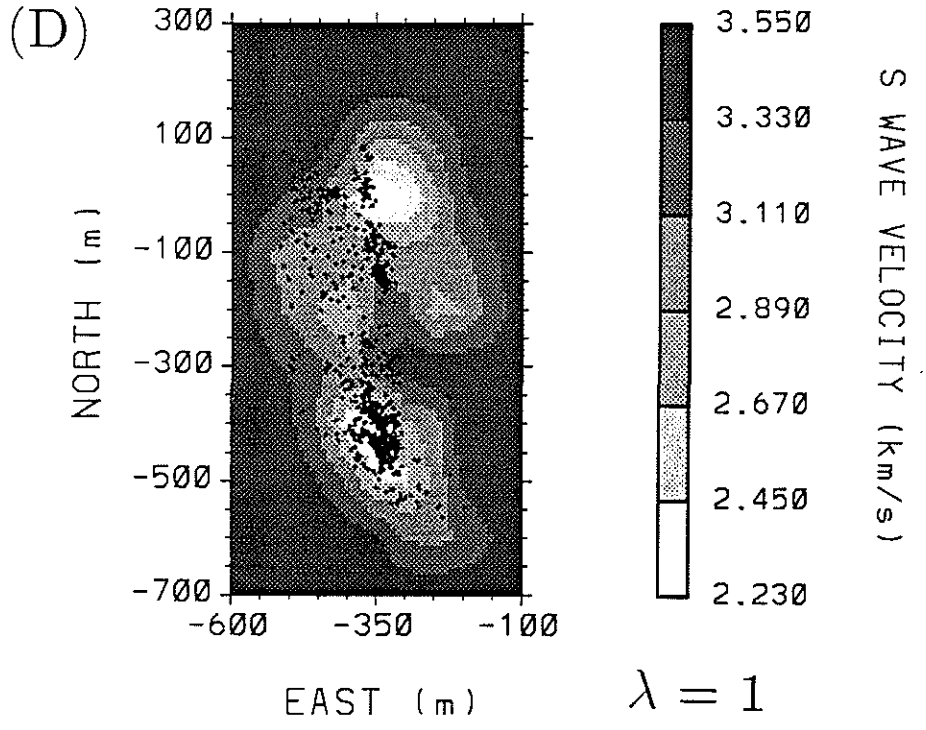
(D)
300
100
-100
-300
-500
-700
NORTH (m)
-600
-350
-100
EAST (m)
3.550
3.330
3.110
2.890
2.670
2.450
2.230
S WAVE VELOCITY (km/s)
λ = 1

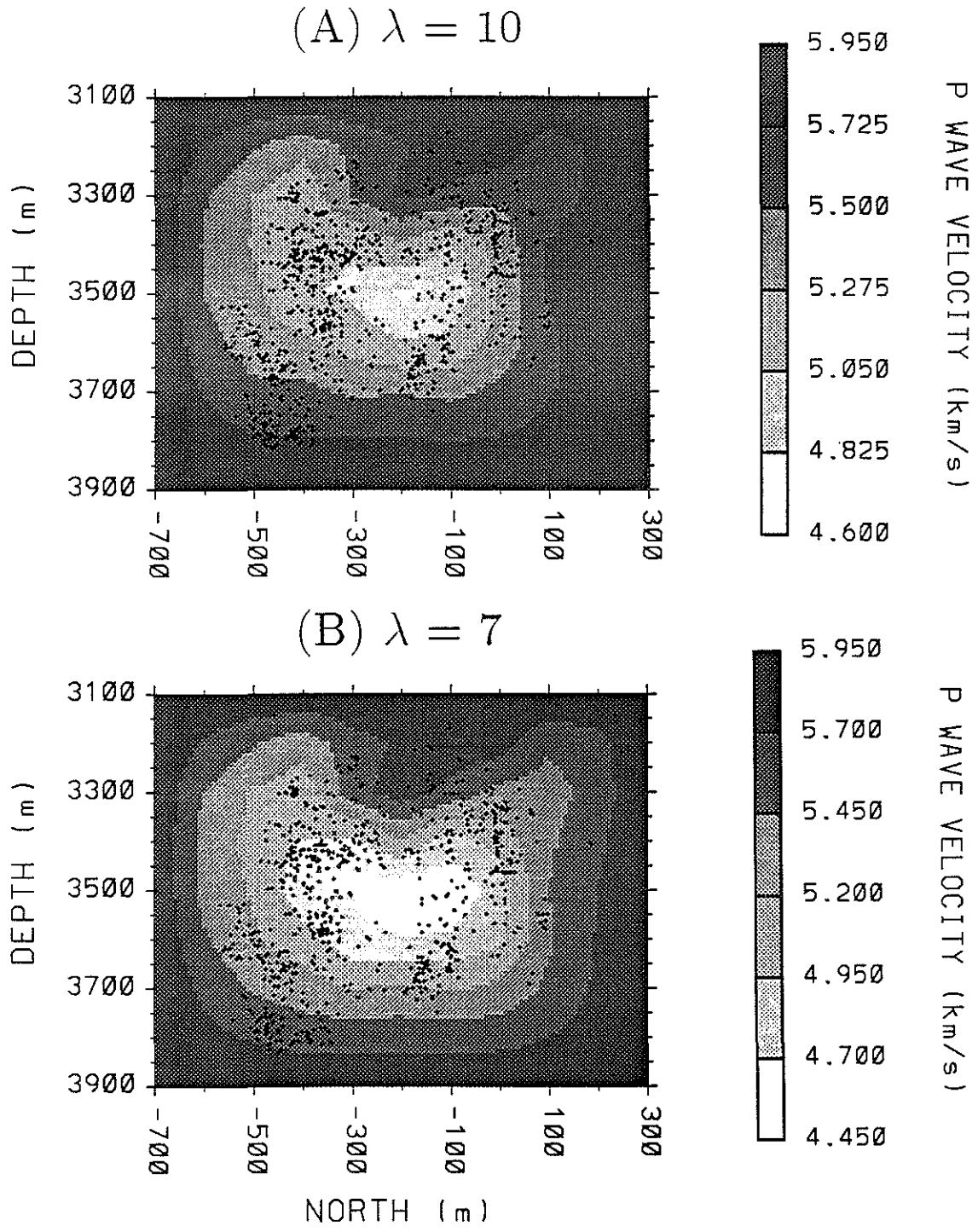

Figure 18: Results of the joint inversion performed with different values of λ. Bent rays used. Vertical North-South V_P cross sections at -350 m East. (A) $\lambda = 10$. (B) $\lambda = 7$. (C) $\lambda = 4$. (D) $\lambda = 1$.

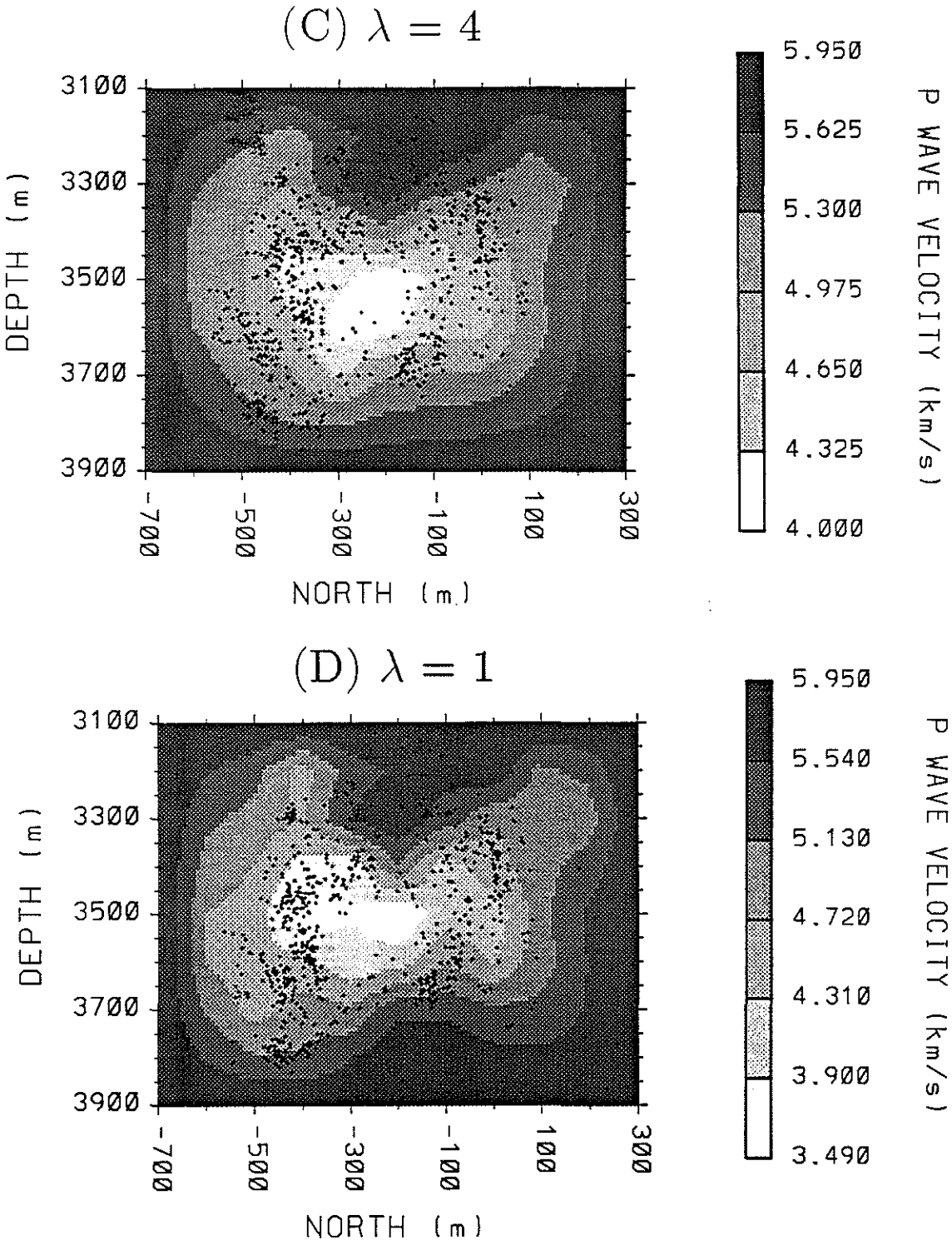
(C) λ = 4
3100
3300
3500
3700
3900
DEPTH (m)
-700
-500
-300
-100
100
300
NORTH (m)
5.950
5.625
5.300
4.975
4.650
4.325
4.000
P WAVE VELOCITY (km/s)
(D) λ = 1
3100
3300
3500
3700
3900
DEPTH (m)
-700
-500
-300
-100
100
300
NORTH (m)
5.950
5.540
5.130
4.720
4.310
3.900
3.490
P WAVE VELOCITY (km/s)

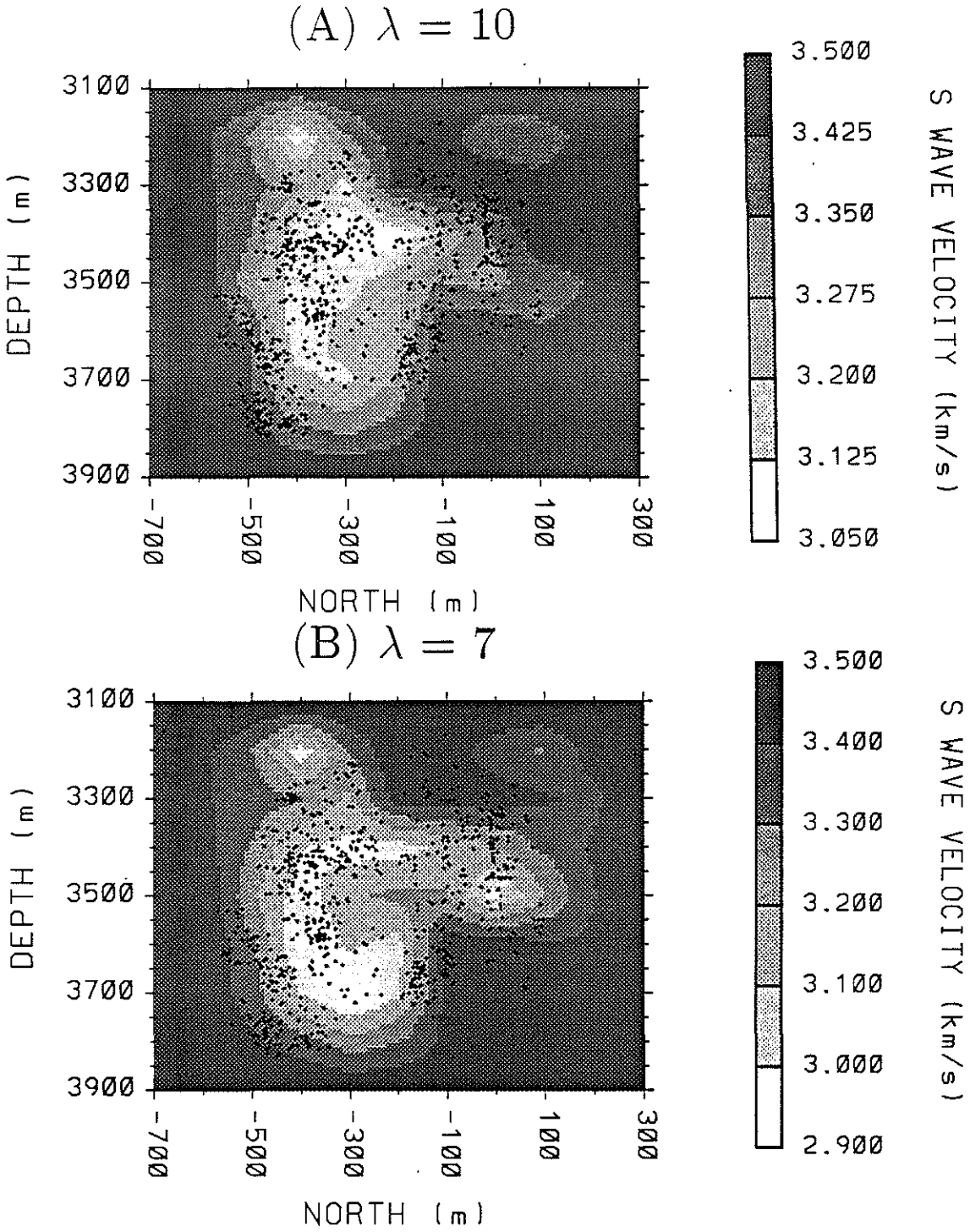

Figure 19: Results of the joint inversion performed with different values of λ. Bent rays used. Vertical North-South V_S cross sections at -350 m East. (A) $\lambda = 10$. (B) $\lambda = 7$. (C) $\lambda = 4$. (D) $\lambda = 1$.

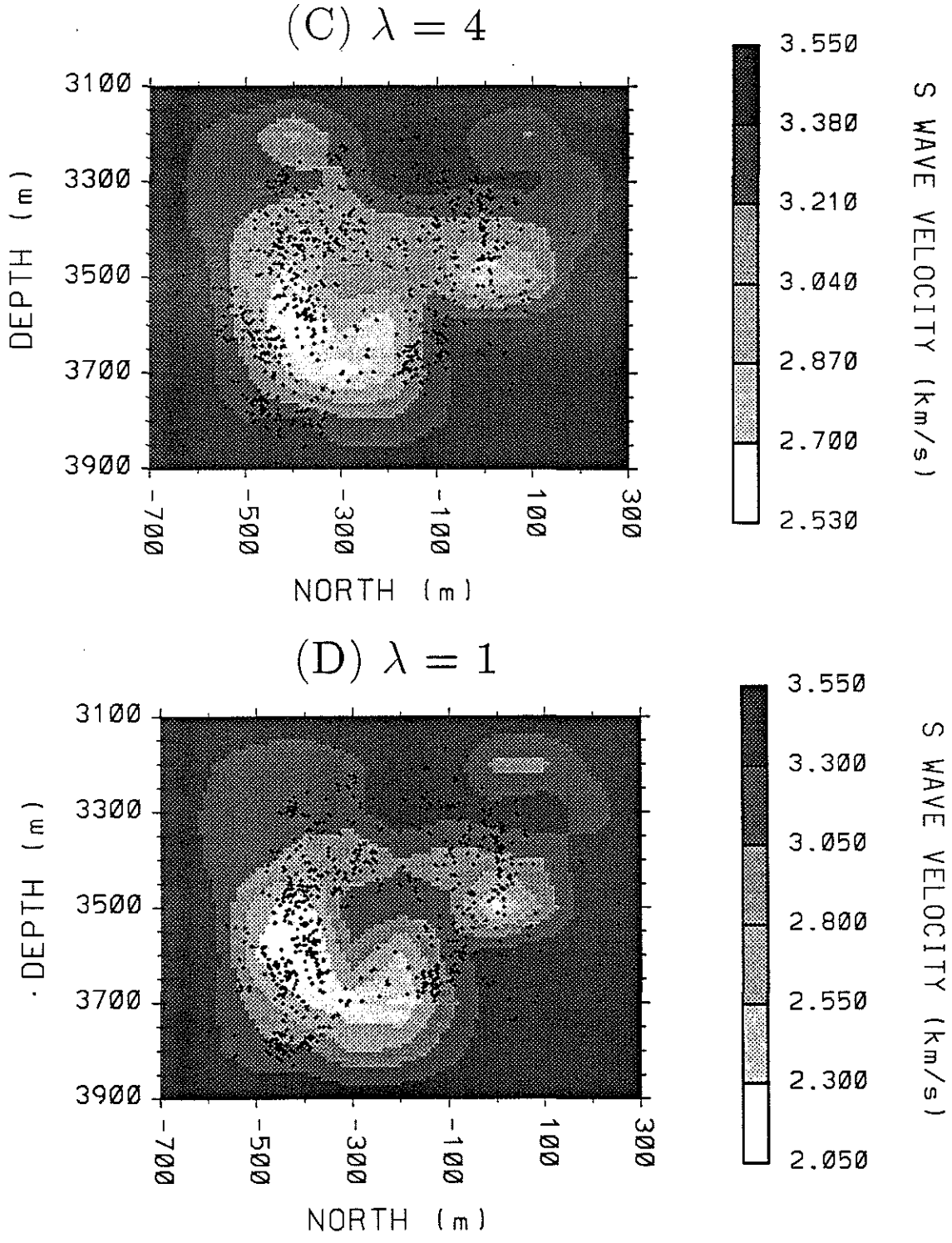
(C) λ = 4
3100
3300
3500
3700
3900
DEPTH (m)
-700
-500
-300
-100
100
300
NORTH (m)
3.550
3.380
3.210
3.040
2.870
2.700
2.530
S WAVE VELOCITY (km/s)
(D) λ = 1
3100
3300
3500
3700
3900
DEPTH (m)
-700
-500
-300
-100
100
300
NORTH (m)
3.550
3.300
3.050
2.800
2.550
2.300
2.050
S WAVE VELOCITY (km/s)

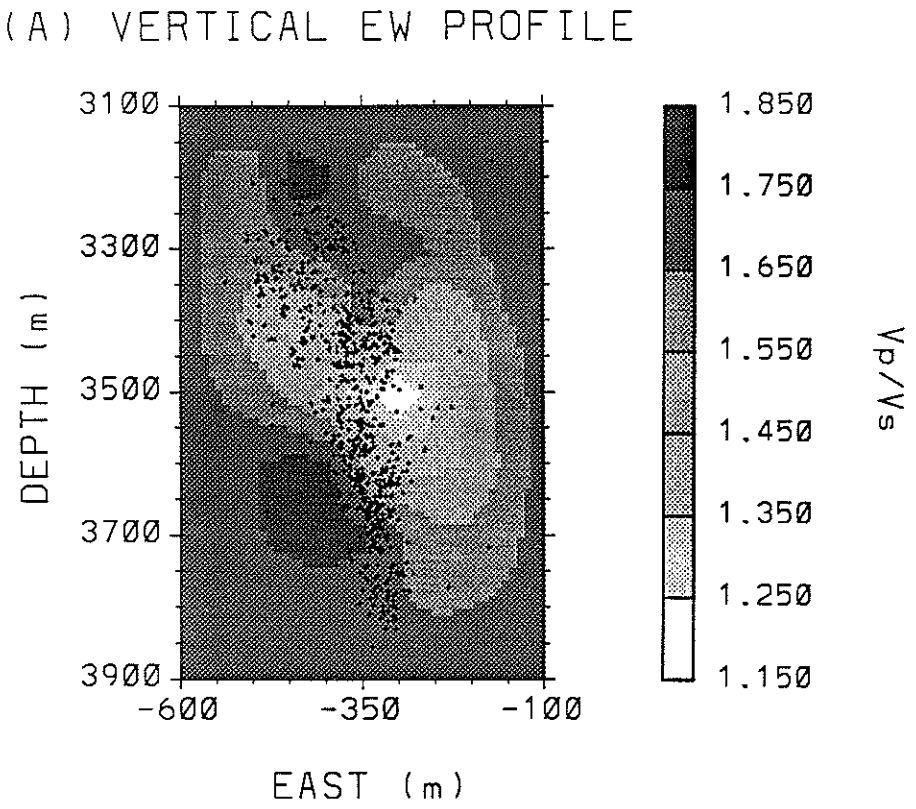

Figure 20: V_P/V_S ratios computed from the results of the inversion with $\lambda = 4$. (A) Vertical East-West cross section at -200 m North. (B) Horizontal cross section at 3500 m depth. (C) Vertical North-South cross section at -300 m East.

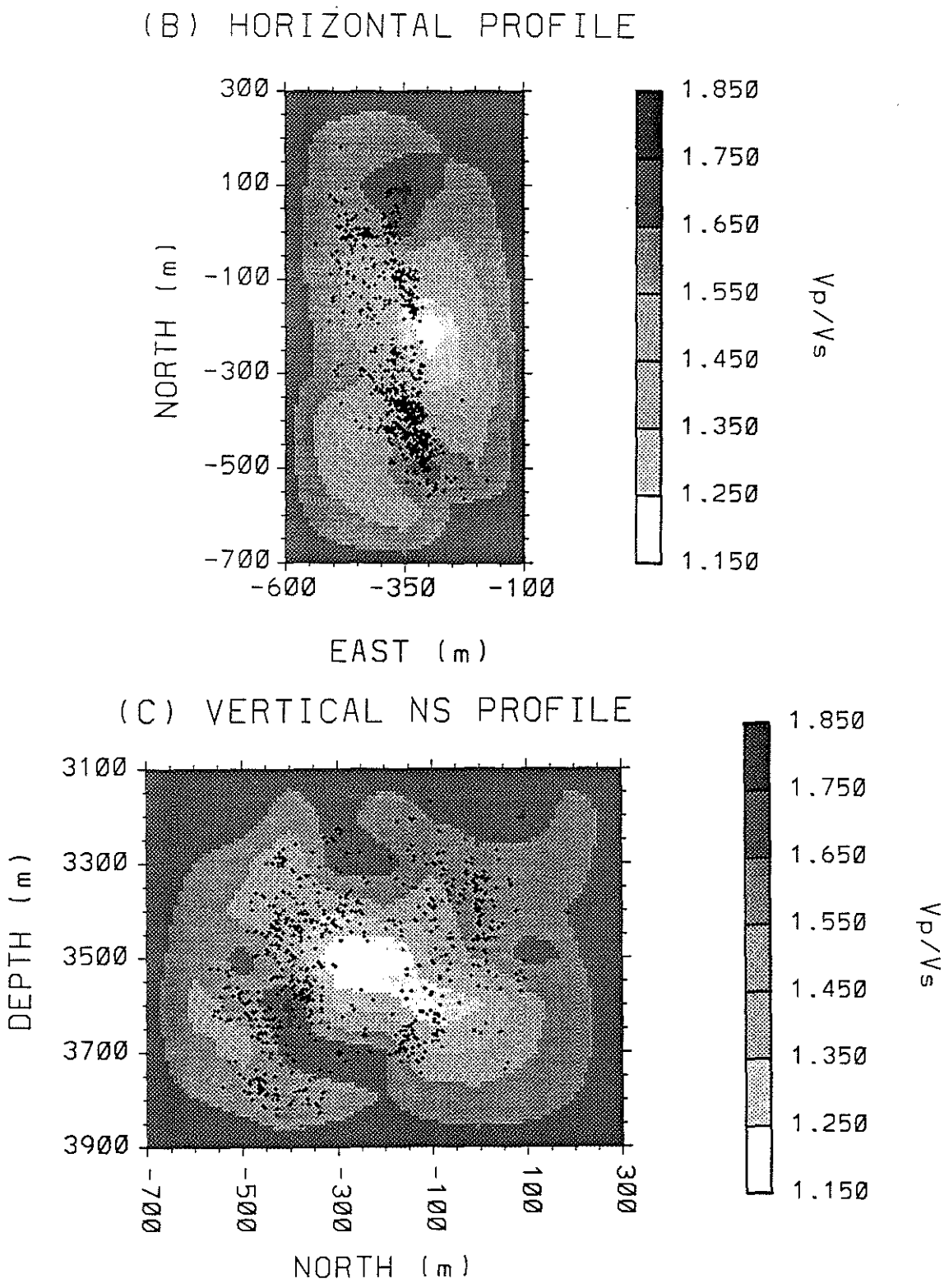
(B) HORIZONTAL PROFILE
300
100
-100
-300
-500
-700
NORTH (m)
-600
-350
-100
EAST (m)
1.850
1.750
1.650
1.550
1.450
1.350
1.250
1.150
Vp/Vs
(C) VERTICAL NS PROFILE
3100
3300
3500
3700
3900
DEPTH (m)
-700
-500
-300
-100
100
300
NORTH (m)
1.850
1.750
1.650
1.550
1.450
1.350
1.250
1.150
Vp/Vs

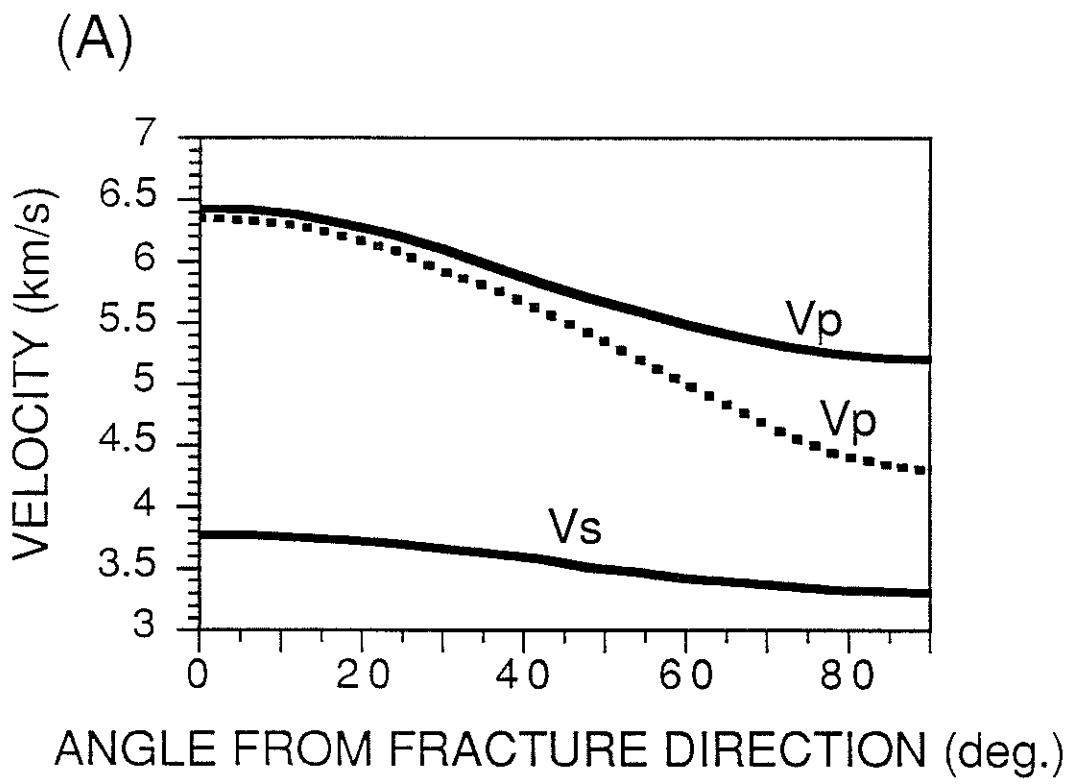

Figure 21: Theoretical velocities for a rock having parallel fractures. Fracture density = 0.02; crack aspect ratio = 0.05. θ is the (phase) angle from the fracture planes. Dotted lines = dry cracks; solid lines = saturated cracks. (A) V_P and the faster V_S (B) V_P/(faster V_S) (Values taken from Cheng, 1978).

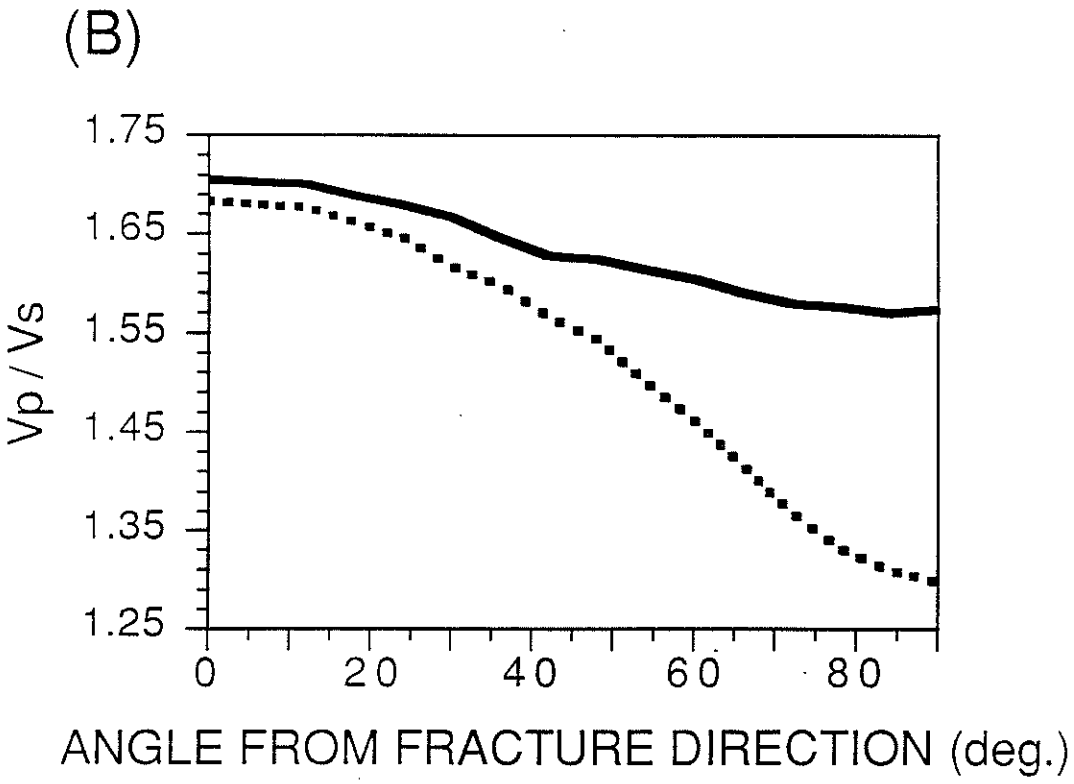
(B)
1.75
1.65
1.55
1.45
1.35
1.25
Vp / Vs
0
20
40
60
80
ANGLE FROM FRACTURE DIRECTION (deg.)

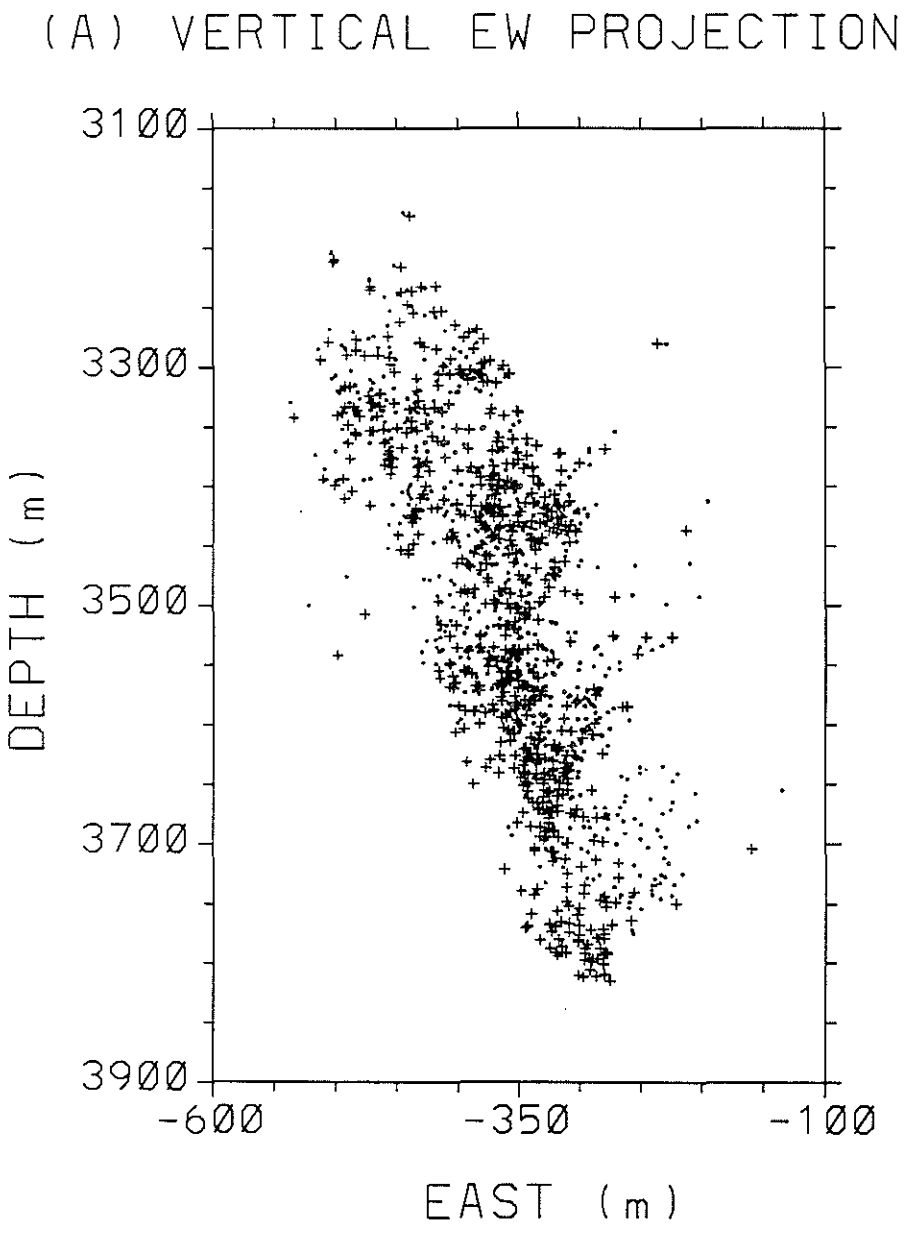

Figure 22: Vertical East-West projections of the initial (dots) and final (plus signs) earthquake locations. (A) Results with $\lambda = 10$. (B) Results with $\lambda = 1$.

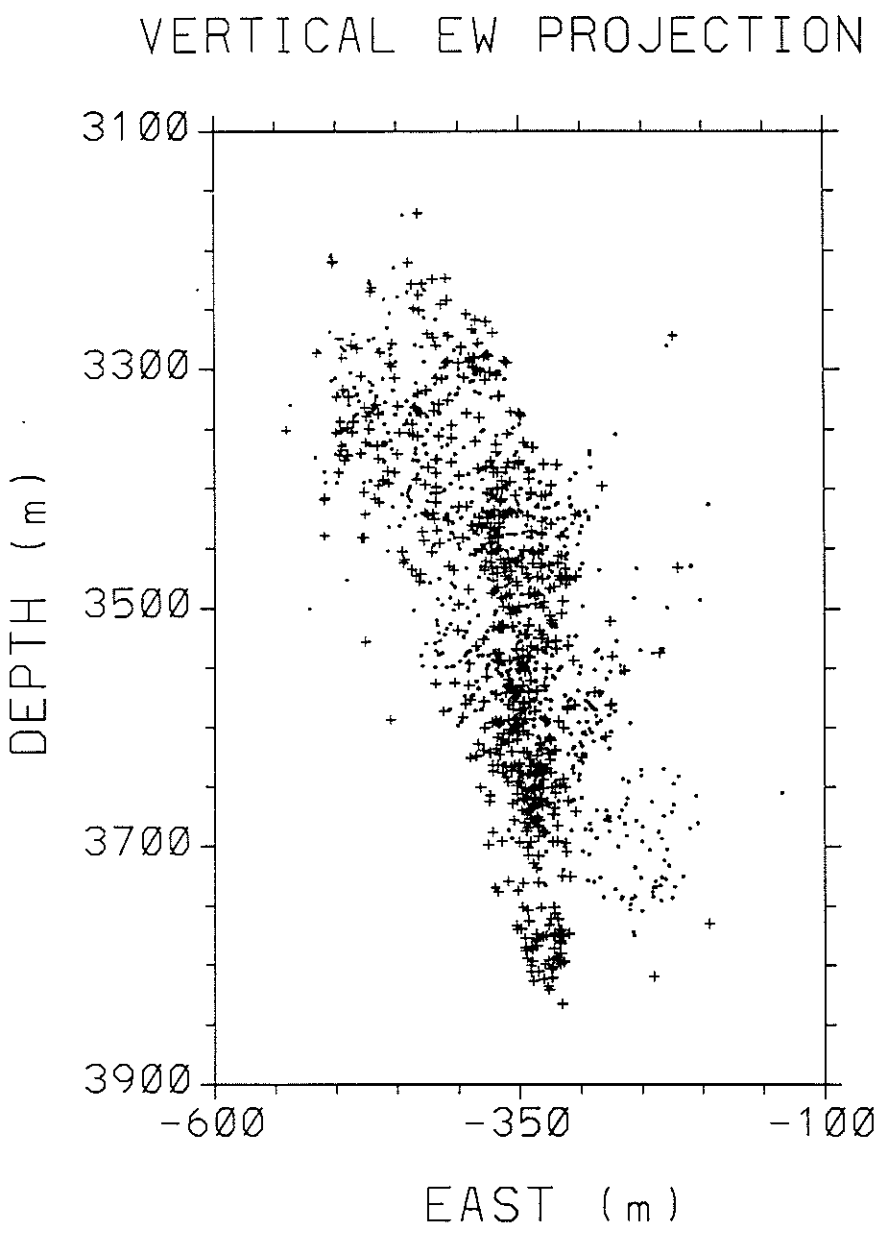
VERTICAL EW PROJECTION
3100
3300
3500
3700
3900
DEPTH (m)
-600
-350
-100
EAST (m)

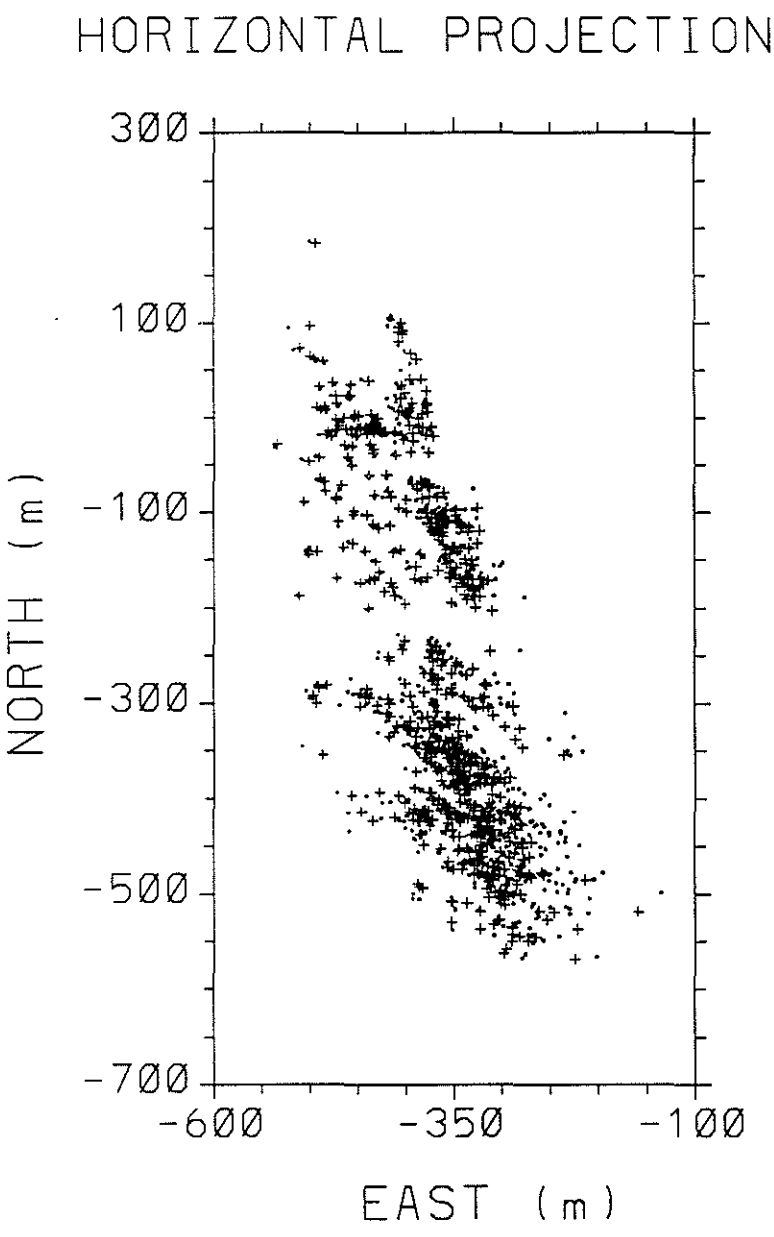

Figure 23: Horizontal projections of the initial (dots) and final (plus signs) earthquake locations. (A) Results with $\lambda = 10$. (B) Results with $\lambda = 1$.

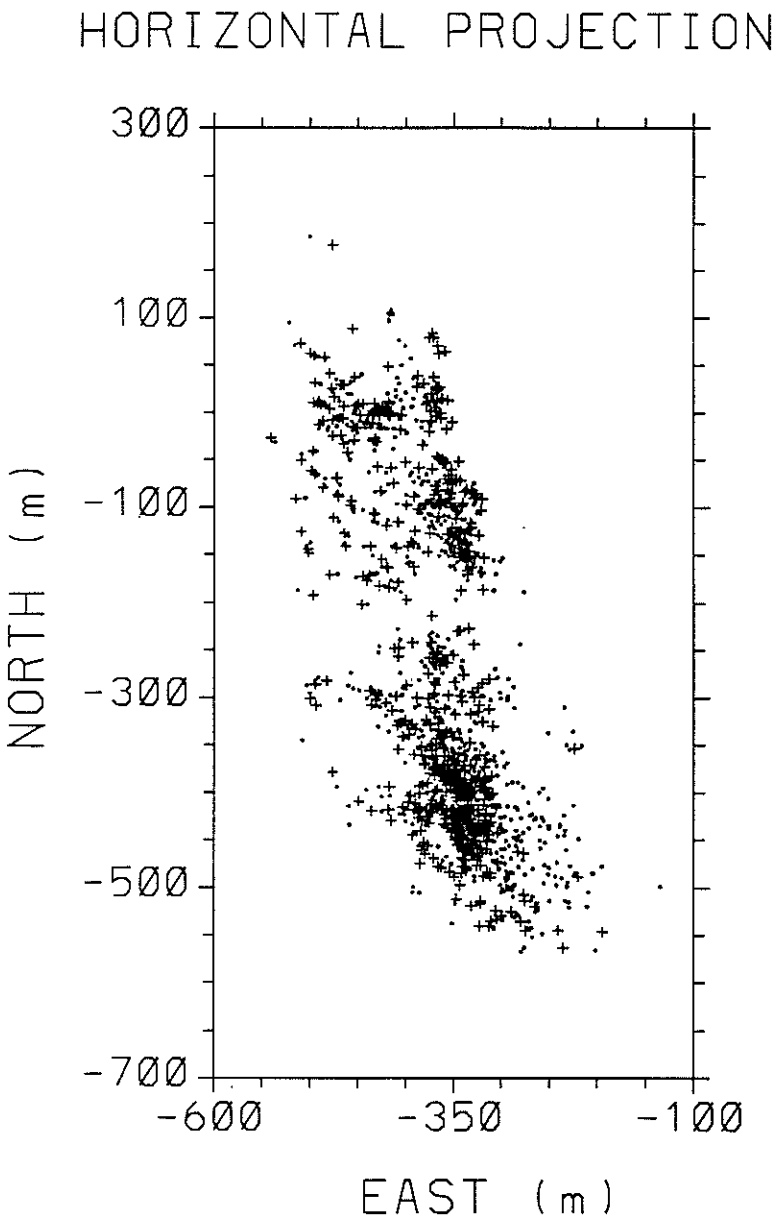
HORIZONTAL PROJECTION
300
100
-100
-300
-500
-700
NORTH (m)
-600
-350
-100
EAST (m)

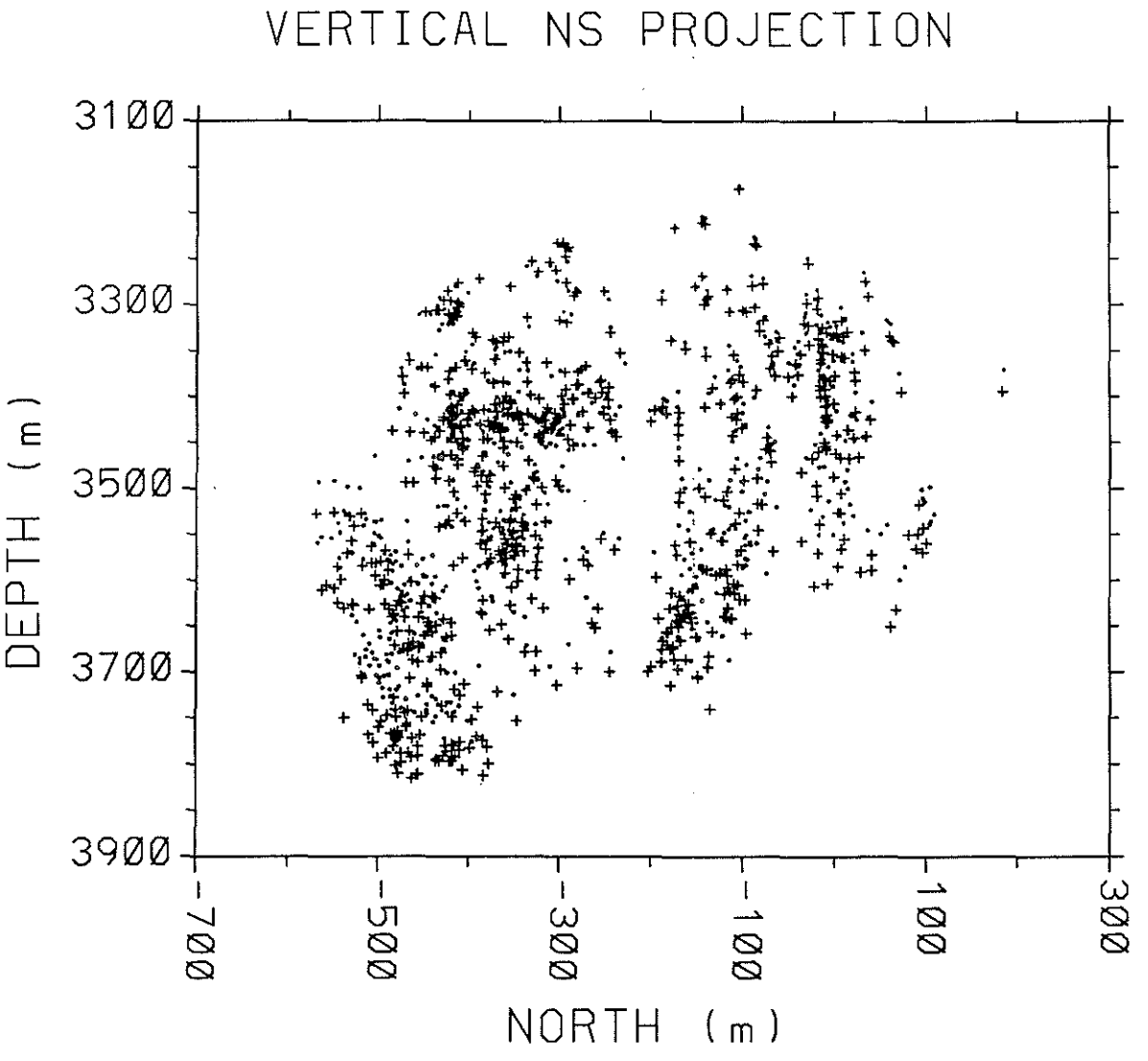

Figure 24: Vertical North-South projections of the initial (dots) and final (plus signs) earthquake locations. (A) Results with $\lambda = 10$. (B) Results with $\lambda = 1$.

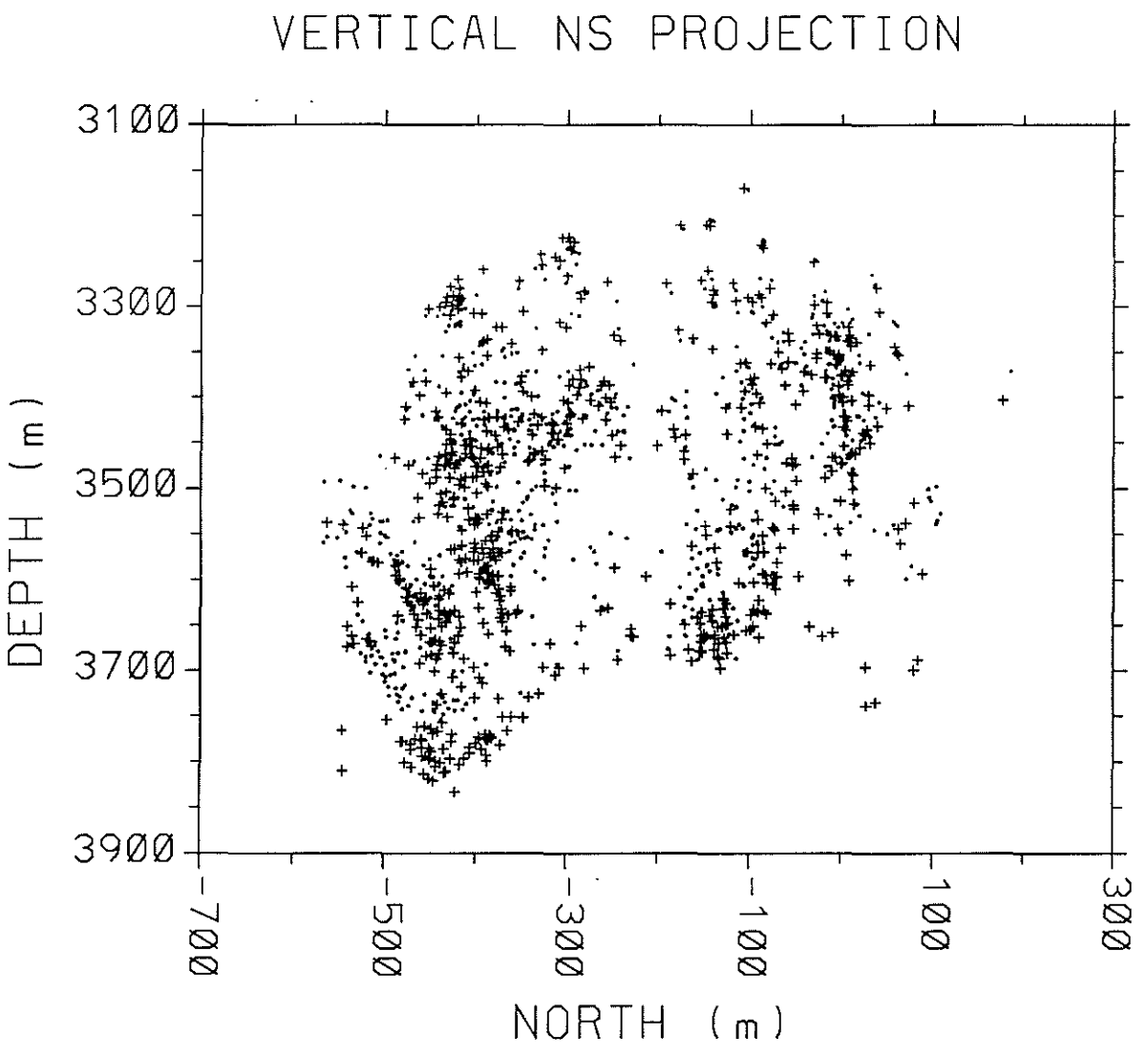
VERTICAL NS PROJECTION
3100
3300
3500
3700
3900
DEPTH (m)
-700
-500
-300
-100
100
300
NORTH (m)

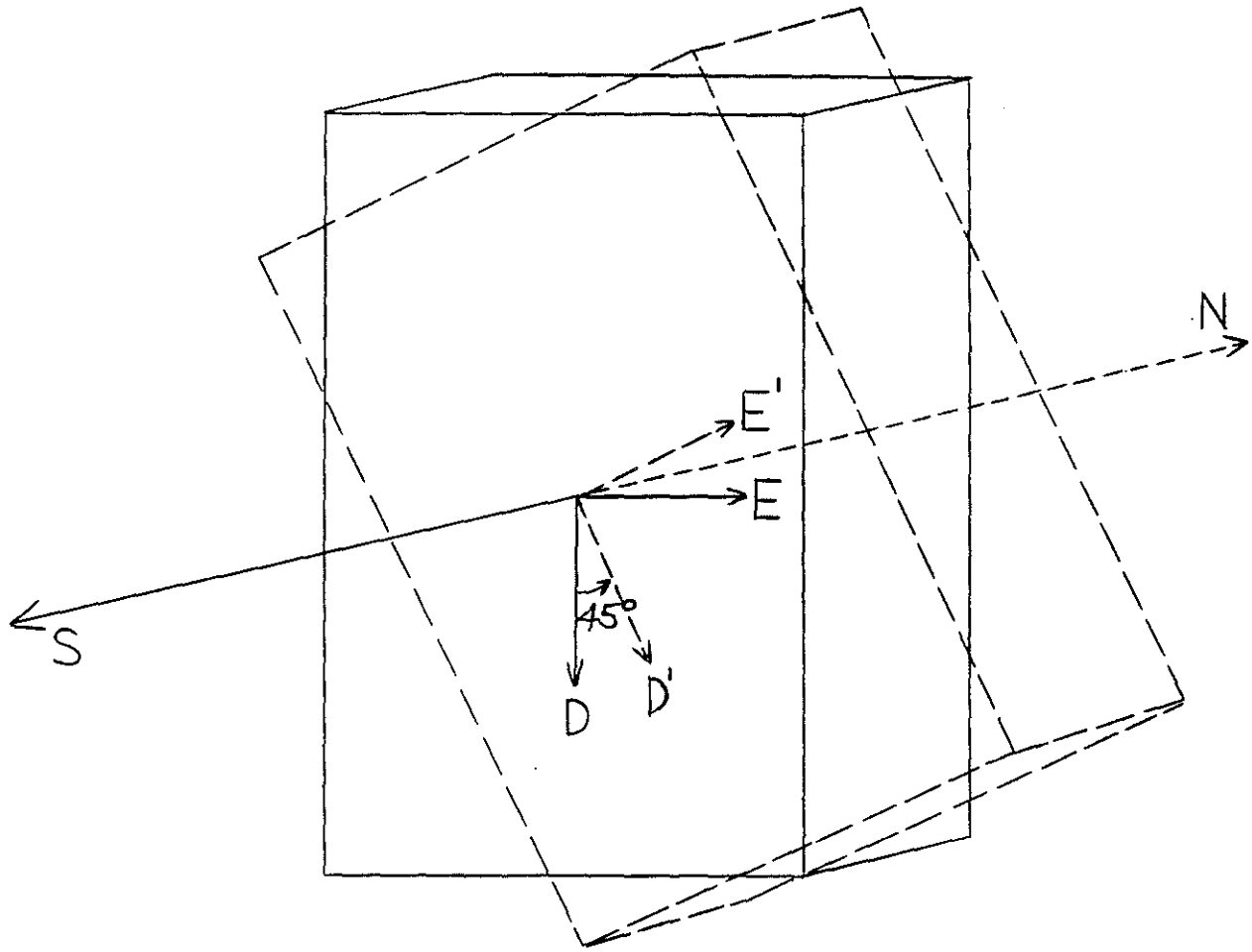

Figure 25: Rotation of the velocity grid used to test whether the final earthquake locations are biased by the grid orientation.

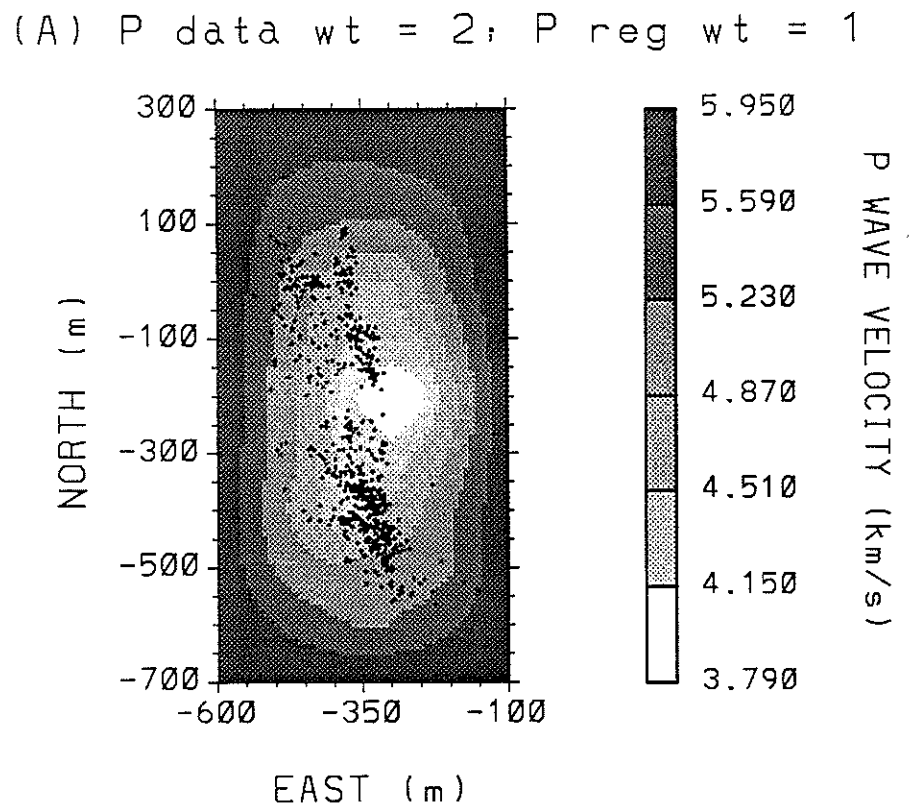

Figure 26: Results of inversions using different weight schemes. Horizontal V_P cross sections at 3500 m depth. $\lambda = 4$; bent rays. (A) P data weight = 2; P regularization weight = 1. (B) P data weight = 2; P regularization weight = 0.59. (C) P data weight = 1; P regularization weight = 0.59.

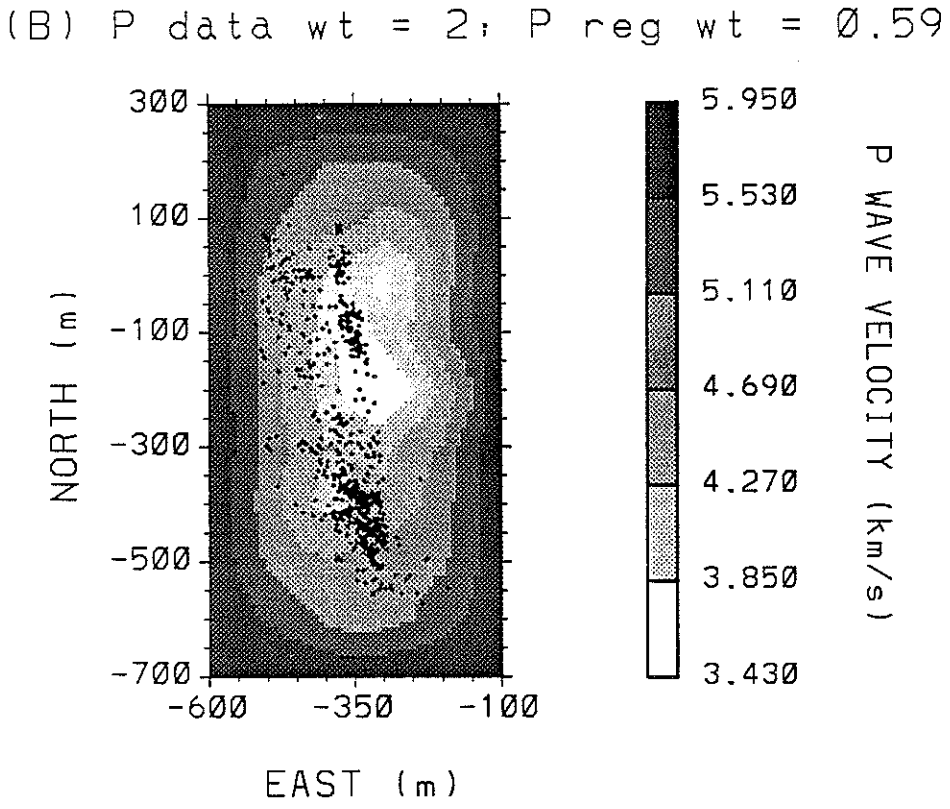
(B) P data wt = 2; P reg wt = 0.59
300
100
-100
-300
-500
-700
NORTH (m)
-600
-350
-100
EAST (m)
5.950
5.530
5.110
4.690
4.270
3.850
3.430
P WAVE VELOCITY (km/s)

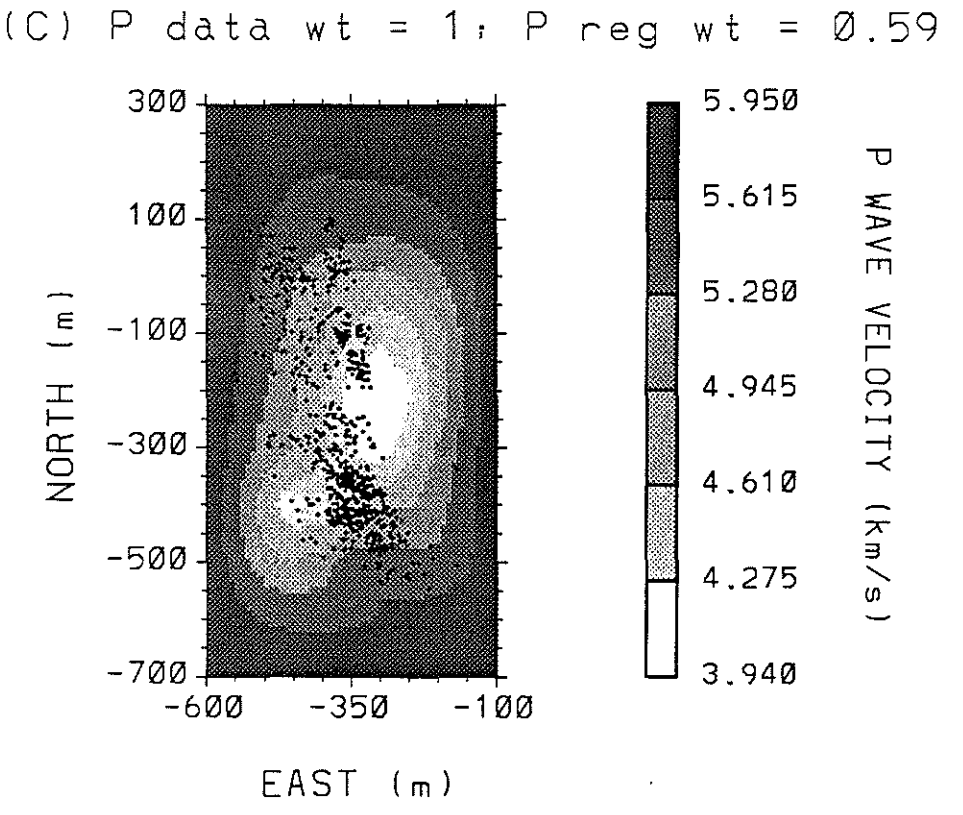
(C) P data wt = 1; P reg wt = 0.59
300
100
-100
-300
-500
-700
NORTH (m)
-600
-350
-100
EAST (m)
5.950
5.615
5.280
4.945
4.610
4.275
3.940
P WAVE VELOCITY (km/s)

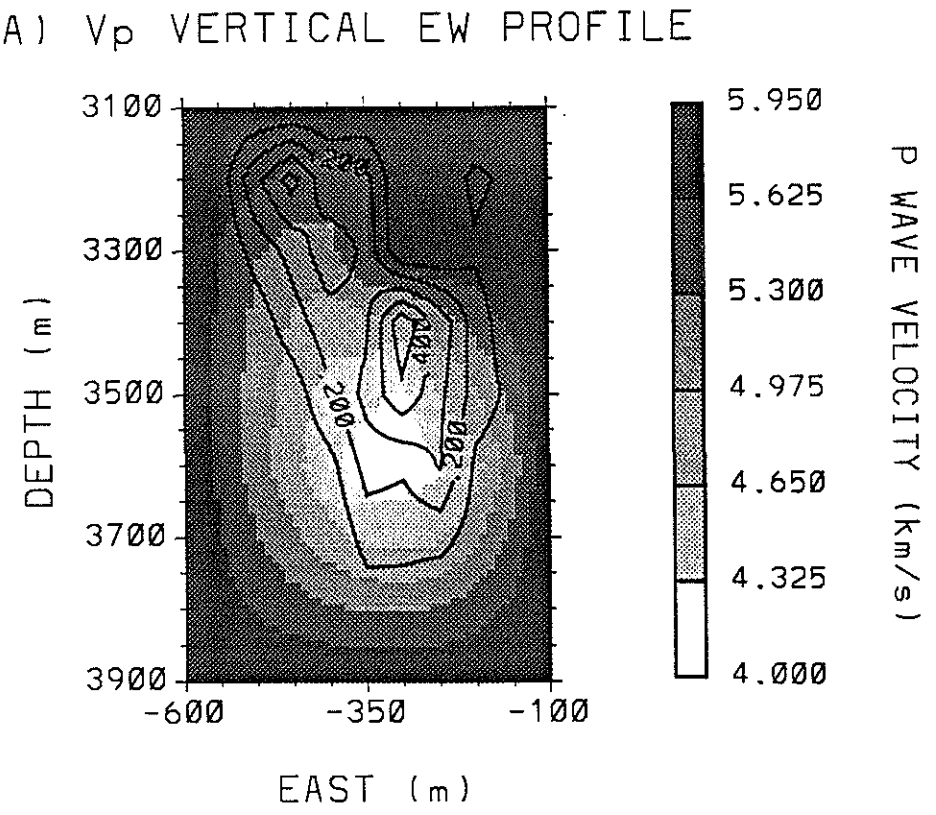

Figure 27: Diagonal elements of the resolution matrix for the inversion from Section 4.5.5 with $\lambda = 4$. The velocities are represented by the gray scale and the resolutions are contoured. Contour interval = 0.1. Vertical East-West cross sections at -300 m North. (A) V_P resolutions (B) V_S resolutions.

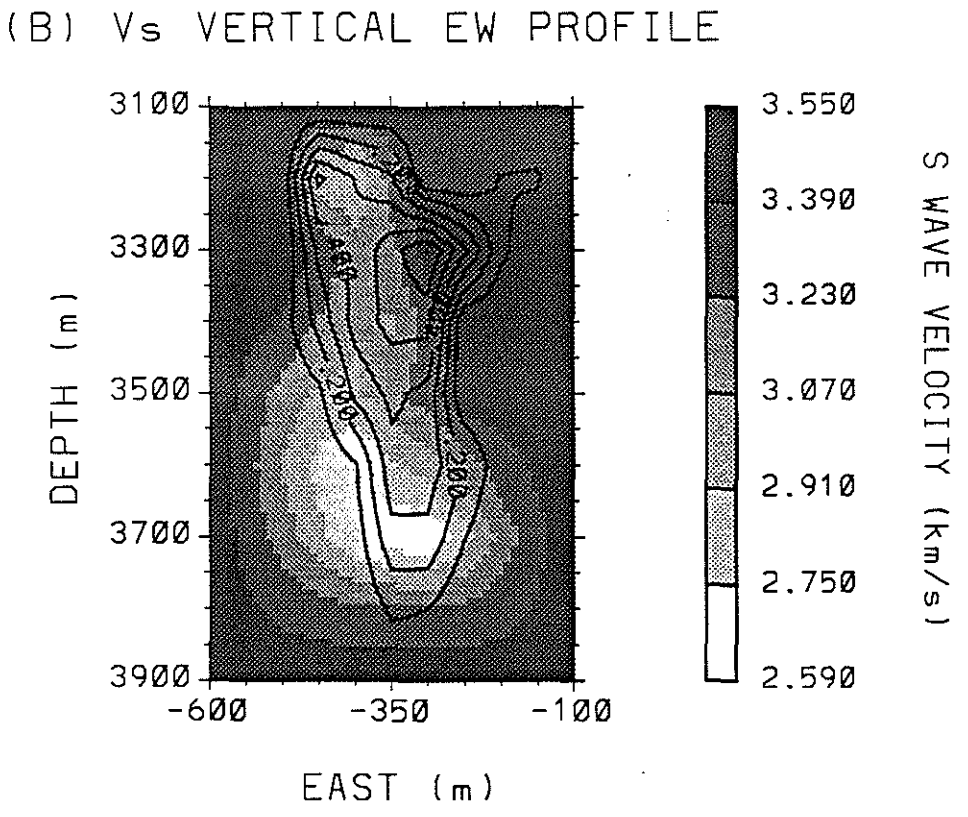
(B) Vs VERTICAL EW PROFILE
3100
3300
3500
3700
3900
DEPTH (m)
-600
-350
-100
EAST (m)
3.550
3.390
3.230
3.070
2.910
2.750
2.590
S WAVE VELOCITY (km/s)

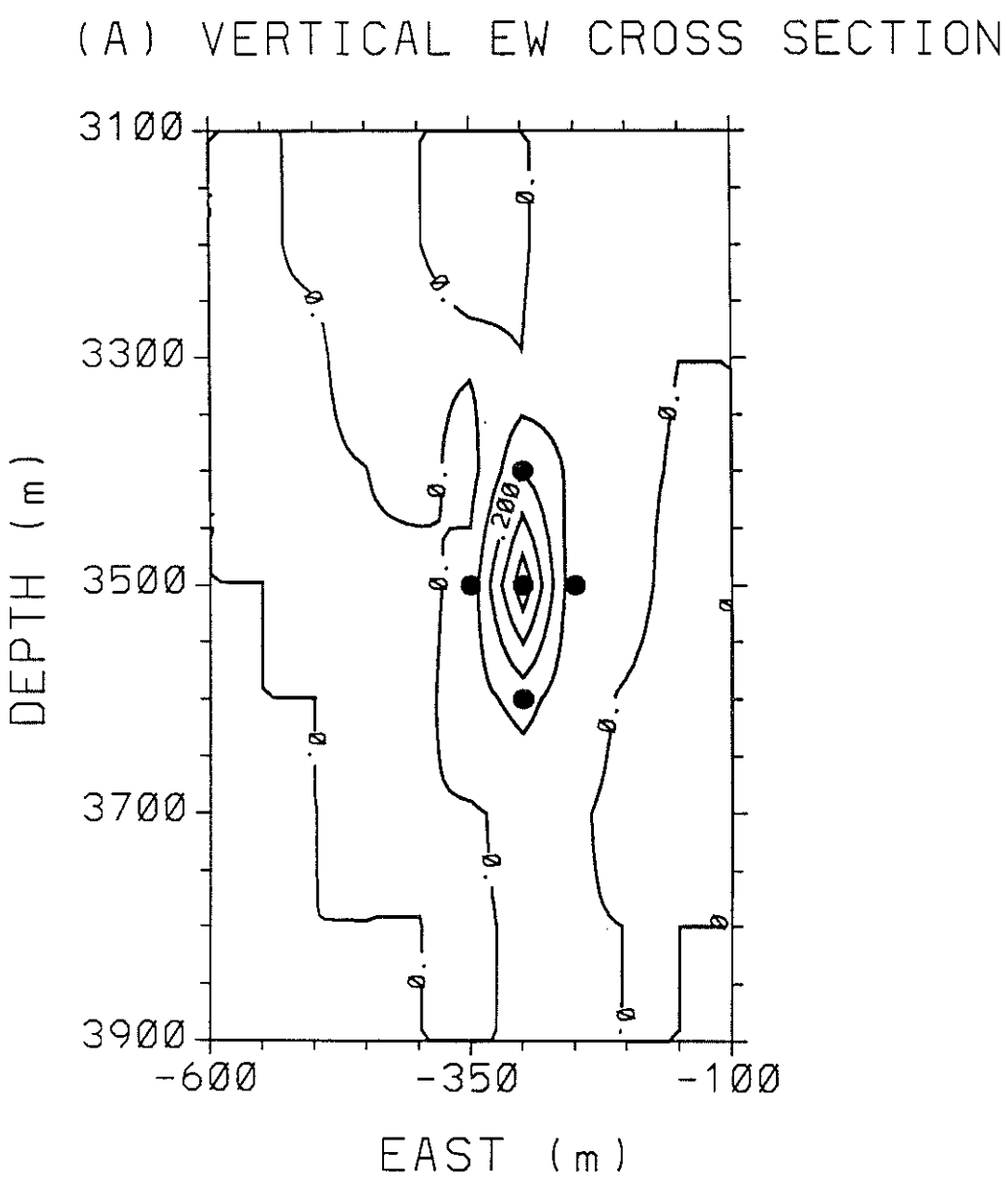

Figure 28: V_P off-diagonal elements of the row of the resolution matrix for the V_P node at (-300 m East, -300 m North, 3500 m depth). Contour interval = 0.1. (A) Vertical East-West cross section at -300 m North. (B) Horizontal cross section at 3500 m depth.

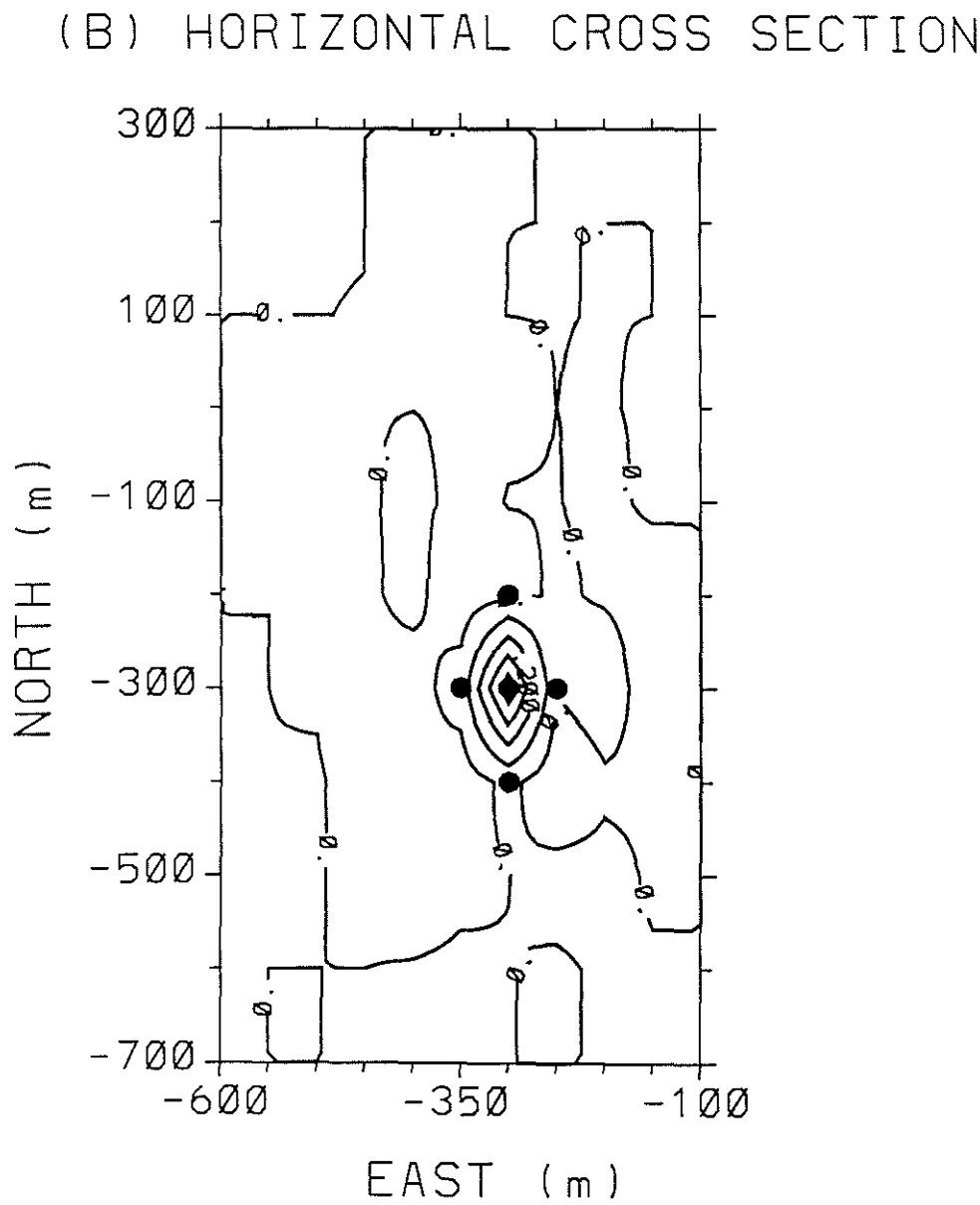
(B) HORIZONTAL CROSS SECTION
300
100
-100
-300
-500
-700
NORTH (m)
-600
-350
-100
EAST (m)
200

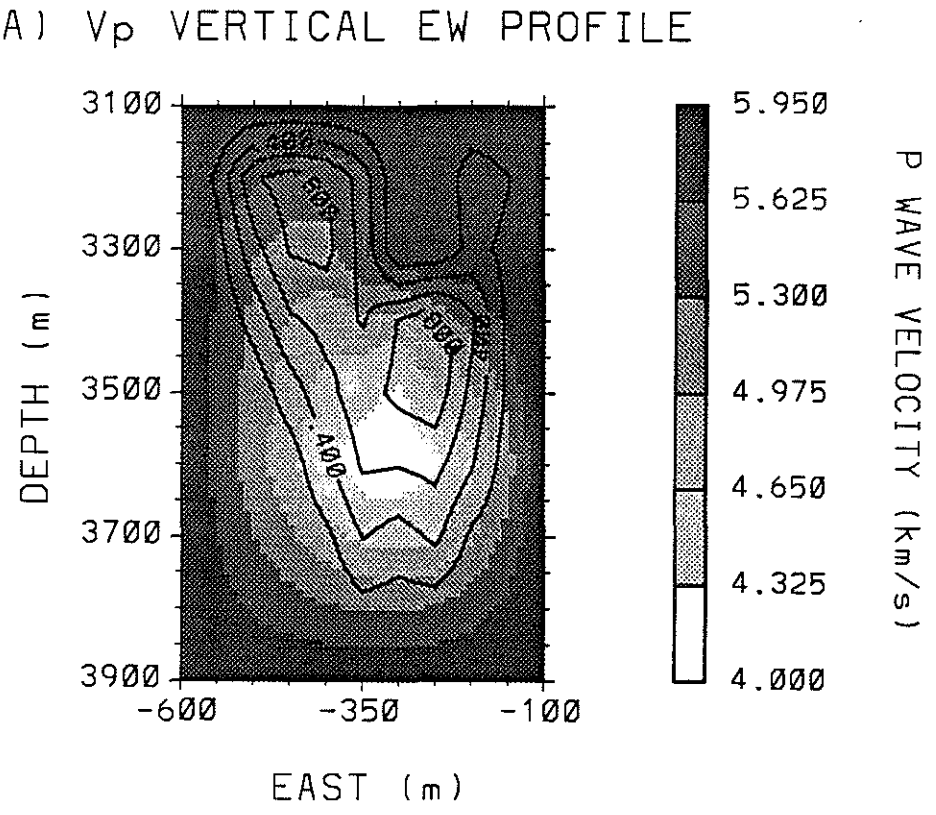

Figure 29: Sums of the diagonal elements of the resolution matrix and the off-diagonal elements corresponding to the adjacent nodes over which the second velocity derivatives are computed. Vertical East-West cross sections at -300 m North. Contour interval = 0.2. (A) V_P resolution sums. (B) V_S resolution sums.

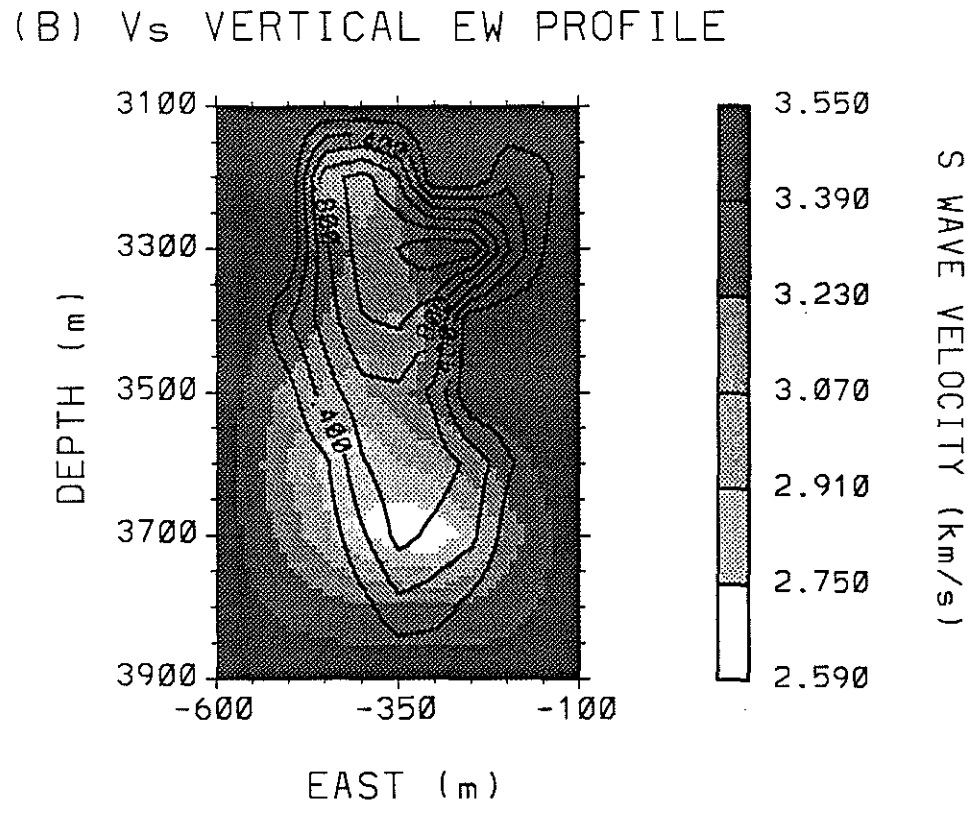
(B) Vs VERTICAL EW PROFILE
3100
3300
3500
3700
3900
DEPTH (m)
-600
-350
-100
EAST (m)
3.550
3.390
3.230
3.070
2.910
2.750
2.590
S WAVE VELOCITY (km/s)

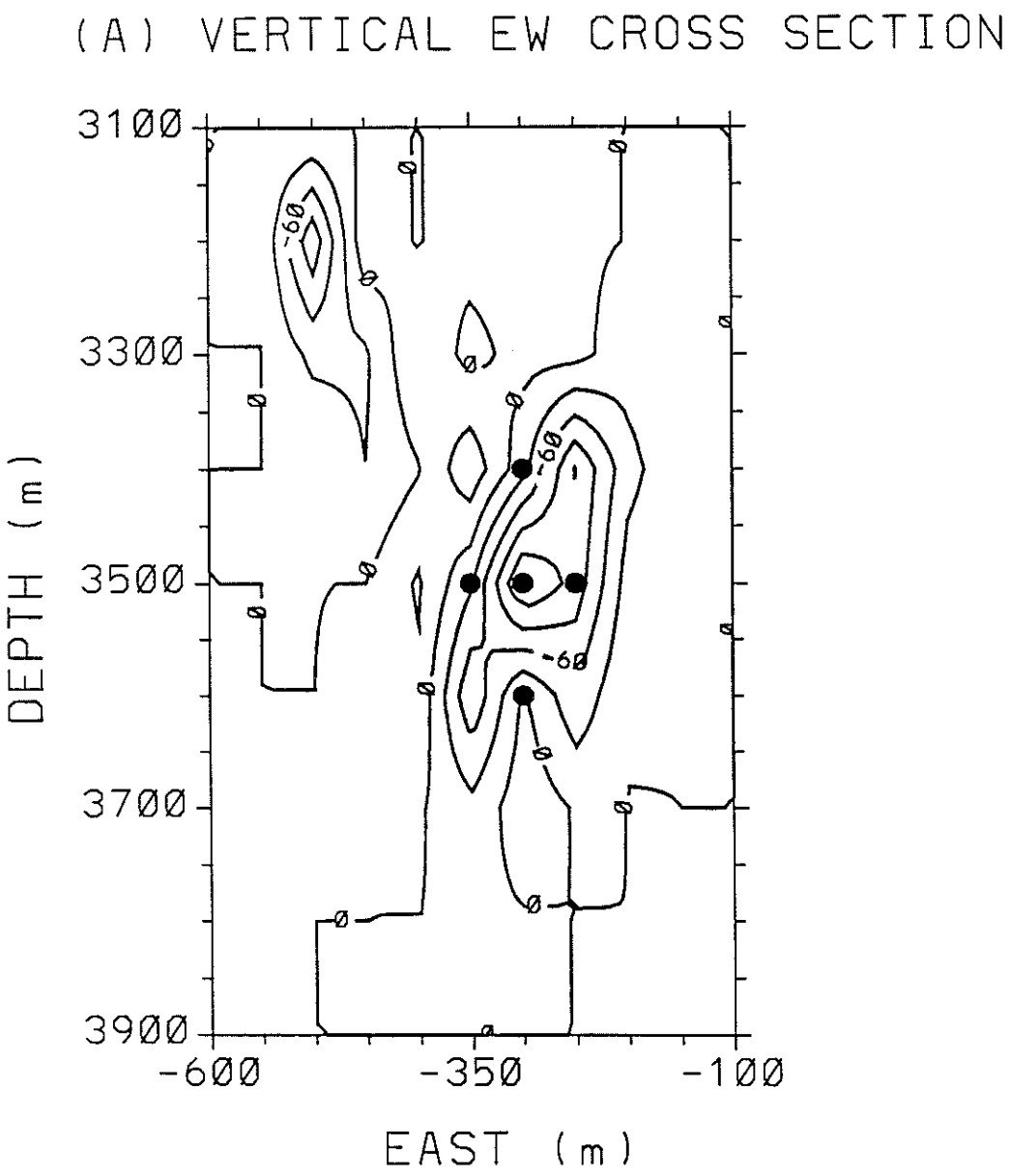

Figure 30: V_S off-diagonal elements of the row of the resolution matrix for the V_P node at (-300 m East, -300 m North, 3500 m depth). Contour interval = 0.03, scaled by 1000. The values are negative. (A) Vertical East-West cross section at -300 m North. (B) Horizontal cross section at 3500 m depth.

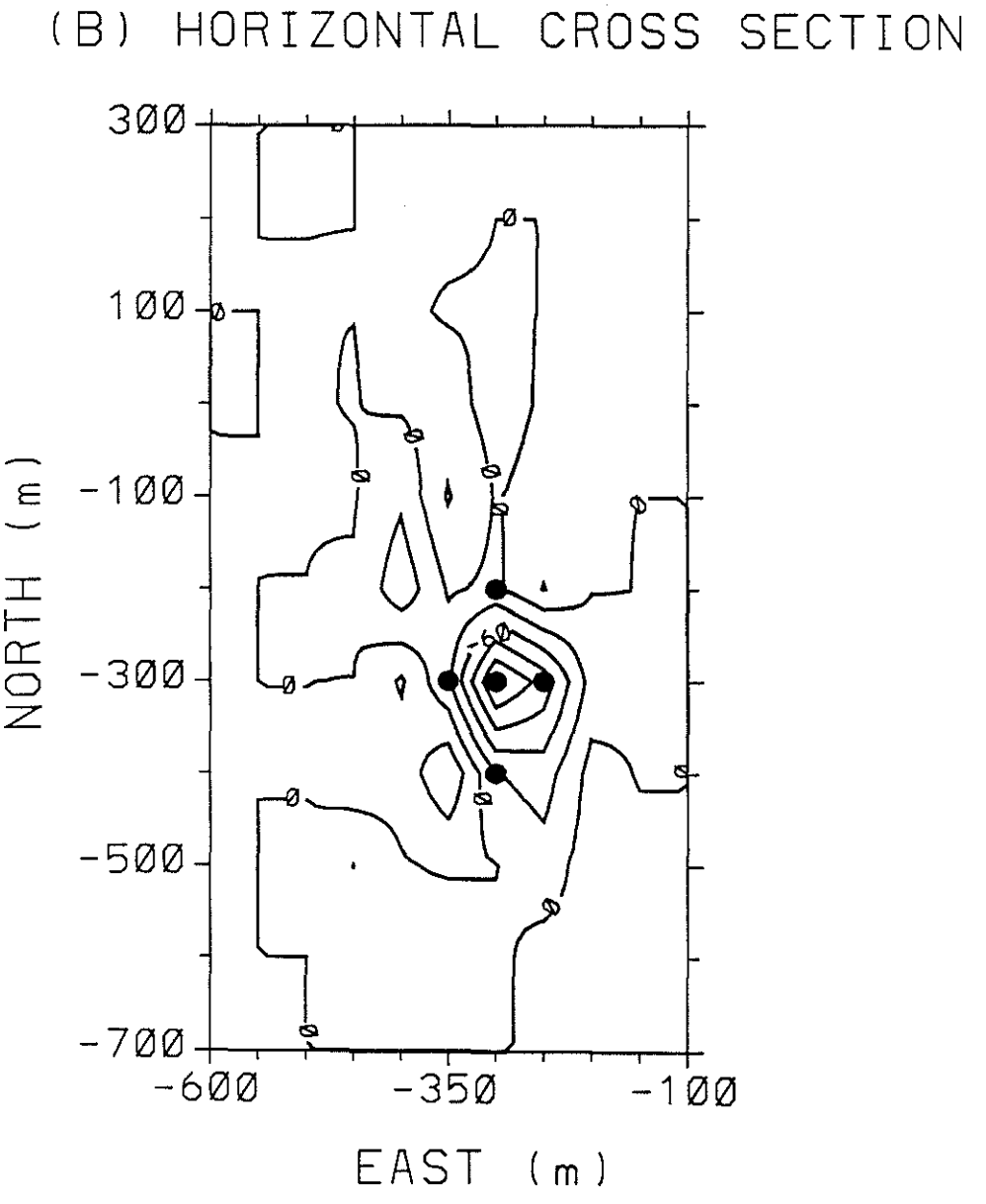
(B) HORIZONTAL CROSS SECTION
300
100
-100
-300
-500
-700
NORTH (m)
-600
-350
-100
EAST (m)

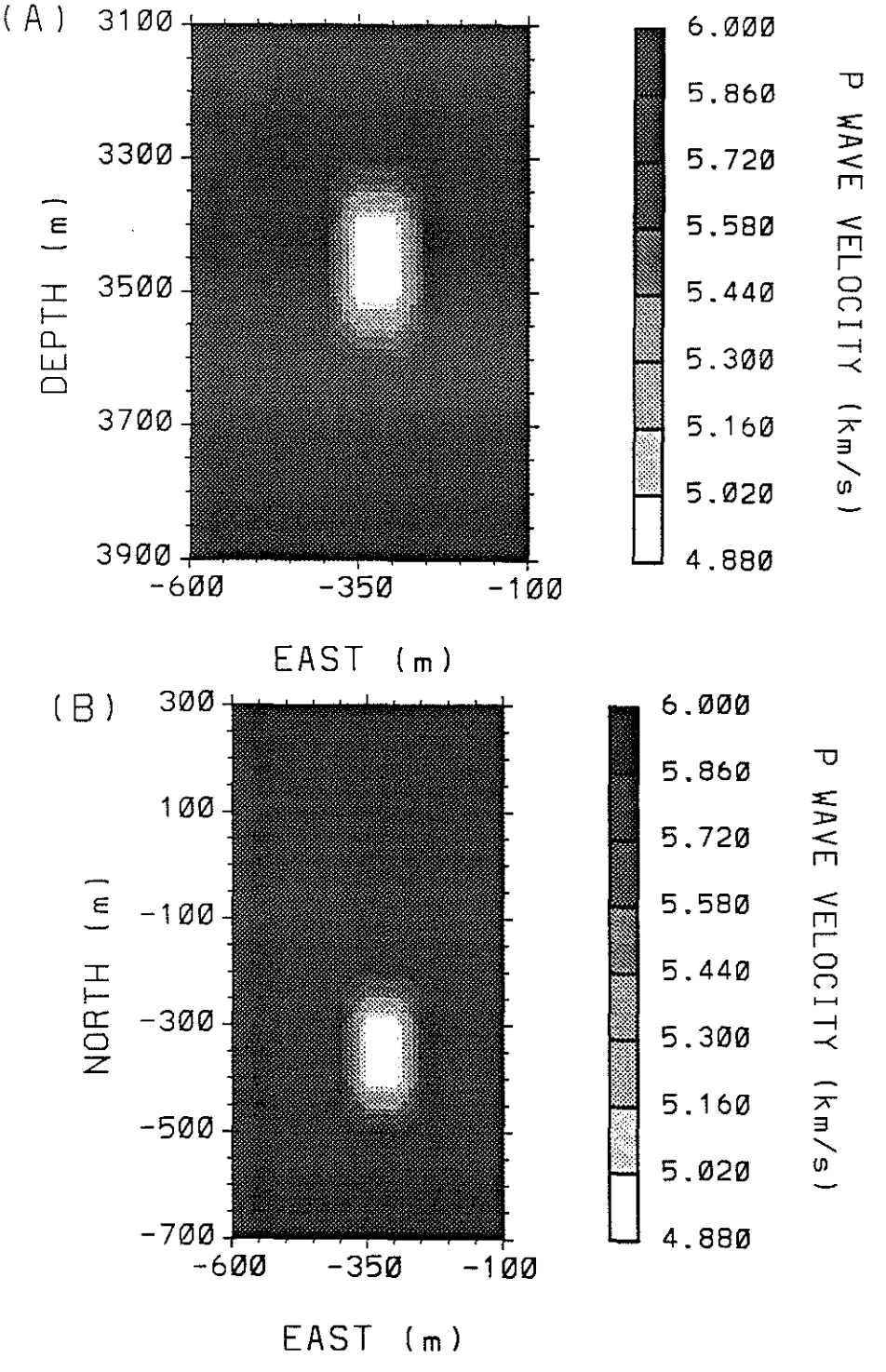

Figure 31: V_P model used to create synthetic arrival time data. (A) Vertical East-West cross section at -350 m North. (B) Horizontal cross section at 3450 m depth.

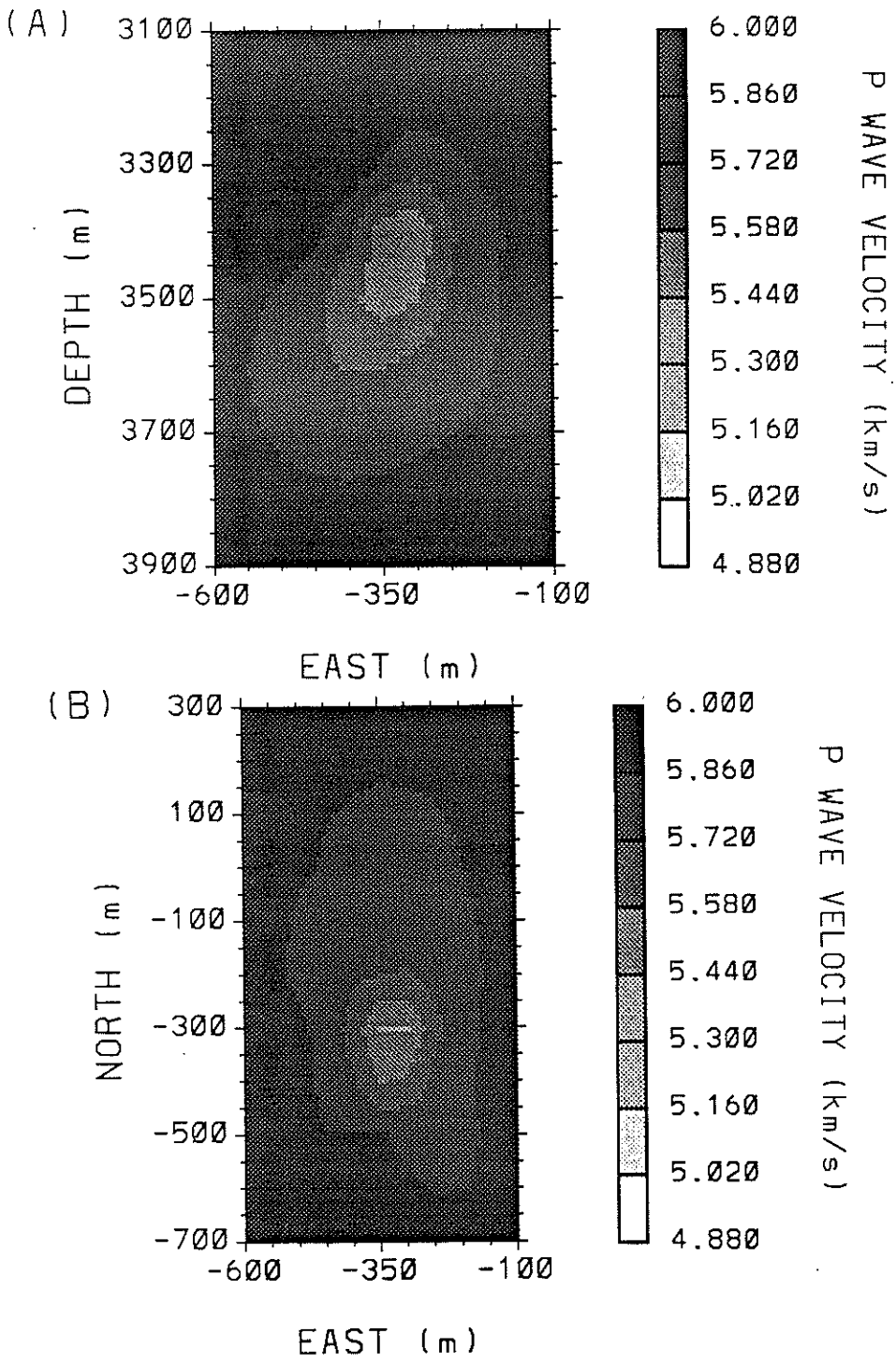

Figure 32: Final P-wave velocity model from the inversion of the synthetic data, plotted using the same velocity scale as in Figure 31. (A) Vertical East-West cross section at -350 m North. (B) Horizontal cross section at 3450 m depth.

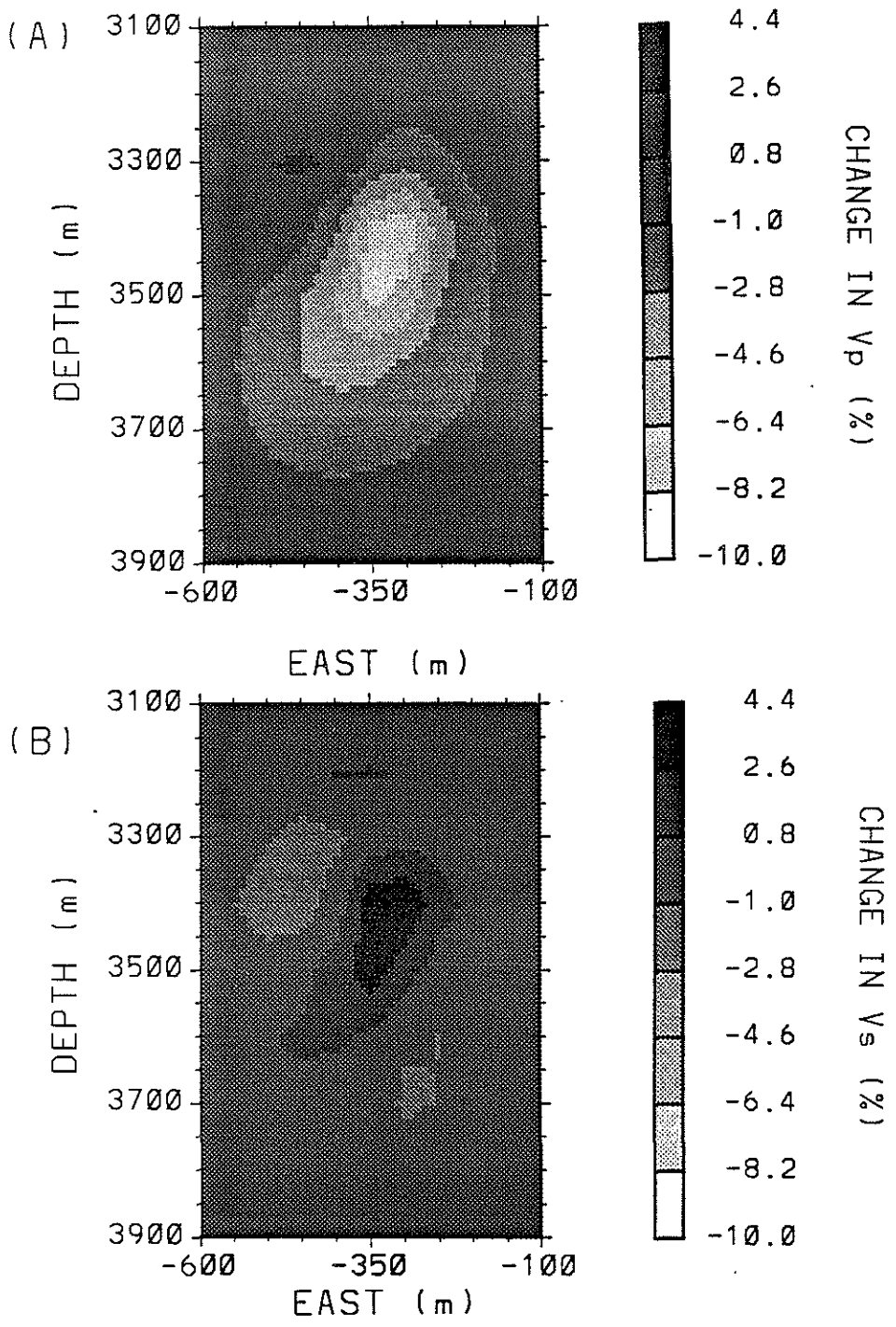

Figure 33: Final velocity models from the inversion of the synthetic data, plotted in terms of percent change from the background velocities. (A) and (B) Vertical East-West V_P and V_S cross sections at -350 m North. (C) and (D) Horizontal V_P and V_S cross sections at 3450 m depth.

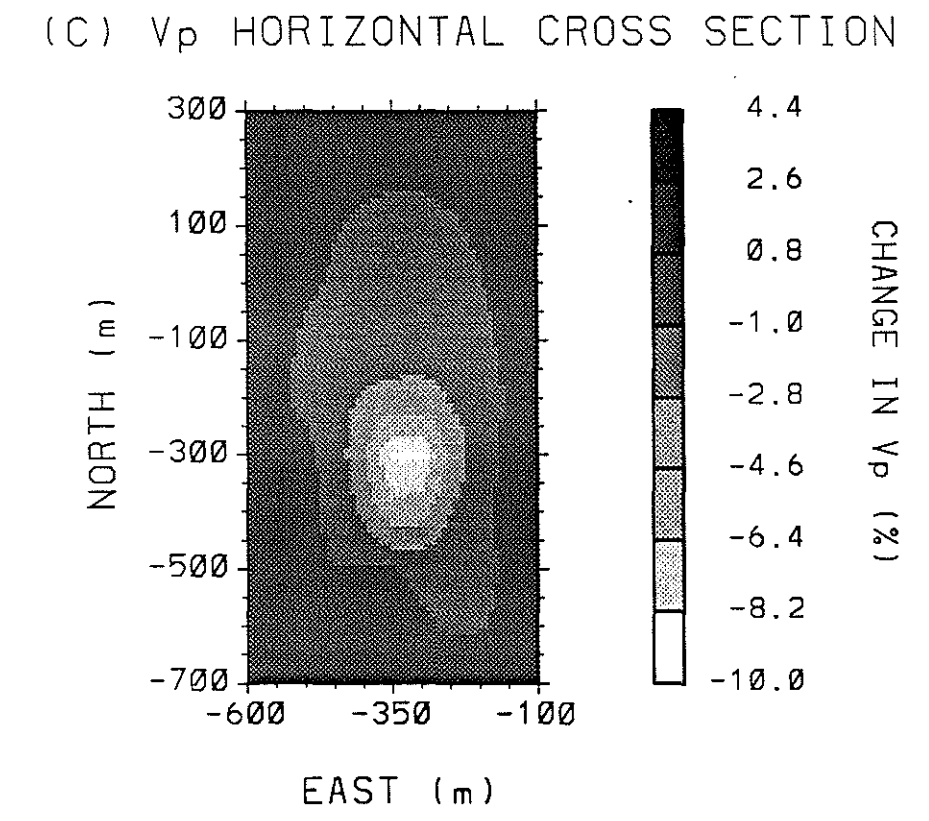
(C) Vp HORIZONTAL CROSS SECTION
300
100
-100
-300
-500
-700
NORTH (m)
-600
-350
-100
EAST (m)
4.4
2.6
0.8
-1.0
-2.8
-4.6
-6.4
-8.2
-10.0
CHANGE IN Vp (%)

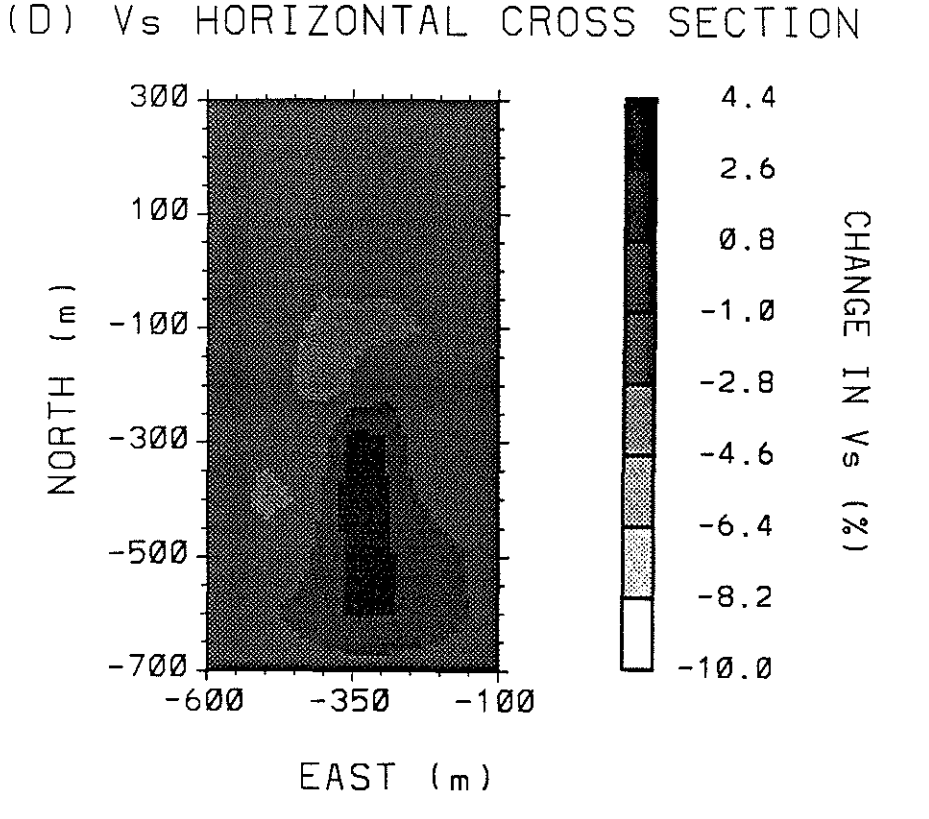
(D) Vs HORIZONTAL CROSS SECTION
300
100
-100
-300
-500
-700
NORTH (m)
-600
-350
-100
EAST (m)
4.4
2.6
0.8
-1.0
-2.8
-4.6
-6.4
-8.2
-10.0
CHANGE IN Vs (%)

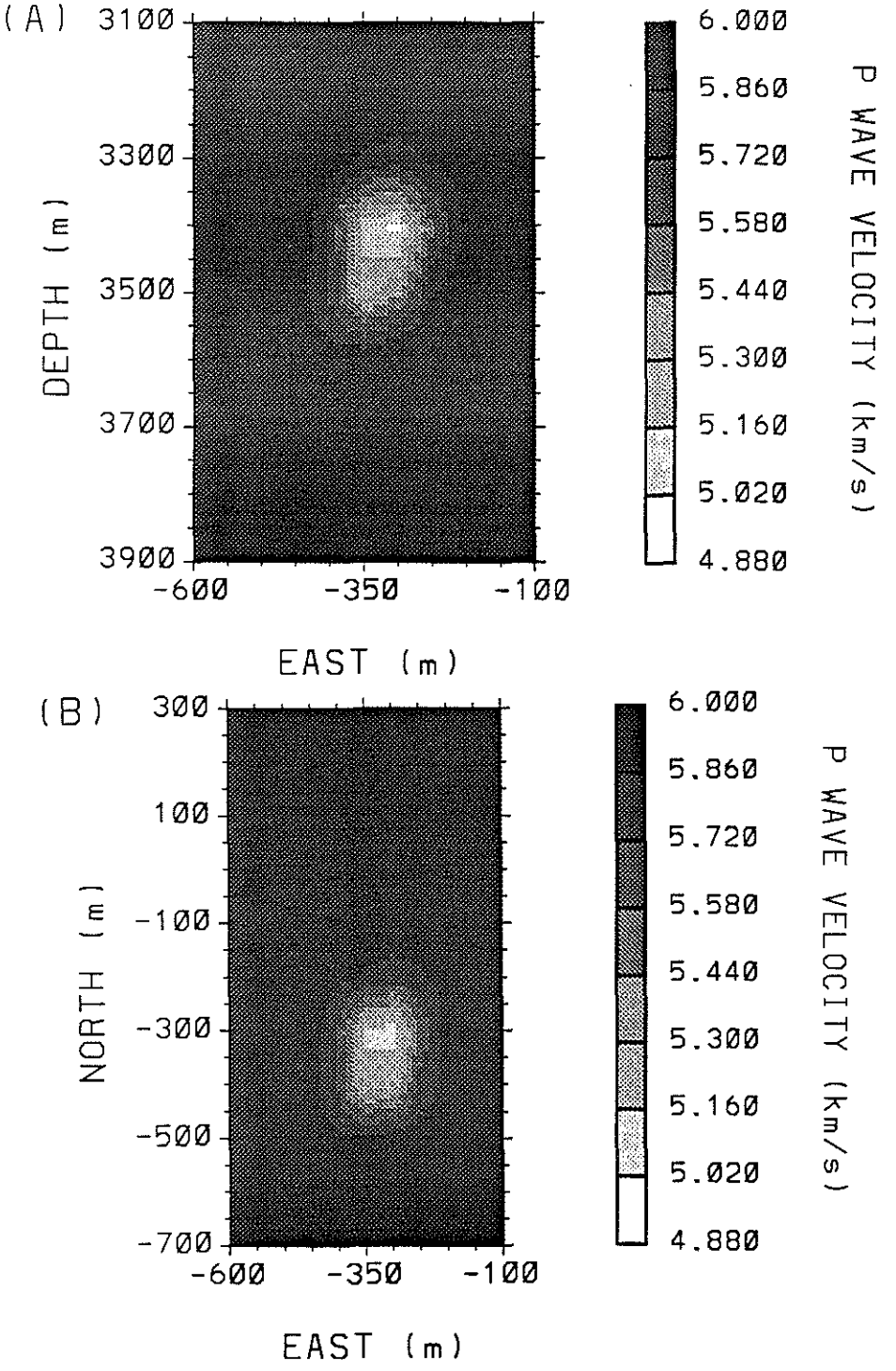

Figure 34: Final V_P values for the inversion of the synthetic data when the hypocenters are fixed at the correct values. (A) Vertical East-West cross section at -350 m North. (B) Horizontal cross section at 3450 m depth.

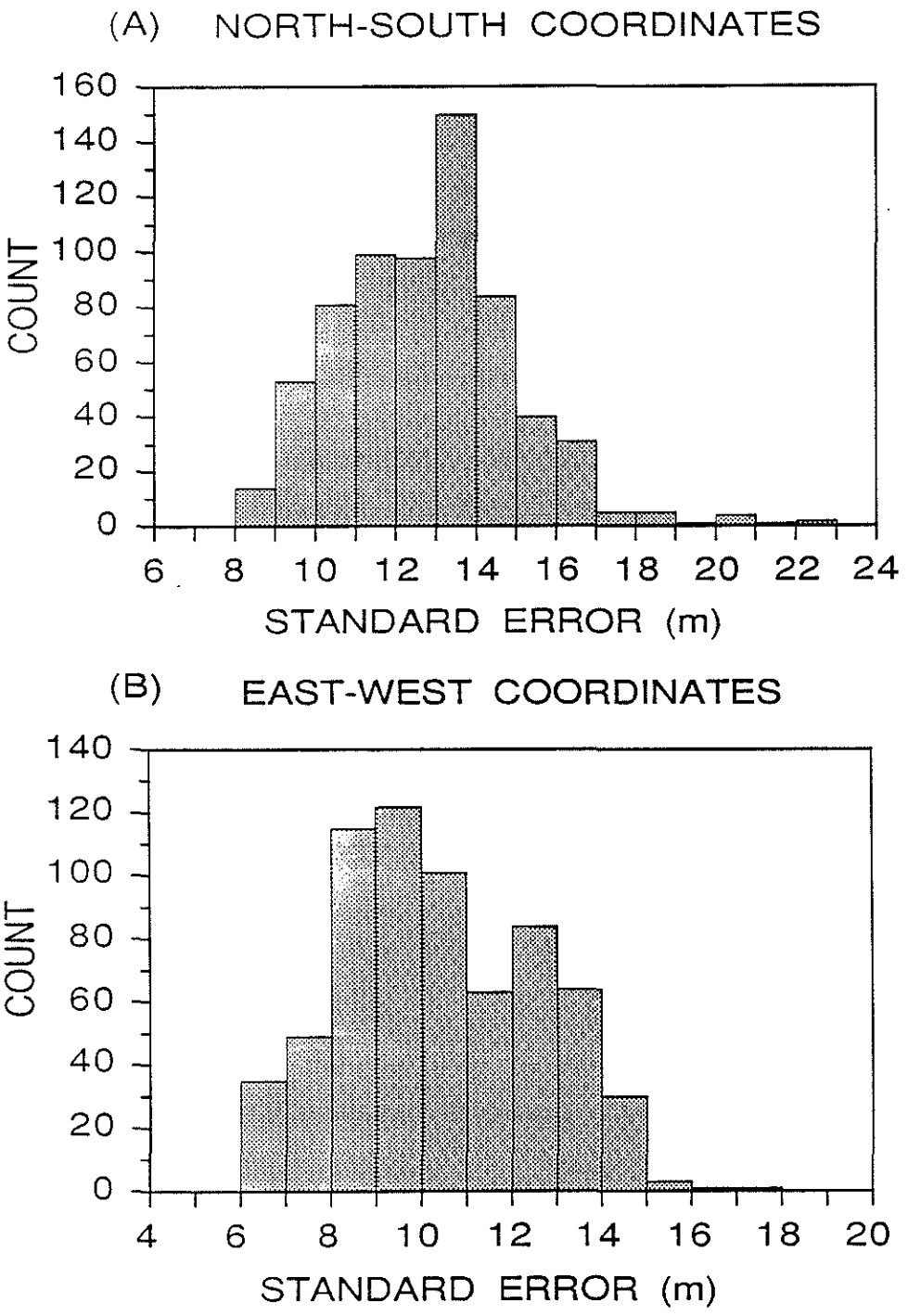

Figure 35: Hypocenter standard errors for the inversion in Section 4.5.5 with $\lambda = 4$. (A) North-South errors. (B) East-West errors. (C) Depth errors. (D) Origin time errors.

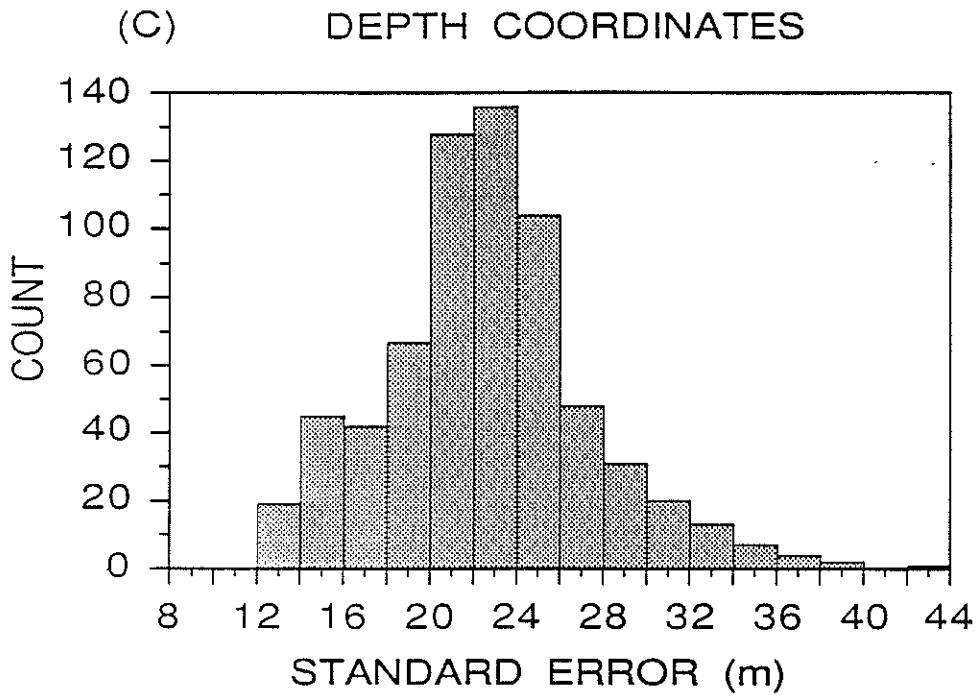
(C)
DEPTH COORDINATES
COUNT
140
120
100
80
60
40
20
0
8
12
16
20
24
28
32
36
40
44
STANDARD ERROR (m)

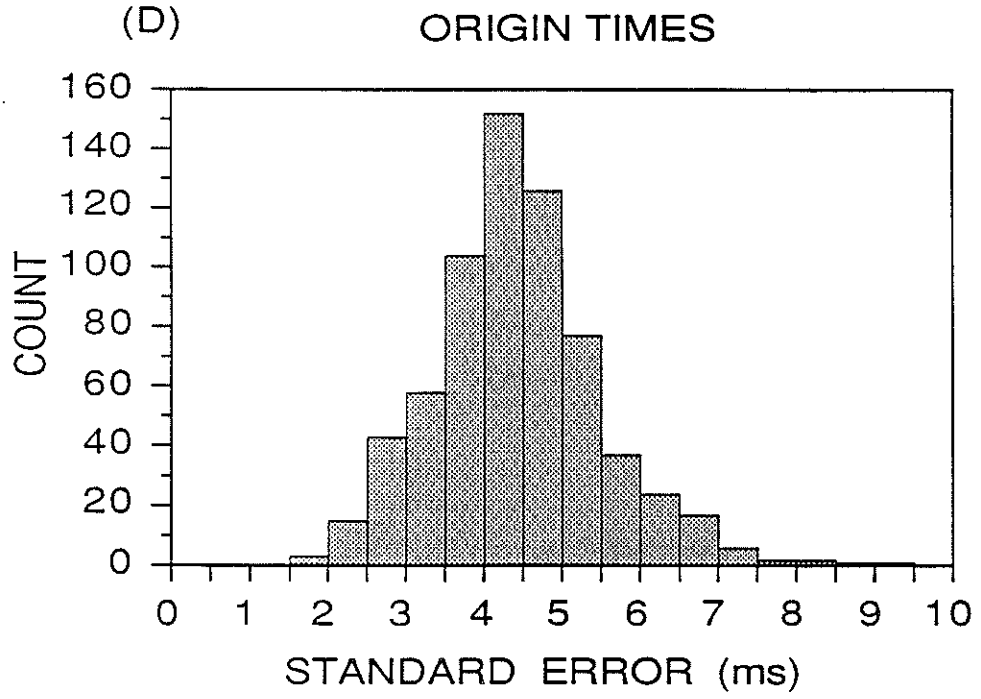
(D)
ORIGIN TIMES
COUNT
160
140
120
100
80
60
40
20
0
0
1
2
3
4
5
6
7
8
9
10
STANDARD ERROR (ms)

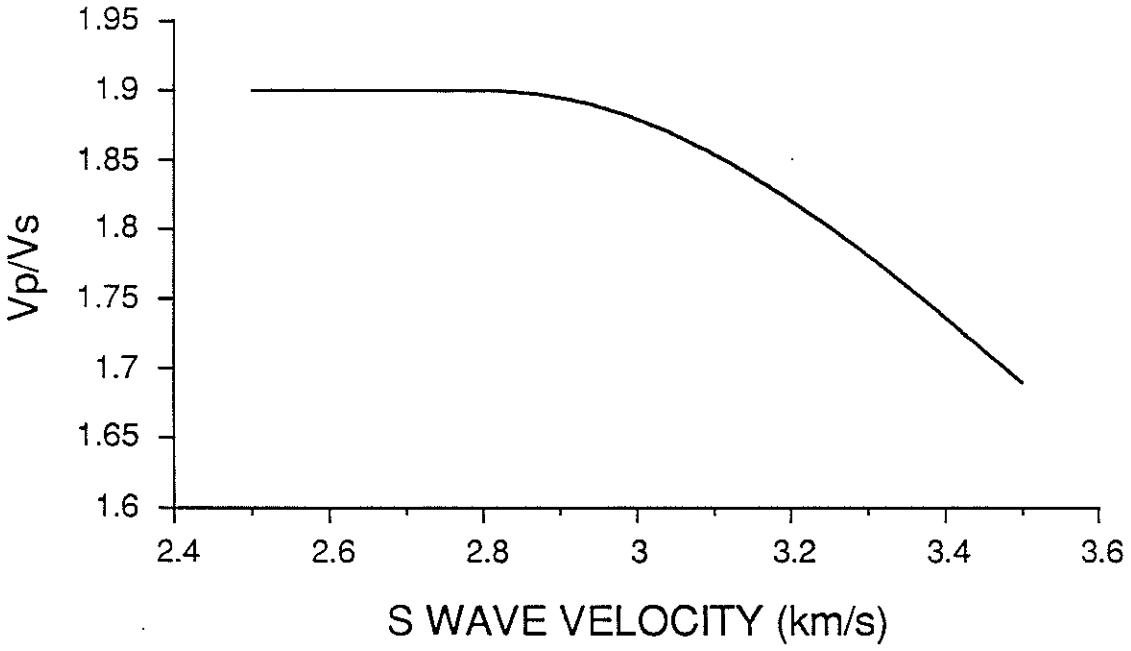

Figure 36: V_P/V_S function used to construct synthetic velocity models.

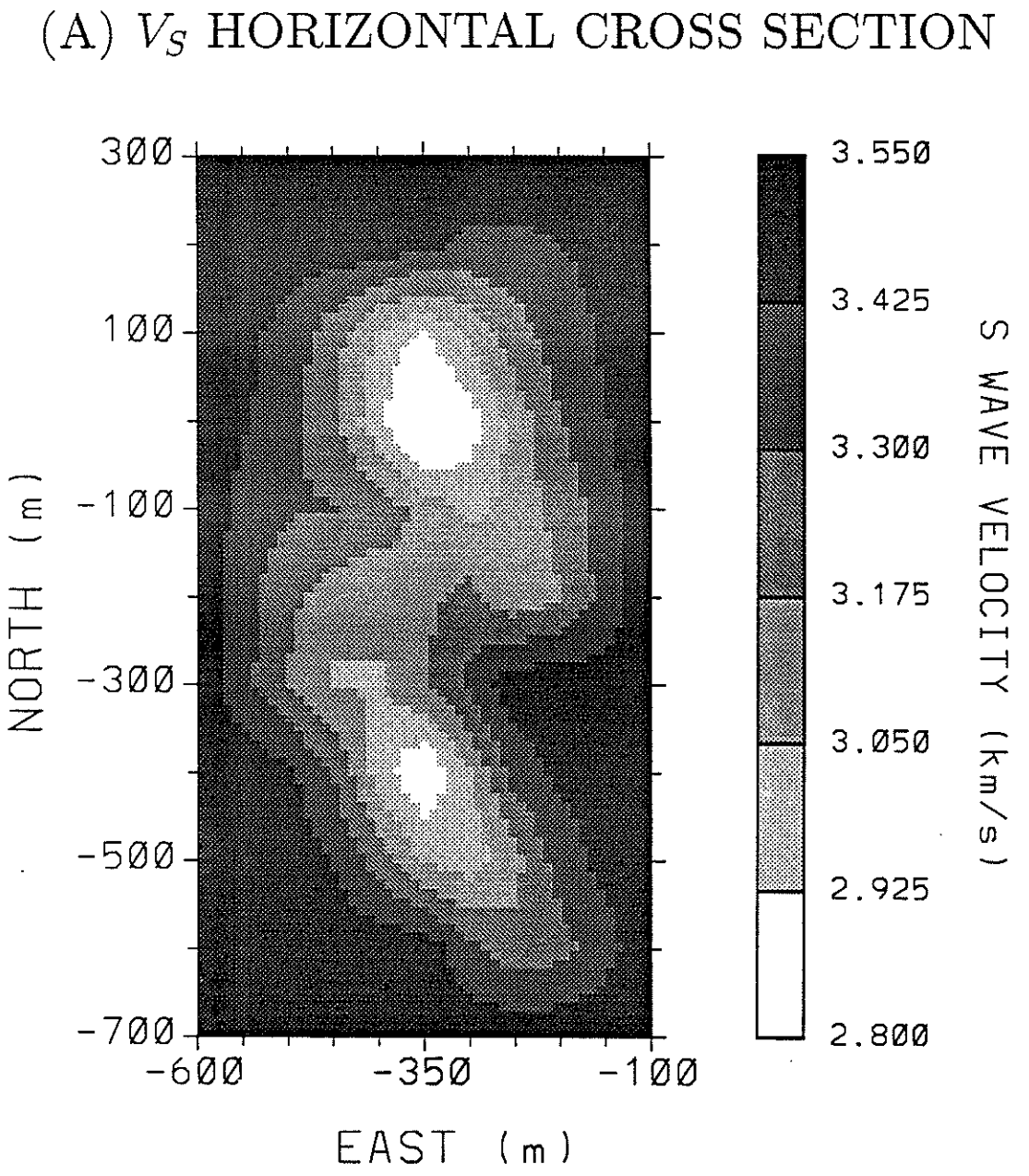

Figure 37: Horizontal cross sections, at 3500 m depth, through the velocity models used to generate synthetic arrival time data. The V_P/V_S ratios are defined by the function shown in Figure 36. (A) V_S (B) V_P (C) V_P/V_S.

(B) V_P HORIZONTAL CROSS SECTION

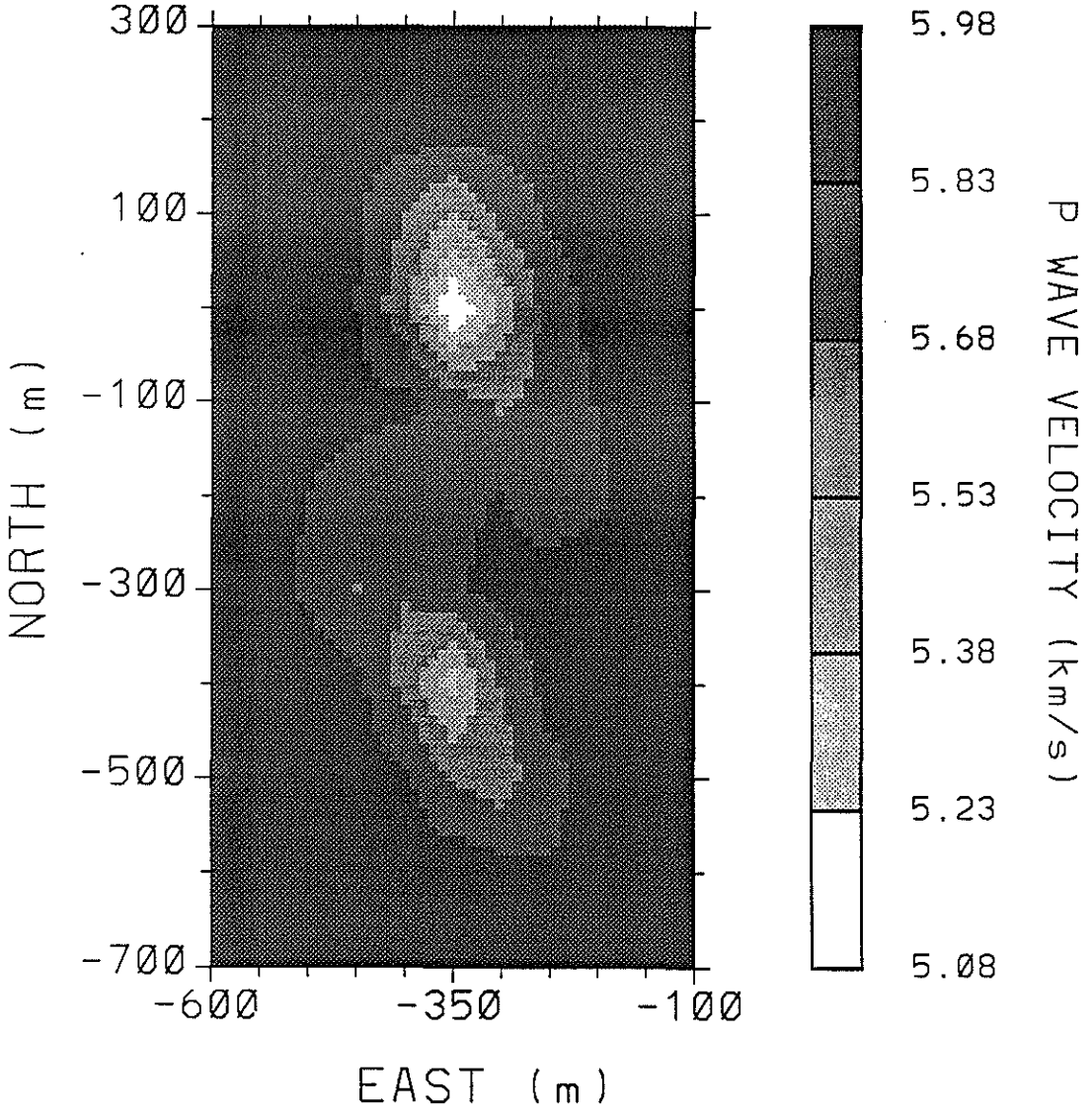

(C) V_P/V_S HORIZONTAL CROSS SECTION

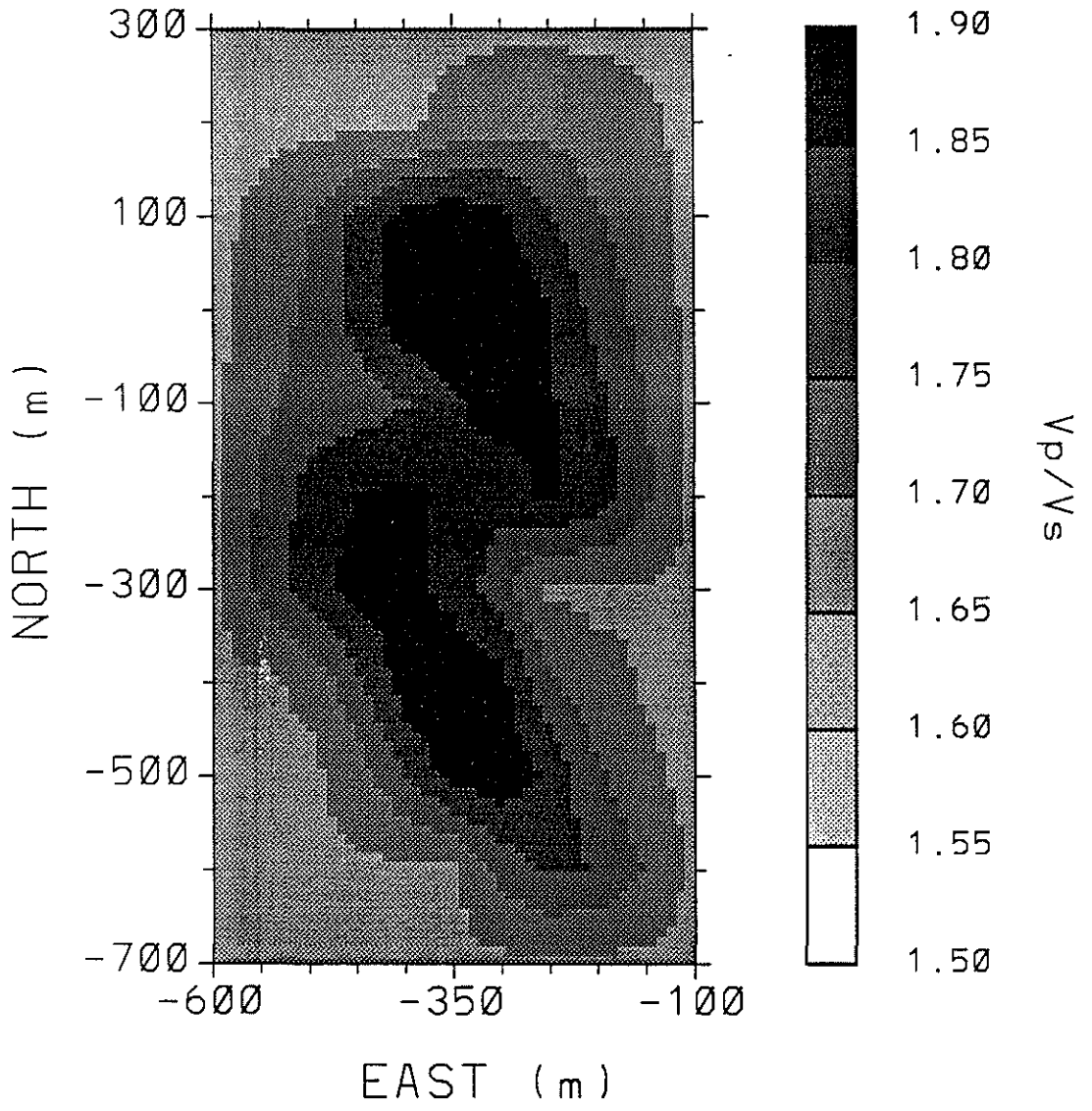

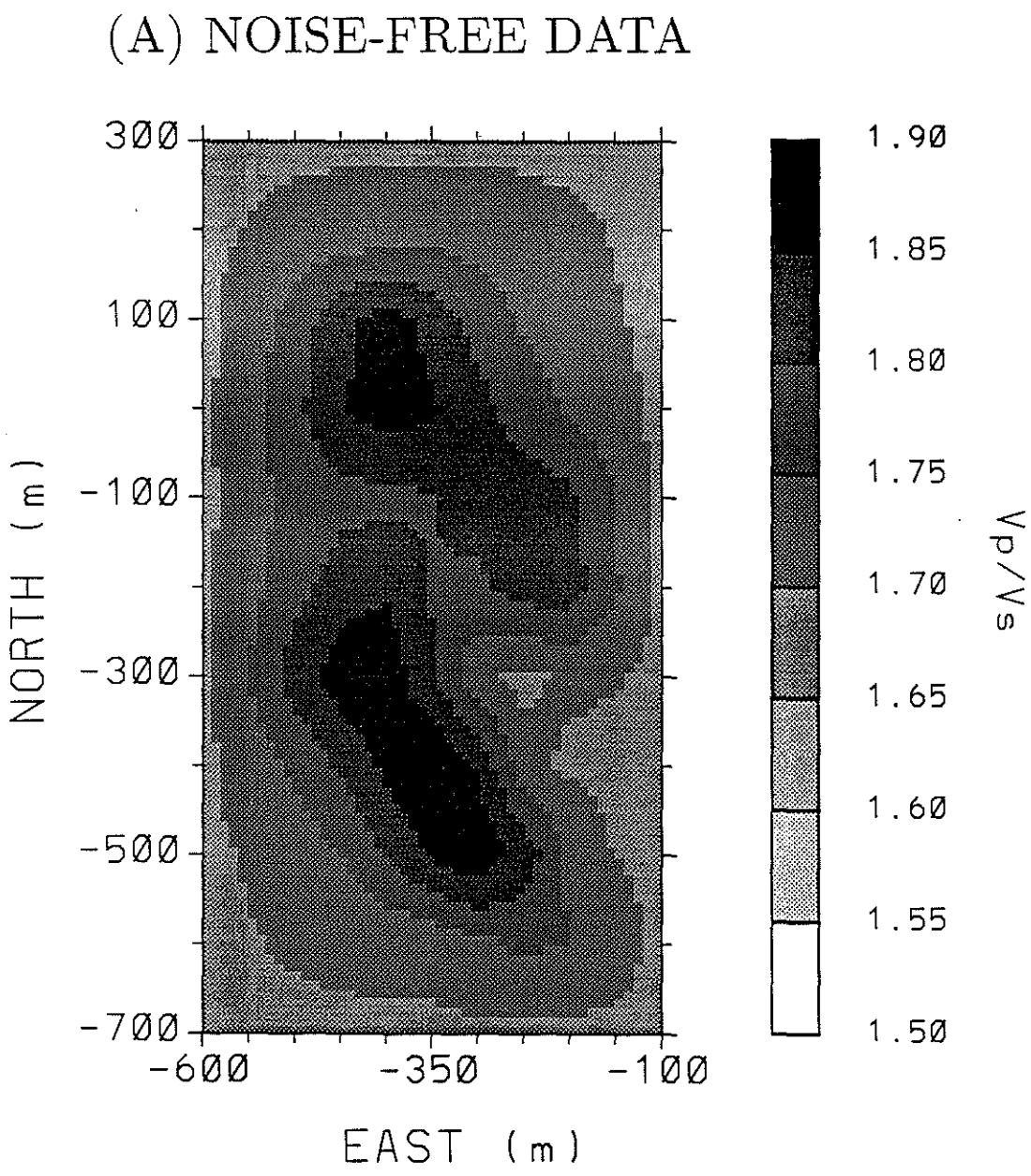

Figure 38: Horizontal cross sections, at 3500 m depth, through the final V_P/V_S structures from inversions of three synthetic data sets: (A) Noise-free data (B) Data with a low noise level (C) Data with a high noise level. The correct V_P/V_S structure is shown in Figure 37c.

(B) DATA WITH LOW NOISE LEVEL

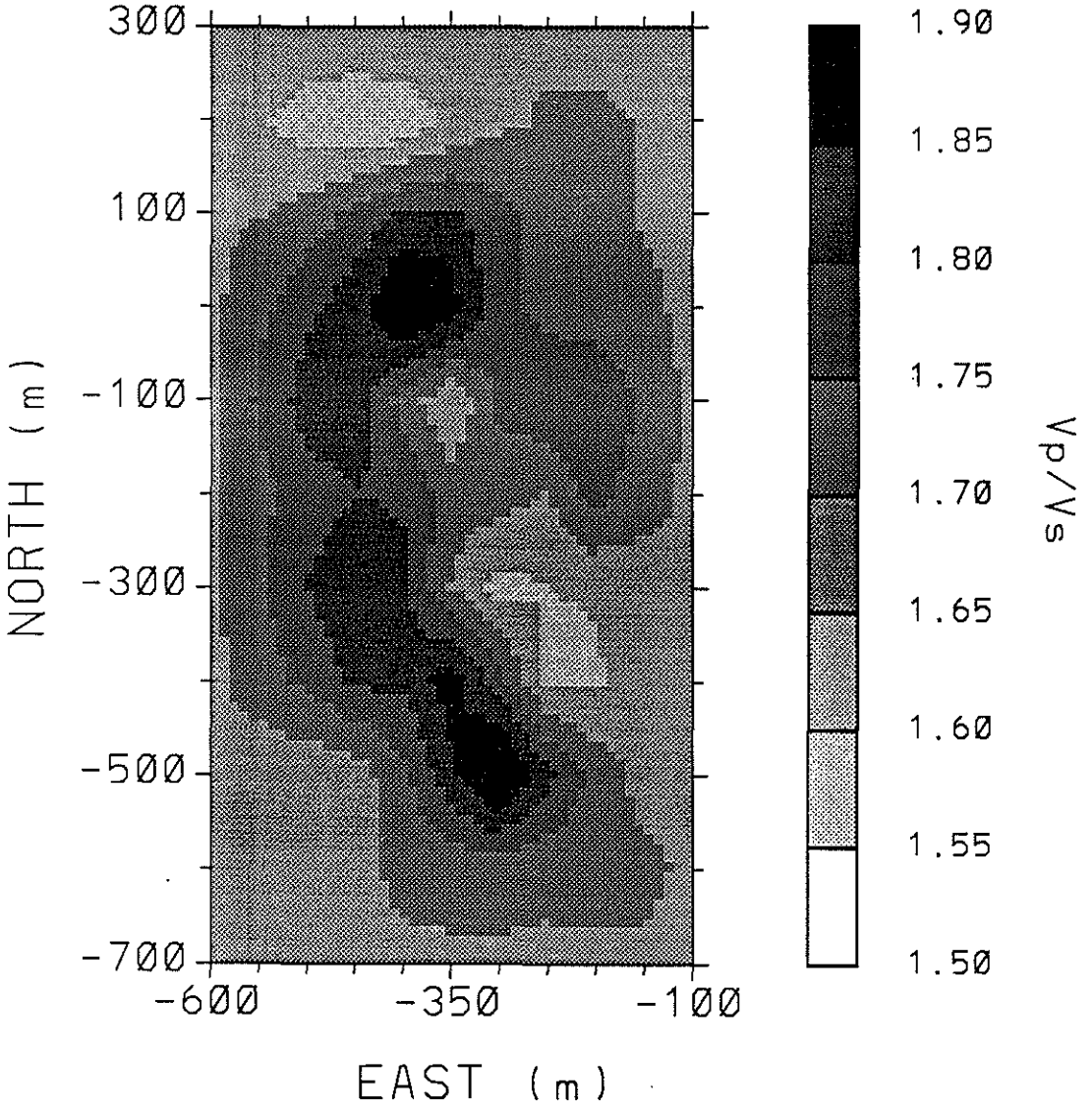

(C) DATA WITH HIGH NOISE LEVEL

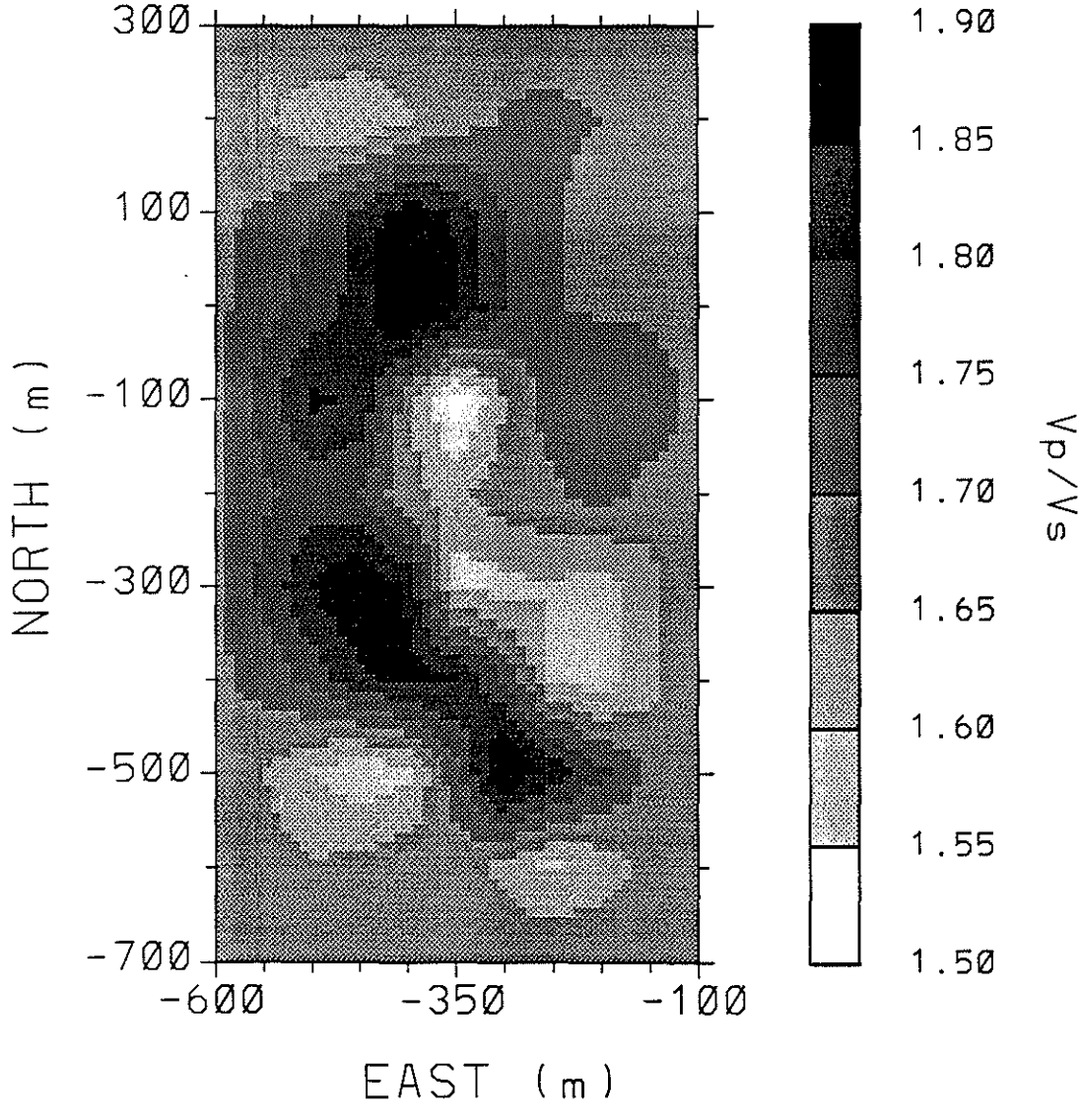

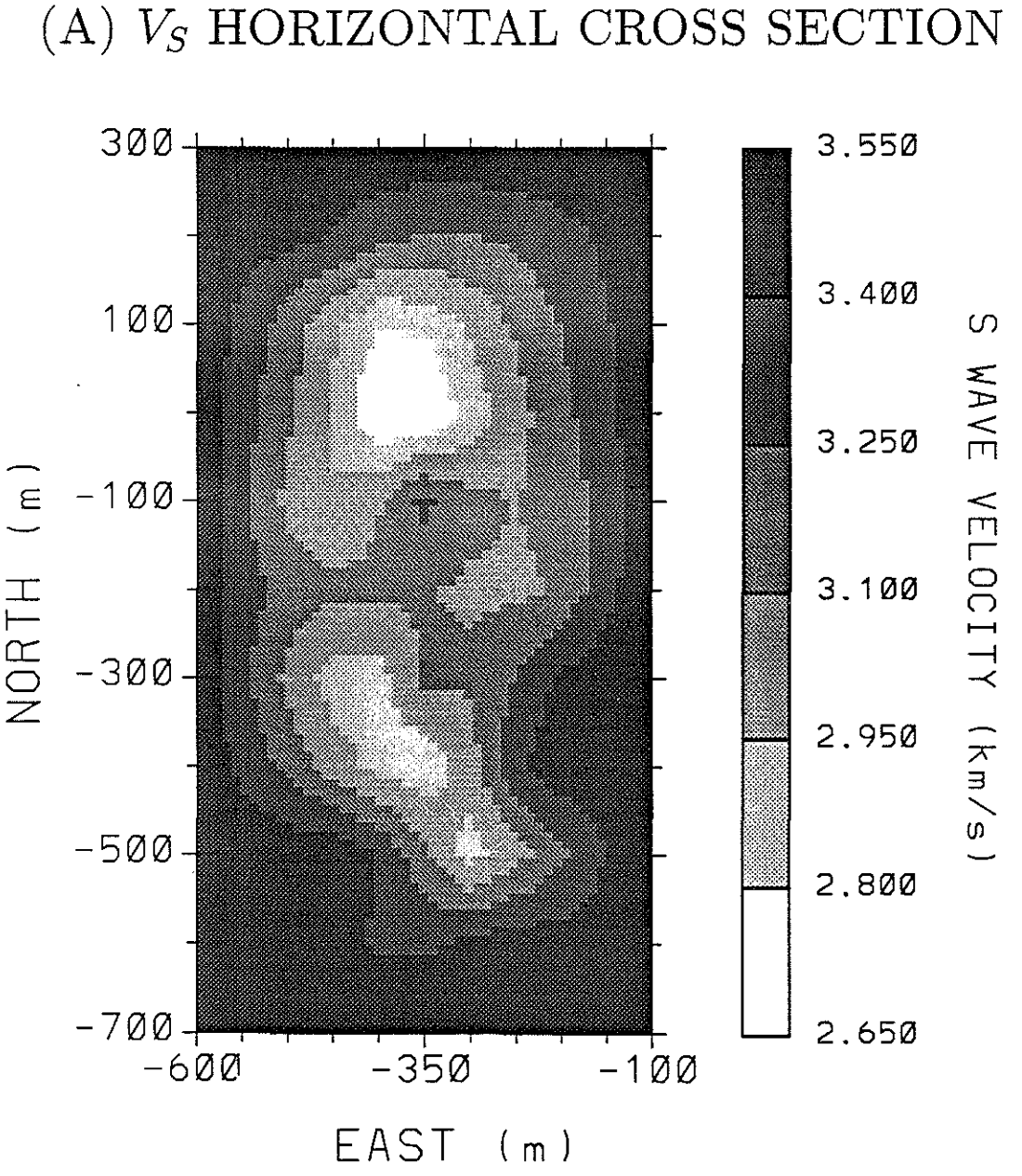

Figure 39: Horizontal cross sections, at 3500 m depth, through the final velocity models for the inversion of the synthetic data having a high noise level. (A)V_S (B) V_P. The correct velocity models are shown in Figure 37a and b.

(B) V_P HORIZONTAL CROSS SECTION

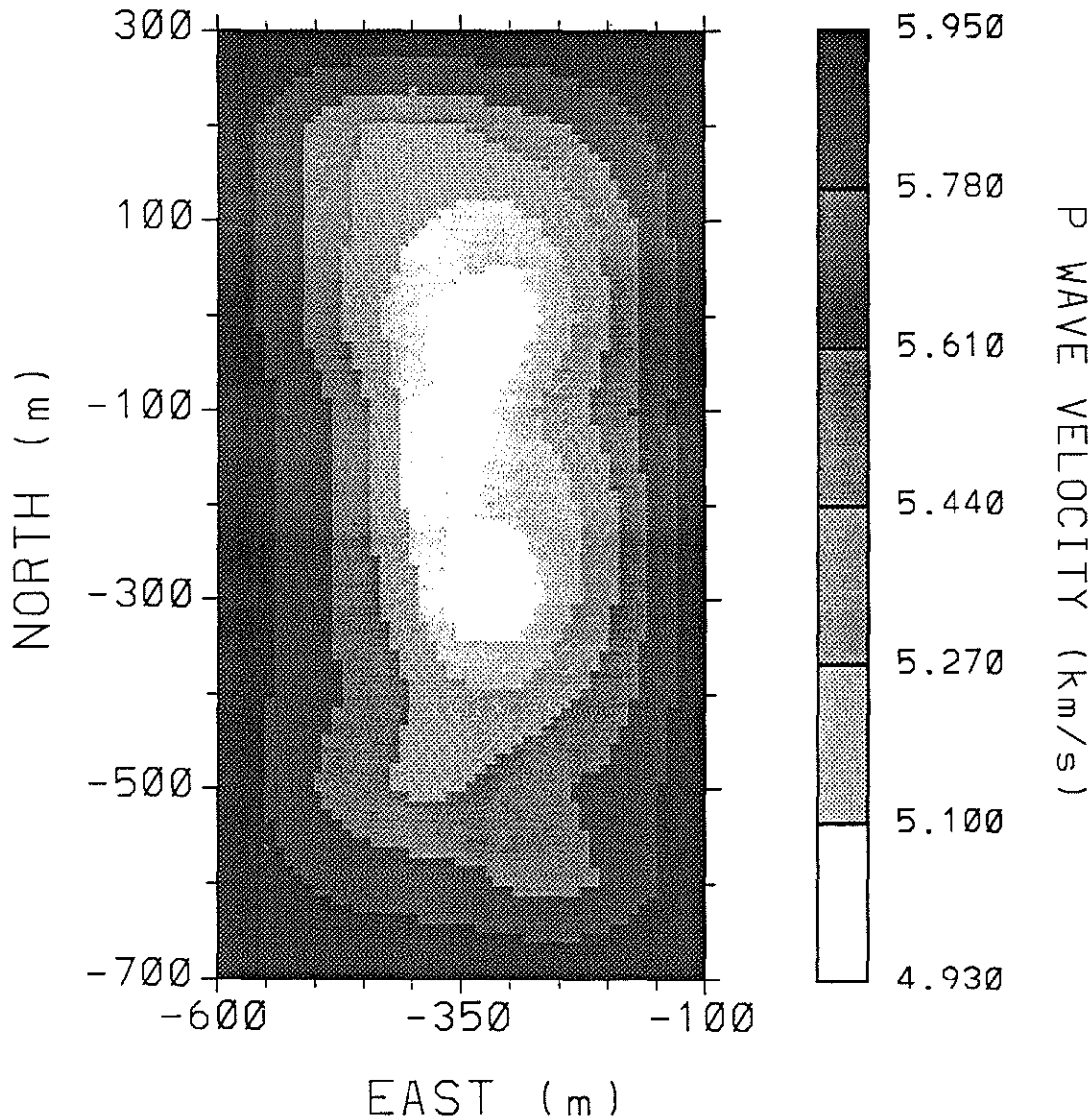

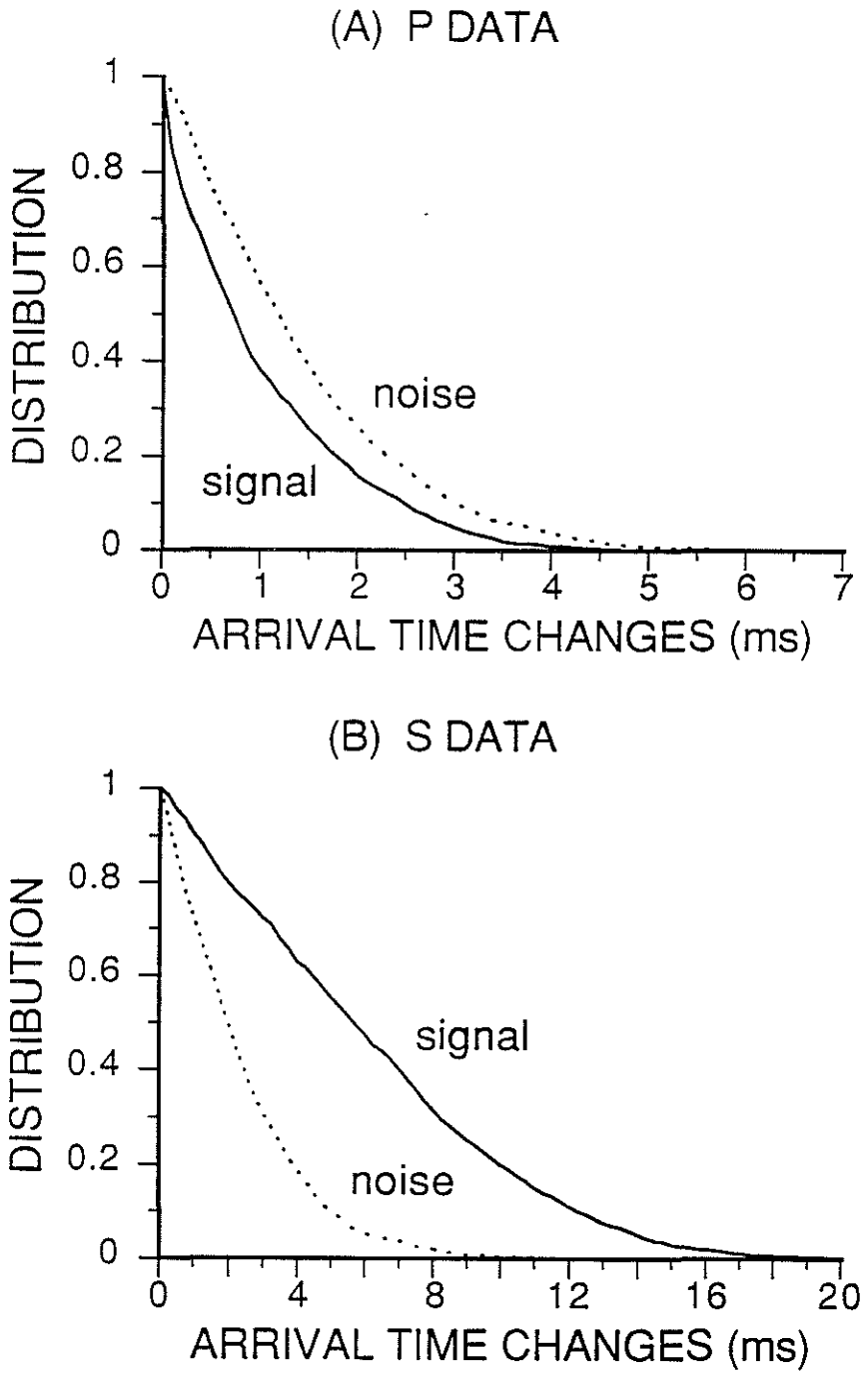

Figure 40: Distributions of the "signal" (solid lines) and noise (dotted lines) for the synthetic data having a high noise level. The velocity models used to generate the data are shown in Figure 37. (A) P data (B) S data. See the text for further explanations.

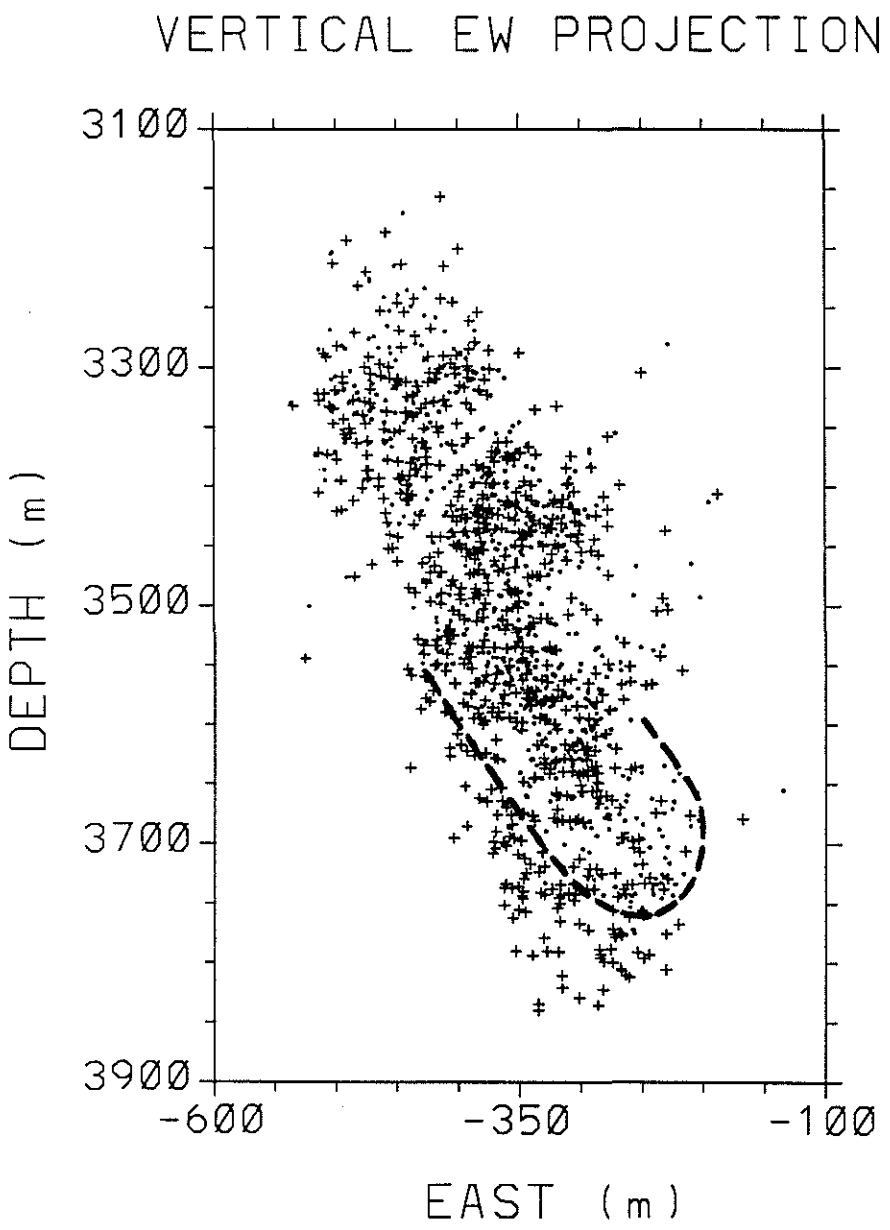

Figure 41: Vertical East-West projection of the correct earthquake locations (dots) and the final locations (plus signs) for the inversion of the synthetic data having a high noise level.

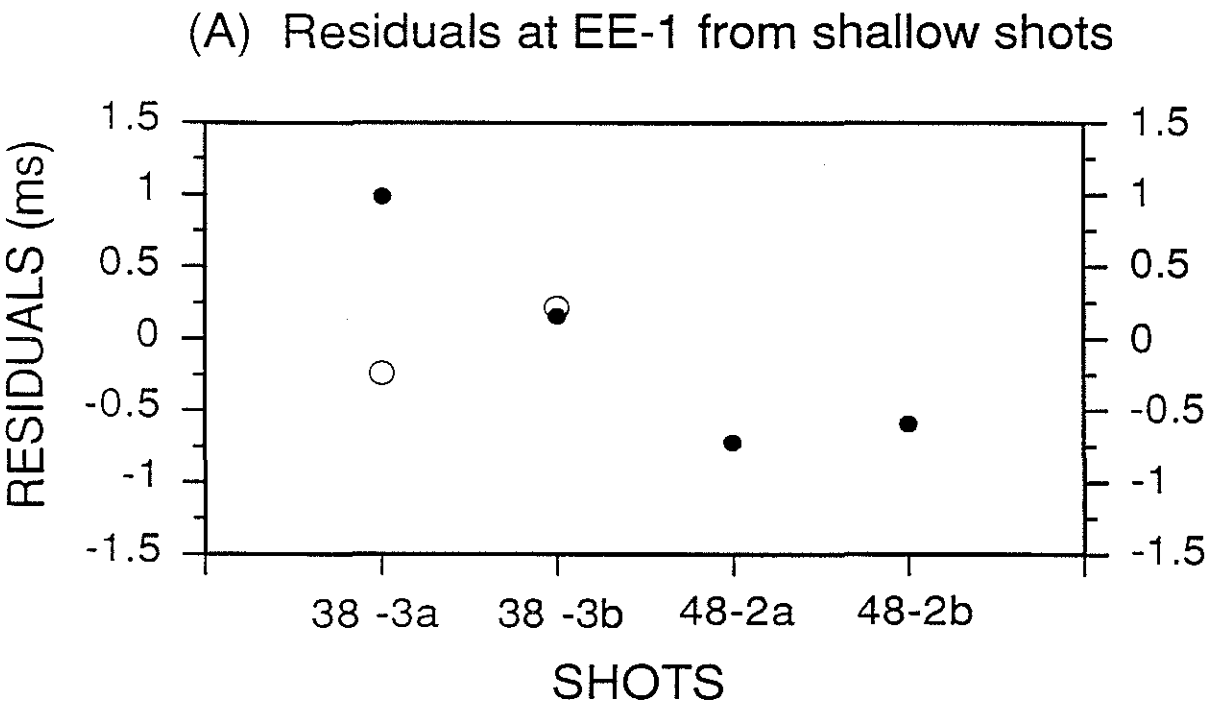

Figure 42: Final shot residuals for the inversion in Section 4.5.5 with $\lambda = 4$. Small filled circles = P residuals; large open circles = S residuals. (A) Residuals for the shallow shots which were used to determine the station corrections at EE-1. (B) Residuals at EE-1 for the deeper shots. (C) Shot residuals at station EE-3.

(B) Residuals at EE-1 from deeper shots

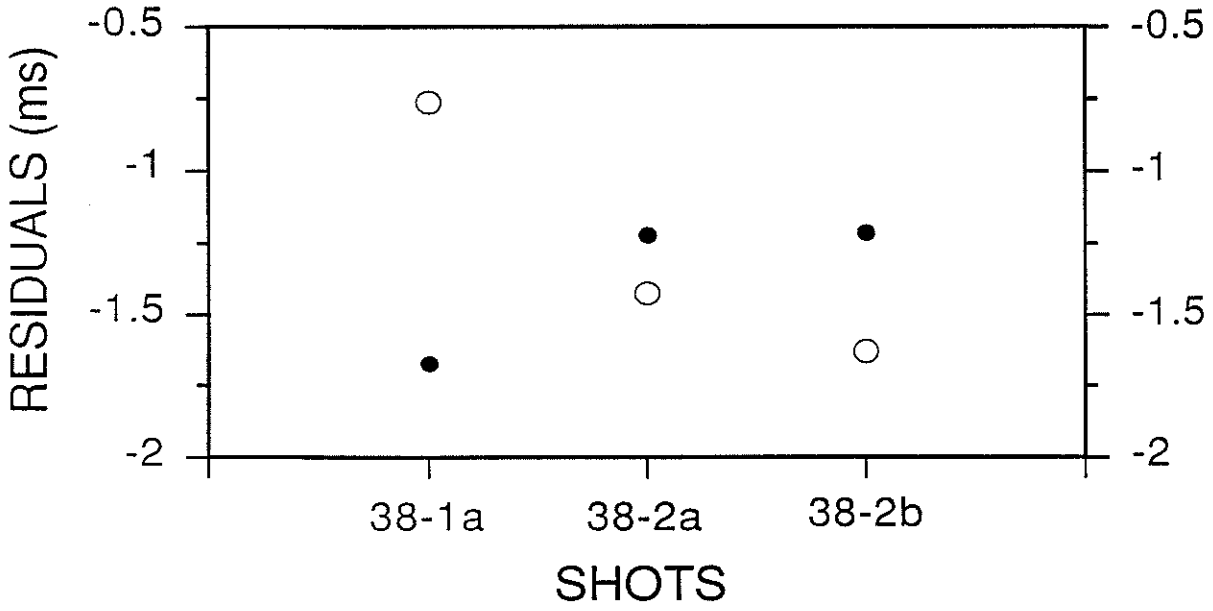

(C) All shot residuals at EE-3

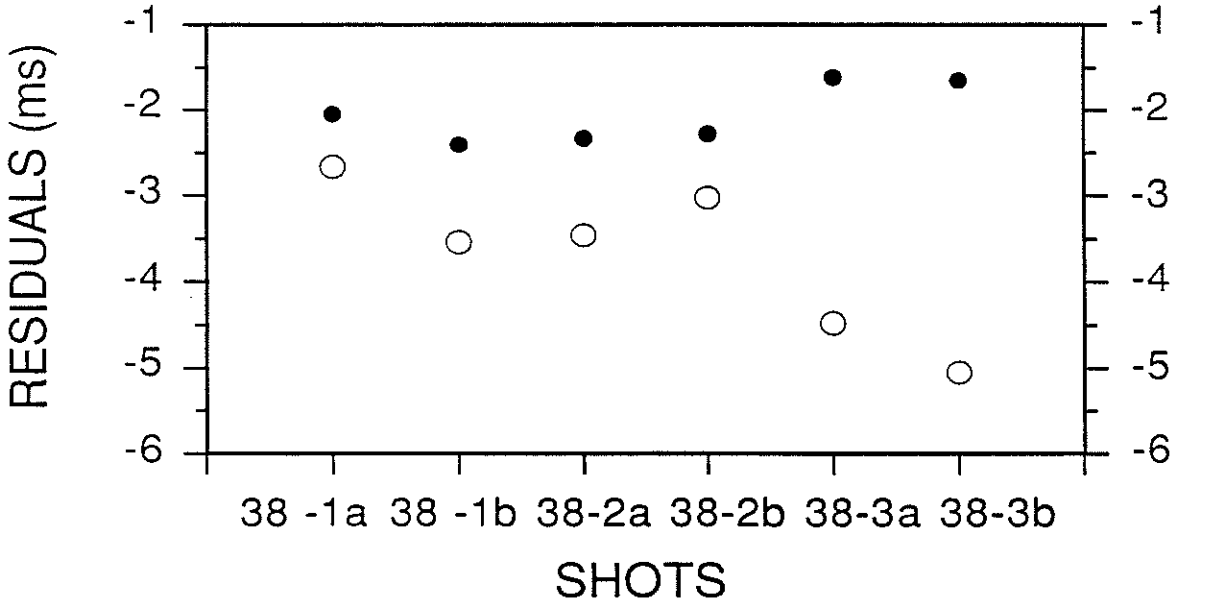

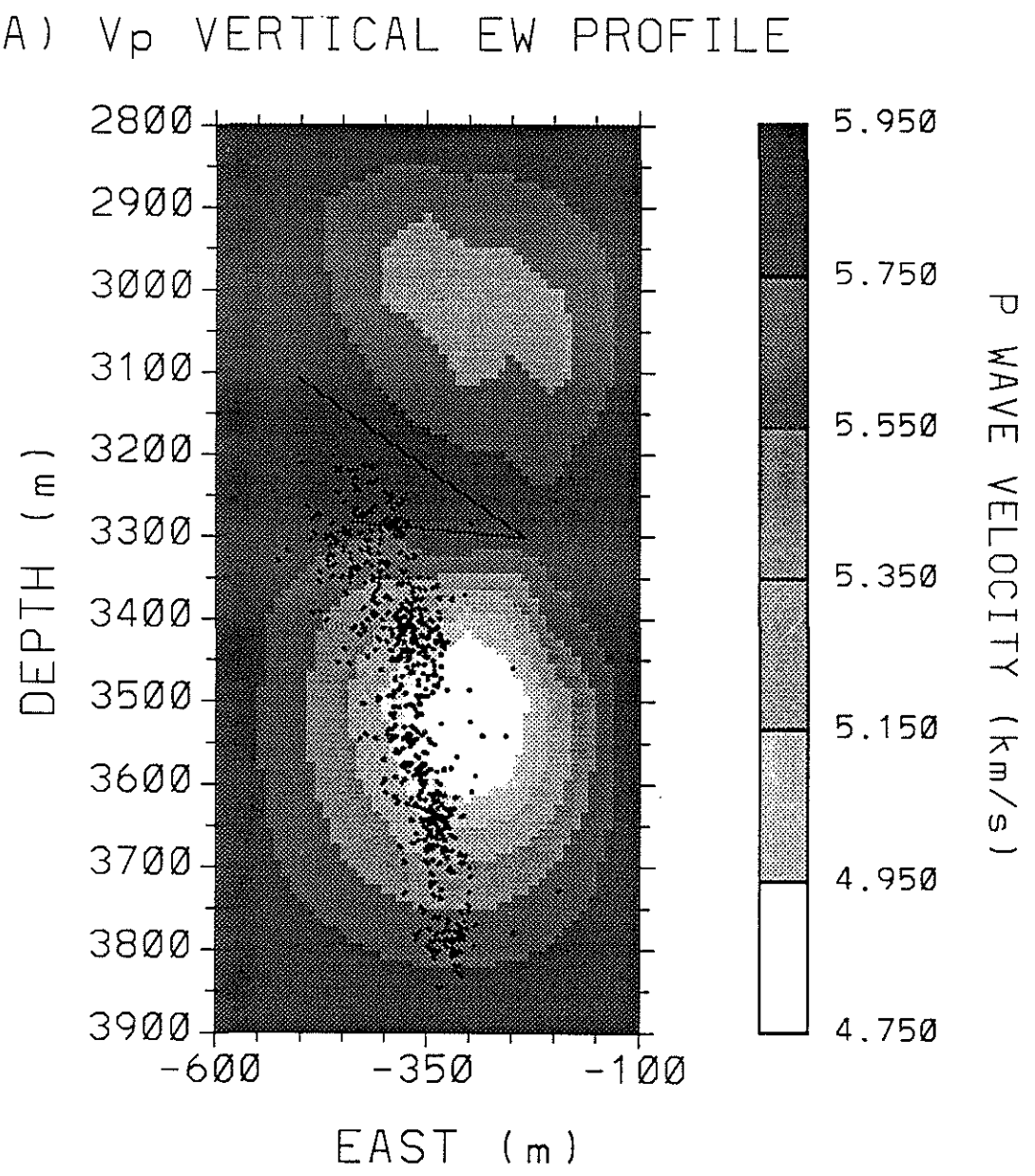

Figure 43: Results for an inversion in which the grid is extended to 2800 m depth. Vertical East-West cross sections at -300 m North. (A) V_P. (B) V_S.

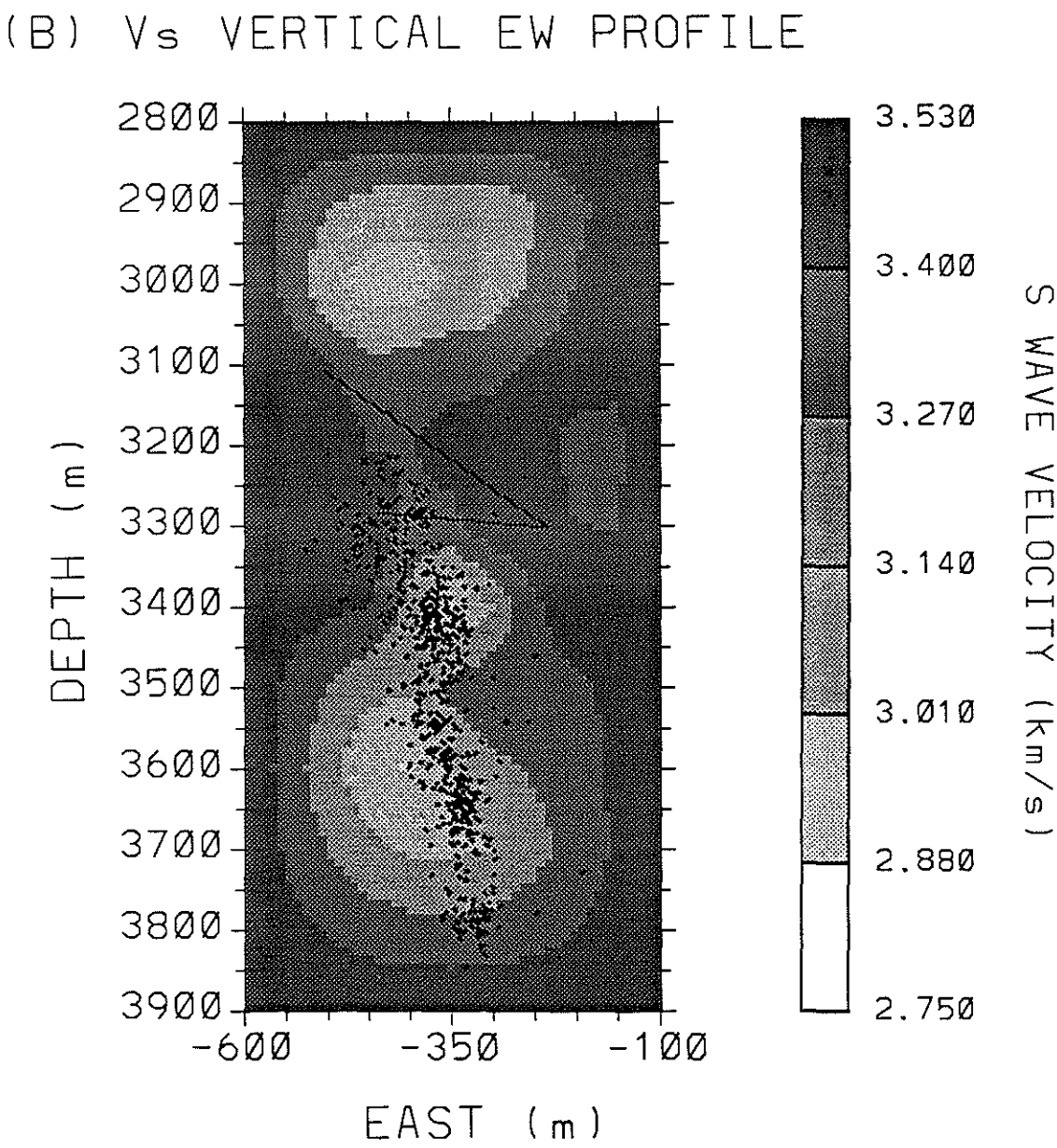
(B) Vs VERTICAL EW PROFILE
2800
2900
3000
3100
3200
3300
3400
3500
3600
3700
3800
3900
DEPTH (m)
-600
-350
-100
EAST (m)
3.530
3.400
3.270
3.140
3.010
2.880
2.750
S WAVE VELOCITY (km/s)

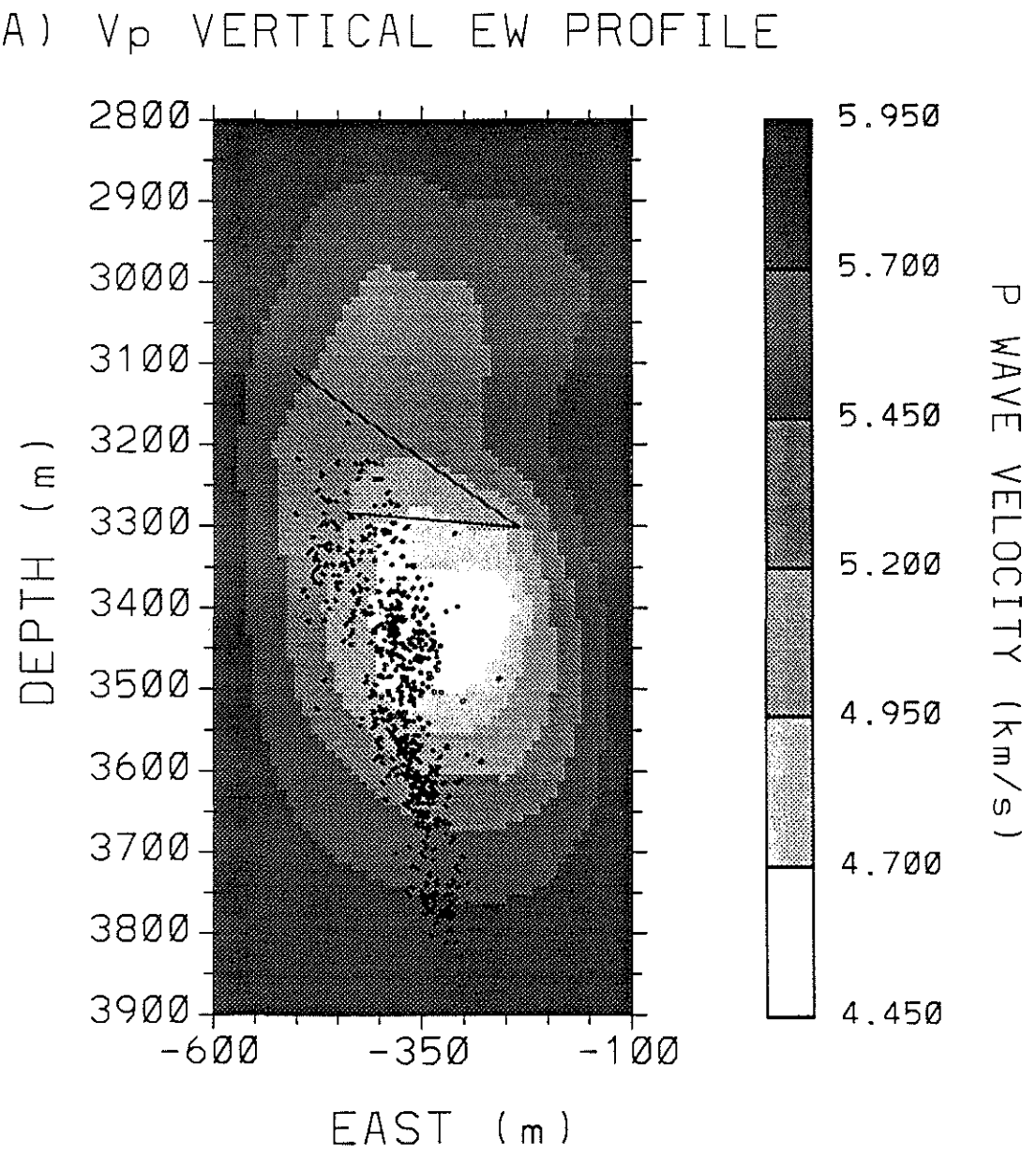

Figure 44: Results for an inversion in which the shot data are not included. Vertical East-West cross sections at -300 m North. (A) V_P. (B) V_S.

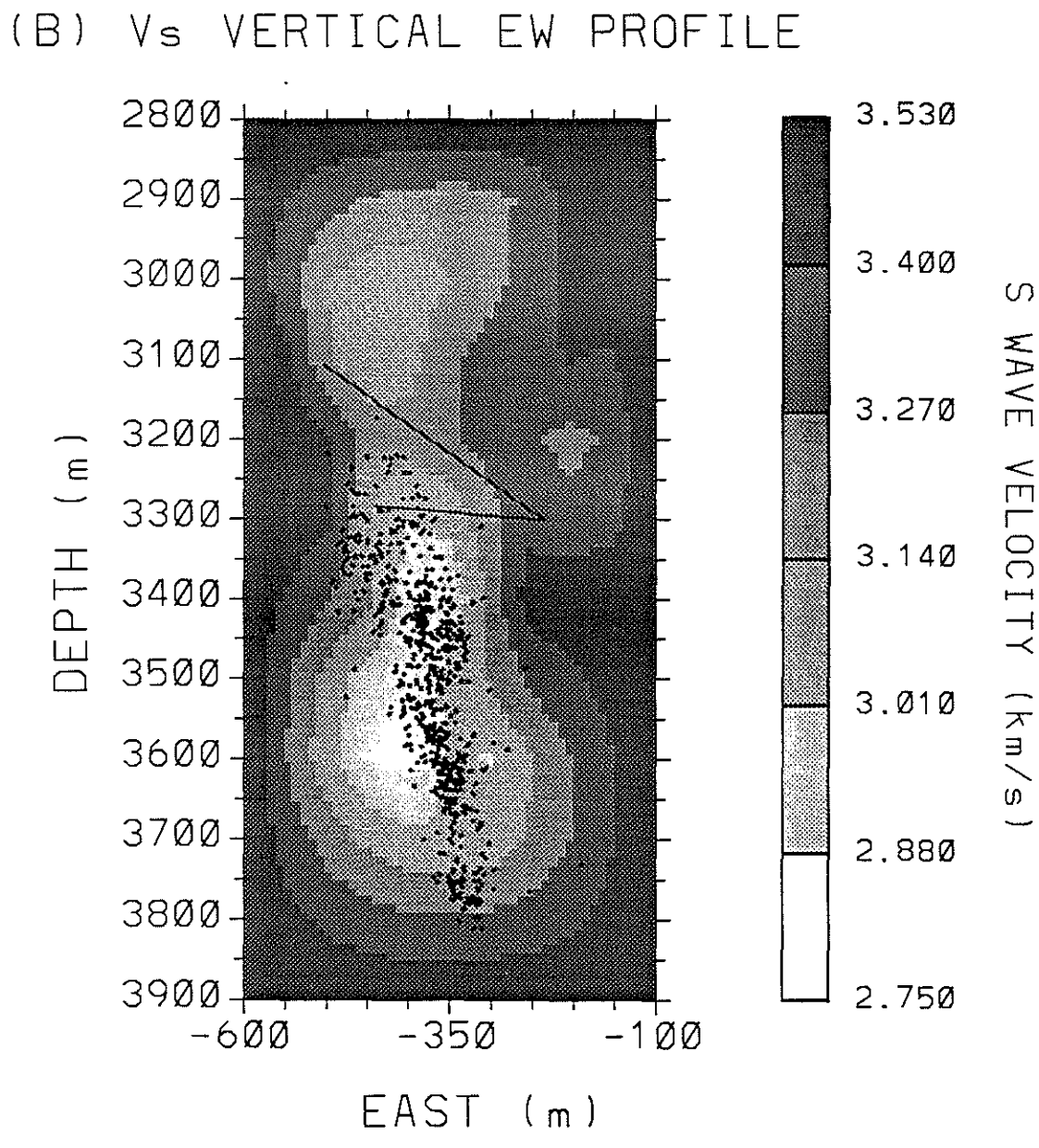
(B) Vs VERTICAL EW PROFILE
2800
2900
3000
3100
3200
3300
3400
3500
3600
3700
3800
3900
DEPTH (m)
-600
-350
-100
EAST (m)
3.530
3.400
3.270
3.140
3.010
2.880
2.750
S WAVE VELOCITY (km/s)

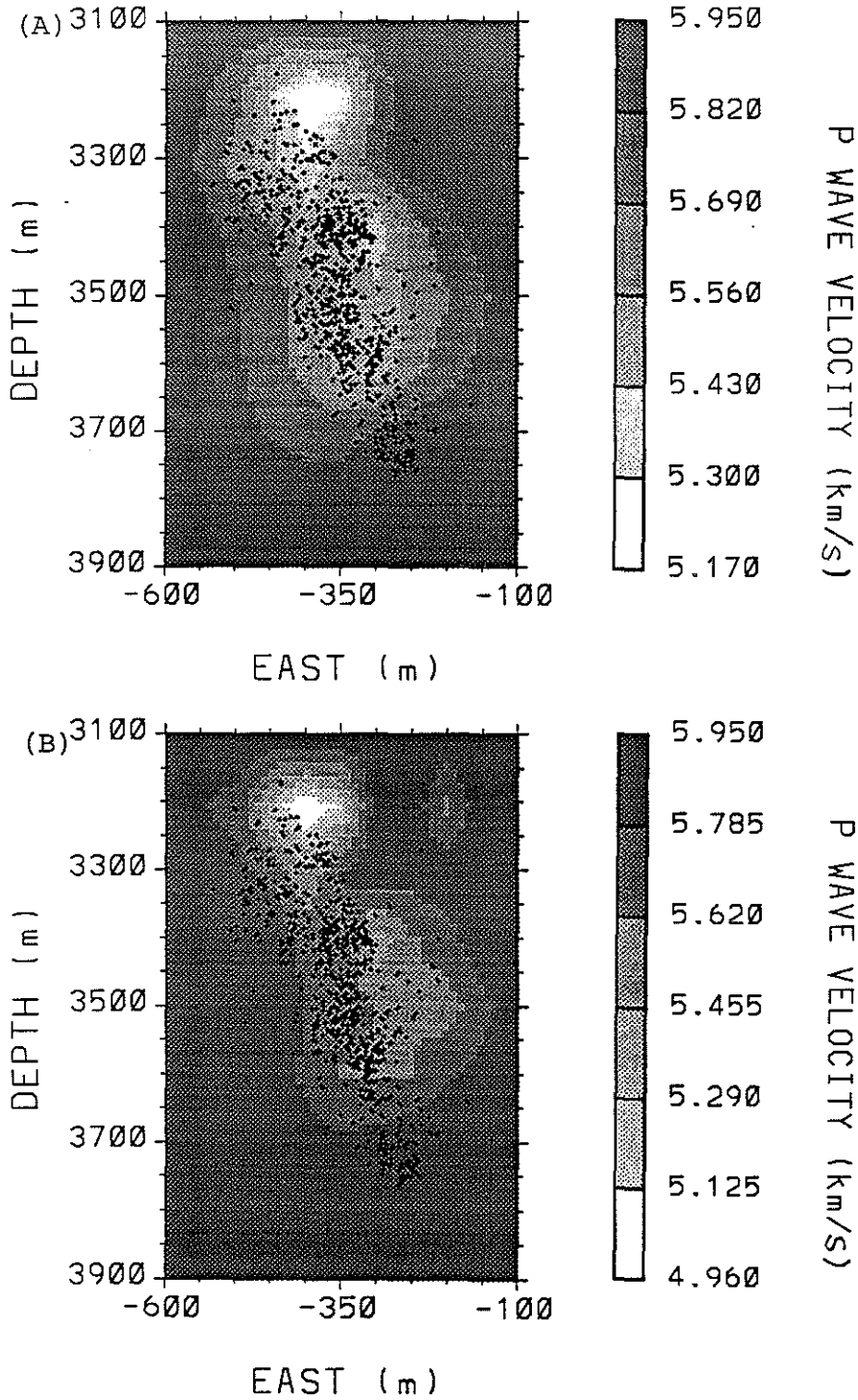

Figure 45: Results of joint inversions performed with a V_P/V_S lower bound of 1.60. Vertical East-West V_P cross sections at -300 m North. (A) $\lambda = 4$. (B) $\lambda = 1$.

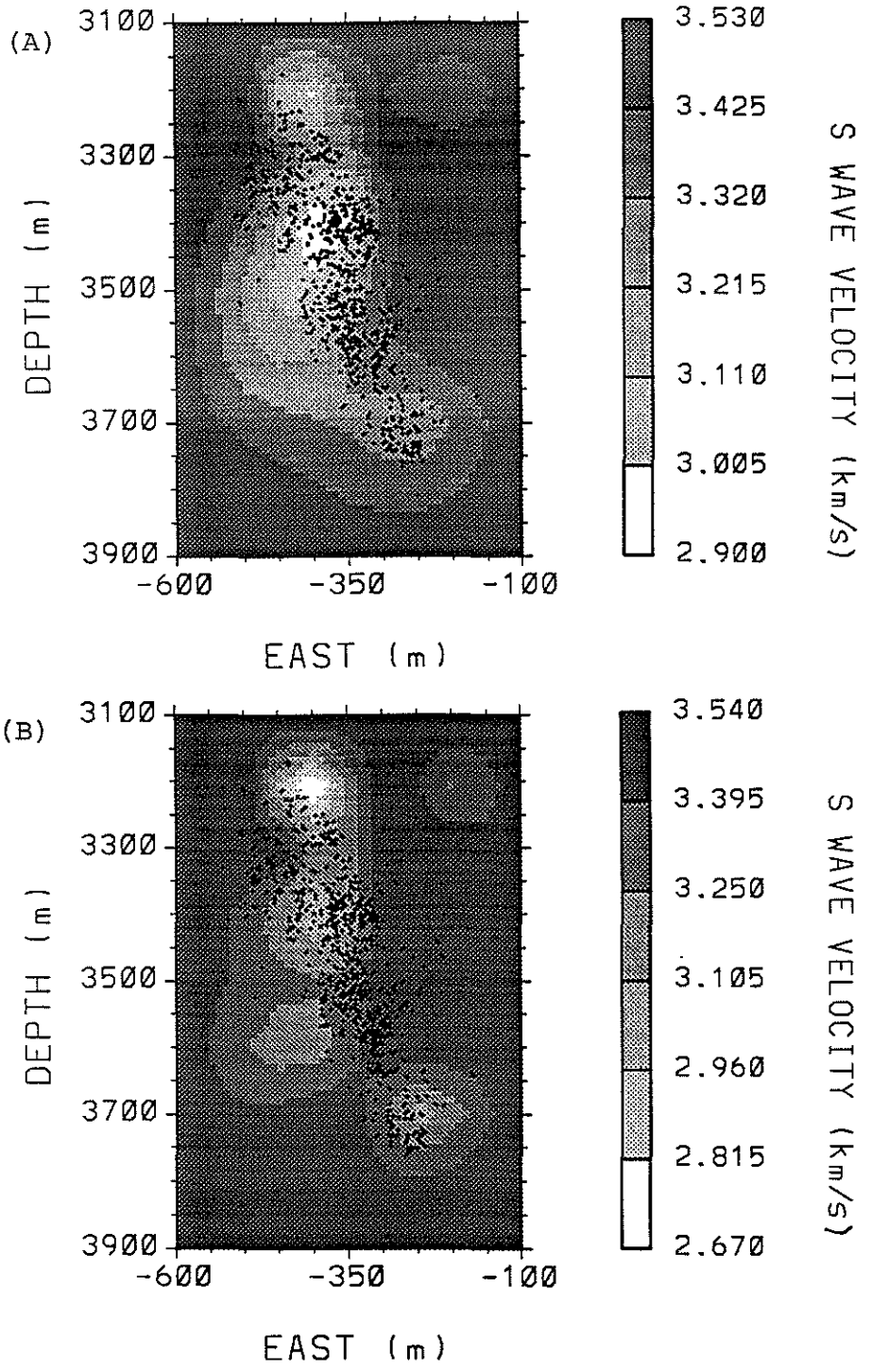

Figure 46: Results of joint inversions performed with a V_P/V_S lower bound of 1.60. Vertical East-West V_S cross sections at -300 m North. (A) $\lambda = 4$. (B) $\lambda = 1$.

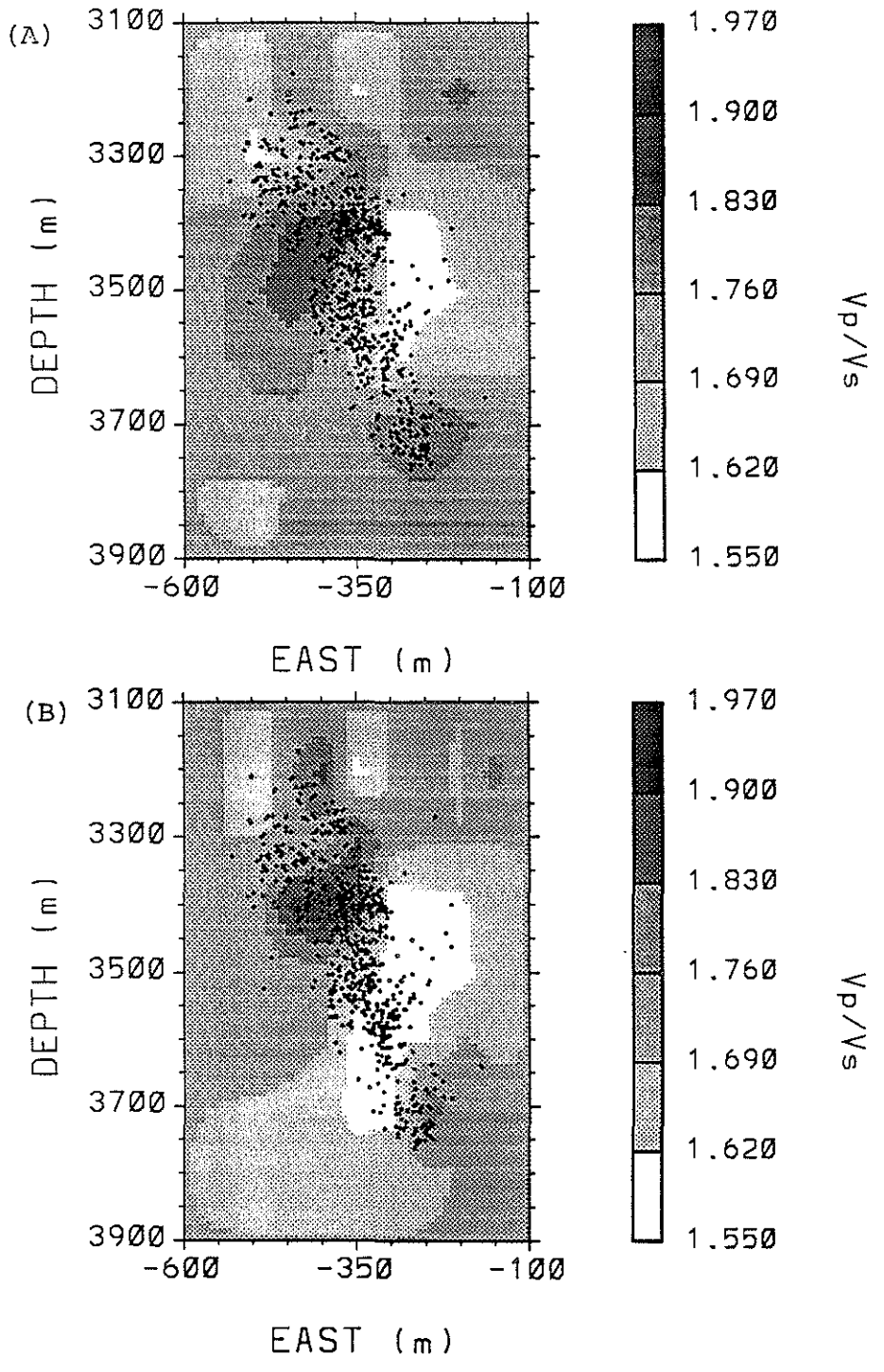

Figure 47: Results of joint inversions performed with a V_P/V_S lower bound of 1.60. Vertical East-West V_P/V_S cross sections at -300 m North. (A) $\lambda = 4$. (B) $\lambda = 1$.

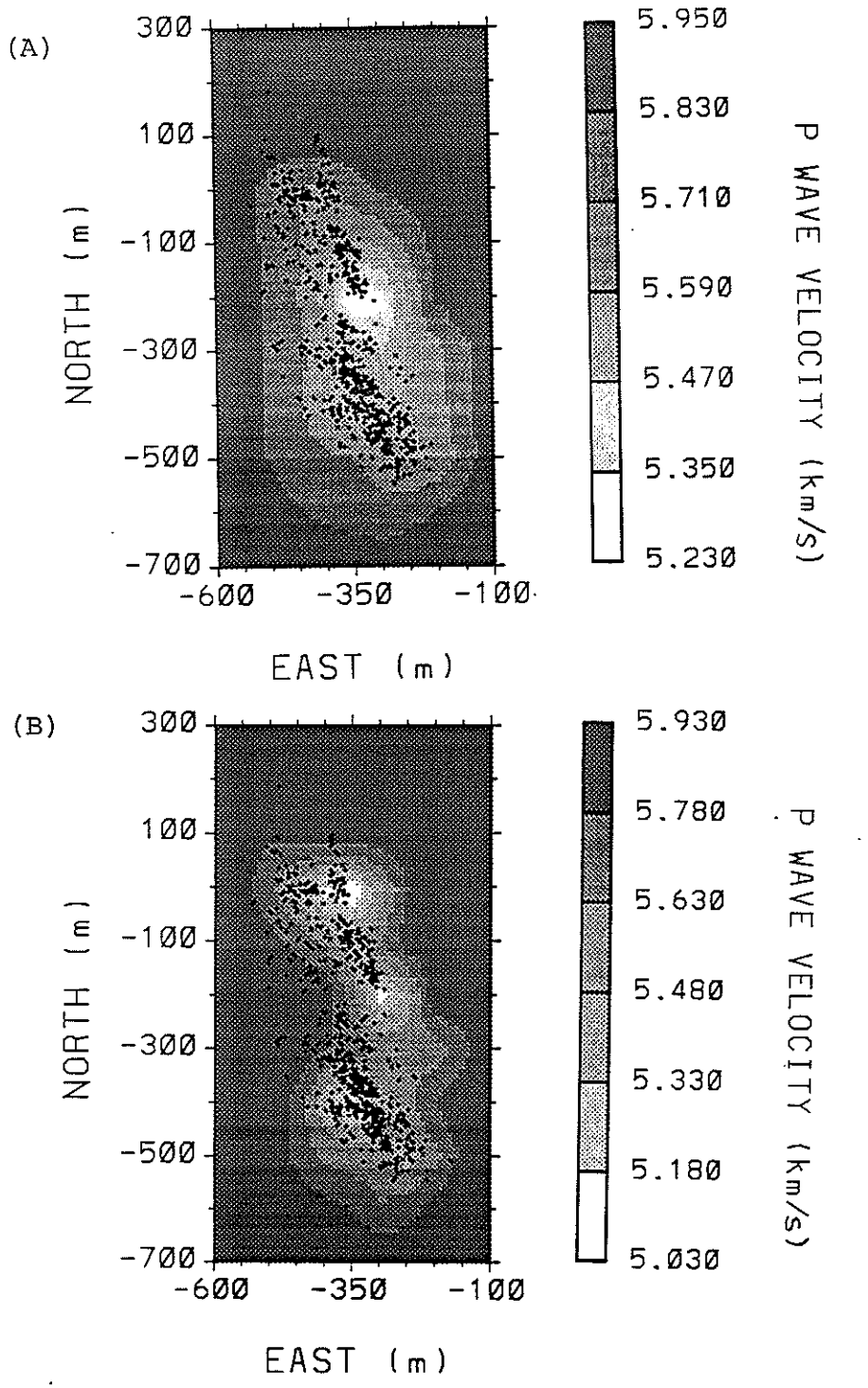

Figure 48: Results of joint inversions performed with a V_P/V_S lower bound of 1.60. Horizontal V_P cross sections at 3500 m depth. (A) $\lambda = 4$. (B) $\lambda = 1$.

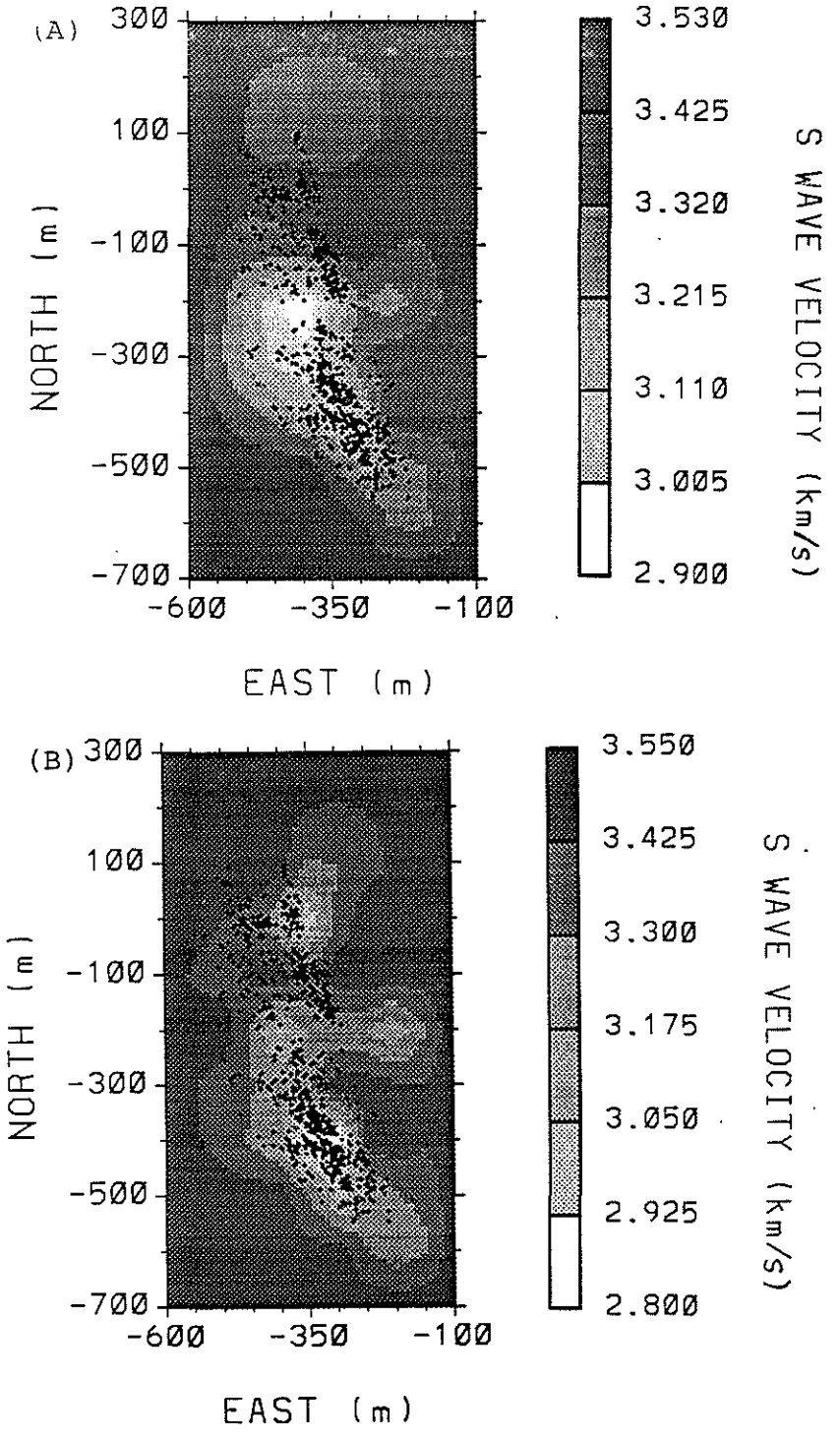

Figure 49: Results of joint inversions performed with a V_P/V_S lower bound of 1.60. Horizontal V_s cross sections at 3500 m depth. (A) $\lambda = 4$. (B) $\lambda = 1$.

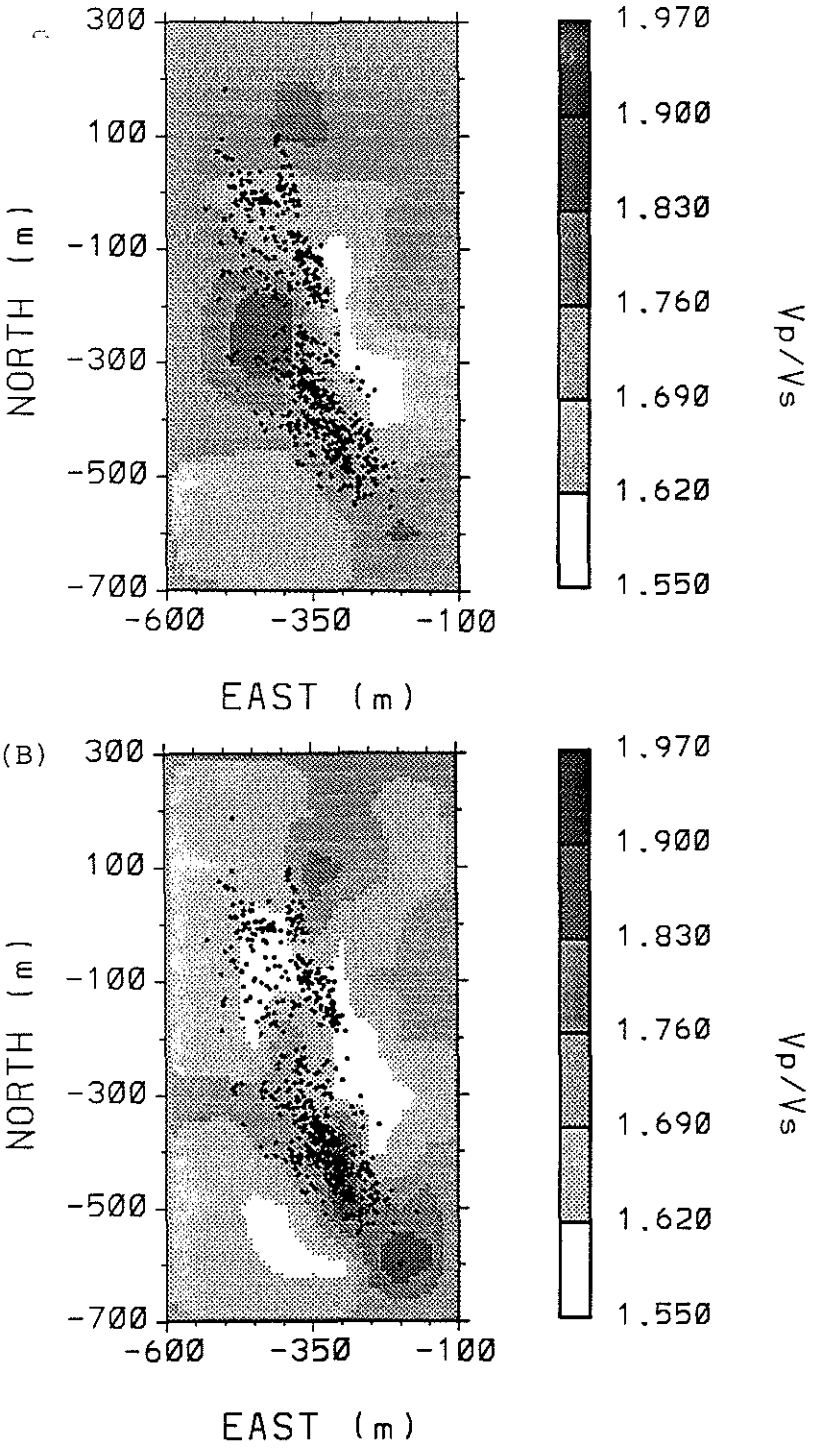

Figure 50: Results of joint inversions performed with a V_P/V_S lower bound of 1.60. Horizontal V_P/V_S cross sections at 3500 m depth. (A) $\lambda = 4$. (B) $\lambda = 1$.

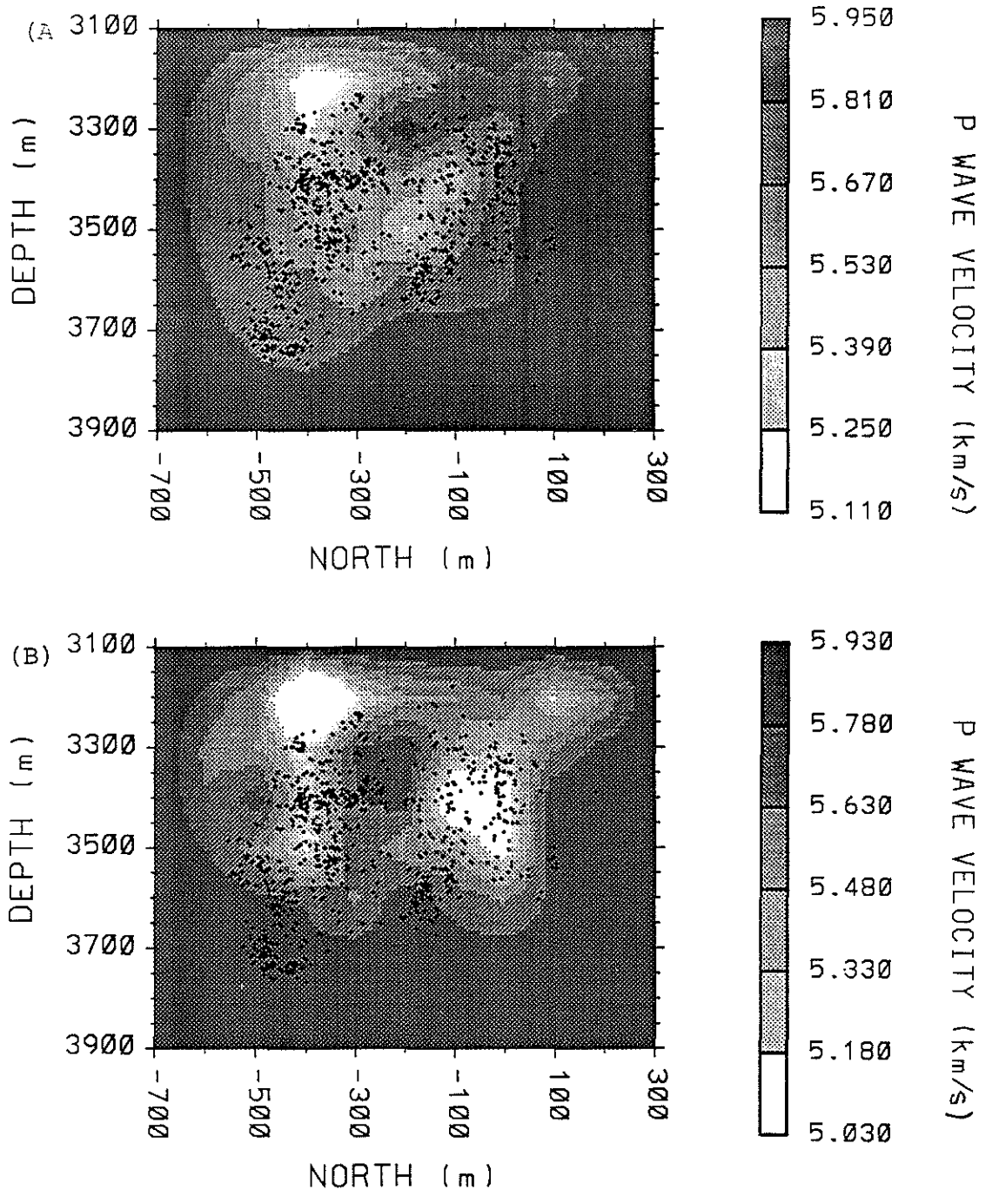

Figure 51: Results of joint inversions performed with a V_P/V_S lower bound of 1.60. Vertical North-South V_P cross sections at -350 m East. (A) $\lambda = 4$. (B) $\lambda = 1$.

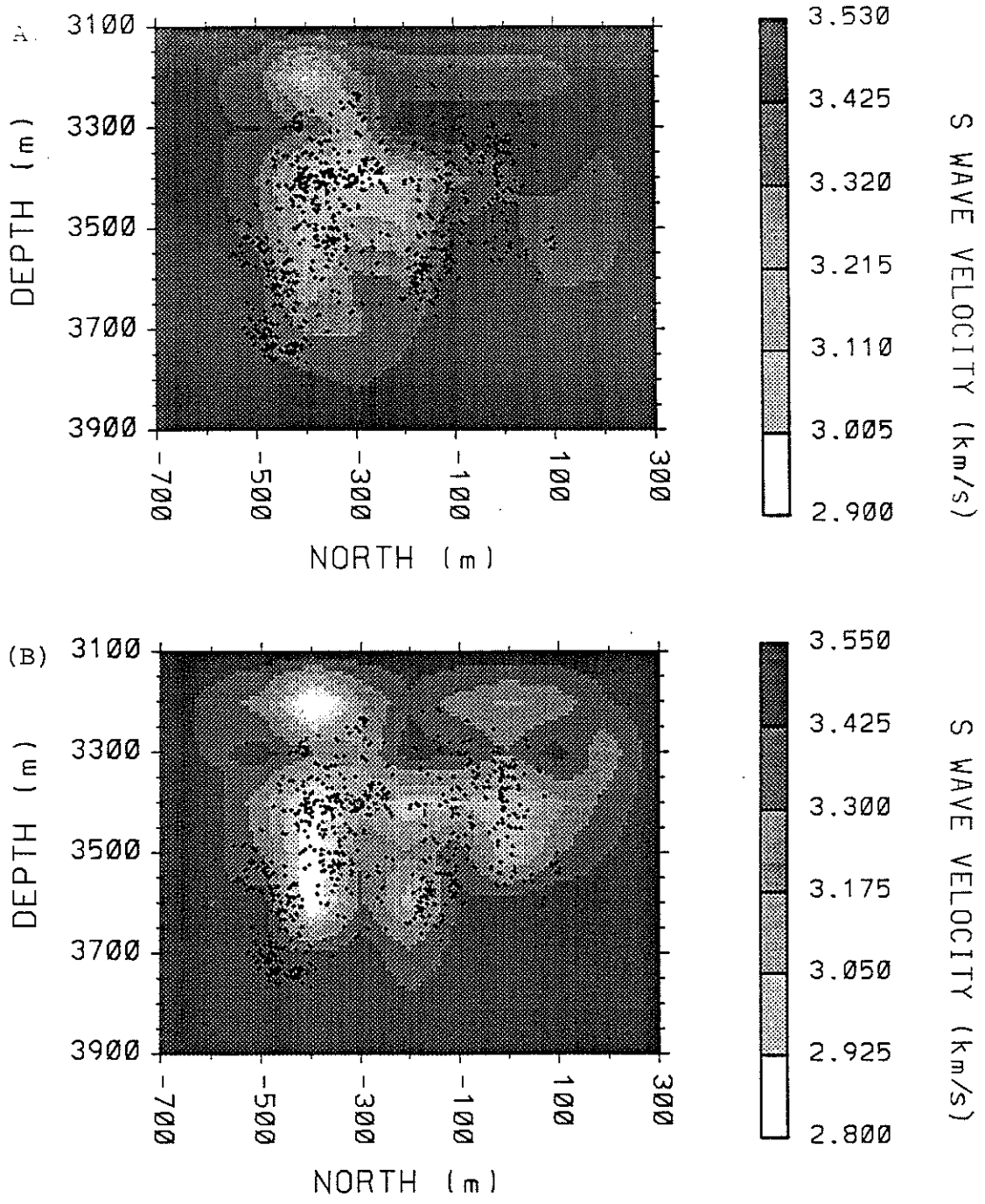

Figure 52: Results of joint inversions performed with a V_P/V_S lower bound of 1.60. Vertical North-South V_S cross sections at -350 m East. (A) $\lambda = 4$. (B) $\lambda = 1$.

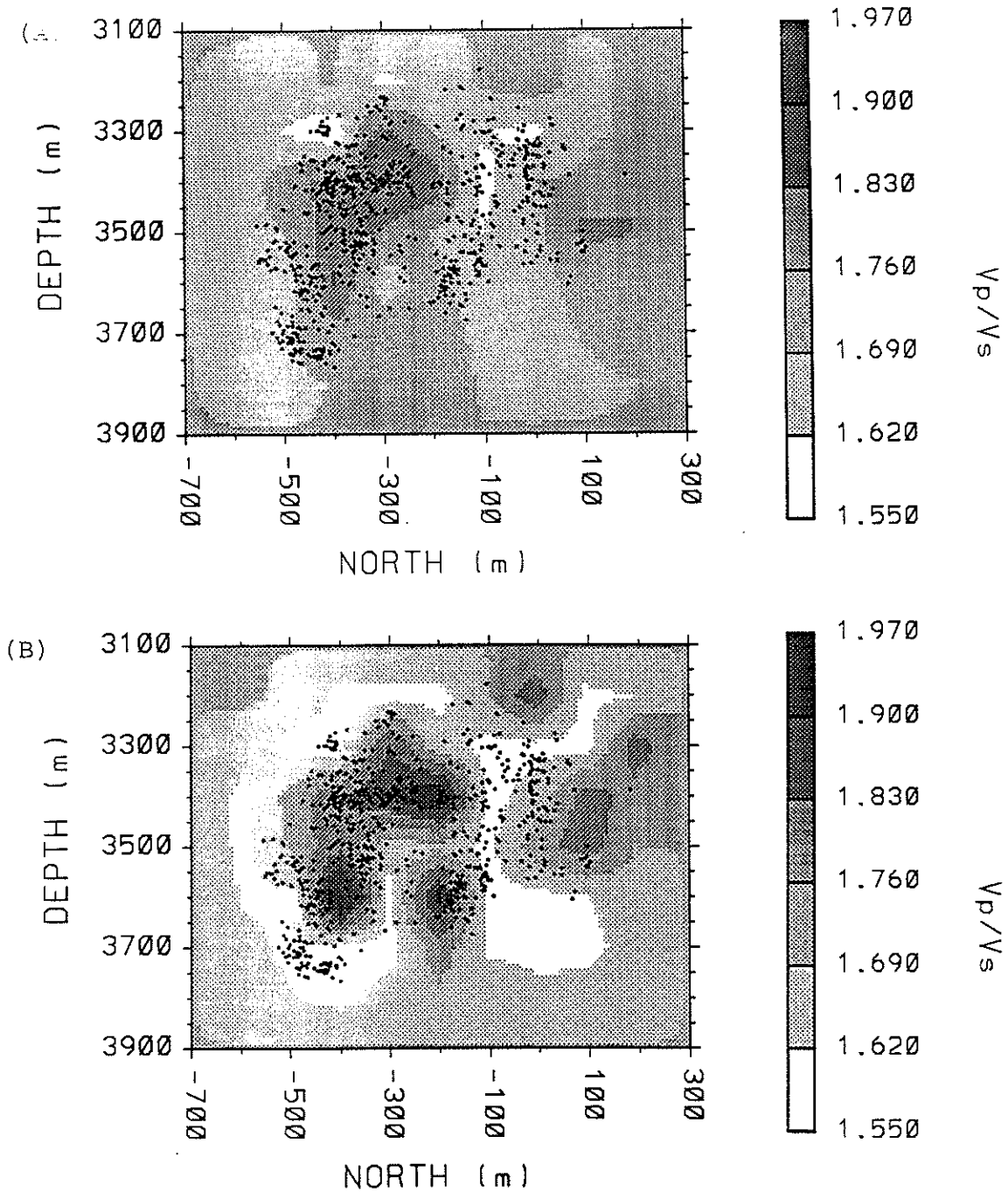

Figure 53: Results of joint inversions performed with a V_P/V_S lower bound of 1.60. Vertical North-South V_P/V_S cross sections at -350 m East. (A) $\lambda = 4$. (B) $\lambda = 1$.

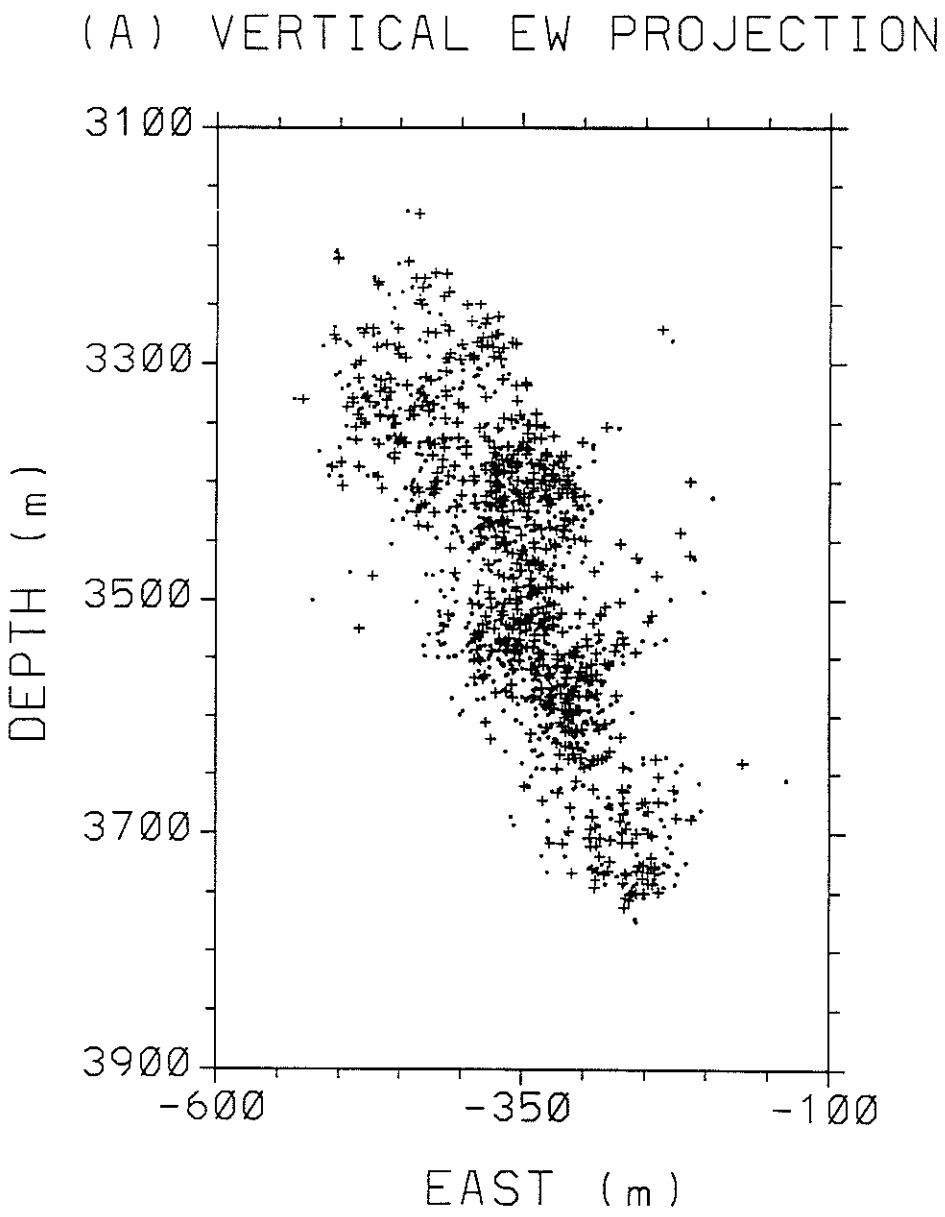

Figure 54: Projections of the initial (dots) and final (plus signs) earthquake locations for the inversion performed with a lower V_P/V_S bound of 1.60 and $\lambda = 1$. (A) Vertical E-W projection (B) Horizontal projection (C) Vertical N-S projection.

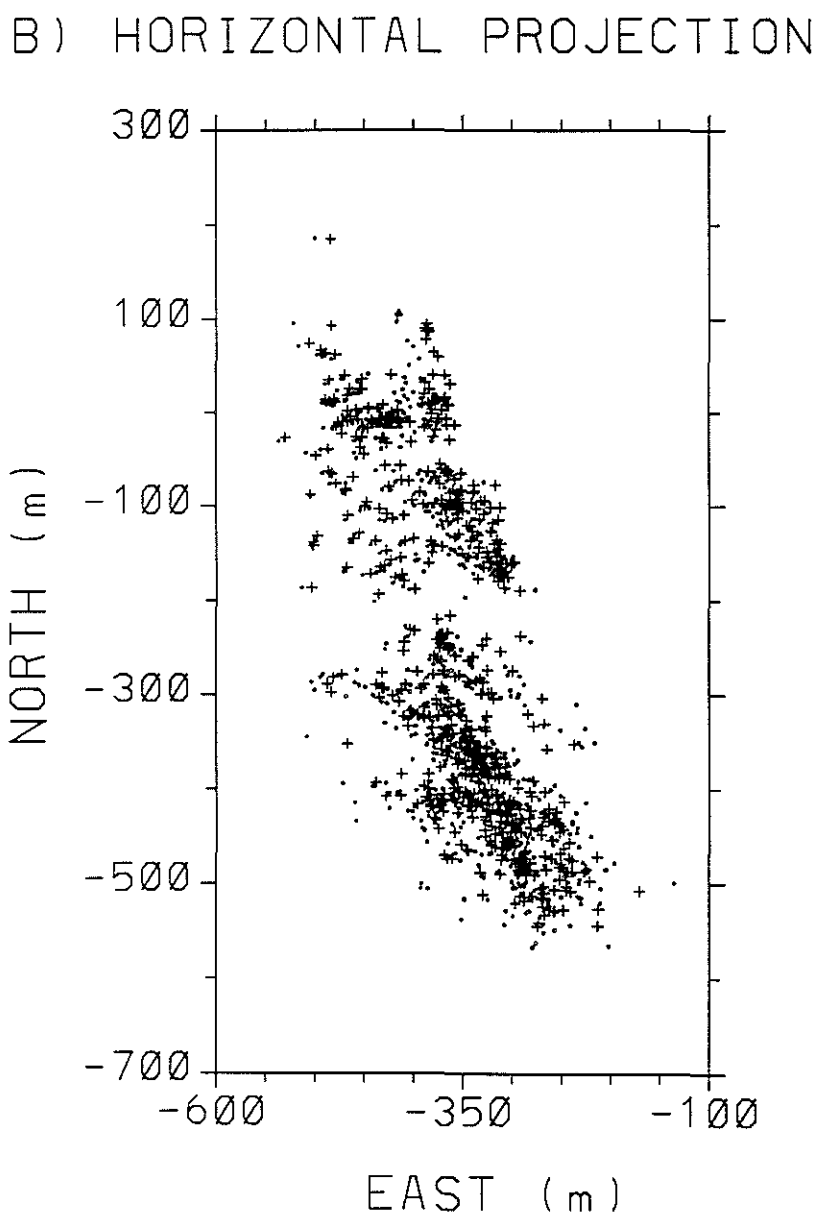
(B) HORIZONTAL PROJECTION
300
100
-100
-300
-500
-700
NORTH (m)
-600
-350
-100
EAST (m)

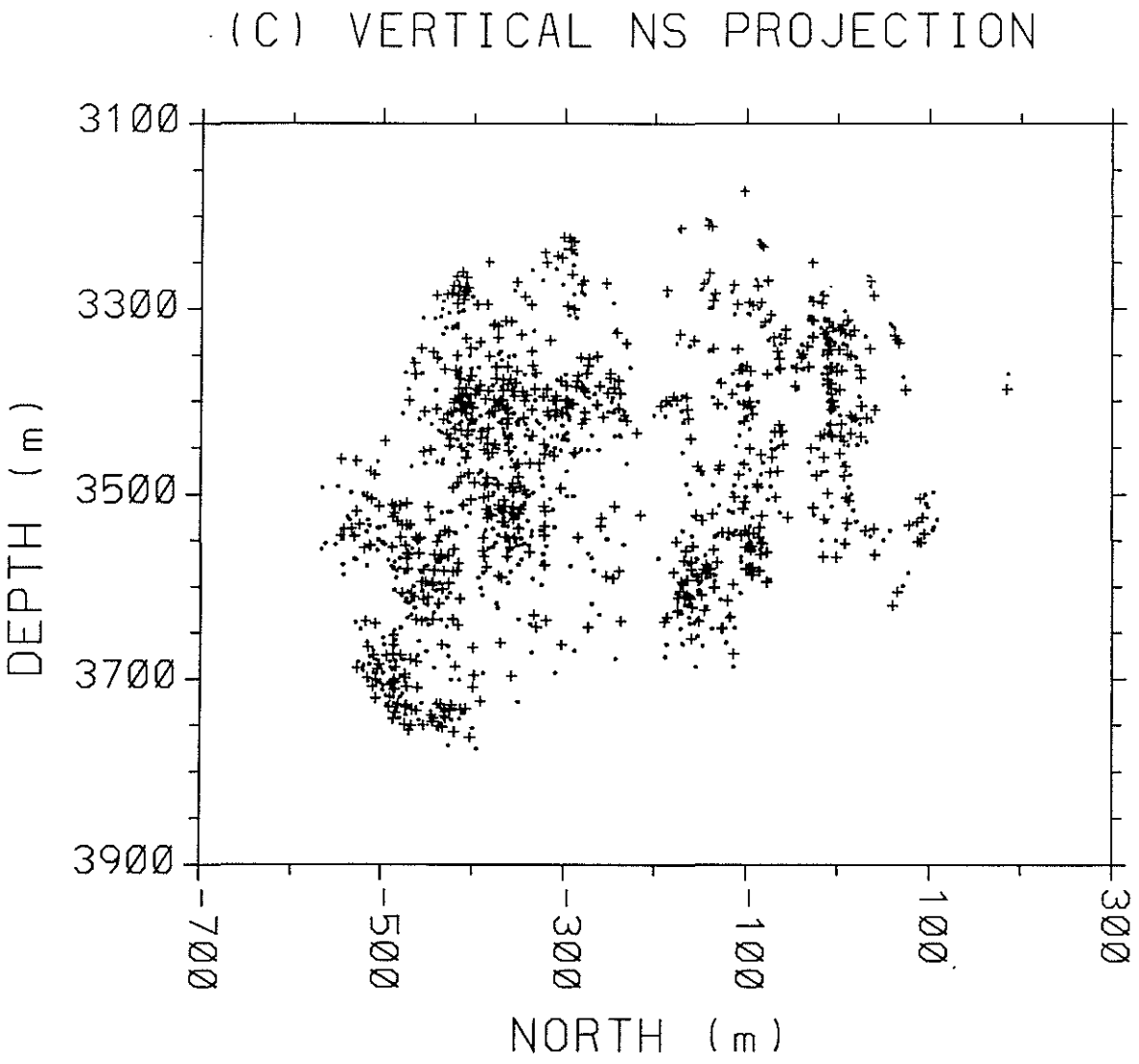
(C) VERTICAL NS PROJECTION
3100
3300
3500
3700
3900
DEPTH (m)
-700
-500
-300
-100
100
300
NORTH (m)